ELECTRONIC AND OPTICAL PROPERTIES OF TWO-DIMENSIONAL SEMICONDUCTORS

Electronic and optical properties of two-dimensional semiconductors: a study of group VI and VII transition metal dichalcogenides and phosphorene-like materials using density-functional and many-body green's-function methods

By Magdalena Laurien, M.Sc.

A Thesis Submitted to the School of Graduate Studies in the Partial Fulfillment of the Requirements for the Degree Doctor of Philosophy

McMaster University © Copyright by Magdalena Laurien December 16, 2021

McMaster University
Doctor of Philosophy (2021)
Hamilton, Ontario (Department of Materials Science and Engineering)

TITLE: Electronic and optical properties of two-dimensional semiconductors: A study of group VI and VII transition metal dichalcogenides and phosphorene-like materials using density-functional and many-body Green's-function methods
AUTHOR: Magdalena Laurien (McMaster University)
SUPERVISOR: Dr. Oleg Rubel
NUMBER OF PAGES: xii, 201

Abstract

In the search for nano-scale, highly customizable materials for next-generation electronic devices, two-dimensional (2D) materials have generated much interest. 2D materials have complex, layer-dependent optical and electronic properties of which many aspects remain yet to be explored and fully understood. The aim of this thesis was to investigate and explain optoelectronic properties of several 2D materials systems towards device design. This was accomplished using predictive physical modelling at the density functional theory level (DFT) as well as many-body theory (GW+BSE).

The optical transitions of bulk ReS_2 and $ReSe_2$ were studied using DFT in comparison with experiment. We found that the orbital composition of the band edges determined the sign of the pressure coefficient of the optical gap. Our results provide a step towards understanding the perceived layer-independence of the optical properties of ReS_2 and $ReSe_2$.

The exciton landscape of MoS_2 monolayer was explored in detail using many-body theory (GW+BSE). We found dark excitons very close to bright excitons and even lower in energy. Our results help reverse the common assumption that the lowest-energy exciton in MoS_2 is bright.

The ideal band offset between recently predicted monolayers of the CaP_3 family was predicted using GW theory. We observed chemical trends in the band offsets and explained their origin. Our results serve as indicators for heterojunction design with these novel materials.

The effective mass of a test set of eighteen semiconductors including several 2D materials was calculated using DFT with semi-local and non-local hybrid exchange-functionals and compared for accuracy with respect to experimental data. Our analysis details the effect of the nonlocal exchange potential on the accuracy of the effective mass. Our results give guidelines for high-throughput calculations of the effective mass for different material classes, including 2D materials.

Acknowledgements

I thank Jesus Christ, my Savior, the only true God, who has created the universe and sustains it by the word of his power, for giving me life and for sustaining me in his tender mercy.

I would like to express my deep gratitude to my project supervisor Prof. Oleg Rubel for giving me the opportunity to undertake graduate studies under his guidance. Thank you for teaching me density functional theory (among many other things!), for being generous with feedback and quick to help with whatever the task on hand.

Special thanks to my collaborators, Robert Oliva and Hongyu Yu and their research groups for their enthusiasm at work. It was a joy to work with you. Many thanks to my Ph.D. supervisory committee, Dr. Adrian Kitai and Dr. Nabil Bassim. Your suggestions for my research were much appreciated. I would like to thank my colleagues from the Rubel group, Chao Zheng, Divyanshu Gupta and Himanshu Saini for sharing this journey with me. Thank you for always being ready to help.

I thank my husband for encouraging and challenging me with his godliness, diligence, kindness and patience. Life with you is a joy. My life would not be the same without the love and kindness of family and friends here and abroad. Thank you! I especially thank my parents for all their efforts in raising me and for always encouraging my scientific curiosity.

Contents

List of Figures

List of Tables

Declaration of Authorship

I, Magdalena Laurien, declare that this thesis titled, "Electronic and optical properties of two-dimensional semiconductors: a study of group vi and vii transition metal dichalcogenides and phosphorene-like materials using density-functional and many-body green's-function methods" and the work presented in it are my own. The major research results of my Ph.D. study were published or have been submitted to peer-reviewed journals. The publications and submitted manuscripts are listed below:

- Robert Oliva, **Magdalena Laurien**, Filip Dybala, Jan Kopaczek, Ying Qin, Sefaattin Tongay, Oleg Rubel, and Robert Kudrawiec. "Pressure dependence of direct optical transitions in ReS_2 and $ReSe_2$." npj 2D Materials and Applications 3, no. 1 (2019): 1-8. (As a co-author of this paper, my contribution to this project accounts for ca. 40%.)

- Hongyu Yu, **Magdalena Laurien**, Zhenpeng Hu, and Oleg Rubel. "Exploration of the bright and dark exciton landscape and fine structure of MoS_2 using G_0W_0-BSE." Physical Review B 100, no. 12 (2019): 125413. (As a co-author of this paper, my contribution to this project accounts for ca. 50%.)

- **Magdalena Laurien**, Himanshu Saini, and Oleg Rubel. "Band alignment of monolayer CaP_3, $CaAs_3$, $BaAs_3$ and the role of p–d orbital interactions in the formation of conduction band minima." Physical Chemistry Chemical Physics 23, no. 12 (2021): 7418-7425.

- **Magdalena Laurien** and Oleg Rubel. "Importance of the nonlocal exchange potential for effective mass calculations in semiconductors: Benchmarking exchange-correlation potentials with the mstar60 dataset." Submitted to a peer-reviewed journal.

To my future children.

Chapter 1

Introduction

1.1 Motivation

Layered materials, also called 2D materials, are crystalline materials in which the constituting atoms are predominantly covalently bound within a two-dimensional plane and linked by weak van-der-Waals (vdW) interactions in the third dimension. Examples of layered materials include graphite and transition metal dichalcogenides (TMDCs) like MoS_2 and WS_2, materials that have been studied for decades and used as lubricant additives.[1, 2, 3] In 2004, Novoselov et al. [4] reported the successful mechanical exfoliation of graphite to one to few and one-layer (1L) graphene and described the extraordinary electrical properties of this material. The researchers showed that single-layer graphene exhibits a strong electric field effect and extremely high carrier mobilities. The discovery of graphene was followed by intense multi-disciplinary research efforts exploring nanofabrication routes and characterization techniques of atomically thin 2D materials. Atomically thin 2D materials show fascinating properties such as superior surface-to-volume ratio, dangling-bond-free surfaces, sizable bandgaps, and layer-dependent properties, making them interesting for both fundamental scientific research and technological applications.[5, 6] In addition, 2D materials are subject to dimensionality effects due to quantum confinement, which affects their optical and electrical properties.[7] One example of layer-dependent properties is the indirect to direct bandgap transition in MoS_2: the bandgap changes from indirect in the bulk to direct in the monolayer.[8] Another example is that dimensionality effects coupled with lack of charge screening lead to a stronger binding energy of an excited electron-hole pair so that optical transition energies are considerably altered in the monolayer limit.[9]

There is a vast number of applications for 2D materials for future electronic and optoelectronic devices. Proof-of-principle devices fabricated with 2D materials include

pn junctions[10], sensors[11], solar cells[12], light-emitting devices[13] and polarizers[14]. Meanwhile, exciting theoretical discoveries lead to unforeseen possibilities, inspiring completely new device concepts.[15, 16, 17]

With the advent of machine learning and high throughput scanning of databases, 2D materials prediction has been accelerated considerably. With the growing library of two-dimensional materials with many different properties, the idea emerged to combine them by stacking them along their van-der-Waals gap to form heterostructures.[18] Two-dimensional materials can be stacked without the requirement of a strict commensurate lattice and with the absence of dangling bonds. The prospect of combining selected materials in a heterostructure creates exciting possibilities for designing quantum materials on-demand.[19]

Many heterostructures have been fabricated, but we are still far from the vision of properties on demand. Also, the rapid increase of computational predictions poses a challenge to the materials science community, as there is an ever-growing disconnect between theoretical discoveries and the experimental realization of new 2D materials.[20] There are several ways to make newly predicted 2D materials more accessible for experimental realization: Computational materials science is a useful tool for predicting complex structure-property relations that facilitate the understanding and help forge pathways to the design of new 2D material fabrication routes and applications.

In this line, the overall objective of this thesis was to advance the design of 2D materials with a focus on their optoelectronic properties, using cutting-edge predictive physical modelling. This objective was pursued in several short-term research projects. We carefully analyzed existing and newly proposed 2D materials with theoretical methods to highlight their properties, advance the understanding of structure-property relationships and thus contribute to the understanding of device design with 2D materials. Understanding the factors that drive material properties is a step towards 2D materials with properties on demand.

1.2 Structure and scientific contribution of this thesis

This thesis is structured as follows:

In Chapter 2, I introduce basic concepts related to my research. In Chapter 3, I give an introduction to the computational method. Subsequently, I present research results obtained during my graduate studies in Chapters 4-7:

Chapter 4 presents a study of the direct optical transitions of bulk ReS_2 and $ReSe_2$. We use density functional theory calculations to assign the optical transitions observed by our collaborators in pressure-dependent photoreflectance experiments. After careful examination of the Brillouin zone, we assign the optical transitions to the high-symmetry Z-point and other k-points located away from the high-symmetry points in the Brillouin zone. Our theoretically predicted pressure coefficients of the bandgaps are in agreement with the experimentally observed pressure coefficient of the optical transitions. We demonstrate that the pressure coefficient is negative, which is in contrast to the positive pressure coefficient of Mo- and W-based transition metal dichalcogenides. We propose that the destabilization of the out-of-plane p_z (and d_z^2) orbitals with increasing pressure is responsible for the observed pressure coefficients. There has been an extensive discussion whether ReS_2 and $ReSe_2$ show layer-independent, monolayer-like optical properties. This has been attributed to weak van-der-Waals bonding between the layers. The pressure coefficient we observe is of the order of magnitude of that of Mo- and W-based transition metal dichalcogenides pointing to equally strong interlayer interactions. Our results thus weaken the argument of small interlayer coupling in ReS_2 and $ReSe_2$.

In Chapter 5, we analyze finite momentum excitons of monolayer MoS_2 using state-of-the-art many-body GW theory and the Bethe-Salpeter-equation (GW+BSE). For the first time, we solve the full BSE for monolayer MoS_2, going beyond the Tamm-Dancoff approximation (TDA). Our results confirm that the TDA is a valid approximation. We show that the lowest energy exciton is not bright, as had been commonly assumed, but indirect and spin-forbidden and therefore optically inaccessible. This is due to the exciton binding energy of the indirect exciton being greater than that of the direct transitions. This was discovered independently at the same time by Ref. [21]. We observe higher exciton binding energies for excitons with the hole located at the Γ point. This prompts us to investigate the linear scaling reported for the exciton binding energy with the quasiparticle bandgap for our case of indirect excitons. Generally, our results corroborate the 1:4 ratio of the binding energy and quasiparticle bandgap. However, we find that the ratio slightly increases for excitons with larger binding energies. We investigate

the relationship between the exciton binding energy and the orbital compositions of the single-particle states. Our results indicate a correlation between a higher proportion of out-of-plane orbital contributions and an increase in the binding energy. We propose that the lack of screening experienced by the out-of-plane orbitals leads to this increase in binding energy. For higher-energy excitons, the linear scaling relationship breaks down due to decreasing binding energies.

In Chapter 6, I calculate the ideal band offsets between recently predicted monolayers of the CaP_3 family using single-shot G_0W_0 theory. The band offset of these materials was previously unknown and earlier band structure calculations were presented using density functional theory. I predict that monolayer CaP_3, $CaAs_3$ and $BaAs_3$ form type-II (staggered) heterojunctions according to the Anderson electron affinity rule. Their quasiparticle bandgaps are 2.1 (direct), 1.8 (direct) and 1.5 eV (indirect), respectively. I investigate structural causes of the conduction band offsets and apply chemical bonding analysis to explain the transition of the direct bandgap in $CaAs_3$ to an indirect gap in $BaAs_3$. I find that the transition is driven by increasing p-d orbital bonding interactions due to the stronger delocalization of $BaAs_3$ 5d orbitals.

In Chapter 7, we present a benchmarking study of effective masses calculated with density functional theory using a perturbation theory approach. I design a data test set called `mstar60` for effective masses comprising of 18 bulk and monolayer semiconductors and 60 effective masses. I benchmark several exchange-correlation functionals with the `mstar60` dataset. For that, I compare the accuracy of effective masses obtained with the semilocal PBE and TB-mBJ/LDA functionals and the hybrid, nonlocal HSE functional with respect to experiment. We reveal that the nonlocal exchange in HSE enlarges the optical transition matrix elements leading to the superior accuracy of HSE in the calculation of effective masses. Specifically, we show that the omission of nonlocal exchange in the calculation of the optical matrix element for HSE leads to errors of about 30% in the effective masses. Finally, we analyze the layer-dependent effective mass renormalization from bulk to monolayer MoS_2 in light of the matrix elements. We show that — in addition to the bandgap change — a decrease in the matrix element contribution is an important factor to explain the effective mass renormalization.

Chapters 4-7 are connected by a common quest for predicting and analyzing optoelectronic properties of 2D materials. In several chapters, we use orbital theory to gain intuitive insight into the optical and electronic properties observed, combining the physics and chemistry view of electronic bandstructures. Chapters 4-7 contribute to the scientific dialogue at the materials science and solid-state physics interface. Together,

they represent an advancement of the understanding of the electronic bandstructure in selected 2D materials.

Many open questions call for further research. In this fast-paced research field of 2D materials, some questions produced by our work have already been partially answered by other authors. In Chapter 4 it remains to connect our conclusions about the interlayer interaction of ReX_2 to the layer-independence of the optical bandgap in the monolayer limit. Ref. [22] addresses this question. In Chapter 5 we show that excitons at the K point have different binding energies, causing the lowest-energy exciton to be dark but we do not have an explanation why excitons at the same location should have different binding energies. In a recent contribution, Ref. [23] connects the different binding energies in monolayer MoS_2 to effective masses and electron-hole exchange interaction. In Chapter 6 future work should be done to construct actual heterostructures to verify the predicted band alignment and to consider excitonic effects. For Chapter 7 it would be intriguing to know whether the nonlocal exchange of the *GW* self-energy operator and eigenvalues would further improve the calculated effective masses.

References

[1] R. S. Title and M. W. Shafer. "Band Structure of the Layered Transition-Metal Dichalcogenides: An Experimental Study by Electron Paramagnetic Resonance on Nb-Doped MoS2". In: *Physical Review Letters* 28.13 (Mar. 1972), pp. 808–810. DOI: 10.1103/PhysRevLett.28.808.

[2] L. F. Mattheiss. "Band Structures of Transition-Metal-Dichalcogenide Layer Compounds". en. In: *Physical Review B* 8.8 (Oct. 1973), pp. 3719–3740. ISSN: 0556-2805. DOI: 10.1103/PhysRevB.8.3719.

[3] Martin B. Dines. "Lithium intercalation via n-Butyllithium of the layered transition metal dichalcogenides". en. In: *Materials Research Bulletin* 10.4 (Apr. 1975), pp. 287–291. ISSN: 0025-5408. DOI: 10.1016/0025-5408(75)90115-4.

[4] K. S. Novoselov et al. "Electric Field Effect in Atomically Thin Carbon Films". en. In: *Science* 306.5696 (Oct. 2004), pp. 666–669. ISSN: 0036-8075, 1095-9203. DOI: 10.1126/science.1102896.

[5] Qing Hua Wang et al. "Electronics and optoelectronics of two-dimensional transition metal dichalcogenides". en. In: *Nature Nanotechnology* 7.11 (Nov. 2012), pp. 699–712. ISSN: 1748-3395. DOI: 10.1038/nnano.2012.193.

[6] Manish Chhowalla et al. "The chemistry of two-dimensional layered transition metal dichalcogenide nanosheets". en. In: *Nature Chemistry* 5.4 (Apr. 2013), pp. 263–275. ISSN: 1755-4349. DOI: 10.1038/nchem.1589.

[7] Tetsuo Ogawa and Yoshihiko Kanemitsu. *Optical Properties of Low-dimensional Materials*. en. World Scientific, 1995. ISBN: 978-981-02-3048-7.

[8] Andrea Splendiani et al. "Emerging Photoluminescence in Monolayer MoS $_2$". en. In: *Nano Letters* 10.4 (Apr. 2010), pp. 1271–1275. ISSN: 1530-6984, 1530-6992. DOI: 10.1021/nl903868w.

[9] Alexey Chernikov et al. "Exciton Binding Energy and Nonhydrogenic Rydberg Series in Monolayer WS 2". en. In: *Physical Review Letters* 113.7 (Aug. 2014). ISSN: 0031-9007, 1079-7114. DOI: 10.1103/PhysRevLett.113.076802.

[10] Riccardo Frisenda et al. "Atomically thin p–n junctions based on two-dimensional materials". en. In: *Chemical Society Reviews* 47.9 (May 2018), pp. 3339–3358. ISSN: 1460-4744. DOI: 10.1039/C7CS00880E.

[11] Cosimo Anichini et al. "Chemical sensing with 2D materials". en. In: *Chemical Society Reviews* 47.13 (July 2018), pp. 4860–4908. ISSN: 1460-4744. DOI: 10.1039/C8CS00417J.

[12] Deep Jariwala et al. "Van der Waals materials for atomically-thin photovoltaics: Promise and outlook". In: *ACS Photonics* 4.12 (Dec. 2017), pp. 2962–2970. ISSN: 2330-4022, 2330-4022. DOI: 10.1021/acsphotonics.7b01103.

[13] Zhiwei Wang et al. "Two-dimensional light-emitting materials: preparation, properties and applications". en. In: *Chemical Society Reviews* 47.16 (2018), pp. 6128–6174. DOI: 10.1039/C8CS00332G.

[14] Alberto Ciarrocchi et al. "Polarization switching and electrical control of interlayer excitons in two-dimensional van der Waals heterostructures". en. In: *Nature Photonics* 13.2 (Feb. 2019), pp. 131–136. ISSN: 1749-4893. DOI: 10.1038/s41566-018-0325-y.

[15] Maja Feierabend et al. "Proposal for dark exciton based chemical sensors". en. In: *Nature Communications* 8 (Mar. 2017), p. 14776. ISSN: 2041-1723. DOI: 10.1038/ncomms14776.

[16] K. F. Mak et al. "The valley Hall effect in MoS2 transistors". en. In: *Science* 344.6191 (June 2014), pp. 1489–1492. ISSN: 0036-8075, 1095-9203. DOI: 10.1126/science.1250140.

[17] Xiaofeng Qian et al. "Quantum spin Hall effect in two-dimensional transition metal dichalcogenides". en. In: *Science* 346.6215 (Dec. 2014), pp. 1344–1347. ISSN: 0036-8075, 1095-9203. DOI: 10.1126/science.1256815.

[18] K. S. Novoselov et al. "2D materials and van der Waals heterostructures". en. In: *Science* 353.6298 (July 2016). ISSN: 0036-8075, 1095-9203. DOI: 10.1126/science.aac9439.

[19] D. N. Basov, R. D. Averitt, and D. Hsieh. "Towards properties on demand in quantum materials". en. In: *Nature Materials* 16.11 (Nov. 2017), pp. 1077–1088. ISSN: 1476-1122, 1476-4660. DOI: 10.1038/nmat5017.

[20] Liangzhi Kou et al. "Two-Dimensional Topological Insulators: Progress and Prospects". In: *The Journal of Physical Chemistry Letters* 8.8 (Apr. 2017), pp. 1905–1919. DOI: 10.1021/acs.jpclett.7b00222.

[21] Thorsten Deilmann and Kristian Sommer Thygesen. "Finite-momentum exciton landscape in mono-and bilayer transition metal dichalcogenides". In: *2D Mater.* 6 (2019), p. 035003.

[22] Byoung Ki Choi et al. "Visualizing Orbital Content of Electronic Bands in Anisotropic 2D Semiconducting ReSe $_2$". en. In: *ACS Nano* 14.7 (July 2020), pp. 7880–7891. ISSN: 1936-0851, 1936-086X. DOI: 10.1021/acsnano.0c01054.

[23] Maciej Bieniek, Ludmiła Szulakowska, and Paweł Hawrylak. "Band nesting and exciton spectrum in monolayer ${\mathrm{MoS}}_{2}$". In: *Physical Review B* 101.12 (Mar. 2020), p. 125423. DOI: 10.1103/PhysRevB.101.125423.

Chapter 2

Basic concepts

In this chapter I cover some of the fundamental concepts related to my research.

2.1 Van-der-Waals interactions

Two-dimensional materials are layered materials: they form covalent bonds within a plane (intra-layer bonds) while out-of-plane bonds consist of comparatively much weaker van-der-Waals interactions. Van-der-Waals interactions have a bond energy of about 10 kJ/mol while covalent bonds may range from 200-1000 kJ/mol. [1] Van-der-Waals interactions are present in all materials but are usually neglected in three-dimensionally bonded crystals because their contribution pales in comparison with the other bonds present (metallic, covalent and ionic). For 2D materials, however, these interactions cannot be neglected because they represent the predominant bonding mechanism out-of-plane. Therefore, we consider here briefly the nature of van-der-Waals interactions and some ways they can be accounted for using density functional theory.

Van der Waals interactions stem from Coulomb attraction of opposite charges. If we consider two fixed point charges Q_1 and Q_2 at a distance D, the interaction force F between them is described by Coulomb's law: [2]

$$F = \frac{Q_1 Q_2}{4\pi\varepsilon\varepsilon_0 D^2}. \tag{2.1}$$

However, the interactions between atoms or molecules are more complicated because their charge cannot be described as a point charge but better with the use of dipoles. These dipoles are either permanent due to the chemical structure, induced by a nearby dipole that polarizes the electron cloud, or completely spontaneous because of quantum

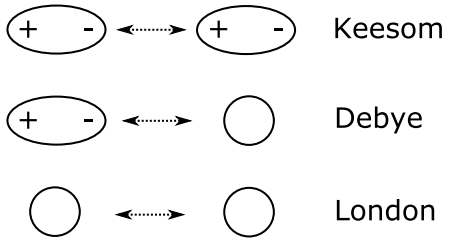

FIGURE 2.1: Types of van-der-Waals forces, classified according to the nature of the dipoles involved in the interaction.

oscillations. Furthermore, these dipoles are usually not fixed but rotating so that each possible rotation and its temperature-dependent probability has to be taken into account for the interaction. Taking dipole rotation fully into account, the van-der-Waals energies are described by an equation that is temperature-dependent and where the energy declines with the 6^{th} power of the distance between the interacting dipoles:

$$V_{\mathrm{vdW}}(D) = -\frac{C_{\mathrm{vdW}}}{D^6}. \tag{2.2}$$

We can glean from this that, due to the oscillating dipole charges, the strength of van-der-Waals interactions for particles like atoms and molecules is only significant for particles that are very close to each other.

The C_{vdW} constant in equation 2.2 is the sum of the contribution of the different types of van-der-Waals interactions: $C_{\mathrm{vdW}} = C_{\mathrm{Keesom}} + C_{\mathrm{Debye}} + C_{\mathrm{London}}$. Depending on the type of the dipoles involved, van-der-Waals interactions are classified into three types (see Figure 2.1):

- Keesom interactions are interactions between two permanent dipoles,
- Debye interactions are interactions between a permanent dipole and an induced dipole,
- And London interactions are interactions between fluctuating induced dipoles. London interactions are also called dispersion interactions. These are interactions stem from spontaneous quantum oscillations that occur between all types of particles, also in otherwise non-polar particles.

The temperature dependence of equation 2.2 is a result of a Boltzmann factor in the Keesom constant: $C_{\mathrm{Keesom}} \propto (k_B T)^{-1}$. The strength of the van-der-Waals interactions decreases with temperature for dipole-dipole interactions as less-energetically favourable

or non-bonding dipole orientations become more probable. These unfavourable orientations become more probable due to the higher (temperature-induced) mobility of the dipoles that helps the molecules overcome the energy barrier of the Arrhenius equation.

While all van-der-Waals bonding effects are significant only at a short range, the London dispersion forces cause wide-range, non-local correlation effects. These correlation effects cannot be captured with the specifically local exchange-correlation functionals used in DFT like the Local Density Approximation (LDA) and Generalized Gradient Approximation (GGA). For these approximations, all van-der-Waals interactions are averaged out into a background potential, which erases the knowledge of correlation effects. Consequently, in systems where van-der-Waals interactions cannot be neglected, we need to correct for the missing correlation effects of the dispersion part.

There are two general approaches for van-der-Waals corrections for DFT, also called dispersion corrections: The corrections can either be density-based or total-energy-based. In the first case, the functional is modified to correctly represent changes to the electron density from dispersion correlation effects. Then, the eigenvalue problem is solved with the modified functional. This approach is also called vdW-DFT. The VV10 functional [3] is an example of density-based van-der-Waals corrections. On the other hand, total-energy-based corrections (also called C6 corrections) add an interaction energy (usually Lennard-Jones based) to the Kohn-Sham energy *after* the eigenvalue problem is solved. The most popular C6 corrections are the PBE-D2 and PBE-D3 corrections by Grimme [4] and Grimme et al. [5]. More information on these approaches can be found in the references. The limits of DFT to accurately capture van-der-Waals effects are illustrated in Figure 2.2. It shows the interlayer binding energy for layered boron nitride calculated without van-der-Waals corrections (GGA) and with a vdW-DF approach. The van-der-Waals corrected energy curve clearly shows an attractive energy holding the boron nitride layers together while the GGA-only approach does not capture the van-der-Waals interlayer bonding at all.

For our study of layered rhenium disulfide and -diselenide in Chapter 4 we employed vdW-DFT corrections. In the study of layered calcium phosphides and arsenides in Chapter 6 we used C6-corrections to relax the bulk structure.

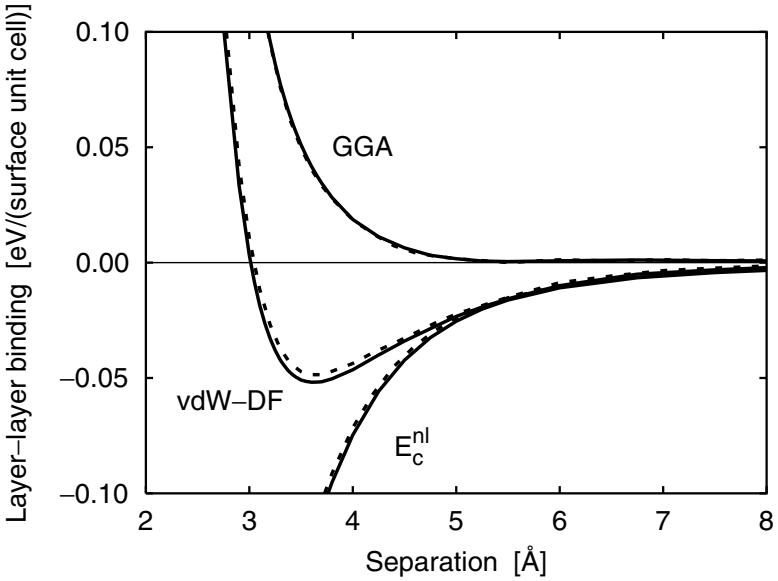

FIGURE 2.2: Dispersion corrections for the interlayer binding energy of layered boron nitride. Shown are the bonding curves calculated with a vdW-DF approach and without van-der-Waals corrections (GGA). The correlation energy curve (E_c^{nl}) is also shown. Reprinted with permission from [6]. Copyright 2003 by the American Physical Society

2.2 Calculation of the electronic bandstructure

Felix Bloch, working on his doctoral thesis tried to explain the conductivity of metals. Why do electrons in metals behave as nearly free electrons when they should be hindered from any movement by the strong potential of the atomic cores? Pursuing an answer, Bloch later recalls that he realized that the electronic waves in the crystal "differed from the plane waves of the free electron only by a periodic modulation"[7]. This was a foundational insight for the development of solid-state physics. With Bloch's theorem, the electronic states can be categorized according to a continuous wavevector k. States that are close in energy form energy bands which can be displayed on a bandstructure plot with respect to k. Bandstructure plots give us information about the fundamental electronic properties of a solid, on whether a solid is conducting or insulating, has a high carrier mobility or good optical properties.

Bloch's theorem states that for a single electron in a crystalline solid we can write the wavefunction as the product of a periodic part $u_n(r)$ and a wavelike part or phase

factor $e^{ik\cdot r}$.

$$\psi_{n,k}(r) = u_n(r)e^{ik\cdot r} \tag{2.3}$$

Here, the wavelike part is equal to the free electron wavefunction $\psi_(r) = e^{ik\cdot r}$. However, the electron is not free but perturbed by the periodic potential $V(r)$ of the crystal lattice, thus the periodic part $u_n(r)$. Now, since $V(r)$ is periodic, we can write $V(r) = V(r + R)$ where R is a reciprocal lattice vector, that is an integer multiple of the reciprocal lattice parameters: $R = n_1a_1 + n_2a_2 + n_3a_3$. In other words, if we jump within the crystal by multiple unit cells, we should expect to feel the same periodic potential. As $u_n(r)$ is the direct result of $V(r)$, it is subject to the same periodicity condition: $u_n(r) = u_n(r+R)$. It can be shown that the electronic properties of a crystal depend on the periodic part $u_n(r)$ of the wavefunction alone.[8] Therefore, according to Bloch's theorem, we need to evaluate the bandstructure only within the first Brillouin zone. Any wavevector k outside the first Brillouin zone can be translated back into the first Brillouin zone. Symmetry operations according to group theory allow us to further reduce the section of the Brillouin zone which we have to consider.[9]

The band structure can be calculated using different approaches. The following approximations are common to all of them: First, we assume a perfect crystal without defects. Second, we apply the Born-Oppenheimer approximation which states that movements of nuclei and electrons can be decoupled because of the heavy mass of the nuclei in comparison with the electrons.[8]. Lastly, we employ the independent electron approximation, which is elaborated in Chapter 3.

One approach is the nearly-free electron model, also called the "empty-lattice" approach.[9] Here we start with a free electron and consider the potential of the ionic lattice to be off initially, to then gradually turn it on until our electrons are nearly free. The energy dispersion of the free electron is parabolic and is given by $E = \hbar^2k^2/(2m_0)$, where E is the energy, k is the wavevector and m_0 is the electron rest mass. The turning on of the potential leads to the opening of band gaps in the parabola at the boundary of the Brillouin zone. This can be seen in Figure 2.3 (a) for the example of a one-dimensional crystal. According to Bloch's theorem, we can fold the bands back into the first Brillouin zone as shown in Figure 2.3 (b). It becomes apparent that there are gaps between the bands, also called forbidden bands, consisting of energy levels that may not be occupied by electrons (Figure 2.3 (c)).

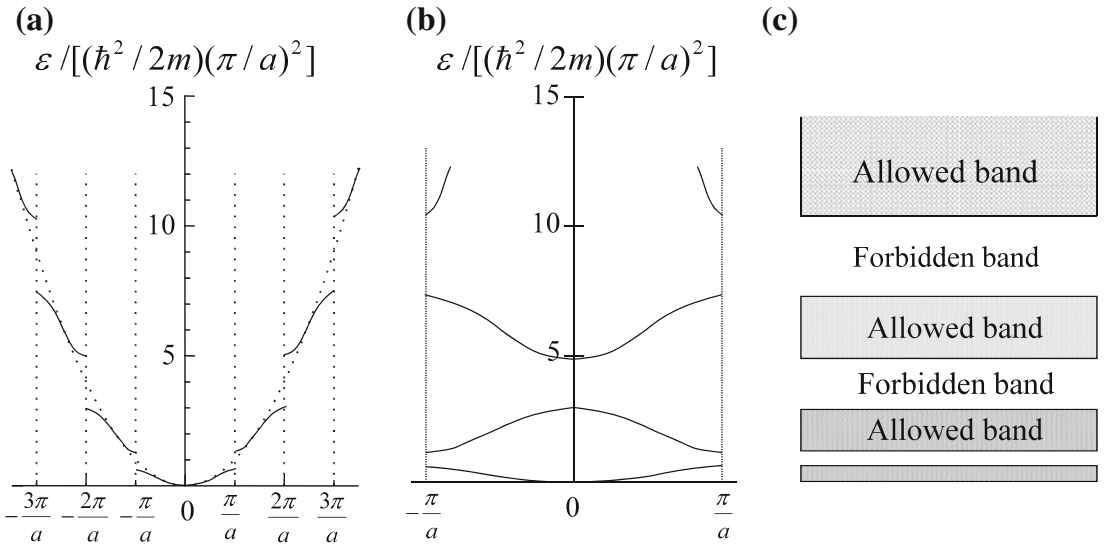

FIGURE 2.3: Energy band structure of one-dimensional crystal obtained from the nearly free electron approximation. (a) Extended zone representation: the weak external potential introduces gaps at the Brillouin zone boundaries, (b) reduced zone representation: the bands are folded back into the first Brillouin zone. (c) Energy bands according to band theory. Energy in units of $\left(\hbar^2/2m\right)(\pi/a)^2$. Reprinted with permission from Hamaguchi [10]. Copyright 2017 by Springer-Verlag Berlin Heidelberg.

The inverse approach to the nearly-free electron model is the tight-binding approach.[9] We start with a tightly bound, that is completely localized, electron residing in an atomic orbital. This gives us straight energy levels in the band structure plot that do not have any dispersion (or curvature). Then we decrease the binding energy and allow orbitals to overlap which creates a dispersion of the bands. Bonding states are now lower in energy than the non-interacting state, antibonding states are higher in energy than the non-interacting state. Figure 2.4 gives an example of a tight-binding bandstructure for a linear chain of fluorine atoms. The unit cell contains one F atom. Each fluorine atom has four orbitals, one 2s and three 2p orbitals, which give rise to four bands in the band structure. Higher-energy atomic orbitals are located higher in the band diagram. The $2p_x$ and $2p_y$ orbitals both form π bonds, because of which two identical, or degenerate, bands are seen in the diagram. As π bonds are weaker than σ bonds, the interaction of the $2p_x$ and $2p_y$ orbitals is weaker with respect to $2p_z$. This can also be seen in the dispersion of the bands, which is less for the π bands. The $2p_z$ σ band runs opposite the other bands because of the point-symmetry of the wavefunction with respect to the node. In simple terms, every other $2p_z$ dumbbell has to be rotated by 180° in order to achieve the bonding state. This rotation is given at π/a.

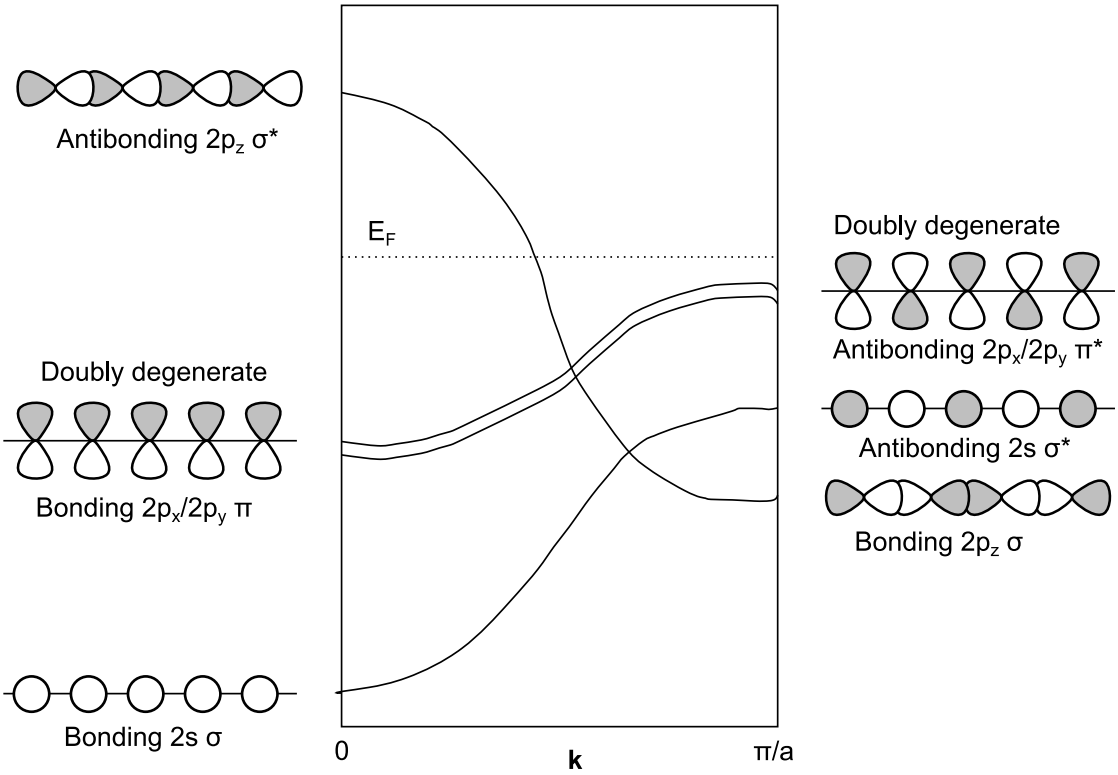

FIGURE 2.4: Energy band structure of one-dimensional fluorine chain in the tight-binding model. Each F atom has four orbitals, one 2s and three 2p orbitals, which give rise to four bands in the band structure. Created with permission after an idea of Dr. Patrick Woodward (Ohio State University) [11]

In density functional theory, we usually calculate the band structure using pseudopotentials or related methods. These are described in Chapter 3.

I would like to mention three aspects of band structures here, as they are directly related to my work.

The first one is spin-orbit coupling (SOC). Spin-orbit coupling adds an extra term H_{SO} to the Hamiltonian,[12, 9]

$$H_{\mathrm{SO}} = -\frac{\hbar}{4m_0^2c^2}\boldsymbol{\sigma}\cdot\boldsymbol{p}\times(\nabla V_0) \propto \mathbf{L}\cdot\mathbf{S}. \tag{2.4}$$

Here, m_0 is the mass of a free electron, c is the velocity of light and $\boldsymbol{\sigma} = (\sigma_x, \sigma_y, \sigma_z)$ represents the Pauli spin matrices. $\boldsymbol{p}$ is the momentum operator and V_0 the Coulomb potential of an atom. $\mathbf{L}$ and $\mathbf{S}$ are the orbital angular momentum and the spin angular

momentum, respectively. They are given in terms of the orbital quantum number l and the spin quantum number s, respectively, as $\boldsymbol{L} = \hbar\sqrt{l(l+1)}$ and $\boldsymbol{S} = \hbar\sqrt{s(s+1)}$.

SOC can lead to the splitting of bands in energy, bands that would be degenerate (at the same energy) if SOC was not considered. This energy splitting is due to the interaction of the spin and the way the electron travels around the nucleus (the orbit). The principle of the origin of SOC is shown in Figure 2.5. From an outside perspective, the nuclei or protons (blue) are fixed and the electron orbits around them (Figure 2.5 a). However, if we change our perspective and take the electron as a reference system, the nucleus seems to orbit around the electron. In this reference system, the orbiting positive charge creates an effective magnetic field that couples to the electron spin. Now, depending on how the spin and orbital angular momentum are aligned, there will either be an energetic stabilization or destabilization of a state, causing an energy splitting between states of different spin.

Figure 2.6 shows the energy splitting of the valence bands in GaAs due to spin-orbit coupling. In the figure, the total angular momentum quantum number $j = l + s$ is given. The coupling leads to energy splitting Δ_0 of the split-off (SO) band with $j = 1-1/2 = 1/2$ and the heavy hole (HH) and light hole (LH) bands ($j = 1+1/2 = 3/2$).

Spin-orbit coupling was important for the calculation of excitons in the MoS_2 monolayer in Chapter 5. Due to SOC, both the valence and conduction bands split in energy in MoS_2 monolayer, leading to the lowest-energy transition being spin-forbidden, that is optically inaccessible (see also Chapter 2.4).

The second aspect concerning band structures that I would like to discuss is the deformation potential. Deformation potentials describe the change of the bandgap with pressure. Deformation potentials are best explained in the conceptual framework of molecular orbital theory and the tight-binding approach to the bandstructure. Figure 2.7 schematically shows the effect of hydrostatic pressure on the bandgap of GaAs. Ga sp^3 orbitals and As sp^3 orbitals form bonding and antibonding orbitals and bands with the bandgap between states of bonding and antibonding character. When hydrostatic pressure is applied, the equilibrium distance between Ga and As atoms decreases. As a result, their bonding as well as antibonding interaction becomes stronger, leading to an increased energy difference between bonding and antibonding states. As a consequence, the band gap increases.

Deformation potentials become important for our discussion of the pressure coefficient of ReX_2 in comparison with MoX_2 in Chapter 4. In our research, we observed a negative

pressure coefficient (closure of the optical bandgap with hydrostatic pressure) for ReX_2 while the pressure coefficient has been shown to be positive for MoX_2 and related group-6 transition metal dichalcogenides [15]. The optical bandgap refers to the first direct transition, as indirect gaps are optically inaccessible. For this reason, in the following discussion we consider always the lowest-energy *direct* bandgap. In MoX_2 the bandgap is located between two states of antibonding character as shown in Figure 2.8. Thus, with hydrostatic pressure, both the conduction band edge and the valence band edge will increase in energy (be destabilized). Now, the amount of destabilization depends on the orbital composition of the band edge. Layered materials have anisotropic properties due to the weak van-der-Waals bonding out-of-plane, in the z-direction. Under hydrostatic pressure, the layers will be compressed more strongly in the out-of-plane direction and the interlayer distance will decrease. This causes additional Coulomb repulsion between antibonding states in the z-direction. Thus, orbitals pointing in the z-direction will be most destabilized by increasing pressure.

As Figure 2.8 shows, the conduction band edge of MoX_2 is composed in big part of Mo d_{z^2} orbitals, while the valence band edge is mostly composed of d and p_{xy} orbitals. Thus, the CBM is destabilized to a greater extent than the VBM and the direct bandgap opens up. MoX_2 crystallizes in the trigonal prismatic phase, which (according to crystal field theory) has the energetic ordering of d-orbitals displayed in Figure 2.9 b. ReX_2 on the other hand crystallizes in a distorted octahedral (1T') phase, which leads to a different ordering of the d-orbitals (Figure 2.9 a). As a result, in the ReX_2 the valence band edge shows more d_{z^2} (and p_z) orbital contributions, which leads to the VBM being destabilized to a greater extent than the CBM. This is the opposite effect than for MoX_2 and thus leads to an effective closing of the bandgap with pressure. For further details see also Choi et al. [16] who followed up on our results described in Chapter 4.

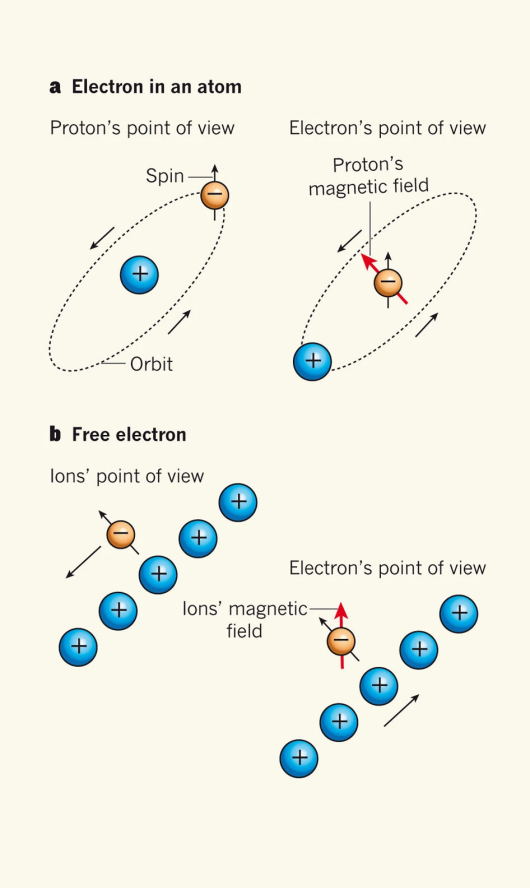

FIGURE 2.5: Principle of spin-orbit coupling. From the nucleus or proton's (blue) point of view, the electron (orange) orbits around the proton. However, when seen from an electron's reference system, the proton orbits around the electron, creating a magnetic field that interacts with the electron spin. a) Illustrated for an atom b) Illustrated for a free electron in a periodic crystal of ions. Reprinted with permission from Chapman and Melo [13]. Copyright 2011 by Nature Publishing Group, a division of Macmillan Publishers Limited. All Rights Reserved.

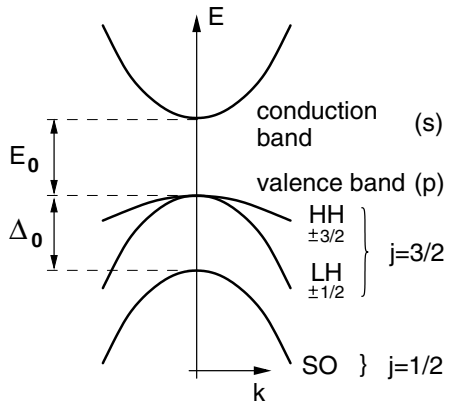

FIGURE 2.6: Spin-orbit coupling in GaAs. The spin-orbit coupling leads to the energy splitting of the split-off (SO) valence band from the heavy-hole (HH) and light-hole (LH) bands. Reprinted with permission from Winkler [12]. Copyright 2003 by Springer-Verlag Berlin Heidelberg.

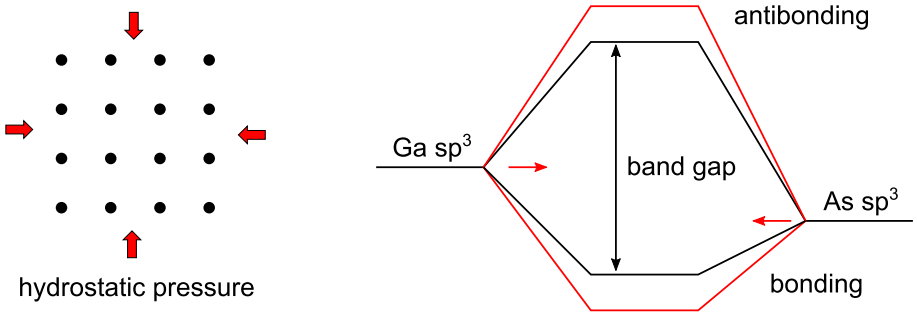

FIGURE 2.7: Deformation potential in GaAs. The bandgap is located between a bonding and an antibonding state. Under hydrostatic pressure, the equilibrium distance between the atoms becomes shorter which intensifies the splitting between bonding and antibonding states (red lines). Thus, the band gap increases.

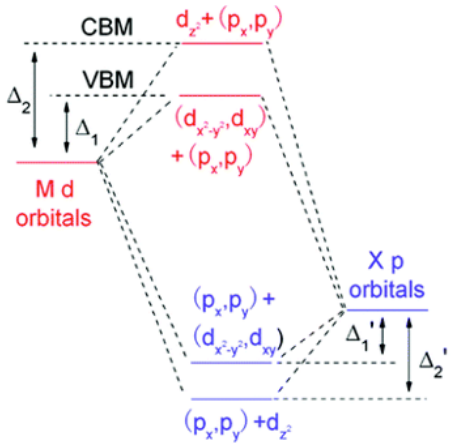

FIGURE 2.8: Molecular orbital diagram for the band edges of MoX_2 (X= S, Se) at the K point. The bandgap is located between two antibonding states. Reprinted with permission from Wang [14]. Copyright 2014 by Springer International Publishing Switzerland.

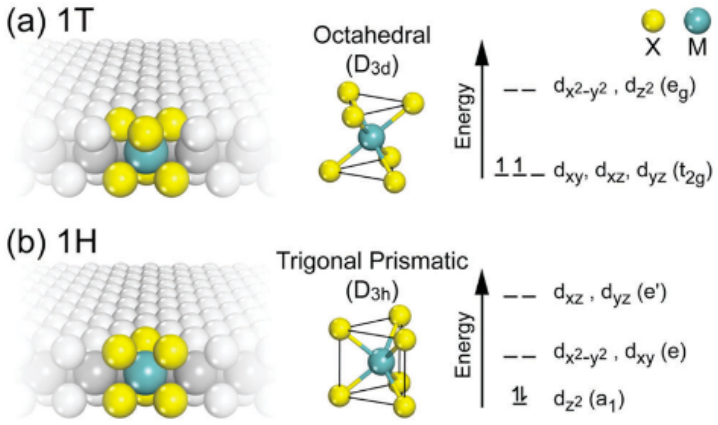

FIGURE 2.9: a) Octahedral (1T) and b) trigonal prismatic polytypes (1H) of transition metal dichalcogenides. The energetic ordering of the d-orbitals depends on the polytype. Reprinted with permission from Samadi et al. [17]. Copyright 2018 by the Royal Society of Chemistry.

The third aspect of bandstructures important for my work is the concept of effective masses. As we have seen previously in the discussion of the nearly-free electron model, the energy dispersion of a free electron is described by the following parabola: $E = \hbar^2 k^2/(2m_0)$. In crystalline materials, the electron is no longer free as it interacts with the periodic potential of the ionic lattice. To describe the energy dispersion of the nearly free electron near a band maximum or minimum of interest in crystalline materials, particularly semiconductors, the mass of the electron m_0 in the parabola is replaced by an effective mass $m*$ that acts as a scaling term to adjust the band curvature. The energy at a point $\boldsymbol{k}$ near the band extremum (which is set to $\boldsymbol{k} = \mathbf{0}$) can then be described in terms of the effective mass as follows:[9]

$$E_{n\boldsymbol{k}} = E_{n\mathbf{0}} + \frac{\hbar^2 k^2}{2m^*} \tag{2.5}$$

The effective mass can be calculated from $\boldsymbol{k} \cdot \boldsymbol{p}$ perturbation theory. Here $\boldsymbol{k}$ signifies a k-vector in momentum space and $\boldsymbol{p}$ is the momentum operator. In $\boldsymbol{k} \cdot \boldsymbol{p}$ perturbation theory, the eigenvalues $E_{n\boldsymbol{k}}$ of a neighboring point to a band extremum of interest are calculated from a second-order perturbation:[9]

$$E_{n\boldsymbol{k}} = E_{n\mathbf{0}} + \frac{\hbar^2 k^2}{2m} + \frac{\hbar^2}{m^2} \sum_{n' \neq n} \frac{|\langle u_{n\mathbf{0}} | \boldsymbol{k} \cdot \boldsymbol{p} | u_{n'\mathbf{0}} \rangle|^2}{E_{n\mathbf{0}} - E_{n'\mathbf{0}}} \tag{2.6}$$

where n and n' represent different bands, $u_{n\mathbf{0}}$ is the eigenfunction of the band at the extremum or starting point $\boldsymbol{k} = \mathbf{0}$ Comparing Equation 2.5 and 2.6, we can calculate the inverse effective mass of a non-degenerate, isotropic band as[9]

$$\frac{1}{m^*} = \frac{1}{m} + \frac{2}{m^2 k^2} \sum_{n' \neq n} \frac{|\langle u_{n\mathbf{0}} | \boldsymbol{k} \cdot \boldsymbol{p} | u_{n'\mathbf{0}} \rangle|^2}{E_{n\mathbf{0}} - E_{n'\mathbf{0}}}. \tag{2.7}$$

The term $M_{n,n'} = \langle u_{n\mathbf{0}} | \boldsymbol{k} \cdot \boldsymbol{p} | u_{n'\mathbf{0}} \rangle$ is the transition matrix element that is also mentioned in Chapter 2.3. In Chapter 7 we calculate the transition matrix elements from density functional theory and then obtain the matrix element with a perturbation theory approach based on Equation 2.7.

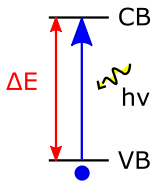

FIGURE 2.10: Schematic of an optical transition between the valence band (VB) and conduction band (CB). Incoming light $h\nu$ stimulates the transition of an electron from the valence band (VB) to the conduction band (CB) that is higher in energy.

2.3 Light-matter interactions

When we shine light on a semiconductor with a photon energy equal to or greater than the fundamental band gap ΔE, electrons from the valence band will be excited into a higher energy state in the empty conduction band (see Fig. 2.10). The driving force for this interaction between light and matter is the electric field of the light. The wavelength of light in the visible spectrum (λ : 300 - 700 nm) is much longer than the interatomic distance (a: ca. 0.3 nm). Thus, the electric field of the light can be assumed to be constant for our purposes. This assumption is called the electric dipole approximation.[18] The electric field of the light couples to the electric dipole moment of the transition between the two bands. During the transition of the electron from one band to the other, the electron is described by a mixture of the two wavefunctions.[19] The charge density may be either in one location or the other, which causes the charge density to oscillate at the frequency $\nu = \frac{(E_c - E_v)}{h}$ with E_c and E_v being the energies of the conduction and valence band, respectively. This oscillation leads to a dipole moment, $\boldsymbol{p} = -q\boldsymbol{r}$, which interacts with the electric field of the light.[19] The spatial vector $\boldsymbol{r}$ indicates the charge separation.

The electromagnetic field can be treated as a perturbation to the Hamiltonian; that is, an additional potential that only slightly alters the Hamiltonian.[18] This perturbation induces the transition. From time-dependent perturbation theory we find the transition amplitude between two mixed states:

$$M_{\mathrm{cv}} = \int \Psi_{\mathrm{c}}^{*} q\boldsymbol{r} \Psi_{\mathrm{v}} d\boldsymbol{r} = \langle \Psi_{\mathrm{c}} | q\boldsymbol{r} | \Psi_{\mathrm{v}} \rangle \tag{2.8}$$

The transition amplitude is also called the optical matrix element. The probability of the transition is the absolute square of the matrix element. The higher $|M_{\mathrm{cv}}|^2$, the more likely the transition.

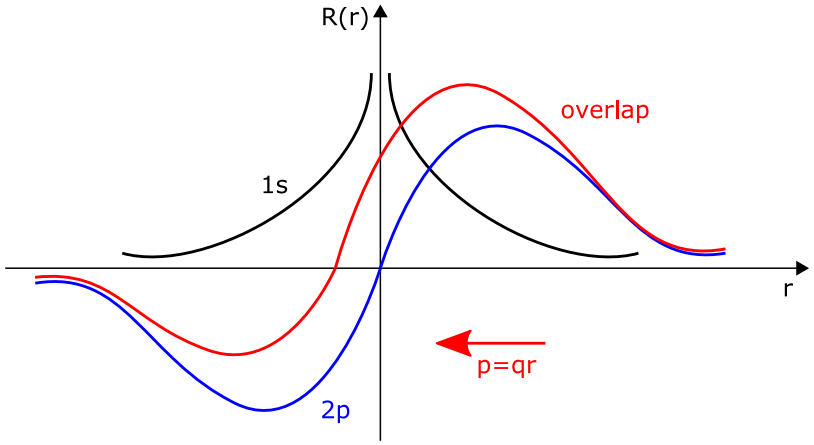

FIGURE 2.11: Illustration of the parity selection rule. Shown are the radial 1s and 2p wavefunctions. When they overlap, the charge density is no longer mirror-symmetric with respect to the vertical axis because they have different parity. This asymmetry causes the dipole. Light interacts with matter only when such a dipole can be formed

The matrix element is used to calculate the imaginary part of the dielectric function, also called spectral function,[9]

$$\varepsilon_2(\omega) = \left(\frac{2\pi e}{m\omega}\right)^2 \sum_{\boldsymbol{k}} |M_{\mathrm{cv}}|^2 \, \delta\left(E_{\mathrm{c}}(\boldsymbol{k}) - E_{\mathrm{v}}(\boldsymbol{k}) - \hbar\omega\right). \tag{2.9}$$

These equations can be generalized to calculate the transition probability between any bands, not only the conduction and valence band, and in any energy direction. If an electron relaxed from its excited state to a lower-energy band, a photon will be emitted that has the energy corresponding to the difference between the two bands.[18]

The transition is subject to selection rules. This means that a transition may not be probable between any two bands but must fulfil certain criteria - the selection rules:[19, 9, 18]

- $\Delta s = 0$, the spin must be conserved in a transition.
- $\Delta l \pm 1$, the parity selection rule. The angular momentum must change by ± 1 for the parity $P = (-1)^l$ to be different between the initial and final state. The parity selection rule ensures that there is a charge dipole when two wavefunctions overlap. This is illustrated in Figure 2.11 for the overlap of the radial 1s and 2p wavefunctions. Only even to odd transitions are allowed. The optical matrix element is zero if $\Delta l = 0$, indicating zero transition probability.

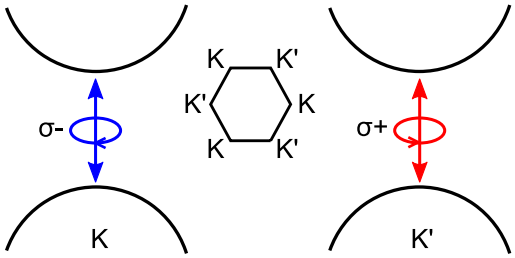

FIGURE 2.12: Illustration of the valley selection rule also called valley-spin locking in monolayers of group-6 transition metal dichalcogenides. Reproduced with permission from Wang [14]. Copyright 2014 by Springer International Publishing Switzerland.

- $\Delta k = 0$, there must be a conservation of momentum; only vertical transitions are allowed. Indirect transitions are not allowed, as the photon carries only a negligible momentum.

In monolayer transition metal dichalcogenides, the spin-selection rule receives a twist, since the band extrema of the K and K' valleys have the same energy but opposite spin. This is due to spin-orbit coupling and broken inversion symmetry in the monolayer. When irradiated with polarized light, it becomes apparent that transitions in one valley are favoured over the other, called spin-valley locking or valley-spin optical selection rule.[20, 21, 22] See Figure 2.12 for an illustration of the valley-selection rule. The valley index becomes a new degree of freedom to encode information on an electron, which is coined 'valleytronics'.

Spin-selection rules are important for determining bright and dark excitons in Chapter 5. The Green's functions used in the many-body theory described in Chapter 3.2 are related to the spectral function.

2.4 Excitons (in 2D materials)

Under light illumination, an electron in a solid can be optically excited and catapulted to a higher-energy band. By this, a charge-carrier pair is created: an electron in the conduction band and a hole in the valence band. These may recombine at any time under the emission of a photon that has the energy of the bandgap. Because of their opposite charges, holes and electrons experience Coulomb attraction which binds them together forming a quasiparticle called exciton. This is shown schematically in Figure 2.13.

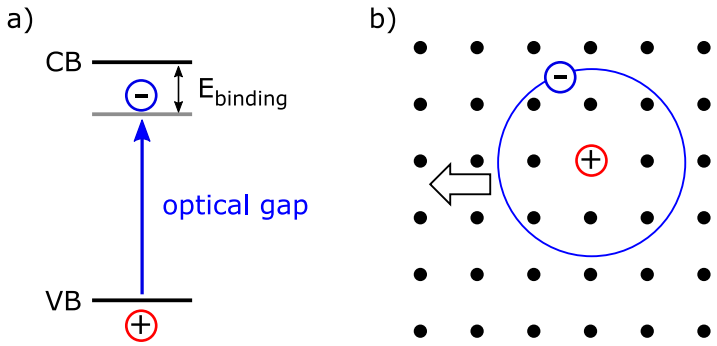

FIGURE 2.13: Schematic showing the bonding between hole and electron in excitons: a) Energy diagram showing that the optical bandgap is smaller than the transport bandgap due to the binding energy between electron and hole. b) Correlated motion of the bound electron and hole.

The electric field between the charges, however, is partially screened by their environment. Depending on the strength of the screening by the dielectric environment, excitons are classified into Frenkel and Wannier-Mott excitons. Frenkel excitons are strongly bound and with the electron and the hole being spatially close, usually within one unit cell. In Wannier-Mott excitons electron and hole are loosely bound and are typically separated by several unit cells (see Figure 2.13b).[23]

In layered semiconductors, excitons display Wannier-Mott behaviour.[24] Because Wannier-Mott excitons are spread out over several unit cells, the wave function of the exciton is affected by confined spatial geometry, expressed in the confinement length L. The effect of confinement on an exciton depends not only on L but also on the effective Bohr radius a_B that describes the spatial extent of the exciton. The ratio of a_B and L defines the dimensionality of an exciton. If we have, say a 3D exciton in a material confined in one direction by L and $a_{B_{3D}} > L$, the exciton becomes a 2D exciton.[23]

Now we assess the effect of confinement on Wannier excitons following the outline of the book of Ogawa and Kanemitsu.[23] For setting up a simple model of the exciton energies in different dimensions, we employ the effective mass approximation, assuming a direct-gap semiconductor and considering one-photon absorption, while neglecting exchange and spin-orbit interactions. We define the total energy of a Wannier exciton as the sum of the kinetic energy of the center of mass motion and the energy of the electron-hole relative motion.

In the following, we focus only on the energy of the electron-hole relative motion which is equivalent to the exciton binding energy. The potential energy is equal to the

unscreened Coulomb potential $V^{3D}(\mathbf{r}) = -e^2/(\epsilon|r|)$, $\mathbf{r} = (x, y, z)$ being the distance between the electron and the hole. When we insert this potential into the Schrödinger equation of the relative electron-hole motion, we can write the eigenvalues of the exciton binding energy E in the 3D case as

$$E_n^{3D} = -\frac{E_{R^*}}{n^2}, \text{ with } \quad E_{R^*} = \frac{\mu e^4}{8h^2\epsilon^2}, \quad \mu \equiv \frac{m_e^* m_h^*}{m_e^* + m_h^*} \tag{2.10}$$

where E_{R^*} is the effective Rydberg energy, n is the principal quantum number, μ is the electron-hole reduced mass, and ϵ is the permittivity. In the ideal 2D case, the relative electron-hole motion is restricted to the x,y plane. Thus, our Coulomb potential becomes $V^{2D}(x, y) = -e^2/(\epsilon\sqrt{x^2 + y^2})$. After solving the Schrödinger equation, we obtain the following expression for the eigenvalues:

$$E_n^{2D} = -\frac{E_{R^*}}{(n - 1/2)^2} \tag{2.11}$$

This shows us that the binding energy of the lowest-energy exciton in 2D is four times higher than the binding energy of a three-dimensional exciton: $E_1^{2D} = 4E_1^{3D}$. We also find that the effective Bohr radius a_B of the 2D exciton is half of the radius of the 3D exciton.

In addition, in the single-layer limit, the screening of the neighbouring layers is missing. This screening effect, besides the quantum confinement effect, considerably increases the binding energy and decreases the distance between electron and hole. The effect of the dielectric environment on the exciton binding energy in the monolayer limit is shown in Figure 2.14.

We can say that the optical properties of 2D materials are dominated by excitonic effects.[24] For example, for 1L $MoSe_2$ on bilayer graphene the exciton binding energy from photoluminescence measurements is 0.55 eV, with the free particle band gap being around 2.15 eV.[25] The exciton binding energy of 1L black phosphorus on a SiO_2/Si substrate measured with polarization-resolved photoluminescence was found to be ca. 0.9 eV with a quasiparticle gap of ca. 2.2 eV.[26] For directly measuring the exciton binding energy, one needs to obtain the optical transition energy and the free particle bandgap. The exciton binding energy can then be calculated as the difference between the free particle bandgap and the optical transition energy (see Figure 2.13). Optical transition energies can be obtained from photoluminescence and photoreflectance measurements.

The free particle bandgap can be measured with scanning tunnelling spectroscopy (STS). Further, s-type excitonic states can be accessed with one-photon spectroscopy and p-type (non-linear) excitonic states with two-photon spectroscopy. From the data of the spectral spacing of the s- and p-type states, the free particle bandgap can be extrapolated.[24, 27]

Bright and dark excitons: Excitons can be either bright, that is optically accessible, or dark (optically inaccessible). Bright excitons are a direct result of illumination. Dark excitons can be created from bright excitons by relaxation processes such as spin-flips and exciton-exciton scattering.[24] Whether a transition is bright or dark depends on optical selection rules. Only direct transitions are bright. Indirect and spin-forbidden transitions are dark. In 2D transition metal dichalcogenides (TMDCs), only transitions between bands with alike spins are allowed. This plays a role, because the strong spin-orbit coupling (SOC) in TMDC monolayers lifts the degeneracy of the bands, creating significant spin splitting in the valence band. For example, in 1L WSe2, the lowest-energy direct transition is dark due to spin-splitting of the valence band and ca. 30 meV lower than the first bright transition.[28] This leads to a quenched photoluminescence peak at lower temperatures, which is opposite to the trend in MoS_2. Even if the lowest-energy exciton is bright, the presence of optically dark excitons can change the optical response of the material by providing relaxation channels for the bright exciton.[29] Similarly, higher-energy indirect excitons can serve as a reservoir of charge carriers for bright transitions lower in energy and thus enhance the optical response in 1L TMDCs.[30] Indirect excitons can be related to the degree of polarization that can be achieved in 1L TMDCs.[31] Further, dark excitons in 1L WSe_2 can be brightened by the application of a magnetic field[32, 33], strain[34] or adsorption of high-dipole molecules[35]. Brightened dark excitons exhibit longer lifetimes than naturally bright excitons.[32, 33] The change in photoluminescent yield associated with the brightening of excitons has been proposed as a novel concept for strain and chemical sensing devices.[35, 34]

Excitonic effects cannot be captured in the single-particle approximation that underlies density functional theory approximations (see Chapter 3) because an exciton consists of two correlated particles, a hole and an electron. Therefore, excitons have to be described with many-body theory which is computationally expensive. In Chapter 4 we compare DFT results with optical band gaps for layered rhenium chalcogenides, thus ignoring excitonic effects. In Chapter 5 we include excitonic effects and analyze dark and bright excitons in monolayer MoS_2 using many-body theory to clarify the nature (dark or bright) of the lowest-energy exciton.

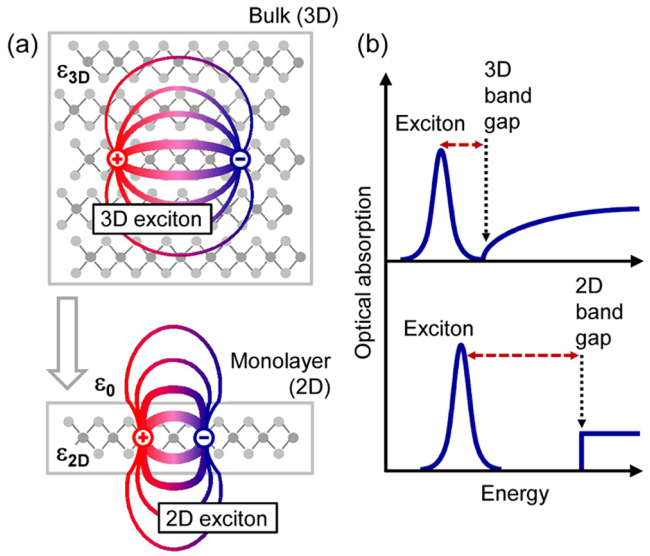

FIGURE 2.14: Influence of the dielectric environment on the exciton binding energy in bulk and monolayer 2D materials. a) For 2D excitons the electric field between hole and electron is no longer screened in the third dimension which leads to an increase in the bonding of hole and electron. b) Schematic of the optical absorption for 3D and 2D excitons. The red dashed arrow indicates the binding energy. Reprinted with permission from [36]. Copyright 2014 by the American Physical Society.

2.5 Heterojunctions - 3D and 2D

When we join two semiconductors with different bandgaps to make a heterostructure, an electronic heterojunction will form at the interface. At this heterojunction, a transition from the electronic structure of the first to the second semiconductor occurs, which causes discontinuities in the valence and conduction band because the bands are not aligned. These discontinuities are also called band offsets. There are three types of possible alignment, straddling (type I), staggered (type II) and broken gap (type III) (see Figure 2.15). Many semiconductor devices are based on heterojunctions; their band alignments are engineered to maximize the device's performance. For example, solar cells need type-II heterojunctions for charge separation of the electron-hole pair created by the incoming light. Tunnelling-field-effect transistors function based on broken gap heterojunctions. Multiple type-I heterojunctions increase the device performance of light-emitting diodes. [37]

Central to heterojunction design is the band alignment. We want to understand and be able to predict the band alignment of two semiconductors. Various theories have

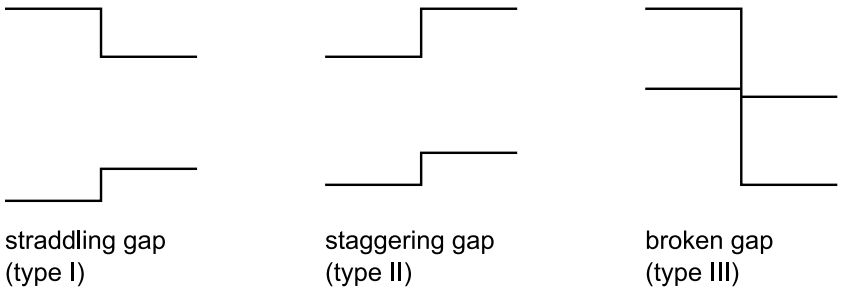

FIGURE 2.15: The three heterojunction band alignment types.

been proposed for the prediction of the band alignment. For our purposes, two band alignment models are important to understand:

1. The electron affinity model by Anderson [38]
2. and the charge neutrality model.

In 1983, Anderson proposed that the conduction band offset of an ideal heterojunction can be calculated by the difference in electron affinity of the two semiconductors. [38] In other words, the vacuum levels are aligned to obtain the band alignment. This model, however, neglects interface effects, like interfacial charges. Figure 2.16 shows energy band diagrams of an ideal heterojunction according to Anderson's band alignment rule. Here, the vacuum levels E_{VAC} of the two materials are aligned. However, now the Fermi levels E_F are not aligned which results in a charge transfer at the junction. The charge transfer will lead to band bending according to Poisson's equation.[39]

The charge neutrality model, on the other hand, postulates that the band alignment is driven by a microscopic dipole that develops at the interface due to induced gap states. [40] The induced gap states near the valence band are acceptor-like while the gap states near the conduction band are donor-like (see Figure 2.17). Somewhere in the middle is a neutral level, the charge neutrality level which is the energetically favourable state. The system forces the bands to align in such a fashion that the microscopic dipole is minimized in order to reach the charge neutrality level (for both materials). This effect is also referred to as Fermi-level pinning.[40]

A schematic heterojunction that includes the surface dipoles is shown in Figure 2.18. The microscopic dipoles change the charge imbalance at the heterojunction and thus affect the alignment and band bending (dashed lines in Fig. 2.18 b).

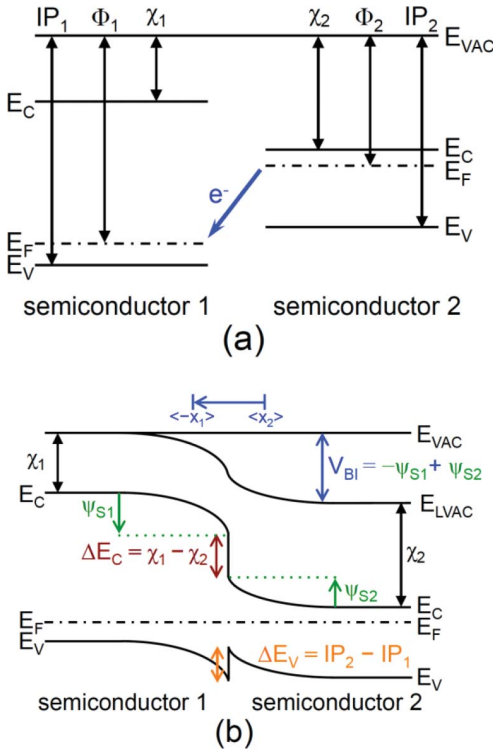

FIGURE 2.16: Ideal heterojunction energy band diagrams (ignoring interface states) for a) an isolated p-type semiconductor and an isolated n-type semiconductor and (b) the corresponding semiconductor heterojunction formed after electron transfer. IP refers to the ionization potential, χ to the electron affinity, and Φ to the work function. ψ_S is the surface potential. Reprinted from Wager and Kuhn [40]. ©2017 The Author(s). Taylor & Francis Group, LLC ©. Reuse permitted under the creative commons license CC BY 4.0.

The charge neutrality model and the Anderson model can be viewed as the two limiting or extreme cases of a common band alignment equation. [41]

$$\phi_n = (\chi_a - \Phi_{S,a}) - (\chi_b - \Phi_{S,b}) + S\,(\Phi_{S,a} - \Phi_{S,b}) \tag{2.12}$$

The interface parameter $0 \leq S \leq 1$ describes to what extend surface charges affect the band alignment. When $S = 0$, induced gap states dominate the band alignment, when $S = 1$, we recover Anderson's model in which surface charges are not taken into account. Comparing experimental results to the limit cases of the equation, we can make a conclusion about the nature of the interface. Many interfaces are governed by a mix of electron affinity and charge neutrality effects, which corresponds to a value of S

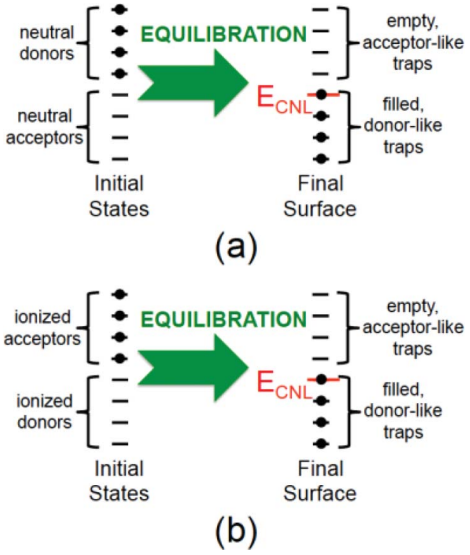

FIGURE 2.17: Illustration of the charge neutrality level shown for (a) neutral or (b) ionized donors and acceptors. Reprinted from Wager and Kuhn [40]. ©2017 The Author(s). Taylor & Francis Group, LLC ©. Reuse permitted under the creative commons license CC BY 4.0.

somewhere between 0 and 1.

For three-dimensional heterojunctions, Anderson's model usually gives a poor description of the band offset due to dangling bonds at the interface contributing to net charges at the interface. This is not automatically true for 2D heterojunctions, though. 2D materials are characterized by weak van-der-Waals bonding out-of-plane, the so-called van-der-Waals gap. As a consequence, for vertically stacked heterojunctions we expect a clean interface without dangling bonds and thus a vanishing interface dipole. Researchers investigated this question for MoS_2 and other group-6 TMDs finding good agreement with Anderson's electron affinity model both theoretically [41, 42] and experimentally [37]. Based on these results we chose the Anderson model as the theoretical basis for the investigation of the band offsets in the potential $CaAs_3$ heterostructures of Chapter 6.

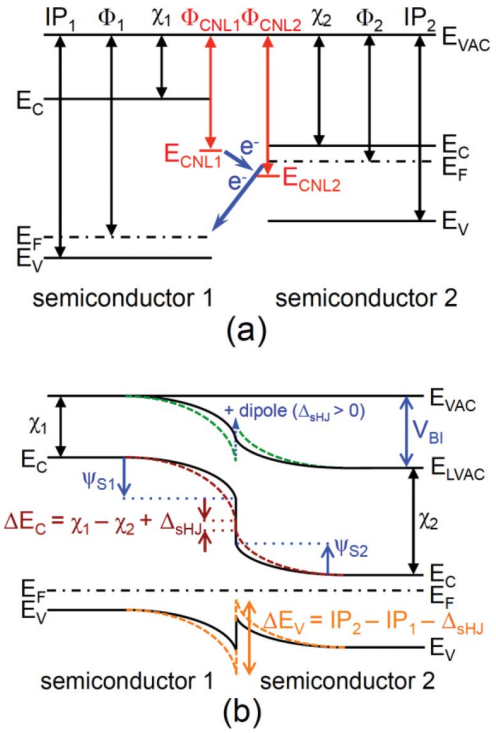

FIGURE 2.18: Non-ideal heterojunction energy band diagrams (including interface states) for a) an isolated p-type semiconductor and an isolated n-type semiconductor and (b) the corresponding semiconductor heterojunction formed after electron transfer. E_{CLN} refers to the charge neutrality level. The charge neutrality level changes the charge imbalance that has to be overcome at the heterojunction and thus the band bending (dotted lines in b). IP refers to the ionization potential, χ to the electron affinity, and Φ to the work function. ψ_S is the surface potential. Reprinted from Wager and Kuhn [40]. ©2017 The Author(s). Taylor & Francis Group, LLC ©. Reuse permitted under the creative commons license CC BY 4.0.

References

[1] William D. Callister and David G. Rethwisch. *Materials Science and Engineering: An Introduction, 9th Edition: Ninth Edition*. en. Wiley Global Education, Nov. 2013. ISBN: 978-1-118-47654-3.

[2] Hans-Jürgen Butt and Michael Kappl. *Surface and Interfacial Forces*. Newark, GERMANY: John Wiley & Sons, Incorporated, 2018. ISBN: 978-3-527-80434-4.

[3] Oleg A. Vydrov and Troy Van Voorhis. "Nonlocal van der Waals density functional: The simpler the better". In: *The Journal of Chemical Physics* 133.24 (Dec.

2010), p. 244103. ISSN: 0021-9606. DOI: 10.1063/1.3521275. URL: https://aip.scitation.org/doi/abs/10.1063/1.3521275 (visited on 04/27/2018).

[4] Stefan Grimme. "Semiempirical GGA-type density functional constructed with a long-range dispersion correction". de. In: *Journal of Computational Chemistry* 27.15 (2006), pp. 1787–1799. ISSN: 1096-987X. DOI: 10.1002/jcc.20495.

[5] Stefan Grimme et al. "A consistent and accurate ab initio parametrization of density functional dispersion correction (DFT-D) for the 94 elements H-Pu". In: *J. Chem. Phys.* 132.15 (Apr. 2010), p. 154104. ISSN: 0021-9606. DOI: 10.1063/1.3382344.

[6] Henrik Rydberg et al. "Van der Waals density functional for layered structures". In: *Physical review letters* 91.12 (2003), p. 126402.

[7] Felix Bloch. "Heisenberg and the early days of quantum mechanics". In: *Physics Today* 29.12 (1976), pp. 23–27.

[8] Feliciano Giustino. *Materials Modelling using Density Functional Theory Properties and Predictions*. Oxford University Press, 2014.

[9] Peter Y. Yu and Manuel Cardona. *Fundamentals of Semiconductors*. Graduate Texts in Physics. Berlin, Heidelberg: Springer Berlin Heidelberg, 2010. ISBN: 978-3-642-00709-5 978-3-642-00710-1. DOI: 10.1007/978-3-642-00710-1.

[10] Chihiro Hamaguchi. *Basic Semiconductor Physics*. en. Graduate Texts in Physics. Cham: Springer International Publishing, 2017. ISBN: 978-3-319-66859-8 978-3-319-66860-4. DOI: 10.1007/978-3-319-66860-4.

[11] mari. *An Introduction to Band Theory, A Molecular Orbital Approach*. en. Sept. 2014.

[12] Roland Winkler. "Introduction". en. In: *Spin—Orbit Coupling Effects in Two-Dimensional Electron and Hole Systems*. Ed. by Roland Winkler. Springer Tracts in Modern Physics. Berlin, Heidelberg: Springer, 2003, pp. 1–8. ISBN: 978-3-540-36616-4. DOI: 10.1007/978-3-540-36616-4_1.

[13] Michael Chapman and Carlos Sá de Melo. "Atoms playing dress-up". en. In: *Nature* 471.7336 (Mar. 2011), pp. 41–42. ISSN: 1476-4687. DOI: 10.1038/471041a.

[14] Zhiming M. Wang, ed. *MoS2: Materials, Physics, and Devices*. en. Vol. 21. Lecture Notes in Nanoscale Science and Technology. Cham: Springer International Publishing, 2014. ISBN: 978-3-319-02849-1 978-3-319-02850-7. DOI: 10.1007/978-3-319-02850-7.

[15] F. Dybała et al. "Pressure coefficients for direct optical transitions in MoS_2, $MoSe_2$, WS_2, and WSe_2 crystals and semiconductor to metal transitions". en. In: *Scientific Reports* 6 (May 2016), p. 26663. ISSN: 2045-2322. DOI: 10.1038/srep26663.

[16] Byoung Ki Choi et al. "Visualizing Orbital Content of Electronic Bands in Anisotropic 2D Semiconducting ReSe $_2$". en. In: *ACS Nano* 14.7 (July 2020), pp. 7880–7891. ISSN: 1936-0851, 1936-086X. DOI: 10.1021/acsnano.0c01054.

[17] Morasae Samadi et al. "Group 6 transition metal dichalcogenide nanomaterials: synthesis, applications and future perspectives". In: *Nanoscale Horiz.* 3.2 (2018), pp. 90–204. ISSN: 2055-6756, 2055-6764. DOI: 10.1039/C7NH00137A.

[18] G. F. Bassani and Giuseppe Pastori Parravicini. *Electronic states and optical transitions in solids*. 1st ed. International series of monographs in the science of the solid state v. 8. Oxford ; New York: Pergamon Press, 1975. ISBN: 978-0-08-016846-3.

[19] Robert Martin Eisberg and Robert Resnick. *Quantum physics of atoms, molecules, solids, nuclei, and particles*. New York: Wiley, 1974. ISBN: 978-0-471-23464-7.

[20] Di Xiao et al. "Coupled Spin and Valley Physics in Monolayers of MoS_2 and Other Group-VI Dichalcogenides". In: *Physical Review Letters* 108.19 (May 2012), p. 196802. DOI: 10.1103/PhysRevLett.108.196802.

[21] Ting Cao et al. "Valley-selective circular dichroism of monolayer molybdenum disulphide". en. In: *Nature Communications* 3.1 (June 2012), pp. 1–5. ISSN: 2041-1723. DOI: 10.1038/ncomms1882.

[22] Kin Fai Mak et al. "Control of valley polarization in monolayer MoS 2 by optical helicity". en. In: *Nature Nanotechnology* 7.8 (Aug. 2012), pp. 494–498. ISSN: 1748-3395. DOI: 10.1038/nnano.2012.96.

[23] Tetsuo Ogawa and Yoshihiko Kanemitsu. *Optical Properties of Low-dimensional Materials*. en. World Scientific, 1995. ISBN: 978-981-02-3048-7.

[24] Gang Wang et al. "Colloquium: Excitons in atomically thin transition metal dichalcogenides". In: *Reviews of Modern Physics* 90.2 (Apr. 2018), p. 021001. DOI: 10.1103/RevModPhys.90.021001.

[25] Miguel M. Ugeda et al. "Giant bandgap renormalization and excitonic effects in a monolayer transition metal dichalcogenide semiconductor". In: *Nature Materials* 13.12 (Dec. 2014), pp. 1091–1095. ISSN: 1476-1122, 1476-4660. DOI: 10.1038/nmat4061. URL: http://www.nature.com/articles/nmat4061 (visited on 06/11/2018).

[26] Xiaomu Wang et al. "Highly anisotropic and robust excitons in monolayer black phosphorus". en. In: *Nature Nanotechnology* 10.6 (June 2015), pp. 517–521. ISSN: 1748-3395. DOI: 10.1038/nnano.2015.71.

[27] Thomas Mueller and Ermin Malic. "Exciton physics and device application of two-dimensional transition metal dichalcogenide semiconductors". en. In: *npj 2D Materials and Applications* 2.1 (Dec. 2018). ISSN: 2397-7132. DOI: 10.1038/s41699-018-0074-2.

[28] Xiao-Xiao Zhang et al. "Experimental Evidence for Dark Excitons in Monolayer WSe 2". en. In: *Physical Review Letters* 115.25 (Dec. 2015). ISSN: 0031-9007, 1079-7114. DOI: 10.1103/PhysRevLett.115.257403.

[29] Fengcheng Wu, Fanyao Qu, and A. H. MacDonald. "Exciton band structure of monolayer MoS 2". en. In: *Physical Review B* 91.7 (Feb. 2015). ISSN: 1098-0121, 1550-235X. DOI: 10.1103/PhysRevB.91.075310.

[30] A. Steinhoff et al. "Exciton fission in monolayer transition metal dichalcogenide semiconductors". en. In: *Nature Communications* 8.1 (Dec. 2017). ISSN: 2041-1723. DOI: 10.1038/s41467-017-01298-6.

[31] M Baranowski et al. "Dark excitons and the elusive valley polarization in transition metal dichalcogenides". en. In: *2D Materials* 4.2 (Feb. 2017), p. 025016. ISSN: 2053-1583. DOI: 10.1088/2053-1583/aa58a0.

[32] Xiao-Xiao Zhang et al. "Magnetic brightening and control of dark excitons in monolayer WSe2". en. In: *Nature Nanotechnology* 12.9 (June 2017), pp. 883–888. ISSN: 1748-3387, 1748-3395. DOI: 10.1038/nnano.2017.105.

[33] Railson Vasconcelos et al. "Dark exciton brightening and its engaged valley dynamics in monolayer WSe 2". en. In: *Physical Review B* 98.19 (Nov. 2018). ISSN: 2469-9950, 2469-9969. DOI: 10.1103/PhysRevB.98.195302.

[34] Maja Feierabend et al. "Dark exciton based strain sensing in tungsten-based transition metal dichalcogenides". In: *Physical Review B* 99.19 (May 2019), p. 195454. DOI: 10.1103/PhysRevB.99.195454.

[35] Maja Feierabend et al. "Proposal for dark exciton based chemical sensors". en. In: *Nature Communications* 8 (Mar. 2017), p. 14776. ISSN: 2041-1723. DOI: 10.1038/ncomms14776.

[36] Alexey Chernikov et al. "Exciton Binding Energy and Nonhydrogenic Rydberg Series in Monolayer WS 2". en. In: *Physical Review Letters* 113.7 (Aug. 2014). ISSN: 0031-9007, 1079-7114. DOI: 10.1103/PhysRevLett.113.076802.

[37] Ming-Hui Chiu et al. "Band alignment of 2D transition metal dichalcogenide heterojunctions". In: *Adv. Funct. Mater.* 27.19 (2017), p. 1603756. ISSN: 1616-3028. DOI: 10.1002/adfm.201603756.

[38] R. L. Anderson. "Germanium-gallium arsenide heterojunctions [Letter to the Editor]". In: *IBM J. Res. Dev.* 4.3 (July 1960), pp. 283–287. ISSN: 0018-8646. DOI: 10.1147/rd.43.0283.

[39] Ben G. Streetman and Sanjay Kumar Banerjee. *Solid State Electronic Devices*. 6th ed. 2006.

[40] John F. Wager and Kelin Kuhn. "Device Physics Modeling of Surfaces and Interfaces from an Induced Gap State Perspective". en. In: *Critical Reviews in Solid State and Materials Sciences* 42.5 (Sept. 2017), pp. 373–415. ISSN: 1040-8436, 1547-6561. DOI: 10.1080/10408436.2016.1223013.

[41] Yuzheng Guo and John Robertson. "Band engineering in transition metal dichalcogenides: Stacked versus lateral heterostructures". In: *Appl. Phys. Lett.* 108.23 (June 2016), p. 233104. ISSN: 0003-6951, 1077-3118. DOI: 10.1063/1.4953169.

[42] Daniel S. Koda et al. "Trends on band alignments: Validity of Anderson's rule in SnS_2- and $SnSe_2$-based van der Waals heterostructures". In: *Phys. Rev. B* 97.16 (Apr. 2018), p. 165402. DOI: 10.1103/PhysRevB.97.165402.

Chapter 3

Computational method

Computational methods have become indispensable for materials research, to facilitate the fundamental understanding of materials as well as advanced materials design. From the fundamental research perspective, modelling allows insight into material structure-property relationships that would be hard to observe in experiment in such detail and to such extent. From the design side, computational materials analysis short-cuts the trial-and-error design process by providing materials characteristics that serve as helpful starting points for the design.

Computational materials science spans many length scales from continuum mechanics to atomistic calculations. Here, we will focus on the smallest, the sub-nanometer to nanometer length scale. For that small systems sizes, model approximations can be kept at a minimum and for this reason the methods presented here are often referred to as *ab initio* (Latin for "from first principles").[1] Ab initio atomistic methods are based on the fundamental principles of quantum mechanics, which allows the prediction of materials properties without relying on empirical parameters. This has the advantage of providing a general and thus powerful model of reality.[1]

Still, we have to be conscious of the fact that in most model calculations we introduce some kind of approximation which limits the predictive power of the method. For this reason, calculated results have to be assessed carefully in the light of experimental results and with consideration of the theoretical limits of the model employed.[2] Further, the most accurate mathematical model can give blatantly wrong results if the calculation parameters have not been converged. Therefore, convergence plays a critical role in computational materials science.

In this work, we are concerned with atomistic simulations in the sub-nanometer to nanometer range. Atomistic simulations depend on the solution of the Schrödinger

equation. The time-independent Schrödinger equation for one electron in a potential energy landscape V(r) can be written as

$$\left[\frac{\boldsymbol{p}^2}{2m_e} + V(r)\right]\psi(r) = E\psi(r), \tag{3.1}$$

where $\mathbf{p} = -i\hbar\nabla$ is the momentum operator, m_e the electron mass and E the eigenvalue energy. The Schrödinger equation can be solved analytically only for the hydrogen atom and very simple molecules. As soon as we look at a system with several electrons, we deal with the many-body Schrödinger equation:

$$\left[-\sum_i \frac{\nabla_i^2}{2} - \sum_I \frac{\nabla_I^2}{2M_I} - \sum_{i,I} \frac{Z_I}{|\mathbf{r}_i - \mathbf{R}_I|} + \frac{1}{2}\sum_{i\neq j} \frac{1}{|\mathbf{r}_i - \mathbf{r}_j|} + \frac{1}{2}\sum_{I\neq J} \frac{Z_I Z_J}{|\mathbf{R}_I - \mathbf{R}_J|}\right]\Psi = E_{\text{tot}}\Psi, \tag{3.2}$$

in Hartree units, where

1. $-\sum_i \frac{\nabla_i^2}{2}$ is the kinetic energy of the electrons i
2. $-\sum_I \frac{\nabla_I^2}{2M_I}$ is the kinetic energy of the nuclei I with mass M_I
3. $-\sum_{i,I} \frac{Z_I}{|\mathbf{r}_i - \mathbf{R}_I|}$ is the Coulomb attraction between electrons and nuclei,
4. $+\frac{1}{2}\sum_{i\neq j} \frac{1}{|\mathbf{r}_i - \mathbf{r}_j|}$ is the Coulomb repulsion between electrons i and j, and
5. $+\frac{1}{2}\sum_{I\neq J} \frac{Z_I Z_J}{|\mathbf{R}_I - \mathbf{R}_J|}$ is the Coulomb repulsion between nuclei I and J.

This equation shows us the complex interdependence of electrons and nuclei, stemming from the electrostatic interactions between them that are called many-body interactions. The guiding principle underlying the methods explained in the subsequent sections is capturing the many-body interactions of this equation in a simplified way without having to compute the interaction terms explicitly.

3.1 Density functional theory

This chapter on density functional The motivation for density functional theory (DFT) comes from the complexity of the many-body Schrödinger equation (see Eq. 3.2). The

solution of the many-body Schrödinger equation, the many-body wave function, has the form of

$$\Psi = \Psi(r_1, r_2, ..., r_N; R_1, R_2, ..., R_M), \tag{3.3}$$

where r are the positions of the N electrons of the system and R are the position of M nuclei. If we discretize the unit cell of an example structure with a grid of N_p points, this means that solving the many-body Schrödinger equation for one quantum state alone would require of us to store N_p^{N+M} complex numbers: We encounter an exponential "wall".[1]

DFT allows us to uncouple the electrons of the many-body Schrödinger equation and to include their interactions using approximate exchange-correlation potentials. This shall be unfolded to some extent in this section based on the excellent textbooks of Feliciano Giustino[1] and Friedhelm Bechstedt[3].

3.1.1 The Hohenberg-Kohn theorems

At the heart of DFT is the realization that the energy of the ground state can be obtained based on the knowledge of the electronic density $n(r)$ only. Instead of having to account for all the interactions of a many-body system (between nuclei and nuclei, electrons and electrons and nuclei and electrons), we can describe the ground state of the system with the density which depends on three spatial variables only (see Fig. 3.1). More exactly stated, the total energy E of the ground state is a universal functional of the density $n(r)$: $E = F[n(r)]$. This is the first Hohenberg-Kohn Theorem.

For any quantum state it holds true that the total energy is a functional of the wave function: $E = F[\Psi(r_1, \ldots, r_N)]$. This means that changes in E are uniquely caused by changes in Ψ. The ground state is a special case by being uniquely dependent on the electron density. This is due to a series of dependencies: $n \rightarrow V_n \rightarrow \Psi \rightarrow E$. The density n uniquely determines the external potential V_n, the external potential uniquely determines the wave function Ψ and Ψ uniquely determines the total energy E. The relations $V_n \rightarrow \Psi$ and $\Psi \rightarrow E$ hold true for any quantum state as mentioned above, but $n \rightarrow V_n$ is only true for the ground state. So, an alternative expression of the first Hohenberg-Kohn Theorem is: the external potential is completely determined by the ground-state density. This is illustrated in Figure 3.2.[1, 3]

We can rationalize this by imagining whether two different external potentials, say V_{n1} and V_{n2}, could both lead to the exact same ground state. We can also ask: Can

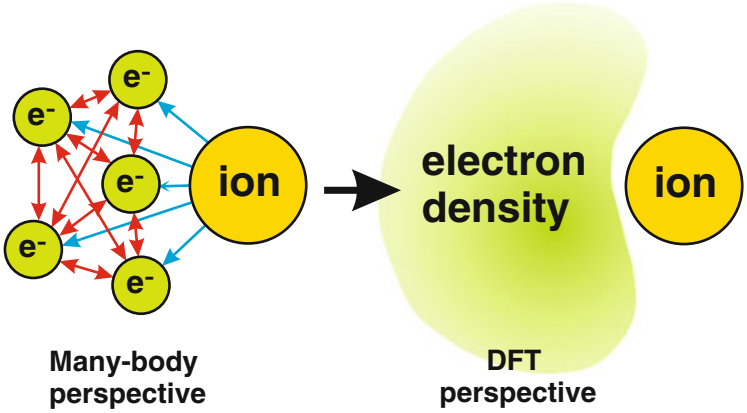

FIGURE 3.1: Illustration of the basic concept of density functional theory: The complicated many-body interactions between electrons and nuclei can be replaced by the electron density that depends on three spatial coordinates only in order to obtain the total energy of the ground state. Reprinted with permission from Bechstedt [3]. Copyright 2015 by the Springer-Verlag Berlin Heidelberg.

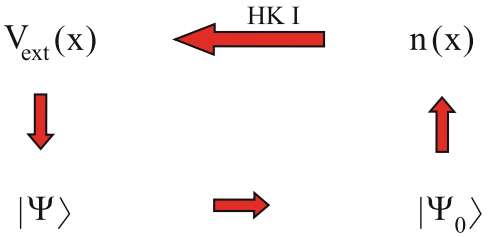

FIGURE 3.2: Dependencies. The dependency $n \rightarrow V_n$ is the contribution of the first Hohenberg-Kohn theorem (HK 1); it is only true for the ground state. Reprinted with permission from Bechstedt [3]. Copyright 2015 by the Springer-Verlag Berlin Heidelberg.

the same external potential lead to two different ground states? We first imagine an external potential: We can start from the free electron gas in which the electrons feel no disturbance. If we introduce a grid of positively charged ions into our electron gas, the electrons will be distracted by it and feel an external potential - they are no longer free. Now in the ground state, every electron has its place - the electrons fill up the energy levels according to Hund's rule and the Pauli principle. In the same system, there cannot be two ways or two ground states to position electrons in. A bit like in a well-ordered room, everything has its place. So we realize that external potential has one unique ground state and that two different external potentials cannot lead to the same ground state.

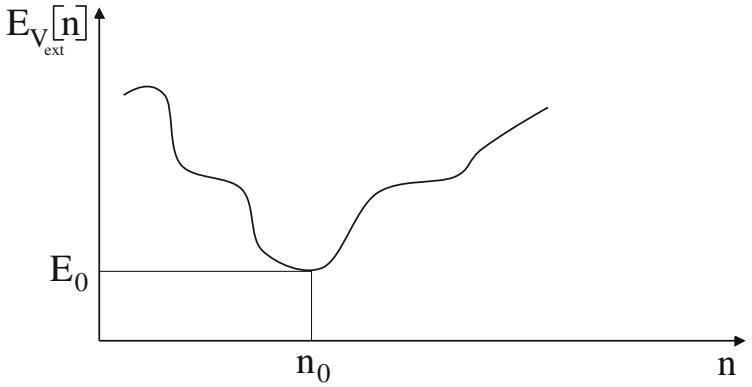

FIGURE 3.3: Schematic of the energy-density landscape. By the variation of the energy functional, we find its minimum and obtain the ground state density n_0. This is the second Hohenberg-Kohn theorem. Reprinted with permission from Bechstedt [3]. Copyright 2015 by the Springer-Verlag Berlin Heidelberg.

On the other hand, if we move to an excited state, it can be compared to a room that has gotten out of order, and the disorder can take many different forms. No matter where the things are scattered, it is a disordered state. So also, an excited state density cannot be uniquely determined by the external potential. This leads us back to an important point: DFT is a ground-state theory.

To determine the ground state energy from the density, we need another ingredient. We need a criterion for finding the ground state. This is contained in the second Hohenberg-Kohn theorem. The theorem states that "for a non-degenerate ground state and a given external potential the energy functional assumes its global minimum value E_0 by varying the density $n(r)$ towards the true ground state density $n_0(r)$" [3]. This is illustrated in Figure 3.3. In summary, the two Hohenberg-Kohn theorems allow us to replace the many degrees of freedom of the many-body problem with the electron density, a function of only three spatial coordinates to obtain the ground state. The ground state is obtained via the variation of an energy functional of the electron density. [3]

3.1.2 The Kohn-Sham formalism

But we do not yet have any information about the form of this functional. The Hohenberg-Kohn theorems do not give us a practical description of how exactly the total energy E_0 depends on the electron density of the ground state. To find the form of the energy

functional, we now turn to the Kohn-Sham ansatz (approach). The principle of the Kohn-Sham ansatz is to construct the many-body, interacting electron density with the help of a non-interacting system. The non-interacting electrons are placed in an effective potential that mimics the electron-electron interactions. The effective potential includes both known and unknown contributions of the electron-electron interaction. The trick is to separate the known contributions and to calculate them exactly while lumping the unknown contributions together in a so-called exchange-correlation functional which we then calculate approximately.[3]

To arrive at the Kohn-Sham equation, we need to take several steps to simplify the many-body equation. First, we apply the clamped nuclei approximation: we assume that the nuclei are fixed for a specific time frame. Thus, the potential energy landscape due to the atomic nuclei does not change while solving the Schrödinger equation and the Hamiltonian becomes a function of the electron coordinates only. This assumption is valid as the mass of nuclei is several magnitudes larger than electronic mass and this makes them static from an electron perspective. After solving the Schrödinger equation for a specific constellation of nuclei, their positions may be changed and the Schrödinger equation solved again for the new constellation, with which atomic movement can be simulated.

The clamped nuclei approximation allows us to remove the kinetic term of the nuclei (second term) from the many-body Schrödinger equation and to replace the Coulomb repulsion between nuclei (fifth term) with a constant added to the energy. We can also state the Coulomb attraction between nuclei and electrons as a sum over the electrons only, rewriting the sum as follows:[1]

$$\sum_{i,I} \frac{Z_I}{|\mathbf{r}_i - \mathbf{R}_I|} = \sum_i V_n(r_i); \text{ with } V_n(r) = \sum I \frac{Z_I}{|\mathbf{r} - \mathbf{R}_I|} \tag{3.4}$$

This in effect decouples the motion of electrons and nuclei. Our wavefunction Ψ is now longer dependent on the nuclei coordinates. We obtain the Schrödinger equation in the form:

$$\left[-\sum_i \frac{\nabla_i^2}{2} - \sum_i V_n(r_i) + \frac{1}{2} \sum_{i \neq j} \frac{1}{|\mathbf{r}_i - \mathbf{r}_j|} \right] \Psi = E\Psi \tag{3.5}$$

Our electrons are, however, still coupled. This coupling we eliminate in a next step, which represents a drastic approximation: We eliminate the Coulomb repulsion between

electrons by rewriting the Hamiltonian as a sum of independent one-electron Hamiltonians $\hat{H}_0$ and dropping the interaction part.[1]

$$\sum_i \hat{H}_0(r_i)\Psi = E\Psi \tag{3.6}$$

The solution Ψ of this equation can be written as a product of the individual wavefunctions ϕ_i. This approximation is called the independent electron approximation. It has weighty consequences, and thus the electron interaction has to be reintroduced in some way to make this model physically meaningful. Thus we now reintroduce the Coulomb interaction using a mean-field approximation, "blanket" repulsion all electrons experience. The interaction term $V_H(r) = \int dr' \frac{n(r')}{|r-r'|}$, also called Hartree potential, depends on the electron charge density $n(r)$. This mean-field Coulomb interaction, however, does not consider the quantum nature of the electrons and two further important aspects must be considered: Electron exchange interactions and electron correlation interactions. The electron exchange arises from the Pauli exclusion principle which states that two electrons of the same spin may not occupy the same quantum state. In brief, the electron exchange can be added by adding another term to the Hamiltonian, the Fock exchange term $V_X(r, r')$. This term is exact, however, it is non-local as we have to integrate over a second position variable r'. Correlation describes the fact that due to Coulomb repulsion, it is less likely to find an electron close to another electron. Mathematically, this is expressed as $|\Psi(r_1, r_2)|^2 < |\phi(r_1)\phi(r_2)|^2$. That means, we must introduce a correction term $V_C(r)$ to account for correlation effects, if we want to keep the product form of the wave function. However, the exact form of the correlation $V_C(r)$ is still missing. Both exchange and correlation effects lower the total energy by reducing the repulsion between electrons that is overpredicted with the mean-field Coulomb interaction approach. [1]

After all these approximations we can write the resulting single-particle Schrödinger equation as follows:[1]

$$\left[-\frac{\nabla_i^2}{2} + V_n(r) + V_H(r) + V_x(r) + V_C(r)\right]\phi_i(r) = \epsilon_i\phi_i(r) \tag{3.7}$$

With ϵ_i being the eigenvalues. This form of the equation is called the Kohn-Sham equation. Now we come back to our original quest: finding a form of the energy functional $E = F[n(r)]$, obtained from the Hohenberg-Kohn theorem. As a result of the

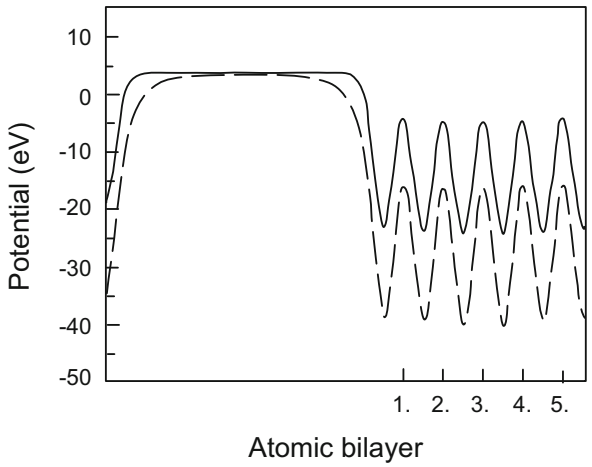

FIGURE 3.4: Plane-average of the potential of the diamond (111)2x1 surface. The dashed line represents the effective Kohn-Sham potential with exchange and correlation effects included. The solid line shows the potential without considering exchange and correlation. Reprinted with permission from [3]. Copyright 2015 by the Springer-Verlag Berlin Heidelberg.

Kohn-Sham ansatz, we can divide the energy functional $F[n]$ into two parts, the total energy functional in the independent electron approximation and the exchange-correlation energy functional E_{xc}. [1]

$$E = F[n]$$
$$= \overbrace{\underbrace{\int d\mathbf{r} n(\mathbf{r}) V_{\mathrm{n}}(\mathbf{r})}_{\text{External potential}} - \underbrace{\sum_i \int d\mathbf{r} \phi_i^*(\mathbf{r}) \frac{\nabla^2}{2} \phi_i(\mathbf{r})}_{\text{Kinetic energy}} + \underbrace{\frac{1}{2} \iint d\mathbf{r} d\mathbf{r}' \frac{n(\mathbf{r}) n(\mathbf{r}')}{|\mathbf{r} - \mathbf{r}'|}}_{\text{Hartree energy}}}^{\text{Total energy in the independent electrons approximation}} + \underbrace{E_{xc}[n]}_{\text{XC energy}}. \tag{3.8}$$

The energy is obtained by an integration of the potential, this is how Equation 3.7 and 3.8 are related. Effectively, we separate the functional into two parts: the contributions that we can describe and the contributions we do not know how to describe. We know the external potential, the kinetic energy and we can add the mean-field Hartree energy. We do not know the correlation and exchange effects. The last term, $E_{xc}[n]$, contains the unknown contributions from the electron exchange and correlation. This part must be approximated to enable the calculation of the ground state energy. If we were able to find an exact expression for $E_{xc}[n]$, density functional theory would be exact. [1, 3]

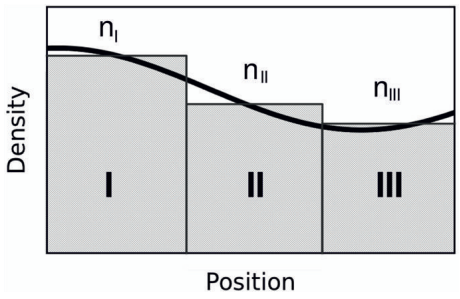

FIGURE 3.5: Working principle of the local density approximation. The electron density landscape is approximated locally by a homogenous electron gas. Reprinted with permission from Giustino [1]. Copyright 2014 by Oxford Publishing Limited (Academic).

The exchange-correlation energy is not negligible; it is of the same order of magnitude as the kinetic energy of the electrons.[1] Figure 3.4 exemplifies the importance of the exchange-correlation effect. The image shows the electrostatic potential of the surface of a diamond slab: the plateau signifies the vacuum region, the oscillations reflect the underlying lattice. With exchange-correlation effects left out (solid line), the binding of the atoms in the slab is severely underestimated in comparison to the potential including exchange-correlation effects (dashed line).

3.1.3 Exchange-correlation functionals

There are several approximations of the exchange-correlation energy functional, the most well-known being the Local Density Approximation (LDA) and the Generalized Gradient Approximation (GGA).[1] The question they address is: How can we take into account the varying electron density across our system? The approach of the LDA is to approximate correlation effects in each local region assuming a homogeneous electron gas for that region (see Fig. 3.5)

This works well for materials for which the electronic density varies only slowly. GGA seeks a more realistic approximation to the inhomogeneous electron density in real materials. It introduces a dependence on the local gradient and is, therefore, an improved version of the LDA.[2] The most popular GGA functional for solid-state physics is the PBE functional named after its authors Perdew, Burke and Ernzerhof.[4]

Experience shows that LDA predicts good elasticity but bad lattice parameters. Hence, it is well suited for surface energy and phonon calculations. As LDA overestimates binding and adhesion it is unsuitable for predicting chemical reactions. On the

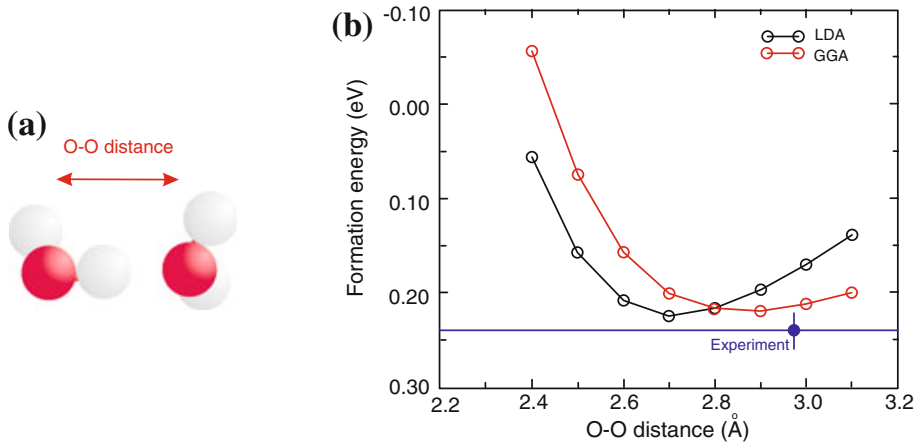

FIGURE 3.6: Prediction of the equilibrium distance of water dimers using LDA and GGA exchange-correlation. a) the water dimer has an equilibrium oxygen-oxygen distance of about 3 Åat which the formation energy is minimized. b) Formation energy predicted with the LDA and GGA exchange-correlation functionals. GGA predicts a larger equilibrium distance and is closer to experiment than LDA. Reprinted with permission from Bechstedt [3]. Copyright 2015 by the Springer-Verlag Berlin Heidelberg.

other hand, GGA gives good lattice parameters but softer elasticity. The prediction of the bandgap is more accurate than with LDA due to the more accurate lattice parameters. The accuracy of phonon calculations with GGA will not be very good because of the soft elasticity. The differences in predictive power between LDA and GGA are shown in Figure 3.6 for the example of the water dimer.

Another way to approximate the exchange and correlation effects, is to construct hybrid functionals. Hybrid functionals include a part of the exact Hartree-Fock exchange together with other exchange-correlation approaches as LDA or GGA. A widely used hybrid functional is the HSE06 functional.[5]

3.1.4 Computational implementation

In DFT calculations, the Kohn-Sham equations are solved self-consistently as an eigenvalue problem. The self-consistency cycle is shown as a flow chart in Fig 3.7: The starting electron density is an initial guess obtained by adding up the electron densities of the isolated atoms. Then, the Hartree potential V_{H} and the exchange potential V_{XC} are calculated based on the starting density. The total potential V_{tot} is inserted in the

Kohn-Sham equations that provide us with an updated electron density. Now the cycle is repeated until convergence is reached.

To solve the Kohn-Sham equation self-consistently, the wavefunctions we solve for need to be rewritten in a computer-friendly way. More accurately, we need to find a way to express the independent particle wavefunctions Φ_i as linear combinations of basis functions. This is how we can discretize the Kohn-Sham partial differential equations. There are two approaches for defining a basis set of functions: atomic orbitals and plane waves. When we choose atomic orbitals as basis functions, we can think of the electron as being bound to an atom and almost completely localized in an atomic orbital. Then, we expand the wave function of a molecule or solid with a basis set of atom-centred orbitals. We can also take the perspective that the electrons are nearly free and can be described by plane waves with a potential acting on them. Then we expand the wave function as a series of plane waves that are periodic according to the Bloch theorem.

In my calculations, I use codes that are based on plane waves. Thus I will focus on the implementation of plane-wave basis sets in the subsequent explanations. In Chapter 3.1.2, we made the independent electron approximation which allows us to represent the many-body wavefunction Ψ with the product of independent electron wavefunctions Φ_i. According to Bloch's theorem, for a crystalline solid we can write the single-electron wavefunction as the product of a periodic part $u_i(r)$ and a wavelike part or phase factor $e^{ik\cdot r}$. [6]

$$\Phi_{i,k}(r) = u_i(r)e^{ik\cdot r} \tag{3.9}$$

with k being a wavevector within the first Brillouin zone. $u_i(r)$ is periodic with the lattice, which means it is the same in every unit cell. The wavelike part acts as an envelope function, modulating the periodic part. Thus, the wavefunction Φ_i is not necessarily periodic with the lattice, but $|\Phi_i|^2$ is. As a result of Bloch's theorem, we have to describe only the electrons of the first unit cell in order to describe the whole lattice.

Because $u_i(r)$ is periodic with the direct lattice parameter, we can expand it with the help of plane waves that have wavevectors that are reciprocal lattice vectors G:

$$u_i(r) = \sum_G c_{i,G} e^{iG\cdot r}, \tag{3.10}$$

where $c_{i,G}$ are the plane wave expansion coefficients. Combining Equations 3.9 and 3.10, we can express the wavefunction as an expansion of discrete plane waves.

$$\phi_{i,k}(r) = \sum_{G} c_{i,k+G} e^{i(k+G)\cdot r}. \tag{3.11}$$

An important parameter to set for each calculation is the plane-wave cutoff. Each plane wave coefficient $c_{i,k+G}$ is associated with a kinetic energy $\frac{\hbar^2}{2m}|k+G|^2$.[3] The energy cutoff determines how many plane waves are included in the linear combination and thus the size of the basis set. However, we would need a very high energy cutoff (that is: many plane waves) to correctly describe the sharp peaks of the real-space wavefunction in the core atomic sphere region (picture). A high cutoff is, however, computationally expensive. On top of this, the expensive core electrons are less important than the valence electrons as electrons in the core usually do not contribute to reactions or bond formations and can be regarded as chemically inert. In the interest of computational cost, several methods have been developed to avoid describing the atomic core region using plane waves. We shall touch on them only briefly here.

The first method is the pseudopotential method. The steep periodic potential is replaced by a pseudopotential that is less steep in the core region and thus smoothens the core wavefunction. At the level of the valence electrons, the pseudopotential merges with the all-electron potential so that the valence electrons are described correctly. With a pseudopotential, valence electrons are described explicitly whereas core electrons are not described explicitly. Quantum Espresso[7, 8], used for calculations in Chapter 6, is a DFT code that can be run using pseudopotentials (among others).

Based on the pseudopotential method, a more accurate method was developed called projector-augmented waves (PAW). Simplifying a little, the basic idea here is that the properties of the all-electron wavefunction Ψ can be described by the properties of the pseudo-wavefunction $\tilde{\Psi}$ augmented by a projector function. Therefore, we can calculate results efficiently in the pseudo-space and afterwards transform them into the all-electron space.[9] The VASP[10, 11] DFT code is based on the PAW formalism.

Another approach to avoid describing the atomic core region using plane waves is to describe the atomic core using local orbitals. This method is called augmented plane waves (APW) and exists in several flavours.[12] With APW, all electrons can be described explicitly: valence electrons are described using plane waves and core electrons using atomic orbitals. WIEN2k[13] is an example of an all-electron code using APW.

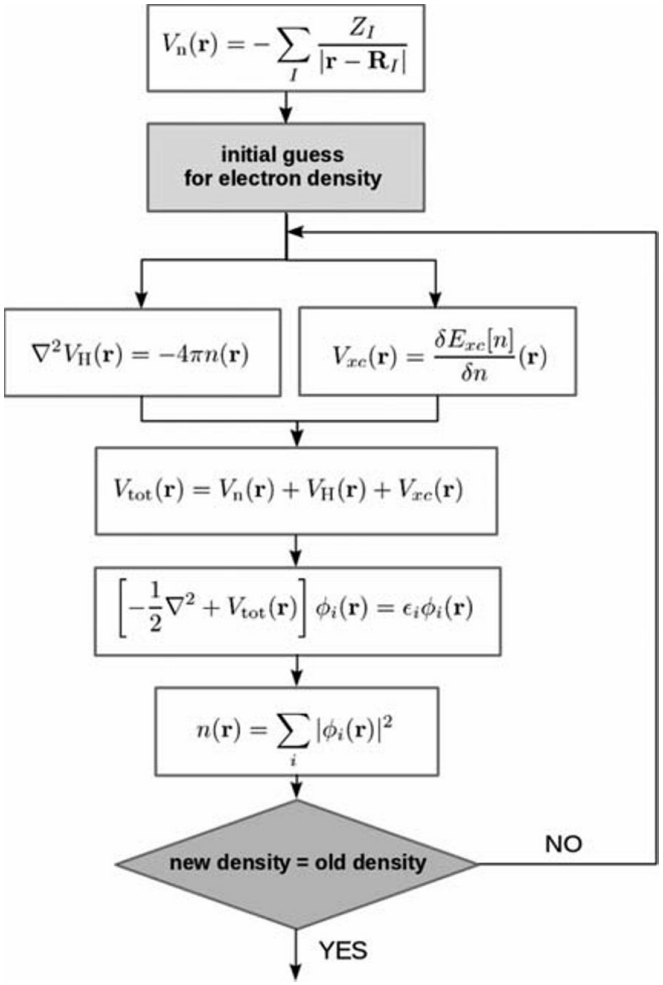

FIGURE 3.7: Self-consistency cycle for computing the ground-state electron density. The starting electron density is an initial guess obtained by adding up the electron densities of the isolated atoms. Then, the Hartree potential $V_{\rm H}$ and the exchange potential $V_{\rm XC}$ are calculated based on the starting density. The total potential $V_{\rm tot}$ is inserted in the Kohn-Sham equations that provide us with an updated electron density. Now the cycle is repeated until convergence is reached. Reprinted with permission from Giustino [1]. Copyright 2014 by Oxford Publishing Limited (Academic).

3.2 Many-body theory

Density functional theory accurately calculates the ground state of a system. However, band gaps are difficult to accurately predict with DFT, as the model of Coulomb repulsion employed does not sufficiently capture electron-electron interactions. This leads to systematic underestimation of band gaps in DFT calculations, also called the band gap problem.[14] In order to calculate excited states, we need to consider interactions between electrons more accurately. There have been considerable efforts to improve the accuracy of DFT, for example by adding a part of the exact Fock-exchange to the exchange-correlation functional in so-called Hybrid functionals.[15, 5]

A different approach to improve the accuracy of bandgap predictions is to move away from the density functional theoretical construct and to consider alternative theories. The Green's function technique as applied in *GW* calculations is an alternative approach to DFT. Figure 3.8 shows the underestimation of band gaps calculated in DFT with the PBE functional. *GW* band gaps agree much better with experiment.

3.2.1 *GW*

This section and the next section (on BSE) draw on the excellent review of Leng et al. [17]. The one-particle Green's function $G(\mathbf{r}_1 t_1, \mathbf{r}_2 t_2)$ describes the motion of a particle in space:[17]

$$\begin{aligned} G(\mathbf{r}_1 t_1, \mathbf{r}_2 t_2) &= -i \left\langle N, 0 \left| T\left[\hat{\psi}(\mathbf{r}_1 t_1)\, \hat{\psi}^\dagger(\mathbf{r}_2 t_2)\right] \right| N, 0 \right\rangle \\ &= \begin{cases} -i \left\langle N, 0 \left| \hat{\psi}(\mathbf{r}_1 t_1)\, \hat{\psi}^\dagger(\mathbf{r}_2 t_2) \right| N, 0 \right\rangle \text{ if } t_1 > t_2 \\ \quad i \left\langle N, 0 \left| \hat{\psi}^\dagger(\mathbf{r}_2 t_2)\, \hat{\psi}(\mathbf{r}_1 t_1) \right| N, 0 \right\rangle \text{ if } t_2 > t_1 \end{cases} \end{aligned} \tag{3.12}$$

Here, $|N, 0\rangle$ is the electron ground state, T is Wick's time operator for ordering the terms according to their time t, with the largest time to the left. $\hat{\psi}^\dagger$ and $\hat{\psi}$ are the fermion creation and annihilation operator, respectively. This equation describes the motion of an electron with the use of creation and annihilation operators: When an electron is removed from a location r_1 at time t_1 and added at another location r_2 at time t_2, its propagation in space and time can be described. The removal of an electron is akin to the creation of a "hole". Thus motions of holes can also be described. If $t_1 > t_2$, the Green's function gives the probability of finding an electron at r_1 at time

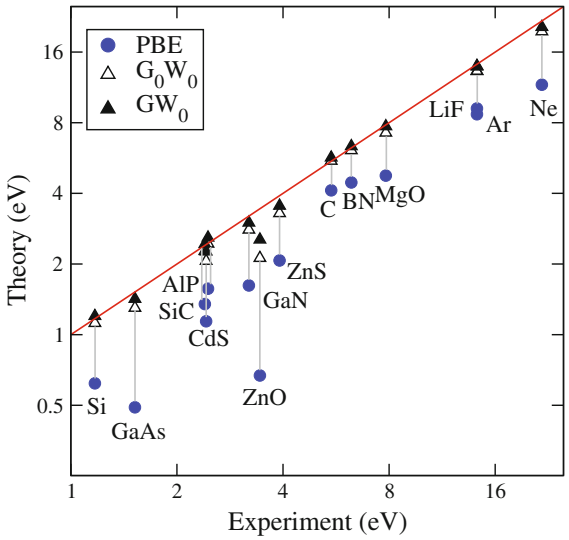

FIGURE 3.8: Calculated band gaps in comparison to experiment. PBE gaps are systematically underestimated. GW_0 and G_0W_0 band gaps based on the Green's function approach described in this chapter agree much better with experiment. GW_0 and G_0W_0 denote non-self-consistent GW calculations (see Chapter 3.2.3). Reprinted with permission from Bechstedt [3]. Copyright 2015 by the Springer-Verlag Berlin Heidelberg. Data from [16].

t_1 after it has been added at r_2, t_2. Conversely, if $t_2 > t_1$, the Green's function gives the probability of finding a hole at r_2 at time t_2 after it has been added at r_1, t_1.[17] Figure 3.9 illustrates the principle of the motion of particles described with creation and annihilation operators. In Figure 3.9 a) a "hole" is added by removing a fish and the motion of the "hole" is tracked until a fish is added back. Similarly, Figure 3.9 b) illustrates the motion of an extra electron in the system.

When we Fourier-transform Equation 3.12 from the time to the frequency domain ($(t_1 - t_2) \rightarrow \omega$) we obtain the Green's function in the Lehmann representation [17]

$$G\left(\mathbf{r}_1, \mathbf{r}_2; \omega\right) = \sum_i \frac{f_i\left(\mathbf{r}_1\right) f_i^*\left(\mathbf{r}_2\right)}{\omega - E_i + i\eta\,\mathrm{sgn}\left(E_i - \mu\right)} \tag{3.13}$$

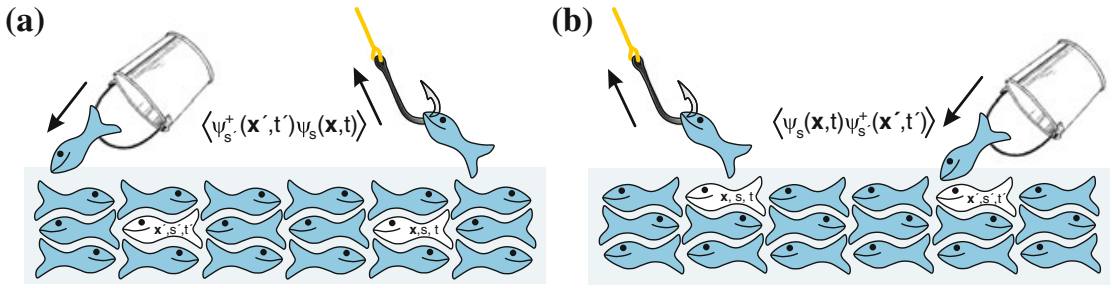

FIGURE 3.9: Illustration of particle propagation using creation and annihilation operators. a) Here a "hole" is added by removing or annihilating a fish and the motion of the "hole" is tracked until a fish is added back. b) Here a fish is created or added first and at a later time removed which illustrates the motion of an extra electron. Reprinted with permission from Bechstedt [3]. Copyright 2015 by the Springer-Verlag Berlin Heidelberg.

with

$$E_i = \begin{cases} E_{N+1,i} - E_{N,0} & \text{if} \quad E_i > \mu \\ E_{N,0} - E_{N-1,i} & \text{if} \quad E_i < \mu \end{cases}$$
$$f_i(\mathbf{r}) = \begin{cases} \langle N,0|\hat{\psi}(\mathbf{r})|N+1,i\rangle & \text{if } E_i > \mu \\ \langle N-1,i|\hat{\psi}(\mathbf{r})|N,0\rangle & \text{if } E_i < \mu \end{cases}. \tag{3.14}$$

Equation 3.13 is similar to the spectral function (see Chapter 2.3). Here E_i are the excitation energies and μ is the chemical potential. Wherever ω reaches an excitation energy, the Green's function has a pole (see Figure 3.10 a). The small shift $i\eta\,\mathrm{sgn}\,(E_i - \mu)$ is required for convergence of the Fourier transform (η is shown in Figure 3.10 a). $f_i\,(\mathbf{r}_1)$ are the Lehmann amplitudes. E_i and $f_i\,(\mathbf{r}_1)$ depend on whether we track an extra electron or a removed electron. If we track an extra electron, E_i is given by $E_{N+1,i} - E_{N,0}$ which is the total energy of the system with an additional electron minus the total energy of the ground state. This energy corresponds to the electron affinity. If we track the removal of an electron, E_i is given by the difference of the total energy of the ground state and the total energy of the system with one electron removed. This energy corresponds to the ionization energy. [17]

Thus, the one-particle Green's function theory parallels photoemission and inverse photoemission spectroscopy measurements (see Figure 3.10 b,c) if we assume the sudden approximation. The electron removal and addition energies appear as poles of the Green's function (see Figure 3.10 a). Thus, the ionization energy I as well as the electron

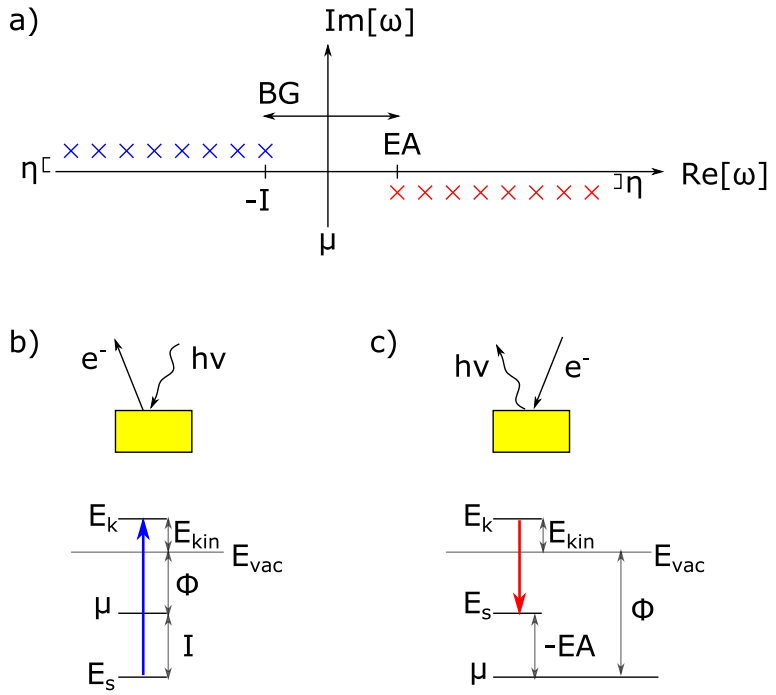

FIGURE 3.10: Physical meaning of the one-particle Green's function. a) Poles of the Green's function (crosses) correspond to excitation energies. Both, ionization energies (I) and electron affinities (EA) can be calculated with the Green's function approach. The propagation of particles in the Green's function using creation and annihilation operators corresponds to b) direct photoemission (removal of an electron) and c) inverse photoemission (addition of an electron) in the sudden approximation. Here E_s is the energy level of the sample, E_k the energy of the continuum, E_{vac} the vacuum level, μ the chemical potential and Φ the work function.

affinity EA can be predicted using the Green's function approach.[17]

The full Green's function can, however, not be solved, and approximations have to be employed. In order to find an approximation, the full one-particle Green's function $G(\mathbf{r}_1, \mathbf{r}_2; \omega)$ can be written as the sum of a non-interacting part $G_0(\mathbf{r}_1, \mathbf{r}_2; \omega)$ and an interacting part using Dyson's equation[17]

$$\begin{aligned} G(\mathbf{r}_1, \mathbf{r}_2; \omega) =& G_0(\mathbf{r}_1, \mathbf{r}_2; \omega) + \iint G_0(\mathbf{r}_1, \mathbf{r}'; \omega) \\ & \times \Sigma(\mathbf{r}', \mathbf{r}''; \omega) G(\mathbf{r}'', \mathbf{r}_2; \omega) \, d\mathbf{r}' d\mathbf{r}''. \end{aligned} \tag{3.15}$$

$\Sigma(\mathbf{r}', \mathbf{r}''; \omega)$ is the self-energy that contains all interactions; the exchange and correlation effects. The principle of the Dyson equation as the sum of an interacting and a

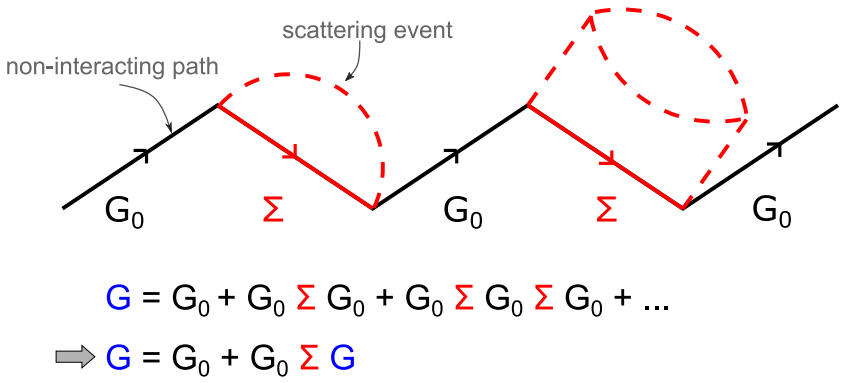

FIGURE 3.11: Principle of the Dyson equation. The interacting part of the Green's function $G_0 \Sigma G$ can be understood as the sum over all possible scattering events along the path. Σ is the self-energy or interaction Kernel. Then all these scattering events are factored in the fully interacting Green's function $G(\mathbf{r}_1, \mathbf{r}_2; \omega)$ so that we arrive at the form of the Dyson equation. After an idea of Christoph Friedrich [18]. Reuse permitted under the creative commons license CC BY 3.0.

non-interacting part is illustrated in Figure 3.11: We can describe the interacting part of the Green's function $G_0 \Sigma G$ by the sum over all possible scattering events along the path. All scattering events are factored in the fully interacting Green's function $G(\mathbf{r}_1, \mathbf{r}_2; \omega)$ so that we arrive at the Dyson equation.

Up to this point, the equation is still exact. Now, the first approximation we make is the quasiparticle approximation. Instead of trying to describe the strong interaction between electrons directly with the bare Coulomb potential v, we add the positive charge cloud that appears around an electron due to correlation effects, creating a quasiparticle (see Figure 3.12 for illustration). We now describe electron-electron interactions by treating them as weakly interacting quasiparticles instead of strongly interacting electrons. This positive charge cloud is often referred to as the Coulomb hole because of the absence of electron density in it. The charge of the electron is screened by the Coulomb hole around it and we can describe the interaction of screened electrons or quasiparticles with the screened Coulomb interaction W. Describing a system of weakly interacting quasiparticles instead of strongly interacting electrons allows us to set up a quasiparticle equation that bears formal similarity with the Kohn-Sham equations that operate in the independent electron approximation. As a result, we can treat the weak interaction between quasiparticles as a perturbation and use the Kohn-Sham eigenvalues and eigenfunctions as starting point to calculate the non-interacting Green's function $G_0(\mathbf{r}_1, \mathbf{r}_2; \omega)$.

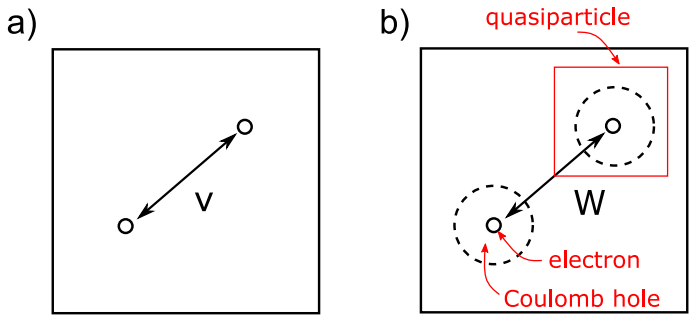

FIGURE 3.12: Illustration of the concept of quasiparticles. a) the interaction between electrons is described directly with the bare Coulomb potential v. b) the interaction between electrons is described using quasiparticles that include the electron and the Coulomb hole around it. The Coulomb hole screens the electron charge and thus allows us to describe the electrons as weakly interaction quasiparticles with the screened Coulomb interaction W. After an idea of Christoph Friedrich [18]. Reuse permitted under the creative commons license CC BY 3.0.

Going back to the Dyson equation (3.15), the bottleneck in this equation is now the calculation of the self-energy or interaction kernel Σ. Hedin[19] proposed to express the self-energy in terms of the screened Coulomb potential W and subsequently introduced the GW approximation in which the self-energy is approximated by the product of the screened Coulomb potential W and the Green's function G, $\Sigma = GW$. Hedin's equations form a set of coupled equations that can be solved in a self-consistent manner.

3.2.2 The Bethe-Salpeter equation

In an exciton, the electron and hole are bound together and their motion is correlated. To describe electron-hole interaction, the motion of both the electron and the hole must be traced simultaneously.[17] For this, the two-particle Green's function theory can be employed. The difference between one-particle propagation and correlated two-particle propagation is illustrated in Figure. 3.13.

Computational codes that seek to calculate excitation energies solve the Bethe-Salpeter equation (BSE). The BSE is the equivalent of the Dyson's equation for the two-particle Green's function, consisting of a non-interacting and an interacting part. The central element of the equation is the interaction kernel K that includes all electron-hole interactions. When the exciton wave function is written as an expansion of the

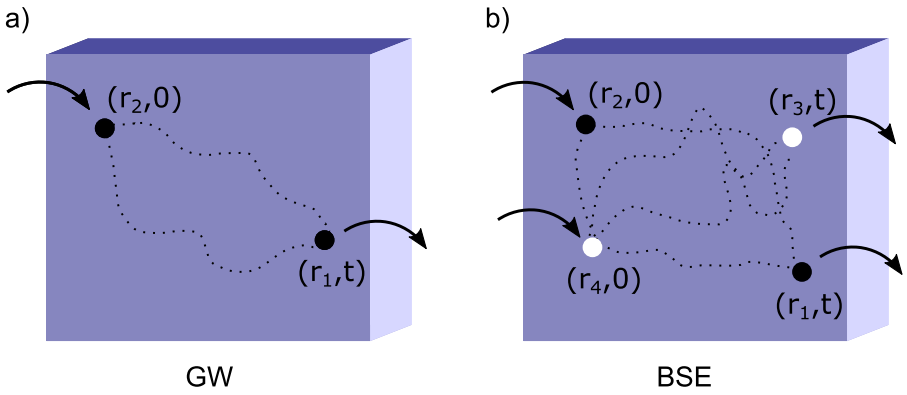

FIGURE 3.13: Comparison of particle propagation for a) single-particle excitations (GW) and b) for excitons (BSE). Excitons consist of two correlated particles, a hole and an electron, that have to be described simultaneously. After an idea of Sohrab Ismael-Beigi.

quasiparticle wave functions, the BSE can be formulated as an eigenvalue problem, in which the eigenvalue solved for is the exciton energy Ω_S (optical band gap energy) [17]

$$(E_c - E_v)\, A^S_{vc} + \sum_{v'c'} K^{AA}_{vc,v'c'}\,(\Omega_S)\, A^S_{v'c'} = \Omega_S A^S_{vc}. \tag{3.16}$$

Where $(E_c - E_v)$ is the energy of the uncorrelated electron-hole pair, and the second term on the left side contains the interaction in the bound electron-hole pair. For bulk and 2D materials, it is sufficient to consider only resonant frequencies in the interaction kernel, which is solving the BSE in the Tamm-Dancoff approximation. For 1D and 0D materials, it is advisable to consider the full BSE which includes resonant-antiresonant coupling.[17]

3.2.3 Computational implementation

GW eigenvalues can be solved for self-consistently. This is, however, rarely done; for two reasons: 1) *GW* calculations are very expensive. 2) An increased number of self-consistent cycles rarely proves beneficial to the accuracy of the results, often the opposite is the case. It is the standard procedure to do non-self-consistent G_0W_0 calculations for which the Green's function G and the screened Coulomb potential W are calculated only once. The typical workflow for G_0W_0 calculations is to first calculate the wavefunctions

and eigenvalues using DFT and then use these as input for the *GW* calculation. In that sense, the *GW* calculation is a many-body perturbation of DFT. The obtained quasiparticle-corrected eigenvalues and wave function are then used to solve the BSE and through that obtain exciton binding energies and optical band gaps. In short, the workflow is DFT-GW-BSE.

Tools with GW and BSE implementations include VASP[10, 11] and BerkeleyGW[20, 21, 22]. *GW* and BSE calculation are very memory intensive as they require a large number of empty states to converge.

References

[1] Feliciano Giustino. *Materials Modelling using Density Functional Theory Properties and Predictions*. Oxford University Press, 2014.

[2] Jürgen Hafner, Christopher Wolverton, and Gerbrand Ceder. "Toward Computational Materials Design: The Impact of Density Functional Theory on Materials Research". en. In: *MRS Bulletin* 31.9 (Sept. 2006), pp. 659–668. ISSN: 1938-1425, 0883-7694. DOI: 10.1557/mrs2006.174.

[3] Friedhelm Bechstedt. *Many-Body Approach to Electronic Excitations*. Vol. 181. Springer Series in Solid-State Sciences. Berlin, Heidelberg: Springer Berlin Heidelberg, 2015. ISBN: 978-3-662-44592-1 978-3-662-44593-8. DOI: 10.1007/978-3-662-44593-8.

[4] John P. Perdew, Kieron Burke, and Matthias Ernzerhof. "Generalized gradient approximation made simple". In: *Phys. Rev. Lett.* 77.18 (Oct. 1996), pp. 3865–3868. DOI: 10.1103/PhysRevLett.77.3865.

[5] Aliaksandr V. Krukau et al. "Influence of the exchange screening parameter on the performance of screened hybrid functionals". In: *J. Chem. Phys.* 125.22 (Dec. 2006), p. 224106. ISSN: 0021-9606. DOI: 10.1063/1.2404663.

[6] Philip Peter Rushton. "Towards a non-local density functional description of exchange and correlation". PhD thesis. Durham University, 2002.

[7] Paolo Giannozzi et al. "QUANTUM ESPRESSO: a modular and open-source software project for quantum simulations of materials". In: *J. Phys. : Condens. Matter.* 21.39 (Sept. 2009), p. 395502. ISSN: 0953-8984. DOI: 10.1088/0953-8984/21/39/395502.

[8] P. Giannozzi et al. "Advanced capabilities for materials modelling with Quantum ESPRESSO". en. In: *Journal of Physics: Condensed Matter* 29.46 (Oct. 2017), p. 465901. ISSN: 0953-8984. DOI: 10.1088/1361-648X/aa8f79.

[9] Xavier Gonze and Fabio Finocchi. "Pseudopotentials Plane Waves–Projector Augmented Waves: A Primer". en. In: *Physica Scripta* 2004.T109 (Jan. 2004), p. 40. ISSN: 1402-4896. DOI: 10.1238/Physica.Topical.109a00040.

[10] G. Kresse and J. Furthmüller. "Efficient iterative schemes for ab initio total-energy calculations using a plane-wave basis set". In: *Phys. Rev. B* 54.16 (Oct. 1996), pp. 11169–11186. DOI: 10.1103/PhysRevB.54.11169.

[11] G. Kresse and J. Furthmüller. "Efficiency of ab-initio total energy calculations for metals and semiconductors using a plane-wave basis set". In: *Comput. Mater. Sci.* 6.1 (July 1996), pp. 15–50. ISSN: 0927-0256. DOI: 10.1016/0927-0256(96)00008-0.

[12] K. Schwarz, P. Blaha, and G. K. H. Madsen. "Electronic structure calculations of solids using the WIEN2k package for material sciences". en. In: *Computer Physics Communications*. Proceedings of the Europhysics Conference on Computational Physics Computational Modeling and Simulation of Complex Systems 147.1 (Aug. 2002), pp. 71–76. ISSN: 0010-4655. DOI: 10.1016/S0010-4655(02)00206-0.

[13] Peter Blaha et al. *WIEN2k: An Augmented Plane Wave Plus Local Orbitals Program for Calculating Crystal Properties*. Techn. Universitat, 2019. ISBN: 978-3-9501031-1-3.

[14] Jason M. Crowley, Jamil Tahir-Kheli, and William A. Goddard. "Resolution of the Band Gap Prediction Problem for Materials Design". In: *The Journal of Physical Chemistry Letters* 7.7 (Apr. 2016), pp. 1198–1203. DOI: 10.1021/acs.jpclett.5b02870.

[15] Axel D. Becke. "Perspective: Fifty years of density-functional theory in chemical physics". In: *J. Chem. Phys.* 140.18 (May 2014), 18A301. ISSN: 0021-9606, 1089-7690. DOI: 10.1063/1.4869598.

[16] M Shishkin and G Kresse. "Implementation and performance of the frequency-dependent G W method within the PAW framework". In: *Physical Review B* 74.3 (2006), p. 035101.

[17] Xia Leng et al. "GW method and Bethe-Salpeter equation for calculating electronic excitations: GW method and Bethe-Salpeter equation". en. In: *Wiley Interdisciplinary Reviews: Computational Molecular Science* 6.5 (Sept. 2016), pp. 532–550. ISSN: 1759-0876. DOI: 10.1002/wcms.1265.

[18] *Many-Body Pertubation Theory - The GW approximation - - Picking Flowers 2019.* Oct. 2019.

[19] Lars Hedin. "New method for calculating the one-particle Green's function with application to the electron-gas problem". In: *Phys. Rev.* 139.3A (1965), A796.

[20] Mark S. Hybertsen and Steven G. Louie. "Electron correlation in semiconductors and insulators: Band gaps and quasiparticle energies". In: *Phys. Rev. B* 34.8 (Oct. 1986), pp. 5390–5413. ISSN: 0163-1829. DOI: 10.1103/PhysRevB.34.5390.

[21] Jack Deslippe et al. "BerkeleyGW: A massively parallel computer package for the calculation of the quasiparticle and optical properties of materials and nanostructures". In: *Comput. Phys. Commun.* 183.6 (June 2012), pp. 1269–1289. ISSN: 0010-4655. DOI: 10.1016/j.cpc.2011.12.006.

[22] Michael Rohlfing and Steven G. Louie. "Electron-hole excitations and optical spectra from first principles". In: *Phys. Rev. B* 62.8 (Aug. 2000), pp. 4927–4944. DOI: 10.1103/PhysRevB.62.4927.

Chapter 4

Pressure dependence of direct optical transitions in ReS_2 and $ReSe_2$

Author contributions:

Robert Oliva wrote the paper, took part in photoreflectance (PR) measurements, and analyzed PR data. I carried out first-principles calculations and contributed to the drafting of the results, discussion and methods sections. Filip Dybala and Jan Kopaczek performed the high-pressure PR experiments. Ying Qin and Sefaattin Tongay. grew the samples. Oleg Rubel planned and supervised the calculations, and Robert Kudrawiec planned the research and coordinated it. All authors discussed the results and commented on the paper.

This chapter was published in npj 2D Materials and Applications 3(1) (2019): 1-8. DOI: 10.1038/s41699-019-0102-x, and is here reproduced under the creative commons license CC BY 4.0.

The supplementary information is available in Appendix A.

Abstract

The ReX_2 system ($X = S$, Se) exhibits unique properties that differ from other transition metal dichalcogenides. Remarkably, its reduced crystal symmetry results in a complex electronic band structure that confers this material in-plane anisotropic properties. In addition, multilayered ReX_2 presents a strong 2D character even in its bulk form. To fully understand the interlayer interaction in this system, it is necessary to obtain an accurate picture of the electronic band structure. Here, we present an experimental and theoretical study of the electronic band structure of ReS_2 and $ReSe_2$ at high-hydrostatic pressures. The experiments are performed by photoreflectance spectroscopy and are analyzed in terms of ab initio calculations within the density functional theory. Experimental pressure coefficients for the two most dominant excitonic transitions are obtained and compared with those predicted by the calculations. We assign the transitions to the Z k-point of the Brillouin zone and other k-points located away from high-symmetry points. The origin of the pressure coefficients of the measured direct transitions is discussed in terms of orbital analysis of the electronic structure and van der Waals interlayer interaction. The anisotropic optical properties are studied at high pressure by means of polarization-resolved photoreflectance measurements.

4.1 Introduction

The ReX_2 crystals ($X = S$, Se) are semiconductors from the family of two-dimensional layered transition metal dichalcogenides (TMDCs) that exhibit special properties. Rhenium-based TMDCs have received increasing interest during the last few years owing to their large in-plane anisotropic properties. These properties result from their particular band structure and reduced crystal symmetry, as well as a strong 2D character that has been attributed to weak van der Waals interlayer bonding even in their bulk form.[1, 2] Besides the large fundamental interest, ReX_2 has also shown to be a highly interesting technoslogical material for many potential applications, including photodetectors,[3, 4, 5, 6, 7, 8] solar cells,[9] photonics,[10] flexible electronics,[11] and field-effect transistors.[12, 13, 14, 15, 16] Remarkably, the small interlayer coupling of ReX_2 opens an exciting field of new possibilities, as it may allow to design bulk devices that retain 2D functionalities only present in single-layered materials.[17] To fully exploit the applications of ReX_2 for developing novel optoelectronic devices, it is crucial to further characterize its fundamental properties. Optical modulation spectroscopy is a very powerful method

to study the optical properties of semiconductors. Owing to its differential-like character, interband-related features are highly enhanced and background signal is suppressed, thus allowing to accurately measure direct optical transitions.[18] So far, different modulation spectroscopies have shown to be very useful for studying the optical transitions of ReX_2: piezoreflectance,[19] electrolyte electroreflectance,[20] thermoreflectance,[21] and polarization-dependent measurements[22, 23, 24] revealed two and three excitonic transitions for ReS_2 and $ReSe_2$, respectively. These works provided evidence that these excitons, which exhibit a strongly polarized dipole character, were confined within single layers. However, the extent to which ReX_2 behaves as stacked decoupled layers has recently been a topic of intense debate.[2, 22, 23, 25, 26, 27] On the one hand, direct photoreflectance (PR) measurements on the electronic dispersion found that ReX_2 indeed exhibits a significant degree of electronic coupling.[22] This result is also supported by angle-resolved photoemission experiments (ARPES), which showed that there exists a significant electronic dispersion along the van der Waals gap.[25, 26] Also, recent calculations show that the fundamental bandgap shrinks by 32.7% in ReX_2 from monolayer to bulk, and the interlayer binding energy is similar to other TMDCs such as MoS_2.[28]

On the other hand, optical, vibrational, and structural measurements indicate that ReX_2 exhibits a strong 2D character. For instance, photoluminescence experiments revealed that the emission energy of ReS_2 is almost independent to the number of layers ($\Delta E \approx -50$ meV from one monolayer to bulk) in contrast with other G6-TMDCs (e.g., $\Delta E \approx -600$ meV for MoS_2).[2] For the case of $ReSe_2$, it was shown that it retains a direct bandgap regardless of its crystal thickness, with excitons strongly confined within single layers for bulk crystals, indicating a weak interlayer interaction.[23] Moreover, the Raman spectrum of monolayer ReS_2 is almost identical to that of bulk, which evidences an ultraweak interlayer coupling.[27] Also, low-frequency Raman measurements showed that interlayer force constant in ReX_2 is significantly smaller than other G6-TMDCs (by a factor of ≈ 40 %).[29] One of the most direct ways to probe interlayer interaction is to modulate the interlayer distance from high-pressure (HP) measurements. In this regard, HP X-ray diffraction measurements show that the bulk modulus of ReX_2 (23-31 GPa)[30, 31] is significantly lower than group 6 TMDCs (57-72 GPa).[32, 33, 34, 35] HP Raman measurements on ReS_2 showed a twofold decreased pressure coefficient of the out-of plane A1g phonon mode with respect to other TMDCs,[2] reinforcing the decoupled behavior in bulk ReS_2.[2]

Also, the large pressure metallization of ReS_2 (70 GPa) in comparison with MoS_2 (19 GPa) has been attributed to the larger interlayer coupling in MoS_2.[36] In spite of

the fundamental properties of this crystal system being relatively well-known at ambient pressure, HP optical measurements are highly desirable to evaluate the degree of electronic interlayer coupling in ReX_2. HP optical measurements are widely employed to obtain detailed structural and band structure information of semiconductors.[37] Moreover, HP optical measurements provide a highly useful benchmark to test first-principles calculations (such as those based on density functional theory) on challenging systems such as TMDCs. For the case of ReX_2, which exhibits weak interlayer forces at ambient pressure, HP optical measurements would shed new light into the role of orbital composition and van der Waals bonding on the excitonic energies and their pressure dependence. To date, the amount of HP optical studies on ReX_2 is scarce. The pressure dependence of the bandgap has only been experimentally investigated for ReS_2 by means of photoluminescence and absorption.[2, 36] These works found that the bandgap of ReS_2 does not increase with pressure and an almost-direct-to indirect bandgap transition takes place around 27 kbar. At higher pressures, calculations suggest that ReS_2 exhibits a metallization and superconducting state.[38]

Despite the previous investigations, there are still many questions that remain to be addressed with regard to the optical properties of ReX_2. First, an experimental assignment of the different excitonic transitions around the bandgap is desirable. So far, piezoreflectance measurements on the $ReSe_{2-x}S_x$ alloy suggested that the nature of the direct band edges is similar for each compositional end member,[39] but electronic dispersion calculations together with ARPES measurements suggested that the first direct electronic transitions take place either at the Z high symmetry point of the Brillouin zone (BZ) or away from the zone center, far from any particular high-symmetry direction.[25, 26, 28, 40, 41] Second, while the orbital composition of the states of ReS_2 has been described for different numbers of layers,[28] the interplay of orbital composition on the pressure dependence on the electronic band structure has not yet been investigated. Finally, the anisotropic properties of ReX_2 at high pressure remain to be explored.

To address these questions, we conduct PR measurements at high-hydrostatic pressure on thin ReS_2 and $ReSe_2$ exfoliated flakes. Polarization-dependent measurements performed at different pressures are used to energetically resolve the different excitonic transitions that exhibit very similar energies. Our results show that the two main direct transitions for ReS_2 and $ReSe_2$ exhibit a negative-pressure coefficient, in contrast to other TMDCs, such as MoS_2, $MoSe_2$, WS_2, or WSe_2.42 Such findings provide valuable information to assess the degree of electronic interlayer coupling and the role of

orbital composition on the energies of the band edge states. We discuss the experimental results in light of ab initio band structure calculations. These calculations are per formed using different functionals and considering different hydrostatic pressures. We find good agreement between the experimental and calculated pressure coefficients for the two main transitions. The experimentally observed transitions are assigned by inspecting the calculated electronic dispersion curves along a large grid of k-points in the whole 3D-BZ. Finally, we discuss the negative sign of the measured pressure coefficients in terms of orbital contributions to the states of the valence and conduction band of each transition and van der Waals interaction.

4.2 Methods

4.2.1 Experimental details

Two samples of different origins were used for each set of ReS_2 and $ReSe_2$ materials. One sample for each material was commercially obtained from HQgraphene, which consisted of thin flakes mechanically exfoliated from synthetic bulk crystals (99.995% purity). These are here labeled as samples I and III for ReS_2 and $ReSe_2$, respectively. The ReS_2 (sample II) and $ReSe_2$ (sample IV) samples were synthesized by the chemical vapor transport growth technique using Re (99.9999% purity), S, or Se (99.9999% purity) pieces. These precursors were mixed at atomic stoichiometric ratios and sealed into 0.5-in. diameter and 9-in.-long quartz tubes at 10-6 Torr. Extra ReI_3 was added as a transport agent to initiate the crystal growth and successfully transport Re, S, and Se atomic species. Closely following Re-S-Se binary-phase diagrams, we have synthesized crystals with temperature variation (drop) of 50 ° C over 5 weeks to complete the growth. Samples were cooled down to room temperature and ampoules were opened in a chemical glove box. The use of two samples grown under different conditions for each material allows to further validate the reproducibility of the here-presented experimental results.

To perform the HP hydrostatic measurements, the samples were mounted inside a UNIPRESS piston cylinder cell. The chosen pressure hydrostatic medium was Daphne 7474, which remained hydrostatic and transparent during the whole measurement, up to pressures of 18 kbar. The pressure was determined by measuring the resistivity of an InSb probe, which provides a 0.1-kbar sensitivity. A sapphire window in the press allowed optical access to perform PR measurements. For the PR measurements, a single grating of 0.55-m focal length and a Si pin diode were used to disperse and detect the

light reflected from the samples. A chopped (270 Hz) 405-nm laser line was pumped into the sample, together with a probe tungsten lamp (power of 150 W). Phase-sensitivity detection of the PR signal was processed with a lock-in amplifier. Further details on the experimental setup can be found elsewhere.[42] All measurements were performed at ambient temperature and pressures up to $\approx$ 18 kbar. At this pressure range, no phase transition was observed and only the Td crystal structure was investigated.

4.2.2 Computational details

Ab initio calculations on the the DFT level were carried out using the Vienna Ab initio Simulation Package (VASP),[43, 44] with the projector augmented wave[45] potentials as implemented by Kresse and Joubert.[46] The SCAN[47] semilocal exchange-correlation functional was employed. SCAN belongs to the meta-general-gradient-approximation (meta-GGA) functionals and has shown to produce more accurate results than conventional GGA functionals at a very comparable computational cost.[47, 48, 49] In particular, SCAN is recommended for electronic structure prediction of materials with heterogeneous bond types[50] (e.g., covalent and van der Waals) as well as layered materials.[48] It is therefore well suited for the band structure prediction of ReX_2. In addition, a revised Vydrov-van Voorhis (rVV10) long-range van der Waals interaction[51, 52, 53] was used.

Structure information of ReS_2 and $ReSe_2$ was taken from Murray et al. [54] and Alcock and Kjekshus,Alcock and Kjekshus [55] respectively. Structure relaxation was undertaken with a Monkhorst-Pack[56] k-mesh of $5\times5\times5$ with the above mentioned basis set and functionals. Seven electrons were considered for the valence of Re (5d5 6s2). The cutoff energy for the plane-wave expansion was set to 323.4 and 282.8 eV for ReS_2 and $ReSe_2$, respectively, which is 25% above the recommended values in the pseudopotential files. Relevant properties (pressure coefficient, bandgaps, and band character) were carefully checked for convergence with the kinetic energy cutoff as it can be seen in Figures S12-S17 of the S.I. Structures were relaxed until the total energy change and the band structure energy change dropped below 10-7 eV, and the residual atomic forces were less than 0.02 eV/Åin their absolute value. Crystallographic information files with atomic structures at 0 and 20 kbar, as used in the calculations, can be accessed through the Cambridge crystallographic data center (CCDC deposition numbers 1862132-1862135).

For calculations of the band structure and optical properties, spin-orbit interaction was taken into account. The cutoff energy was set to normal accuracy, which is 258.7

eV for ReS_2 and 226.2 eV for $ReSe_2$. High-density gamma-centered k-mesh calculations ($34 \times 34 \times 34$) were performed to investigate possible VBM and CBM located off the symmetry points.

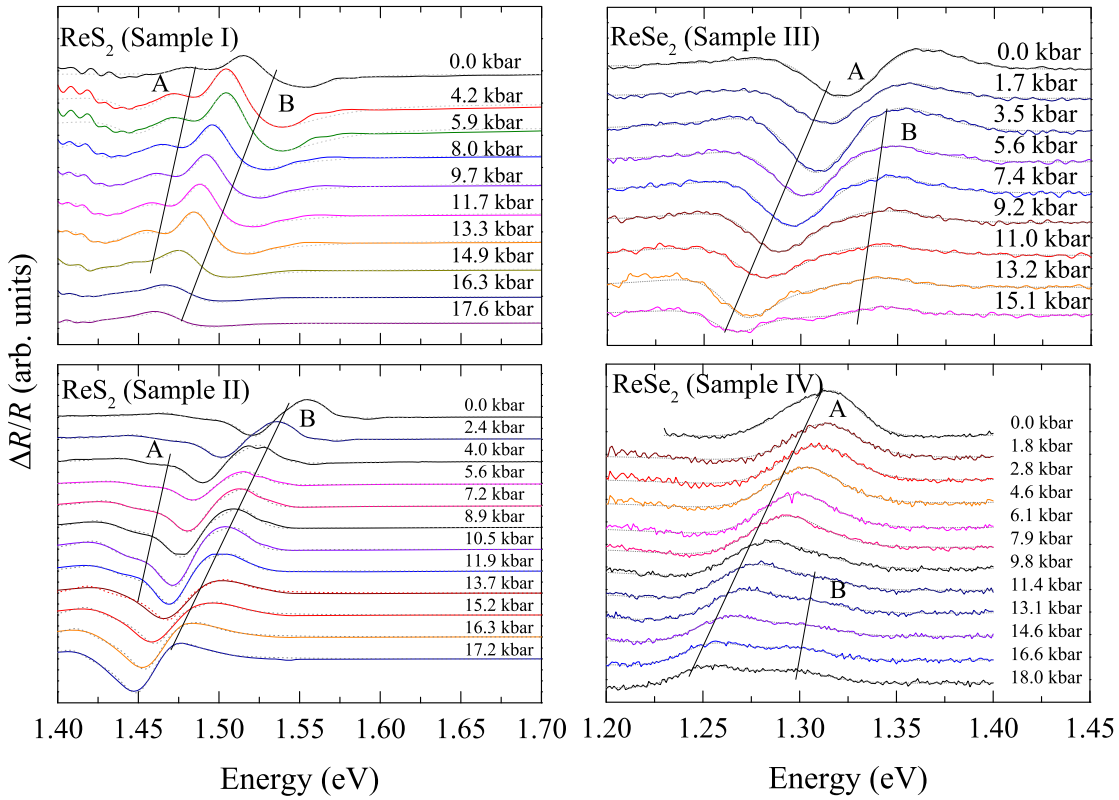

FIGURE 4.1: Photoreflectance spectra obtained at different pressures for ReS_2 (sample I and II) and $ReSe_2$ (sample III and IV). Straight lines around the fitted transition energies are shown as a guide to the eye for transitions A and B. Both features decrease in energy with increasing pressure for all studied samples. Fittings are shown as dotted gray curves.

4.3 Results

We conducted PR measurements in order to determine the pressure dependence of the first two direct optical transitions in ReX_2. To ensure the reproducibility of the experimental results, samples obtained from different sources and grown in different conditions are used for the experiments. The PR spectra obtained for ReS_2 and $ReSe_2$ at different pressure values are shown in Fig. 4.1. Two main features can be observed for all samples, which correspond to the direct excitonic transitions A and B. These excitonic transitions have been previously reported at ambient pressure from modulated spectroscopies for ReS_2[19, 21] and $ReSe_2$.[57] The strongest transition (i.e., B for ReS_2 and A for $ReSe_2$) is clearly visible at all pressures. The weakest transition merges at high (low) pressure

for ReS_2 ($ReSe_2$) as a consequence of different pressure coefficients between the A and B transitions. It is worth noting that weaker, energetically close transitions have been previously reported from low-temperature and polarization measurements for ReS_2[20] and $ReSe_2$.[23, 24] We are able to resolve these transitions from polarization-dependent measurements at different pressures (shown in the Supplementary Information, S.I.). Our polarization measurements allow us to conclude that the relative amplitude and angular dependence for each transition are preserved at the studied pressure range (i.e., up to 20 kbar). Hence, the sample orientation and structural stability are maintained throughout the studied pressure range. The energy of each transition was obtained from the PR spectra by fitting the Aspnes formula,[58] given by

$$\frac{\Delta R}{R}(E) = \mathrm{Re}\left[\sum_{j=1}^{n} C_j e^{i\theta_j}\left(E - E_j + i\Gamma_j\right)^{-m}\right] \tag{4.1}$$

where n, C and θ are the number of transitions, amplitude, and phase fo the resonance, E_j and Γ are the energy and broadening parameter of the transition, respectively. For excitonic transitions we take $m = 2$. Two transitions are enough to successfully reproduce all the spectra shown in Fig. 4.1 (dotted curves). Note that the differences in line shape between different samples of the same compound are accounted for by different phase values of the resonance, defined by different built-in electric fields and differences in chopper settings. However, the fitted energy values of the transitions are not affected by these differences. For the fitting procedure, we left all parameters unfixed for the spectrum obtained at ambient pressure, while only the amplitude and the energy of the transition were left as free parameters for spectra at higher pressures, since these are expected to change with pressure. The pressure dependence of the energy of each transition is plotted in Fig. 4.2 for both samples.

As can be seen in Fig. 4.2, the energy of the transition A (red symbols) decreases with increasing pressure at a different rate than the energy of the transition B (blue symbols). Note that the fitted energies of the transition B between different samples of the same material are scattered to a certain degree. This can be attributed to two factors: i) sample misorientations and ii) uncertainties in the fitting procedure that naturally arise for weak PR features energetically close ($\approx$ 60 meV) to a strong PR transition with a relatively strong broadening parameter (typically $\approx$ 20 meV). Despite uncertainties in the fitted energies of transition B, the pressure coefficient of different samples of the same material was consistent. For ReS_2, the fitted pressure coefficient of the B transition, -4.2 meV/kbar, is much larger than that of the A transition, -2.3 meV/kbar. The latter

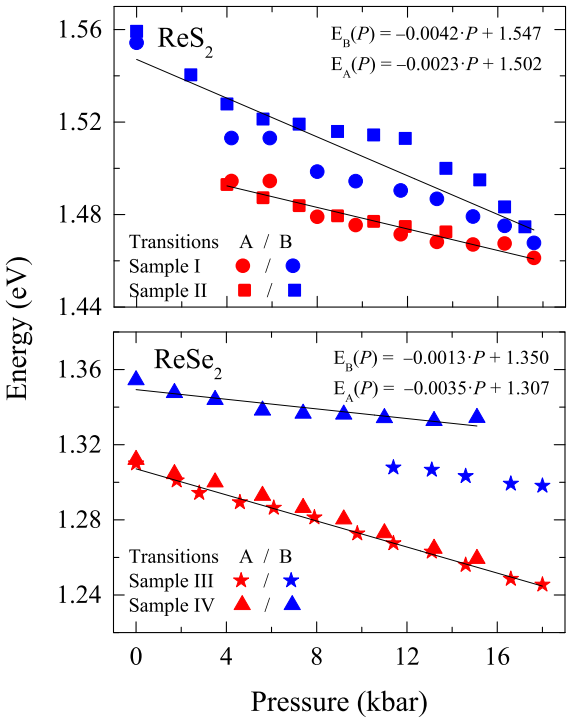

FIGURE 4.2: The energy of the fitted transitions in the photoreflectance experiments is plotted as a function of pressure for ReS_2 (up) and $ReSe_2$ (bottom). The fitted energies of transitions A and B are shown in red and blue colors, respectively. Linear fits have been performed for both transitions and fitted values are included in the figure.

value is in agreement with previous HP photoluminescence (PL) measurements, which yielded a pressure coefficient of -2.0 meV/kbar.[36] In contrast, for $ReSe_2$, the pressure coefficient of the A transition, -3.5 meV/kbar, is more pronounced than that of the B transition, -1.3 meV/kbar. The latter result is qualitatively in agreement with the reported absorption measurements, which show a redshift of the absorption edge with increasing pressure.[2] The fact that the pressure coefficient of the A transitions is much larger for $ReSe_2$ and smaller for ReS_2 (with respect to the B transition), evidences that the origin of the transitions is different for each material, as discussed in the next section.

First-principles calculations were carried out in order to assign the experimentally observed transitions and to provide further insight into the electronic and optical properties of ReX_2. The electronic band structure and the optical matrix element were calculated for a k-path intersecting the first BZ in a three dimensional manner. Figure 4.4 shows the electronic dispersion curves for 0 kbar (black curves) and 20 kbar (red curves), as obtained from density functional theory (DFT) calculations within the

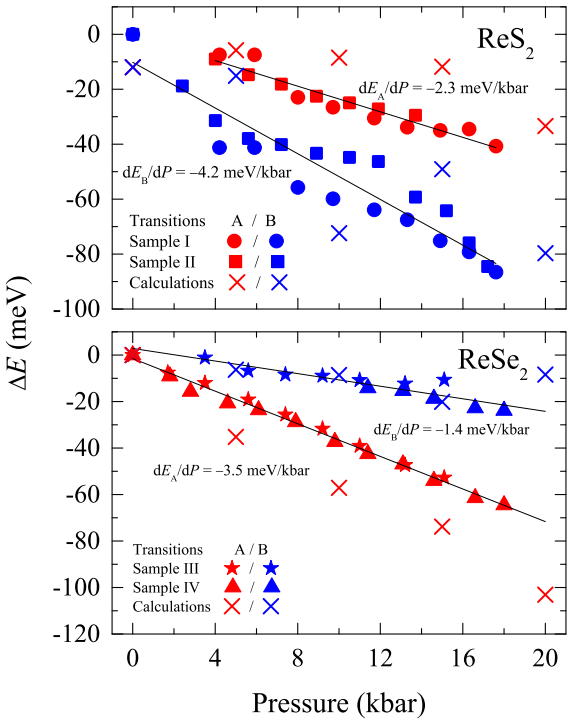

FIGURE 4.3: Electronic dispersion curves for ReS_2 (left) and $ReSe_2$ (right) as calculated using the SCAN functional at zero pressure (black curves) and 20 kbar (red curves). The corresponding matrix elements have been calculated for each k-point, the stronger transitions are located around Z and K1 for ReS_2 and around Z and J1 points for $ReSe_2$. In the lower panels, the direct bandgap energy is plotted along the studied wave vectors.

meta-generalized gradient approximation (GGA) strongly constrained and appropriately normed (SCAN) functional.[47] The normalized values of the optical matrix element as well as the bandgap value along the k-path are also shown. The first and second direct transitions for ReS_2 ($ReSe_2$) are at Z (J1) and K1 (Z) points, respectively. Note that the matrix element maxima correspond with the bandgap minima, which indicate that these transitions are optically active. The calculated quasi-direct gaps for ReS_2 and $ReSe_2$ are 1.2 and 1.15 eV, respectively. These values are smaller than the measured optical gaps, around 1.5 and 1.31 eV, respectively. The discrepancies between calculations and experiments are accounted for by the systematic bandgap under estimation of the meta-GGA functional (SCAN) used. This functional neither accounts for independent particle effects nor for excitonic effects.[48] To better reproduce the experimental values, we performed calculations at a higher level of theory using the hybrid functional

HSE06.[49] At this level of theory, our calculations are able to predict the bandgap energies more accurately, around 1.42 and 1.43 eV (including the excitonic binding energy) for ReS_2 and $ReSe_2$, respectively. More detail on the HSE06 calculations can be found in the S.I.

Owing to the complex band structure of ReX_2, which exhibits very close direct and indirect bandgaps in energy and position in the k-space,[25, 28] some computational considerations should be taken into account. For instance, a number of theoretical works predict the valence band maximum (VBM) of bulk ReS_2 to be either at Γ[2, 36, 59] or at Z.[60] This may result from choosing only a few high-symmetry paths for the calculation of the band structure, or choosing functionals that fail to capture the details of the complex electronic structure of ReX_2. Hence, in order to accurately describe the band structure of complex materials like ReX_2, it is important to consider the whole 3D-BZ, and to devote careful attention to the choice of the functional. Recent contributions show that the choice of the functional influences the number and location of VBM and conduction band minimum (CBM) in ReX_2.[25, 41, 60] The results of the meta-GGA SCAN functional employed here seem to reproduce the experimental results well and with low computational cost.

The location of the fundamental direct gap of ReS_2, predicted by our calculations to be at Z, is in agreement with recent direct measurements of the band dispersion using ARPES[25, 40, 41] and a recent theoretical study employing quasiparticle approximations.[28] For the case of $ReSe_2$, our high-density k-mesh calculations predict an indirect fundamental bandgap of 1.10 eV, with both the VBM and the CBM located away from high-symmetry points (named J2 and J3, respectively, coordinates shown in Table S1 of the S.I.). This is in agreement with recent studies, which also found an indirect bandgap with the VBM close to the J2 point.[26, 60] Several other studies that take only high-symmetry k-paths into account for evaluating the band structure predict either direct or indirect bandgaps for $ReSe_2$ near the Z or Γ point.[23, 28, 38, 61, 62] It has also been suggested that the indirect and the direct bandgap are close in energy, and the discussion about the nature of the fundamental bandgap for $ReSe_2$ is still ongoing.[60, 61, 62, 26] At higher pressure, an overall narrowing of the bandgap takes place along the whole BZ with increasing pressure, as previously evidenced in theoretical studies.[38, 63] This trend can be seen in the lowest panel of Fig. 4.4 and results in an enhancement of the indirect nature of the fundamental gap for both ReS_2 and $ReSe_2$ at HP.

To assign the A and B transitions, we compare the experimental and calculated pressure dependence of the first two direct transitions. This is shown in Fig. 4.3, where the

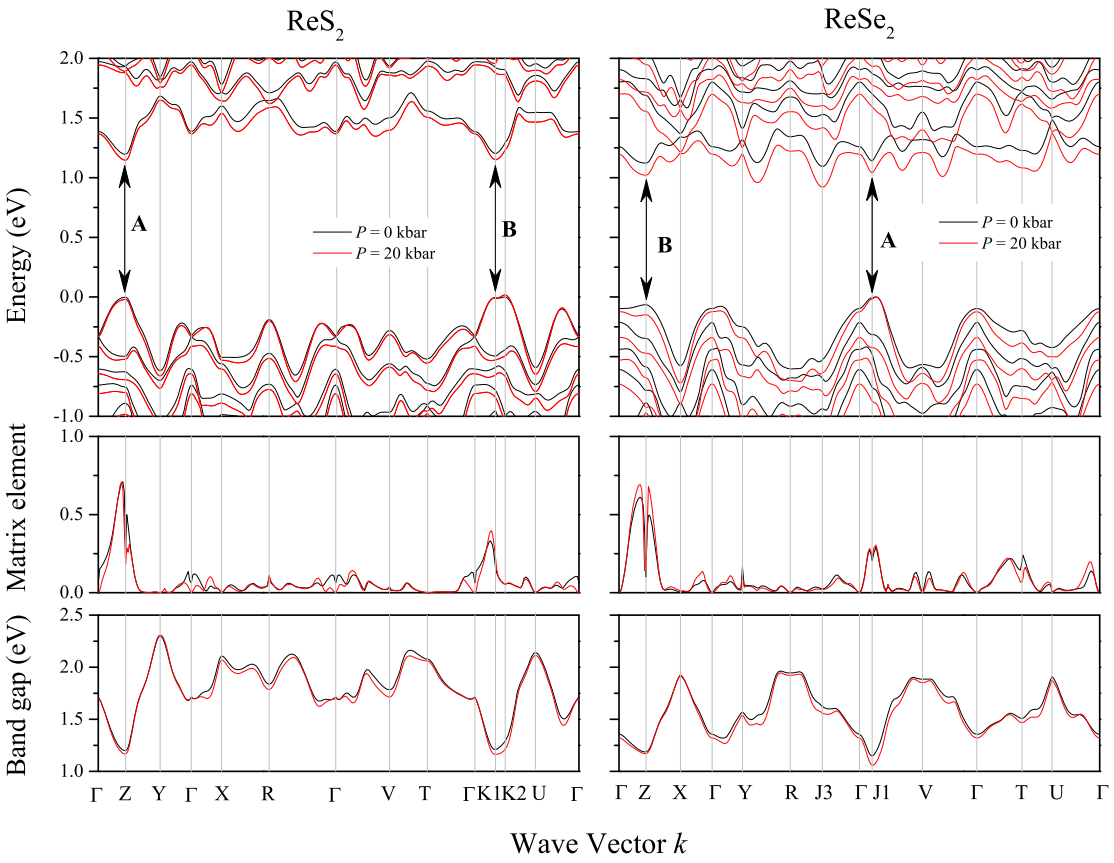

FIGURE 4.4: Increment of exciton energy versus pressure plotted for the transitions A (red color) and B (blue color) from measurements on ReS_2 (top) and $ReSe_2$ (bottom), as well as the calculated values of the transport bandgap using the SCAN functional (crosses). The straight lines are linear fits to the experimental values. Pressure coefficients of each transition are included .

pressure dependence of the variation of energy is plotted for both, calculated bandgaps (crosses) and measured excitonic transitions (full symbols). The figure plots the variation of energy rather than absolute values. This allows to directly compare theoretical calculations with experimental results, neglecting energetic differences arising from the DFT bandgap underestimation and excitonic binding energy. As can be seen in the figure, our calculations predict distinct pressure coefficients for each transition, which is also observed experimentally. The calculated pressure coefficients of ReS_2 (-1 and -3.4 meV/kbar) and $ReSe_2$ (-4.2 and -0.7 meV/kbar) slightly differ from the measured values. We attribute the differences to the effect of structural distortion at high pressure on the position of the maximum of the matrix elements in the reciprocal space. Taking this into account, the differences between calculated and experimental pressure coefficients

agree within the experimental and calculated errors (which are lower than ±0.3 and ±1.2 meV/kbar, respectively). Most importantly, the qualitative trend is reproduced in our calculations, namely a negative pressure coefficient of distinct magnitude for both transitions. After comparing the pressure coefficients (see Fig. 4.3), transitions A (red symbols) and B (blue symbols) are unambiguously assigned to the Z (J1) and K1 (Z) k-point for ReS_2 ($ReSe_2$), respectively. The calculated pressure coefficients within the SCAN functional can be reproduced by HSE06 calculations (differences in the pressure coefficients are below ±0.5 meV/kbar, as shown in Tables S3 and S4 in the S.I.), which further supports the provided assignation.

The current assignation of the transition A at the J1 k-point for $ReSe_2$ is in contrast with previous assumptions that all the excitonic transitions took place around the Z point of the BZ.[23] This result should be taken into account for future work on the compositional dependence of the bandgap of the $ReSe_{2-x}S_x$ alloy, since J1 is away from either Z or K1 (coordinates are shown in Table S1 of the S.I.). Previous absorption[64] and piezoreflectance[39] measurements along the entire composition range found evidence that the nature of the bandgaps is similar for the $ReSe_{2-x}S_x$ compositional end members. However, while we found that both direct excitonic transitions are similar in energy (the transition energy in J1 is only $\approx$ 40 meV below that at Z), they belong to different k-points between different compositional end members. Hence, it is expected that the compositional dependence of the lowest direct transition (i.e., transition A) exhibits a crossover from the J1 for $ReSe_2$ to Z for ReS_2.

4.4 Discussion

Owing to its different crystallographic structure, the optoelec tronic properties of ReX_2 are drastically different from those of group 6 TMDCs. Remarkably, the pressure coefficient of the first direct optical transition is negative, in contrast to other TMDCs. Figure 4.5 shows the pressure coefficient of the first direct optical transition for MX2 TMDCs ($M = Mo$, W, and Re and $X = S$ and Se), as measured by HP PR spectroscopy elsewhere,[65] together with the present experimental results for ReX_2. While MoX2 and WX2 exhibit positive-pressure coefficients, this is not the case for ReX_2, which exhibits negative-pressure coefficients. As a general trend, a closing of the bandgap with increasing pressure (i.e., negative pressure coefficient) is expected for all TMDCs, since all TMDCs metallize at HP (metallization takes place around 350 kbar for ReX_2). Still, while their indirect bandgaps decrease with pressure, all group 6 TMDCs exhibit

a positive-pressure coefficient of the direct gaps.[63, 66] Such striking difference is accounted for by the particular crystallographic structure of ReX_2, and the particular electronic configuration of Re: with respect to group 6 transition metals, rhenium compounds possess one more valence electron, and the valence and conduction band states are importantly characterized by the Re-d orbitals. To investigate the physical origin of the negative direct pressure coefficient, and its connection with the reduced van der Waals interaction in ReX_2, we performed an orbital analysis of the states associated with the A and B transitions.

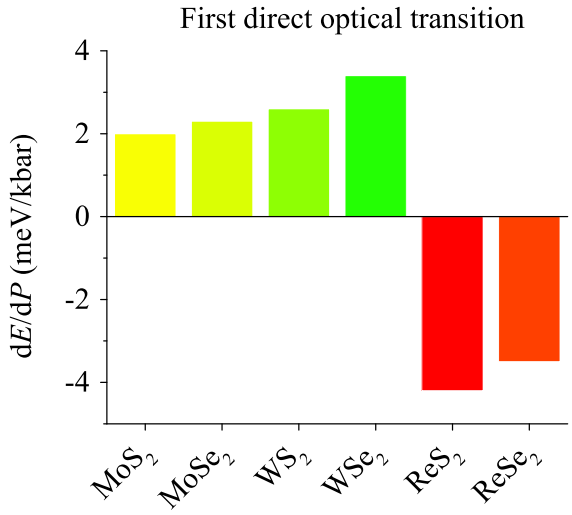

FIGURE 4.5: Histogram showing the pressure coefficient of the first direct optical transitions of MoX_2 and WX_2 published elsewhere42 and ReX_2 (X = S and Se), as obtained from high-pressure photoreflec tance measurements .

The orbital composition of the states of the A and B direct transitions is shown in Table 4.1 for ReS_2 and $ReSe_2$. The CBM and VBM of ReS_2 are dominated by Re-dz2 orbitals, in agreement with recent calculations,[25] while for $ReSe_2$, the orbital contributions are more diverse. In the table, Re-d_{z^2} and X-p_z orbital contributions, which importantly contribute to the band edge states[25] and show out-of-plane character,[40, 26] are highlighted since these are expected to be highly sensitive to the interlayer interaction. The z-axis denotes the out-of-plane direction, so that z orbitals are located at least partially within the van der Waals gap. With increasing pressure, states with large contributions from Re-d_{z^2} and X-p_z orbitals destabilize, and therefore rise in energy with increasing pressure. Such destabilization has been attributed to Coulomb repulsion of antibonding p orbitals between interlayer chalcogen atoms for MoS_2.[67, 68,

Material	k-point	Transition	Orbital composition
ReS_2	Z	A	VBM: 33 % d_{z^2} + 20 % d_{xz} + 15 % p_z + 14 % d_{xy}
			CBM: 33 % d_{z^2} + 22 % p_x + 18 % $d_{x^2-y^2}$ + 14 % d_{xy}
	K1	B	VBM: 32 % d_{z^2} + 22 % p_z + 15 % d_{xz} + 12 % d_{xy}
			CBM: 31 % d_{z^2} + 20 % p_x + 19 % $d_{x^2-y^2}$ + 14 % d_{xy}
$ReSe_2$	J1	A	VBM: 50 % p_z + 15 % d_{z^2} + 12 % p_y + 7 % $d_{x^2-y^2}$
			CBM: 21 % $d_{x^2-y^2}$ + 21 % d_{z^2} + 16 % p_y + 12 % d_{yz}
	Z	B	VBM: 31 % d_{yz} + 25 % $d_{x^2-y^2}$ + 17 % d_{z^2} + 9 % p_z
			CBM: 32 % d_{z^2} + 30 % p_y + 14 % $d_{x^2-y^2}$ + 6 % p_z

TABLE 4.1: Calculated orbital composition of the important extrema (transitions A and B) of the electronic band structure of ReS_2 and $ReSe_2$. The highly interlayer-affected orbitals are p_z, d_{yz} and d_{z^2}. The d orbital contributions come solely from Re atoms, while p_z orbitals are primarily of chalcogen atoms.

69] Similarly, d_{z^2} orbitals are fairly delocalized and directed perpendicular to the layers. The role of orbital contribution to the bandgap dependence on interlayer distance is well studied for other TMDCs, and is the state-of-the-art explanation for the direct-to-indirect bandgap crossover of MoS_2 at its transition from monolayer to bulk.[67, 70] Quantitatively, increasing pressure has a similar effect on the electronic structure as increasing the number of layers, i.e., pressure results in a stronger interaction of electrons along the van der Waals gap and a reduction of interlayer distance. In fact, the pressure and strain dependence of the bandgap of MoX_2 has been explained in terms of orbital contributions to the bandgap states.[71, 72] Hence, larger contributions of the Re-d_{z^2} and X-p_z orbitals in the VBM with respect to the CBM would result in a narrowing of the bandgap with increasing pressure, which is the case for ReX_2 as discussed in detail below.

The orbital interplay on the bandgap reduction of ReX_2 with increasing pressure/strain has been previously hinted[11, 36], but never evaluated from orbital analysis. For the case of ReS_2, the highest contribution to the analyzed states arises from Re-d_{z^2} . In Table 4.1, it can be seen that larger contributions of the p_z orbital take place in the VBM with respect to the CBM. Hence, at higher pressures, the VBM experiences a stronger destabilization than the CBM, resulting in a narrowing of the bandgap, as observed experimentally. Furthermore, the transition at K1 (i.e., transition B) exhibits a significantly higher contribution from the S-p_z states, which accounts for its more negative pressure coefficient with respect to the transition at Z (i.e., transition A), as observed experimentally (see Fig. 4.3). Similarly, for the case of $ReSe_2$, the contributions from the Se-p_z and Re-d_{z^2} orbitals to the VBM are large, which implies a large

redshift of the transition at J1 (i.e., transition A) with increasing pressure, in agreement with the experimentally observed large negative pressure coefficients for the transition A (see Fig. 4.3). In contrast, the transition at Z (i.e., transition B) shows only moderate contributions of Se-p_z in the VBM. To account for the negative pressure coefficient of transition B, we suggest that the Re-d_{yz} orbitals might play a significant role. In conclusion, the bandgap narrowing with increasing pressure on the transitions A and B of ReX_2 is mainly accounted for by an increased contribution of X-p_z orbitals in the VBM.

So far, it has been shown that the negative-pressure coefficients observed for the direct transitions in ReX_2 can be qualitatively explained from orbital theory. However, the value of the pressure coefficient could be influenced by the reduced van der Waals interactions present in ReX_2 with respect to other TMDCs. To elucidate whether ReX_2 exhibits a decreased van der Waals interaction with respect to MoS_2, we compare the effect of orbital interplay on the pressure coefficient between both compounds. For MoS_2, a negative pressure coefficient of the indirect bandgap has been predicted to be in the range -3.79 to -7.9 meV/kbar.[65] Such a low-pressure coefficient is a consequence of a strong blueshift of the VBM at Γ, where the orbital contributions from d_{z^2} and p_z orbitals are strong, i.e., 60% Mo-d_{z^2} + 30% S-p_z.[67] However, the contribution of the d_{z^2} and p_z to the CBM (at K) is in the same order of magnitude, i.e., 86% Mo-d_{z^2} + 9% S-p_{xy} + 5% S-p_z. Since the direct pressure coefficients of ReS_2 and $ReSe_2$ (i.e., -4.2 meV/ kbar and -3.5 meV/kbar) are similar to the indirect pressure coefficient in MoS_2, we conclude that the decreased van der Waals interactions in ReX_2 (as evidenced by HP XRD [30, 31]) and low frequency Raman measurements[29]) do not play a significant role in its pressure coefficient.

To summarize, we performed HP PR measurements on ReS_2 and $ReSe_2$ samples obtained from different sources and grown on different conditions. Our results reveal that two main excitonic transitions decrease in energy with increasing pressure for each material. For the case of ReS_2, the obtained pressure coefficients for the A and B transitions are -2.3 and -4.2 meV/kbar, respectively, and for $ReSe_2$, -3.5 and -1.3 meV/kbar, respectively. Polarization-resolved measurements allowed to measure a third transition for ReS_2, as well as determining the crystal orientation and assessing the structural stability up to 20 kbar in ReX_2.

The electronic band structure of ReS_2 and $ReSe_2$ was calculated from ab initio calculations within the density functional theory, using the meta-GGA SCAN functional. We probed the whole BZ in order to explore all the possible direct transitions around the bandgap. The calculations were performed at different pressure values, which allowed

the comparison of the experimental and theoretical results and assignment of each transition. For ReS_2, the transitions A and B were assigned to Z and K1 k-points of the BZ, whereas for $ReSe_2$, the A and B transitions were assigned to the J1 and Z points, respectively (with both K1 and J1 located away from the high symmetry k-points). The negative pressure coefficients measured in ReX_2 were explained in terms of orbital analysis. This allowed us to conclude that the destabilization of the p_z orbital with increasing pressure is mostly responsible for the measured pressure coeffi cients. This work evidences that ReX_2 does not exhibit a strong electronic decoupling and hence the optoelectronic properties of few-layered ReX_2 could be drastically different from the bulk form.

Acknowledgements

This work was supported by the National Science Centre (NCN) Poland OPUS 11 no. 2016/21/B/ST3/00482. R.O. acknowledges the support by POLONEZ 3 no. 2016/23/P/ ST3/04278. This project is carried out under POLONEZ program, which has received funding from the European Union's Horizon 2020 research and innovation program under the Marie Sklodowska-Curie grant agreement No. 665778. F.D. acknowledges the support from NCN under Fuga 3 grant no. 2014/12/S/ST3/00313. We thank Xavier Rocquefelte for discussions regarding the structure of transition metal dichalcogenides. M.L. and O.R. would like to acknowledge the funding provided by the Natural Sciences and Engineering Research Council of Canada under the Discovery Grant Program RGPIN-2015-04518. The computations were performed using Compute Canada (Calcul Quebec and Compute Ontario) resources, including the infrastructure funded by the Canada Foundation for Innovation. Finally, S.T. acknowledges funding provided by National Science Foundation DMR-1552220 and DMR-1838443.

References

[1] Bhakti Jariwala et al. "Synthesis and Characterization of ReS $_2$ and ReSe $_2$ Layered Chalcogenide Single Crystals". en. In: *Chemistry of Materials* 28.10 (May 2016), pp. 3352–3359. ISSN: 0897-4756, 1520-5002. DOI: 10.1021/acs.chemmater.6b00364.

[2] Sefaattin Tongay et al. "Monolayer behaviour in bulk ReS_2 due to electronic and vibrational decoupling". en. In: *Nature Communications* 5 (Feb. 2014), p. 3252. ISSN: 2041-1723. DOI: 10.1038/ncomms4252.

[3] Enze Zhang et al. "ReS2-Based Field-Effect Transistors and Photodetectors". en. In: *Advanced Functional Materials* 25.26 (2015), pp. 4076–4082. ISSN: 1616-3028. DOI: 10.1002/adfm.201500969.

[4] Jing-Kai Qin et al. "Photoresponse Enhancement in Monolayer ReS2 Phototransistor Decorated with CdSe–CdS–ZnS Quantum Dots". In: *ACS Applied Materials & Interfaces* 9.45 (Nov. 2017), pp. 39456–39463. ISSN: 1944-8244. DOI: 10.1021/acsami.7b10349.

[5] Shengxue Yang et al. "High-Performance Few-layer Mo-doped $ReSe_2$ Nanosheet Photodetectors". en. In: *Scientific Reports* 4 (June 2014), p. 5442. ISSN: 2045-2322. DOI: 10.1038/srep05442.

[6] Erfu Liu et al. "High Responsivity Phototransistors Based on Few-Layer ReS2 for Weak Signal Detection". en. In: *Advanced Functional Materials* 26.12 (2016), pp. 1938–1944. ISSN: 1616-3028. DOI: 10.1002/adfm.201504408.

[7] Enze Zhang et al. "Tunable Ambipolar Polarization-Sensitive Photodetectors Based on High-Anisotropy ReSe2 Nanosheets". In: *ACS Nano* 10.8 (Aug. 2016), pp. 8067–8077. ISSN: 1936-0851. DOI: 10.1021/acsnano.6b04165.

[8] Mohammad Najmzadeh et al. "Multilayer ReS2 lateral p–n homojunction for photoemission and photodetection". en. In: *Applied Physics Express* 9.5 (Mar. 2016), p. 055201. ISSN: 1882-0786. DOI: 10.7567/APEX.9.055201.

[9] Ah-Jin Cho et al. "Electric and photovoltaic characteristics of a multi-layer ReS2/ReSe2 heterostructure". In: *APL Materials* 5.7 (July 2017), p. 076101. DOI: 10.1063/1.4991028.

[10] Kedi Wu et al. "Domain Architectures and Grain Boundaries in Chemical Vapor Deposited Highly Anisotropic ReS2 Monolayer Films". In: *Nano Letters* 16.9 (Sept. 2016), pp. 5888–5894. ISSN: 1530-6984. DOI: 10.1021/acs.nanolett.6b02766.

[11] Shengxue Yang et al. "Tuning the Optical, Magnetic, and Electrical Properties of ReSe2 by Nanoscale Strain Engineering". In: *Nano Letters* 15.3 (Mar. 2015), pp. 1660–1666. ISSN: 1530-6984. DOI: 10.1021/nl504276u.

[12] Erfu Liu et al. "Integrated digital inverters based on two-dimensional anisotropic ReS2 field-effect transistors". eng. In: *Nature Communications* 6 (May 2015), p. 6991. ISSN: 2041-1723. DOI: 10.1038/ncomms7991.

[13] Chris M. Corbet et al. "Improved contact resistance in ReSe2 thin film field-effect transistors". In: *Applied Physics Letters* 108.16 (Apr. 2016), p. 162104. ISSN: 0003-6951. DOI: 10.1063/1.4947468.

[14] Chris M. Corbet et al. "Field Effect Transistors with Current Saturation and Voltage Gain in Ultrathin ReS2". In: *ACS Nano* 9.1 (Jan. 2015), pp. 363–370. ISSN: 1936-0851. DOI: 10.1021/nn505354a.

[15] Omar B. Mohammed et al. "ReS2-based interlayer tunnel field effect transistor". In: *Journal of Applied Physics* 122.24 (Dec. 2017), p. 245701. ISSN: 0021-8979. DOI: 10.1063/1.5004038.

[16] Shengxue Yang et al. "Layer-dependent electrical and optoelectronic responses of ReSe2 nanosheet transistors". en. In: *Nanoscale* 6.13 (June 2014), pp. 7226–7231. ISSN: 2040-3372. DOI: 10.1039/C4NR01741B.

[17] Muhammad Hafeez et al. "Rhenium dichalcogenides (ReX2, X = S or Se): an emerging class of TMDs family". en. In: *Materials Chemistry Frontiers* 1.10 (Sept. 2017), pp. 1917–1932. ISSN: 2052-1537. DOI: 10.1039/C6QM00373G.

[18] Robert Kudrawiec and Jan Misiewicz. "Optical Modulation Spectroscopy". en. In: *Semiconductor Research: Experimental Techniques*. Ed. by Amalia Patane and Naci Balkan. Springer Series in Materials Science. Berlin, Heidelberg: Springer, 2012, pp. 95–124. ISBN: 978-3-642-23351-7. DOI: 10.1007/978-3-642-23351-7_4.

[19] C. H. Ho et al. "Temperature dependence of energies and broadening parameters of the band-edge excitons of ReS_2 and $ReSe_2$". In: *Physical Review B* 55.23 (June 1997), pp. 15608–15613. DOI: 10.1103/PhysRevB.55.15608.

[20] C. H. Ho et al. "Electronic structure of ReS 2 and ReSe 2 from first-principles calculations, photoelectron spectroscopy, and electrolyte electroreflectance". en. In: *Physical Review B* 60.23 (Dec. 1999), pp. 15766–15771. ISSN: 0163-1829, 1095-3795. DOI: 10.1103/PhysRevB.60.15766.

[21] C. H. Ho, H. W. Lee, and C. C. Wu. "Polarization sensitive behaviour of the band-edge transitions in ReS 2 and ReSe 2 layered semiconductors". en. In: *Journal of Physics: Condensed Matter* 16.32 (2004), p. 5937. ISSN: 0953-8984. DOI: 10.1088/0953-8984/16/32/026.

[22] Ozgur Burak Aslan et al. "Linearly Polarized Excitons in Single- and Few-Layer ReS $_2$ Crystals". en. In: *ACS Photonics* 3.1 (Jan. 2016), pp. 96–101. ISSN: 2330-4022, 2330-4022. DOI: 10.1021/acsphotonics.5b00486.

[23] Ashish Arora et al. "Highly Anisotropic in-Plane Excitons in Atomically Thin and Bulklike 1T'-ReSe2". In: *Nano Letters* 17.5 (May 2017), pp. 3202–3207. ISSN: 1530-6984. DOI: 10.1021/acs.nanolett.7b00765.

[24] Yu-Ci Jian et al. "Optical and Electrical Properties of Au- and Ag-Doped ReSe2". en. In: *Japanese Journal of Applied Physics* 52.4S (Feb. 2013), 04CH06. ISSN: 1347-4065. DOI: 10.7567/JJAP.52.04CH06.

[25] D. Biswas et al. "Narrow-band anisotropic electronic structure of ReS2". In: *Physical Review B* 96.8 (Aug. 2017), p. 085205. DOI: 10.1103/PhysRevB.96.085205.

[26] Lewis S. Hart et al. "Electronic bandstructure and van der Waals coupling of ReSe 2 revealed by high-resolution angle-resolved photoemission spectroscopy". en. In: *Scientific Reports* 7.1 (July 2017), p. 5145. ISSN: 2045-2322. DOI: 10.1038/s41598-017-05361-6.

[27] Yanqing Feng et al. "Raman vibrational spectra of bulk to monolayerReS_2 with lower symmetry". In: *Physical Review B* 92.5 (Aug. 2015), p. 054110. DOI: 10.1103/PhysRevB.92.054110.

[28] J. P. Echeverry and I. C. Gerber. "Theoretical investigations of the anisotropic optical properties of distorted 1 T ReS 2 and ReSe 2 monolayers, bilayers, and in the bulk limit". en. In: *Physical Review B* 97.7 (Feb. 2018). ISSN: 2469-9950, 2469-9969. DOI: 10.1103/PhysRevB.97.075123.

[29] Etienne Lorchat, Guillaume Froehlicher, and Stéphane Berciaud. "Splitting of Interlayer Shear Modes and Photon Energy Dependent Anisotropic Raman Response in N-Layer ReSe2 and ReS2". In: *ACS Nano* 10.2 (Feb. 2016), pp. 2752–2760. ISSN: 1936-0851. DOI: 10.1021/acsnano.5b07844.

[30] Dongbin Hou et al. "High pressure X-ray diffraction study of ReS2". In: *Journal of Physics and Chemistry of Solids* 71.11 (2010), pp. 1571–1575.

[31] Yu-Cheng Kao et al. "Anomalous structural phase transition properties in ReSe2 and Au-doped ReSe2". In: *The Journal of chemical physics* 137.2 (2012), p. 024509.

[32] Xuefei Wang et al. "Pressure-induced iso-structural phase transition and metallization in WSe2". en. In: *Scientific Reports* 7.1 (May 2017), p. 46694. ISSN: 2045-2322. DOI: 10.1038/srep46694.

[33] Avinash P. Nayak et al. "Pressure-induced semiconducting to metallic transition in multilayered molybdenum disulphide". en. In: *Nature Communications* 5.1 (May 2014), p. 3731. ISSN: 2041-1723. DOI: 10.1038/ncomms4731.

[34] Zhao Zhao et al. "Pressure induced metallization with absence of structural transition in layered molybdenum diselenide". en. In: *Nature Communications* 6.1 (June 2015), p. 7312. ISSN: 2041-1723. DOI: 10.1038/ncomms8312.

[35] Nirup Bandaru et al. "Structural stability of WS2 under high pressure". In: *International Journal of Modern Physics B* 28.25 (Oct. 2014), p. 1450168. ISSN: 0217-9792. DOI: 10.1142/S0217979214501689.

[36] Yalan Yan et al. "Associated Lattice and Electronic Structural Evolutions in Compressed Multilayer ReS2". In: *The Journal of Physical Chemistry Letters* 8.15 (Aug. 2017), pp. 3648–3655. ISSN: 1948-7185. DOI: 10.1021/acs.jpclett.7b01031.

[37] *High Pressure Semiconductor Physics I*. en. Academic Press, Sept. 1998. ISBN: 978-0-08-086452-5.

[38] Dawei Zhou et al. "Pressure-induced metallization and superconducting phase in ReS 2". en. In: *npj Quantum Materials* 2.1 (Mar. 2017), p. 19. ISSN: 2397-4648. DOI: 10.1038/s41535-017-0023-x.

[39] C. H. Ho et al. "Piezoreflectance study of band-edge excitons of $ReS_{2-x}Se_x$ single crystals". In: *Physical Review B* 58.19 (Nov. 1998), pp. 12575–12578. DOI: 10.1103/PhysRevB.58.12575.

[40] James L. Webb et al. "Electronic band structure of ReS2 by high-resolution angle-resolved photoemission spectroscopy". In: *Physical Review B* 96.11 (Sept. 2017), p. 115205. DOI: 10.1103/PhysRevB.96.115205.

[41] P. Eickholt et al. "Location of the valence band maximum in the band structure of anisotropic 1 T' - ReSe 2". en. In: *Physical Review B* 97.16 (Apr. 2018). ISSN: 2469-9950, 2469-9969. DOI: 10.1103/PhysRevB.97.165130.

[42] R. Kudrawiec and J. Misiewicz. "Photoreflectance spectroscopy of semiconductor structures at hydrostatic pressure: A comparison of GaInAs/GaAs and GaInNAs/GaAs single quantum wells". en. In: *Applied Surface Science*. Proceedings of the E-MRS 2005 Spring Meeting Symposium P: Current trends in optical and X-ray metrology of advanced materials for nanoscale devices 253.1 (Oct. 2006), pp. 80–84. ISSN: 0169-4332. DOI: 10.1016/j.apsusc.2006.05.073.

[43] G. Kresse and J. Furthmüller. "Efficient iterative schemes for ab initio total-energy calculations using a plane-wave basis set". In: *Phys. Rev. B* 54.16 (Oct. 1996), pp. 11169–11186. DOI: 10.1103/PhysRevB.54.11169.

[44] G. Kresse and J. Furthmüller. "Efficiency of ab-initio total energy calculations for metals and semiconductors using a plane-wave basis set". In: *Comput. Mater. Sci.* 6.1 (July 1996), pp. 15–50. ISSN: 0927-0256. DOI: 10.1016/0927-0256(96)00008-0.

[45] P. E. Blöchl. "Projector augmented-wave method". In: *Phys. Rev. B* 50.24 (Dec. 1994), pp. 17953–17979. DOI: 10.1103/PhysRevB.50.17953.

[46] G. Kresse and D. Joubert. "From ultrasoft pseudopotentials to the projector augmented-wave method". In: *Phys. Rev. B* 59.3 (Jan. 1999), pp. 1758–1775. DOI: 10.1103/PhysRevB.59.1758.

[47] Jianwei Sun, Adrienn Ruzsinszky, and John P. Perdew. "Strongly Constrained and Appropriately Normed Semilocal Density Functional". In: *Phys. Rev. Lett.* 115.3 (July 2015), p. 036402. DOI: 10.1103/PhysRevLett.115.036402.

[48] I. G. Buda et al. "Characterization of Thin Film Materials using SCAN meta-GGA, an Accurate Nonempirical Density Functional". en. In: *Scientific Reports* 7 (Mar. 2017), p. 44766. ISSN: 2045-2322. DOI: 10.1038/srep44766.

[49] Aliaksandr V. Krukau et al. "Influence of the exchange screening parameter on the performance of screened hybrid functionals". In: *J. Chem. Phys.* 125.22 (Dec. 2006), p. 224106. ISSN: 0021-9606. DOI: 10.1063/1.2404663.

[50] Jianwei Sun et al. "Accurate first-principles structures and energies of diversely bonded systems from an efficient density functional". en. In: *Nature Chemistry* 8.9 (Sept. 2016), pp. 831–836. ISSN: 1755-4349. DOI: 10.1038/nchem.2535.

[51] Oleg A. Vydrov and Troy Van Voorhis. "Nonlocal van der Waals density functional: The simpler the better". In: *The Journal of Chemical Physics* 133.24 (Dec. 2010), p. 244103. ISSN: 0021-9606. DOI: 10.1063/1.3521275. URL: https://aip.scitation.org/doi/abs/10.1063/1.3521275 (visited on 04/27/2018).

[52] Riccardo Sabatini, Tommaso Gorni, and Stefano de Gironcoli. "Nonlocal van der Waals density functional made simple and efficient". In: *Physical Review B* 87.4 (Jan. 2013), p. 041108. DOI: 10.1103/PhysRevB.87.041108.

[53] Haowei Peng et al. "Versatile van der Waals Density Functional Based on a Meta-Generalized Gradient Approximation". In: *Physical Review X* 6.4 (Oct. 2016), p. 041005. DOI: 10.1103/PhysRevX.6.041005.

[54] H. H. Murray et al. "Structure of Rhenium Disulfide". In: *Inorganic Chemistry* 33.19 (Sept. 1994), pp. 4418–4420. ISSN: 0020-1669. DOI: 10.1021/ic00097a037.

[55] N. W. Alcock and A. Kjekshus. "THE CRYSTAL STRUCTURE OF ReSe$sub 2$". English. In: *Acta Chemica Scandinavica (Denmark) Divided into Acta Chem. Scand., Ser. A and Ser. B* Vol: 19 (Jan. 1965). DOI: 10.3891/acta.chem.scand.19-0079.

[56] Hendrik J. Monkhorst and James D. Pack. "Special points for Brillouin-zone integrations". In: *Physical Review B* 13.12 (June 1976), pp. 5188–5192. DOI: 10.1103/PhysRevB.13.5188.

[57] S. Y. Hu et al. "Growth and characterization of tungsten and molybdenum-doped ReSe2 single crystals". en. In: *Journal of Alloys and Compounds*. Proceedings of the 14th International Conference on Solid Compounds of Transition Elements (SCTE 2003) 383.1 (Nov. 2004), pp. 63–68. ISSN: 0925-8388. DOI: 10.1016/j.jallcom.2004.04.009.

[58] D. E. Aspnes. "Third-derivative modulation spectroscopy with low-field electroreflectance". en. In: *Surface Science* 37 (June 1973), pp. 418–442. ISSN: 0039-6028. DOI: 10.1016/0039-6028(73)90337-3.

[59] Mathias Gehlmann et al. "Direct observation of the band gap transition in atomically thin ReS$_2$". In: *Nano Letters* 17.9 (Sept. 2017), pp. 5187–5192. ISSN: 1530-6984, 1530-6992. DOI: 10.1021/acs.nanolett.7b00627. arXiv: 1702.04176.

[60] Surani M. Gunasekera et al. "Electronic Band Structure of Rhenium Dichalcogenides". en. In: *Journal of Electronic Materials* (Mar. 2018). ISSN: 0361-5235, 1543-186X. DOI: 10.1007/s11664-018-6239-0.

[61] Daniel Wolverson et al. "Raman Spectra of Monolayer, Few-Layer, and Bulk ReSe2: An Anisotropic Layered Semiconductor". In: *ACS Nano* 8.11 (Nov. 2014), pp. 11154–11164. ISSN: 1936-0851. DOI: 10.1021/nn5053926.

[62] Huan Zhao et al. "Interlayer interactions in anisotropic atomically thin rhenium diselenide". en. In: *Nano Research* 8.11 (Nov. 2015), pp. 3651–3661. ISSN: 1998-0124, 1998-0000. DOI: 10.1007/s12274-015-0865-0.

[63] YuKai Zhuang et al. "Deviatoric stresses promoted metallization in rhenium disulfide". en. In: *Journal of Physics D: Applied Physics* (2018). ISSN: 1361-6463. DOI: 10.1088/1361-6463/aab5a7.

[64] C. H Ho et al. "Crystal structure and band-edge transitions of ReS2-xSex layered compounds". en. In: *Journal of Physics and Chemistry of Solids* 60.11 (Nov. 1999), pp. 1797–1804. ISSN: 0022-3697. DOI: 10.1016/S0022-3697(99)00201-2.

[65] F. Dybała et al. "Pressure coefficients for direct optical transitions in MoS_2, $MoSe_2$, WS_2, and WSe_2 crystals and semiconductor to metal transitions". en. In: *Scientific Reports* 6 (May 2016), p. 26663. ISSN: 2045-2322. DOI: 10.1038/srep26663.

[66] P. G. Naumov et al. "Pressure-induced metallization in layered ReSe2". en. In: *Journal of Physics: Condensed Matter* 30.3 (Dec. 2017), p. 035401. ISSN: 0953-8984. DOI: 10.1088/1361-648X/aa9f52.

[67] Morasae Samadi et al. "Group 6 transition metal dichalcogenide nanomaterials: synthesis, applications and future perspectives". In: *Nanoscale Horiz.* 3.2 (2018), pp. 90–204. ISSN: 2055-6756, 2055-6764. DOI: 10.1039/C7NH00137A.

[68] Tianshu Li and Giulia Galli. "Electronic Properties of MoS $_2$ Nanoparticles". en. In: *The Journal of Physical Chemistry C* 111.44 (Nov. 2007), pp. 16192–16196. ISSN: 1932-7447, 1932-7455. DOI: 10.1021/jp075424v.

[69] V. Sorkin et al. "Nanoscale Transition Metal Dichalcogenides: Structures, Properties, and Applications". en. In: *Critical Reviews in Solid State and Materials Sciences* 39.5 (Sept. 2014), pp. 319–367. ISSN: 1040-8436, 1547-6561. DOI: 10.1080/10408436.2013.863176.

[70] Wencan Jin et al. "Direct Measurement of the Thickness-Dependent Electronic Band Structure of MoS_2 Using Angle-Resolved Photoemission Spectroscopy". In: *Phys. Rev. Lett.* 111.10 (2013), p. 106801. DOI: 10.1103/PhysRevLett.111.106801.

[71] Priya Johari and Vivek B. Shenoy. "Tuning the Electronic Properties of Semiconducting Transition Metal Dichalcogenides by Applying Mechanical Strains". In: *ACS Nano* 6.6 (June 2012), pp. 5449–5456. ISSN: 1936-0851. DOI: 10.1021/nn301320r.

[72] Xiaofeng Fan et al. "The Electronic Properties of Single-Layer and Multilayer MoS $_2$ under High Pressure". en. In: *The Journal of Physical Chemistry C* 119.19 (May 2015), pp. 10189–10196. ISSN: 1932-7447, 1932-7455. DOI: 10.1021/acs.jpcc.5b00317.

Chapter 5

Exploration of the bright and dark exciton landscape and fine structure of MoS_2 (using G_0W_0-BSE)

Author contributions:

Oleg Rubel conceived the idea. Hongyu Yu and I performed the calculations and data analysis. Hongyu and I wrote the manuscript. All authors reviewed the manuscript. The project was supervised by Oleg Rubel. Hongyu Yu and I contributed equally to this work.

This chapter was published in Physical Review B, 100(12) (2019), p. 125413, DOI: 10.1103/PhysRevB.100.125413. Reproduced with permission. Copyright 2019 by the American Physical Society.

The supplementary information is available in Appendix B.

Abstract

Spectral ordering between dark and bright excitons in transition metal dichalcogenides is of increasing interest for optoelectronic applications. However, little is known about dark exciton energies and their binding energies. We report the exciton landscape including momentum-forbidden dark excitons of MoS_2 monolayer using single shot GW-Bethe Salpeter equation (G_0W_0-BSE) calculations. We find the lowest-energy exciton to be indirect at ($K'_v \rightarrow K_c$) in agreement with recent GdW-BSE calculations [2D Mater. 6, 035003 (2019)]. We also find that by large, the lowest-energy dark exciton binding energies (E_b) scale with the quasiparticle energies (E_g) according to the empirical $E_b/E_g = 0.25$ rule. Differences in exciton binding energies are explained using an orbital theory.

5.1 Introduction

Two-dimensional transition metal dichalcogenides (TMDCs) like monolayer (ML) MoS_2 exhibit an intricate electronic fine structure that offers an abundance of possibilities to manipulate their optical and electrical properties and exploit them for novel devices. A fascinating aspect of ML materials that sets them apart from their bulk equivalents is the behavior of excitations: Quasi-particles formed by an excited electron and a hole (excitons) experience a greater Coulomb attraction in a monolayer material because of the lack of screening in the third dimension. These excitonic effects dominate the optical response of ML TMDCs.

Excitons can be either bright (optically accessible) or dark (optically inaccessible). Dark excitons can be classified according to two main characteristics: spin and location in momentum space of the electron and hole. Spin-forbidden dark excitons are quasiparticles where the electron and the hole occupy the same position in momentum space, however, their spin is opposite and thus radiative recombination is not possible. Momentum-forbidden dark excitons consist of an electron and a hole located at different points in momentum space. Unassisted recombination is not possible for these indirect excitons either, thus they are dark.

Besides the bright states, dark excitons have a considerable influence on the optical response of TMDC MLs.[1] For example, spectral closeness of dark excitons to bright excitons can cause a significant drop of the photoluminescent yield in ML MoS_2 [2].

Similarly, higher-energy momentum-forbidden dark excitons can serve as a reservoir of charge carriers for bright transitions that are lower in energy and thus enhance the response for TMDC MLs [3]. Indirect excitons have also been related to the achievable degree of circular polarization in TMDC MLs [4] and the formation of quantum dots in bilayer WSe_2 [5]. In addition, dark excitons in WSe_2 can be activated or brightened, i.e. the photoluminescence intensity increases, in the presence of a magnetic field which leads to the creation of bright excitons with long and tunable life times.[6, 7] Brightening can also be achieved by strain [8] or the adsorption of high-dipole molecules [9], allowing for completely new device concepts in the design of high-sensitivity sensors.

Knowledge of the spectral relation of dark and bright excitons is important to fully understand the optical response of monolayer TMDCs.[1, 10] This is especially crucial for ML MoS_2 for which the ordering of the lowest-energy bright and dark excitons is still being discussed [11, 12, 13]. The spectral ordering of bright and dark excitons depends mainly on the amount of band splitting caused by spin-orbit coupling as well as difference of the exciton binding energies. Initially, the emphasis was placed on studying direct excitons.[14] However, comprehensive quantitative studies of the excitonic landscape including indirect, finite-momentum excitons are scarce. Important contributions were made first by Malic et al. [15] who calculated the optical response of group-VI TMDCs. They emphasized the importance of excitonic corrections to the band structure that can lead to a change of the band character from direct to indirect or affect the ordering of bright and dark states. However, their results showed only qualitative trends. Berghäuser et al. [16] obtained the exciton landscape of monolayer MoS_2 and other group-VI TMDCs using pump-probe experiments and an empirically parameterized quantum model. According to their study, the lowest-energy state for ML MoS_2 is a dark (indirect) exciton with its hole located at Γ_v and the electron located at K'_c ($\Gamma_v \rightarrow K'_c$). Very recently, Deilmann and Thygesen [17] reported calculations of the exciton landscape including indirect excitons in the GdW+BSE scheme, where the approximation $dW = W - W_{\text{metal}}$ enables a higher computational efficiency[18]. They found the excitonic state of monolayer MoX_2 to be dark (indirect) and located at $K_v \rightarrow K'_c$.

In this report, we use *ab initio* calculations [single-shot GW (G_0W_0) + BSE beyond the Tamm-Dancoff approximation (TDA)] to explore the whole bright and dark excitonic landscape of ML MoS_2 to contribute to the ongoing discussion. According to our results, the exciton ground state is a dark indirect exciton at $K_v \rightarrow K'_c$. We show that lowest-energy spin-forbidden and indirect excitons obey the universal relationship between exciton energy and exciton binding energy proposed for bright excitons in ML 2D

materials[19]. We discuss the variations in the binding energies in the light of orbital theory. We also show that the relationship breaks down for higher-energy excitons.

5.2 Methods

5.2.1 G_0W_0+BSE calculations

We performed G_0W_0-BSE *ab initio* calculations. The procedure for GW-BSE calculations is as follows: In the GW step the electronic ground state previously obtained using density functional theory [20] is corrected for quasiparticle effects. This correction is obtained by solving for the self-energy which includes the many-body exchange-correlation interactions in a single shot. In Hedin's method [21], the self-energy is approximated by the product of the one-particle Green's function G and the screened Coulomb potential W. The quasiparticle corrected energies and wave functions are used as input for the BSE which describes interactions of electron-hole pairs and directly yields the optical excitation energies. The exciton wave function is constructed as an expansion in terms of quasiparticle wave functions, and then the BSE can be solved self-consistently as an eigenvalue problem. In most cases, it is sufficient to solve the BSE in the TDA [22, 23, 24]:

$$\left(E_{c\mathbf{k}+\mathbf{Q}} - E_{v\mathbf{k}}\right) A^{(S,\mathbf{Q})}_{vc\mathbf{k}} + \sum_{v'c'k'} K^{AA}_{vc\mathbf{k},v'c'\mathbf{k}'}(\mathbf{Q}) A^{(S,\mathbf{Q})}_{v'c'\mathbf{k}'} = \Omega^{(S,\mathbf{Q})} A^{(S,\mathbf{Q})}_{vc\mathbf{k}}. \tag{5.1}$$

Here $\Omega^{(S,\mathbf{Q})}$ is the exciton energy (the eigenvalue), $E_{v\mathbf{k}}$ ($E_{c\mathbf{k}+\mathbf{Q}}$) are the energies of the valence band (conduction band) obtained in the GW step, $A^{(S,\mathbf{Q})}_{vc\mathbf{k}}$ are expansion coefficients for the exciton wave function, and K is the interaction kernel which contains all the electron-hole interactions. Details concerning the mathematical form of K can be found in Leng et al. [24]. The index $\mathbf{Q}$ denotes a momentum transfer by a certain $\mathbf{Q}$ vector. Here, we went beyond the TDA, including resonant-antiresonant coupling (K^{AB}, K^{BA}):[24]

$$\begin{cases} \left(E_{c\mathbf{k}+\mathbf{Q}} - E_{v\mathbf{k}}\right) A^{(S,\mathbf{Q})}_{vc\mathbf{k}} + \sum_{v'c'k'} K^{AA}_{vc\mathbf{k},v'c'\mathbf{k}'}(\mathbf{Q}) A^{(S,\mathbf{Q})}_{v'c'\mathbf{k}'} \\ \qquad + \sum_{v'c'k'} K^{AB}_{vc\mathbf{k},v'c'\mathbf{k}'}(\mathbf{Q}) B^{(S,\mathbf{Q})}_{v'c'\mathbf{k}'} = \Omega^{(S,\mathbf{Q})} A^{(S,\mathbf{Q})}_{vc\mathbf{k}} \\ \left(E_{c\mathbf{k}+\mathbf{Q}} - E_{v\mathbf{k}}\right) B^{(S,\mathbf{Q})}_{vc\mathbf{k}} + \sum_{v'c'k'} K^{BB}_{vc\mathbf{k},v'c'\mathbf{k}'}(\mathbf{Q}) B^{(S,\mathbf{Q})}_{v'c'\mathbf{k}'} \\ \qquad + \sum_{v'c'k'} K^{BA}_{vc\mathbf{k},v'c'\mathbf{k}'}(\mathbf{Q}) A^{(S,\mathbf{Q})}_{v'c'\mathbf{k}'} = \Omega^{(S,\mathbf{Q})} B^{(S,\mathbf{Q})}_{vc\mathbf{k}} \end{cases} \tag{5.2}$$

Where $B_{vc\mathbf{k}}^{(S,\mathbf{Q})}$ are expansion coefficients for the antiresonant part of the exciton wave function.

The main reason to conduct calculations beyond the TDA for our work was that the software used does not recommend the calculation of finite-momentum excitons within the TDA. The TDA has been shown to break down for nanoscale systems [25, 26, 27] and to deviate from experiment for finite-momentum excitons in silicon.[28] However, we do not expect the resonant-antiresonant coupling to have a great effect on the optical properties of a ML TMDC.

To the best of our knowledge, solving the BSE beyond the TDA has not yet been reported for group-VI metal transition dichalcogenides. In the following we describe the details of our settings used to perform the G_0W_0-BSE beyond TDA calculations.

5.2.2 Computational details

The calculations were performed with the Vienna ab initio package (VASP) [29, 30], version 5.4.4. The projector-augmented wave method [31, 32] was used to treat core and valence electrons with 14 electrons for Mo, and 6 electrons for S explicitly included in the valence states. The plane-wave energy cutoff was set to 400 eV. Recommended GW projector-augmented wave potentials supplied by VASP were employed for all atoms. The Perdew-Burke-Ernzerhof[33] exchange-correlation functional was used to obtain the electronic ground state with density functional theory[34, 35]. To ensure minimal interlayer coupling, monolayers were separated by 21.5 Å of vacuum which is sufficient for the longitudinal component of the macroscopic static dielectric tensor to be close to unity. Atomic positions and lattice vectors were fully relaxed with a tolerance of 0.01 eV/Å. Only the c vector (out-of-plane vector) was fixed during the relaxation procedure. Electronic minimization was performed with a tolerance of 10^{-7} eV and convergence accelerated with Gaussian smearing of the Fermi surface by 0.05 eV. The Brillouin zone was sampled with a $12 \times 12 \times 1$ Γ-centered k-point mesh in order to include high symmetry points in the k mesh and ensure sufficient accuracy of the exciton binding energy that is highly dependent on the density of the k mesh[36]. After structure relaxation, we obtained a lattice constant of 3.185 Å, a metal-chalcogen (M-X) bond length of 2.414 Å, and a chalcogen-chalcogen X-X bond length of 3.12838 Å. The obtained lattice constant is close to the experimental lattice constant of bulk MoS_2 ($a = 3.16$ Å) [37, 38, 39] and in excellent agreement with other computational studies[40, 41, 42]. The M-X bond length is in very good agreement with experimental data [43, 44].

For all calculations following the relaxation procedure, we considered spin-orbit coupling and included 640 bands (26 of them occupied) in order to have enough empty bands for the ensuing GW calculations. Further, the orbitals were enforced to have real values at the Gamma point and points at the edge of the Brillouin zone and as a consequence the symmetry was turned off.

We calculated the quasiparticle band structure at the single-shot G_0W_0 level of theory. For the response function we set a cutoff of 250 eV; this parameter controls how many G-vectors are included in the GW-calculation. The number of frequency grid points was set to 96. For visualizing the quasiparticle band structure we applied Wannier interpolation using the WANNIER90 program[45].

The BSE calculations were carried out beyond the Tamm-Dancoff approximation using the full BSE Hamiltonian [28], which means that resonant-antiresonant coupling is included. For solving the BSE, we considered 6 occupied bands and 8 virtual (unoccupied) bands of the quasiparticle band structure as a basis for excitonic eigenstates. To obtain finite-momentum excitons, we iterated over all possible $\mathbf{Q}$ vectors that could be selected for the given k mesh in the first Brillouin zone (in total 144) and additional $\mathbf{Q}$ vectors outside the first Brillouin zone to include the $K'_v \rightarrow K_c$, $K_v \rightarrow K'_c$ and $K'_v \rightarrow \Lambda_c$ transitions. For all $\mathbf{Q}$ vectors, we obtained the lowest 100 eigenstates as output. We chose the k point with the biggest contribution to the exciton wave function (highest amplitude) for each eigenstate as the momentum vector of the hole of the exciton. Exciton binding energies were calculated by subtracting the BSE eigenvalues from the GW band gap matching the position of hole and electron of the exciton in momentum space. To distinguish between spin-parallel and spin-antiparallel states, the spinor up and down components (α and β) were determined from spin projections as described in Refs. Giustino [46] and Zheng, Yu, and Rubel [47].

We would like to point out certain limits of our methods. The G_0W_0-BSE procedure as implemented in VASP and as used for this work does not provide the option to truncate the Coulomb interaction between periodic images. Carefully conducted studies[48, 49] show that Coulomb truncation is essential for achieving convergence of the GW band energy corrections, as without the truncation the periodic images of the monolayer increase the dielectric function, especially in the low $\mathbf{Q}$ limit. Further, a very high k mesh up to $300 \times 300 \times 1$ is required in order to converge the exciton binding energy to within 0.1 eV.[49] As our G_0W_0 calculations and the BSE beyond TDA calculations were conducted without considering geometrical and time reversal symmetries, the computational cost precludes the use of fine k meshes (due to excessive memory requirements).

However, the errors of not truncating the Coulomb interaction and using a coarse k mesh partly cancel out.[48]

We conducted convergence tests that suggest that the total error of the quasiparticle band gap is below 0.1 eV and the variation of the spectral spacing with k grid density is ca. one order of magnitude smaller than the actual energy spacing [50].

5.3 Results and discussion

We will first discuss the effect of including the resonant-antiresonant coupling (going beyond the TDA). The TDA affects only the BSE step of the calculations. We performed a comparative BSE calculation employing the TDA to investigate the effects of the absence of resonant-antiresonant coupling on the optical properties of ML MoS_2. The results are identical to the full BSE calculations, differences are negligible. This is true for the spectral spacing of the excitons [51] as well as for the dielectric response (data not shown).

Now we turn to the results of the main calculations. The quasiparticle band structure of monolayer MoS_2 is shown in Fig. 5.1. The bands are obtained by Wannier interpolation of the GW eigenvalues. The band structure shows a direct band gap of ca. 2.43 eV at the K and K$'$ points. These points are equivalent (except for their spin) because of the time-reversal symmetry. Besides K and K$'$, Λ and Λ' are related via time-reversal symmetry. For future discussions we will only refer to one of the via time-reversal symmetry related transitions.

The optical response of TMDC monolayers is dominated by the presence of excitons and their binding energies. As a result, the optical energy gap is much smaller than the quasiparticle band gap. This can be seen when considering the absorption spectrum of ML MoS_2 for the direct transitions ($\mathbf{Q} = 0$) obtained from our BSE calculations (Figure 5.2a). The A and B excitons are located at ca. 1.8 eV and 1.95 eV, implying binding energies of about 0.62 and 0.48 eV, respectively. The spin-forbidden dark exciton is slightly lower in energy than the bright exciton. The absorption spectrum is in good qualitative agreement with experiments[52, 53] as well as other theoretical studies[54, 55]. The energies of the A and B peak are blue-shifted in comparison to experiment. This comes about for two reasons; missing substrate effects[56] as well as k grid dependent binding energies. The denser the k grid, the smaller (i.e., better converged) the binding energies become [36, 57].

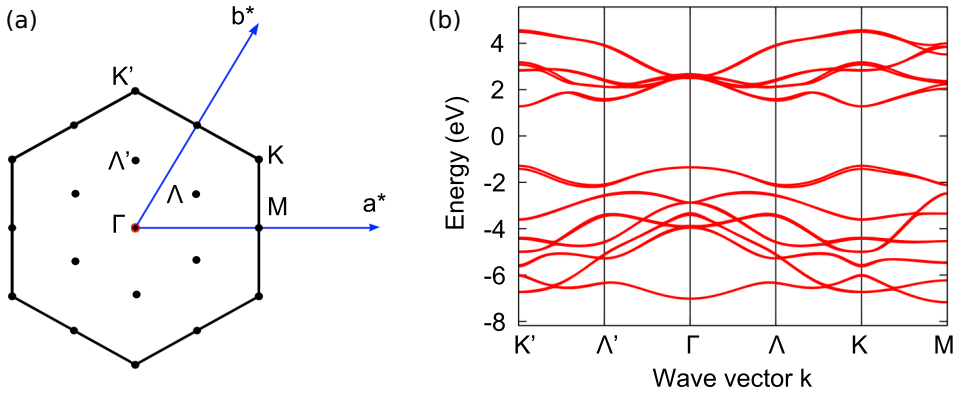

FIGURE 5.1: (a) First Brillouin zone of monolayer MoS_2 and (b) quasi-particle band structure after Wannier-interpolation. The direct band gap is located at K (K′).

The values obtained from our calculations for the band gap and exciton binding energies are in good agreement with experiment. Using scanning tunneling spectroscopy and optical reflectance contrast measurements for MoS_2 on fused silica, Rigosi et al. [58] obtained a binding energy of the bright excitons of 0.31 ± 0.04 eV and an electronic band gap of 2.17 ± 0.1 eV. The results of our calculation with $E_b = 0.624$ eV and $E_g = 2.42$ eV are slightly higher than the experimental values because the calculations are obtained for a free-standing monolayer and a relatively coarse k mesh. Other computational studies using GW-BSE found results that are quite close to ours obtaining 2.42 eV for the band gap and 0.57 eV for bright exciton binding energy [19]. The difference in the Eb can be explained with the k mesh density: Jiang et al. [19] used a k mesh of $16 \times 16 \times 1$ (our calculations: $12 \times 12 \times 1$) and the binding energy strongly depends on the k mesh [36]. For example, in our convergence calculations for the lowest-energy direct exciton at the K point, we found an exciton binding energy of 0.551 eV for a k grid of $15 \times 15 \times 1$ and nearly a twice as large binding energy of 1.061 eV for a k grid of $6 \times 6 \times 1$ [57].

Figure 5.2b shows the spectra for indirect excitons with a $\mathbf{Q}$ vector of (-1/3, 2/3, 0). This $\mathbf{Q}$ vector captures the the $K'_v \rightarrow K_c$ and $\Gamma_v \rightarrow K'_c$ transitions. It becomes clear that there exists a smaller-energy exciton that is indirect at $K'_v \rightarrow K_c$ with an exciton energy of less than 1.8 eV.

To capture the effect of all important indirect excitons on the quasiparticle band structure, we plot the exciton band structure in a two-dimensional fashion. This allows us to show the renormalization of the eigenvalues caused by direct, indirect, and dark excitons at the same time. In Fig. 5.3 the landscape of bright and dark excitons in ML

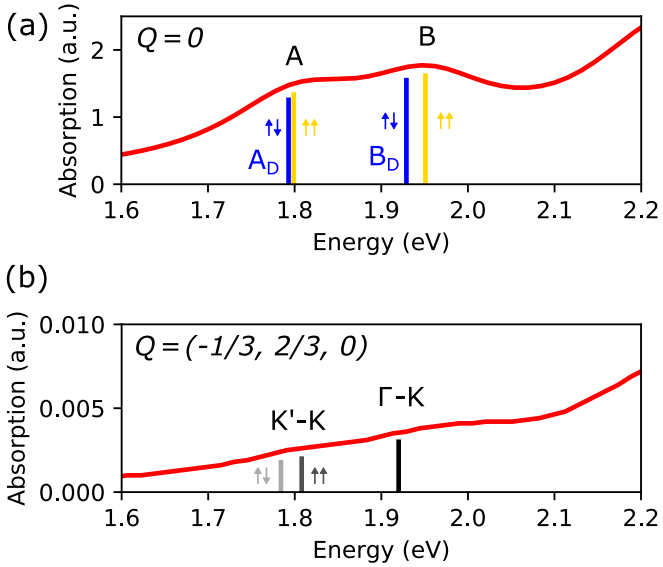

FIGURE 5.2: Absorption spectra of MoS_2. Shown is the imaginary part of the dielectric function obtained from the BSE calculation. (a) $\mathbf{Q} = 0$ denotes the absorption spectrum of the direct transitions. The first two absorption peaks denote the A and B excitons located at the K point. The dark (spin-forbidden) exciton is lower in energy than the bright exciton for both A and B excitons. (b) $\mathbf{Q} = (-1/3, 2/3, 0)$ captures the the $K'_v \rightarrow K_c$ and $\Gamma_v \rightarrow K'_c$ transitions. The indirect exciton at $K'_v \rightarrow K_c$ is clearly lower in energy than the dark direct exciton at K.

MoS_2 is shown for the most important points in momentum space.

To accommodate momentum forbidden dark excitons, the k vectors of the electron and hole of an exciton are displayed separately on the two axes of the graph. Further, we distinguish between spin-up and spin-down states to allow for the visualization of spin-forbidden excitons. As a result, bright excitons are seen on the dashed red diagonal line, spin-forbidden direct excitons are on the dotted blue line, and momentum-forbidden excitons are located to the sides. Also, spin-allowed excitons are distributed in the lower half of the plot while spin-forbidden excitons being placed in the upper half. Each bubble represents an exciton; the colour displays the exciton energy and the radius of the bubble corresponds to the exciton binding energy. The symmetry of the wave function Φ of the exciton can be expressed as:

$$\Phi\left(\mathbf{k}_h, \mathbf{k}_e, \mathbf{s}_h, \mathbf{s}_e\right) = \Phi^*\left(-\mathbf{k}_h, -\mathbf{k}_e, -\mathbf{s}_h, -\mathbf{s}_e\right). \tag{5.3}$$

As a result, excitons $|\mathbf{k}_h, \mathbf{k}_e, \mathbf{s}_h, \mathbf{s}_e\rangle$ and $|-\mathbf{k}_h, -\mathbf{k}_e, -\mathbf{s}_h, -\mathbf{s}_e\rangle$ should have the same properties. As necessitated by our procedure, we calculated the whole Brillouin zone

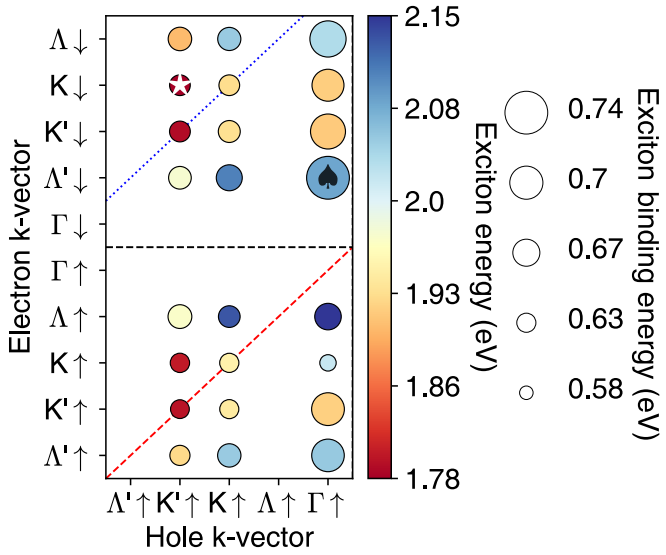

FIGURE 5.3: MoS_2 exciton landscape including dark and bright excitons. The color scale reflects the exciton energy and the circle size represents the exciton binding energy. In order to display finite-momentum excitons, hole and electron k vectors are displayed separately on the horizontal and vertical axis, respectively. The lowest-energy exciton (star) is located at $K'_v \uparrow \rightarrow K_c \downarrow$ and is therefore momentum-forbidden. The highest binding energy (spades) occurs for an indirect exciton at $\Gamma_v \uparrow \rightarrow \Lambda'_c \downarrow$.

irrespective of time reversal symmetry. Because of this, our results showed computational inaccuracies in the single-digit meV range for the band energies (and the K point exciton energies) between per definition of time reversal symmetry identical states. The energy values presented here are always chosen from the exciton with the lower energy of the two (by time reversal symmetry) identical states. Due to time reversal symmetry we show only one half of the hole states in Fig 5.3. The other half would be equal to the first by center symmetry. Although unoccupied, we chose to include the Λ_v and the Γ_c states to preserve the center symmetry.

The exciton with the largest binding energy of 0.712 eV (marked with a spade) is located at $\Gamma_v \uparrow$ (hole) and $\Lambda'_c \downarrow$ (electron) ($\Gamma_v \uparrow \rightarrow \Lambda' \downarrow$). The lowest-energy exciton (marked with a star) has an energy of 1.784 eV and is located at $K'_v \uparrow \rightarrow K_c \downarrow$. This implies that after considering excitonic effects, we find a change of the optical band gap location of MoS_2 with regards to the transport band gap: the optical band gap is now indirect. The exciton at $K'_v \uparrow \rightarrow K_c \downarrow$ is 15 meV lower in energy than the bright exciton at K and 9 meV lower in energy than the spin-forbidden direct exciton at K. The band ordering is illustrated in Fig. 5.4.

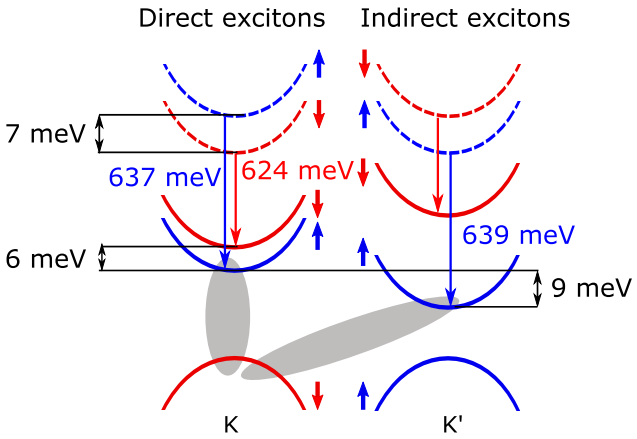

FIGURE 5.4: Schematic diagram of the lowest-energy excitons at the K-K′ valley of ML MoS_2. The ordering of solid energy bands corresponds to the exciton-corrected energies. The dashed conduction bands denote the quasiparticle band ordering. The lowest-energy exciton is indirect and located at K-K'. The lowest direct exciton is located at K and spin-forbidden (dark). This result is linked to spin-orbit coupling and the differences in the exciton binding energies which are higher for the spin- and momentum-forbidden excitons than for the bright exciton (637, 639, and 624 meV, respectively).

Besides the evaluation of the spin-states, dark and bright excitons can be distinguished by their oscillator strength. The oscillator strength of bright excitons is several magnitudes higher than of dark excitons [12]. In Fig. 5.5 we show the oscillator strength (bubble size) obtained from solving the BSE paired with the quasiparticle band gap (colour map) in a similar fashion to the exciton landscape. We find that the direct, spin-allowed excitons at K and K′ are about 1400 times higher in oscillator strength than their spin-forbidden equivalents.

Figure 5.5 also shows that our GW calculations predict a direct band gap at K with the valence and conduction band having the same spin. The lower-energy spin-forbidden excited state after considering excitonic effects arises due to different exciton binding energies (E_b) of the dark and the bright exciton: The E_b of the indirect dark exciton ($E_b = 0.637$ eV) is about 13 meV higher than the binding energy of the bright exciton ($E_b = 0.624$ eV) while the spin splitting of the conduction band is only about 7 meV (see Fig. 5.4). Thus, after considering excitonic effects, the spin- transition at K is lower in energy than the spin-allowed transition. These results are in agreement with Qiu, da Jornada, and Louie [11] and Deilmann and Thygesen [17] who also found that the dark exciton at K is lower in energy than the bright exciton. Echeverry et al. [12], using the GW-BSE method came to the opposite conclusion. Qiu, Jornada, and Louie

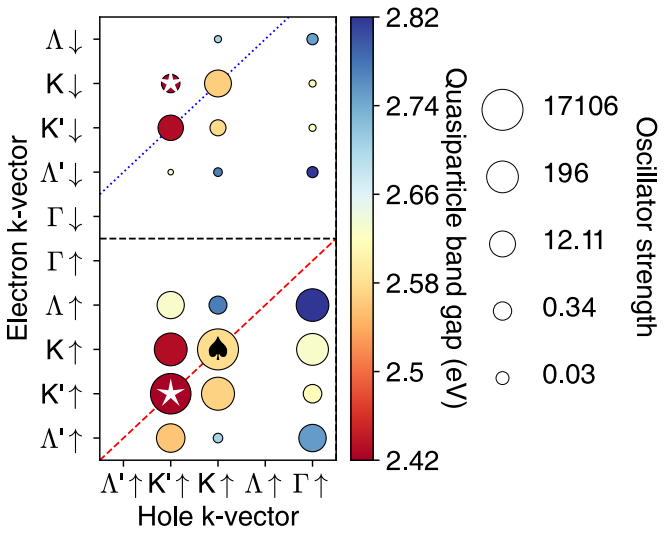

FIGURE 5.5: MoS_2 quasiparticle band gaps (color scale) and oscillator strengths (bubbles in a log scale) for bright and dark excitons. The quasiparticle band gap (star) is located at $K' \uparrow$ ($K \downarrow$). An indirect band gap of equal energy is located at $K'_v \uparrow$ - $K_c \downarrow$. The oscillator strength of the bright transitions is several magnitudes larger than that of the dark transitions; the highest oscillator strength corresponds to the $K'_v \uparrow \rightarrow K'_c \uparrow$ transition (spades).

[49] attribute the differing results in the literature to different settings of the density functional theory, GW and BSE parameters.

Now we will discuss the binding energies of the whole exciton landscape in more detail. Most of the holes of the excitons locate at Γ or K and the electrons of the excitons locate at the Λ or K (see Fig. 5.3). Interestingly, the exciton binding energy of the excitons whose hole is at Γ is almost always higher than of excitons whose hole is located at K. For bulk semiconductors this effect could be explained with the effective mass differences as holes at the Γ point are heavier than holes at the K point [59]. However, for the binding energies of 2D materials the effective mass does not play a significant role, provided the polarizability is large (which is the case for MoS_2).[59, 19]

Further, it is well known that the high binding energy of 2D materials originates from the lack of screening in the third dimension. Hence, we expect one factor for the different binding energies to be differences in screening depending on the position of the electron in real space. To qualitatively compare the amount of screening experienced by different excitons, we performed an orbital analysis for the valence and conduction band states of each exciton. The basic idea is that electrons occupying orbitals pointing perpendicular to the layer experience less screening than electrons of orbitals confined within the plane

of the monolayer. By convention, z is taken as the out-of-plane axis. It is well known, that for monolayer MoS_2 Γ_v exhibits high contributions of the Mo-d_{z^2} and S-p_z orbitals while the K_v state is mainly composed of d_{xy} orbitals.[43] For our calculations we find the Γ_v state to consist of ca. 77 % d_{z^2} + 22 % p_z and the K_v state of 41 % d_{xy} + 41 % $d_{x^2-y^2}$. Thus we can expect excitons at Γ_v to experience less screening and consequently have higher binding energies than excitons at K_v.

Figure 5.6 shows the relationship between the quasiparticle band gap and exciton binding energy, including the lowest-energy bright, spin-forbidden and momentum-forbidden excitons. Generally, excitons at large quasiparticle band gaps have larger exciton binding energies. We included a dashed line in the figure that represents the $E_b/E_g = 0.25$ rule for excitons of 2D materials proposed by Jiang et al. [19]. Momentum-allowed excitons follow the rule that the exciton binding energy is about 0.25 of quasiparticle band gap [19] irrespective of their spin. Momentum-forbidden excitons also generally follow the trend of the exciton binding energy being about 0.25 of the band gap but with more scattering (ratios from 0.23 to 0.28). The insert of Figure 5.6 shows a trend for indirect excitons: the higher the binding energy E_b, the higher is the ratio E_b/E_g. What causes this relationship?

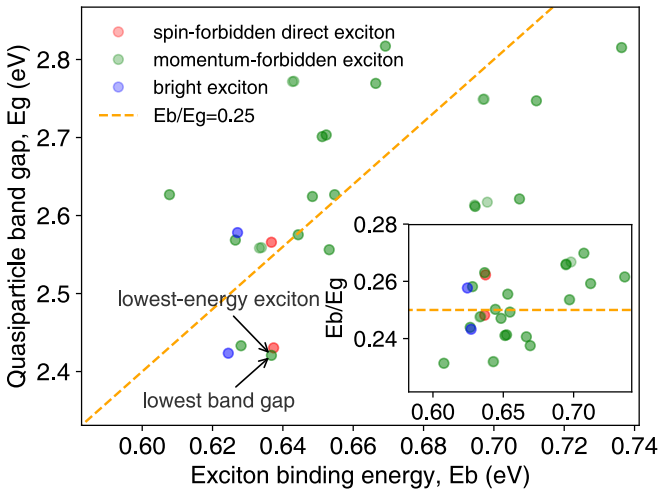

FIGURE 5.6: Ratio of the exciton binding energy (E_b) and quasiparticle band gap (E_g) for MoS_2. Bright excitons (blue), spin-forbidden excitons (red) and momentum-forbidden excitons (green) are shown. The relationship of $E_b/E_b = 0.25$ according to Jiang et al. [19] is shown by a dashed line. The insert shows the ratio E_b/E_g over E_b. All excitons are contained in the E_b/E_g range of 0.23 - 0.28 and thus not to far from the 0.25 rule.

In order to explore this in more detail we will next consider the exciton landscape including higher-energy excitons, up to 100 per **Q** vector, and their orbital compositions.

We determined the d_{z^2} and p_z orbital contributions of the hole and electron states of each exciton and plotted the sum of them against the E_b/E_g ratio (Figure 5.7). For the lowest-energy excitons, excitons with higher E_b/E_g ratios show a higher percentage of d_{z^2} and p_z orbitals. In other words, there exists a correlation between the E_b/E_g ratio on the orbital contributions. This result explains the range in the E_b/E_g ratio observed in Figure 5.6. It can also be seen that the direct excitons (red circles in Figure 5.7) are confined to a narrow region of d_{z^2} and p_z percentage, just below 50 %. As a result, the E_b/E_g ratio does not scatter as much for the direct lowest-energy excitons as for the indirect excitons. However, upon including higher-energy excitons, the $E_b/E_g = 0.25$ relationship completely breaks down; the E_b/E_g ratio also becomes largely independent of the orbital composition. The relationship of binding energy and orbital contributions becomes less clear and has vanished when the 100 lowest-energy excitons for each $\mathbf{Q}$ vector are included. We attribute this to the weaker electron-hole interactions for excitons with higher energies. At these energies, excitons are closely spaced and decrease rapidly in binding energy, behaving as uncorrelated electron-hole pairs.[55] The decrease of the E_b/E_g ratio with quasiparticle energy is shown in the Supplemental Material [60].

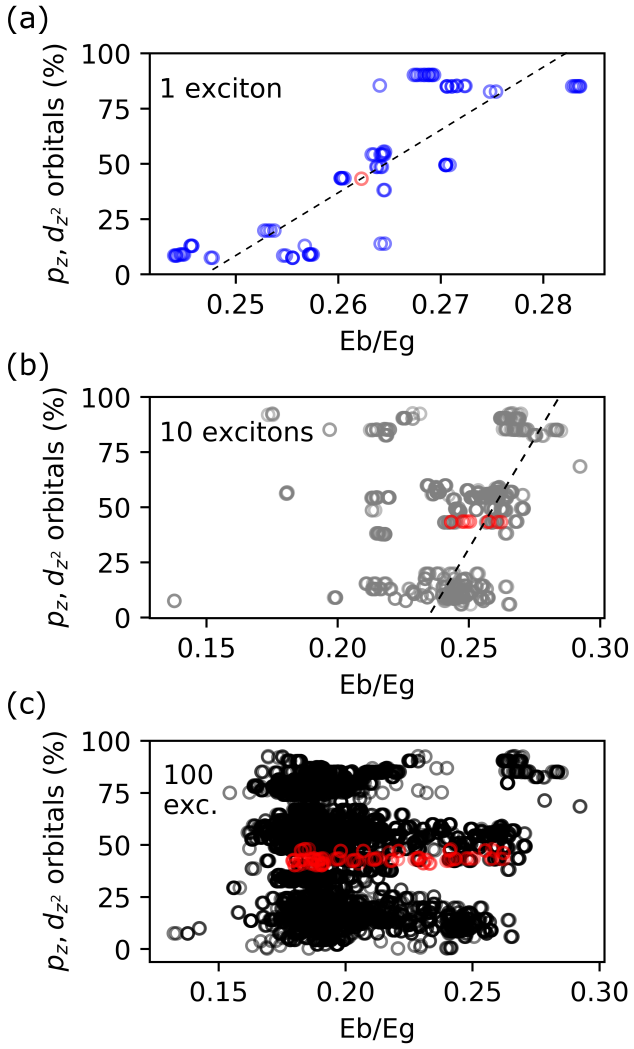

FIGURE 5.7: Orbital contributions to valence and conduction band states of indirect excitons in MoS_2 over the ratio of the exciton binding energy (E_b) and quasiparticle band gap (E_g) for MoS_2. Direct excitons are also shown (red). (a) For the lowest-energy excitons (1 exciton per **Q** vector) there is a clear dependence of the E_b/E_g ratio on the contributions of the p_z and d_{z^2} orbitals (a line is included as guide to the eye). (b), (c) The more higher-energy excitons are included for each **Q** vector, the less obvious this dependence becomes and finally vanishes (10 and 100 lowest-energy excitons). At higher energies, exciton charge carriers are screened and hole and electron progressively behave as free charge carriers causing the binding energy to decrease.

5.4 Conclusion

In conclusion, we performed calculations of finite-momentum excitons in MoS_2 monolayer within and beyond the first Brillouin zone. It is found that the holes of the lowest-energy excitons are located at the Γ or K valleys, while the electrons reside in the K or Λ valleys. Our calculations predict the lowest-energy exciton to be indirect at K-K′ which is in agreement with recent GdW-BSE calculations [17]. The energy difference between the indirect exciton at K-K′ and the spin-forbidden direct exciton at K-K is about 9 meV. The bright exciton is located at K and 15 meV higher in energy than the lowest-energy exciton at K-K′. We also discussed the exciton binding energies. The ratio of $E_b/E_g = 0.25$ found for bright excitons in monolayer 2D materials holds true approximately for dark and indirect excitons. Excitons contained in orbitals that point out of plane and thus experience less local screening show higher binding energies. The relation of exciton binding energies to orbital composition and the $E_b/E_g = 0.25$ relation both break down for higher-energy excitons.

Acknowledgements

H.Y. acknowledges support by the National Science Fund of China for Talent Training in the Basic Sciences (No. J1103208). M.L. and O.R. acknowledge funding provided by the Natural Sciences and Engineering Research Council of Canada under the Discovery Grant Programs RGPIN-2015-04518. Calculations were performed using a Compute Canada infrastructure supported by the Canada Foundation for Innovation under John R. Evans Leaders Fund.

References

[1] Thomas Mueller and Ermin Malic. “Exciton physics and device application of two-dimensional transition metal dichalcogenide semiconductors”. In: *npj 2D Materials and Applications* 2.1 (2018), p. 29.

[2] Fengcheng Wu, Fanyao Qu, and A. H. MacDonald. “Exciton band structure of monolayer MoS 2”. In: *Phys. Rev. B* 91.7 (2015), p. 075310.

[3] Alexander Steinhoff et al. “Exciton fission in monolayer transition metal dichalcogenide semiconductors”. In: *Nat. Commun.* 8.1 (2017), p. 1166.

[4] Michal Baranowski et al. "Dark excitons and the elusive valley polarization in transition metal dichalcogenides". In: *2D Mater.* 4.2 (2017), p. 025016.

[5] Jessica Lindlau et al. "The role of momentum-dark excitons in the elementary optical response of bilayer WSe 2". In: *Nat. Commun.* 9.1 (2018), p. 2586.

[6] Xiao-Xiao Zhang et al. "Magnetic brightening and control of dark excitons in monolayer WSe 2". In: *Nat. Nanotechnol.* 12.9 (2017), p. 883.

[7] Railson Vasconcelos et al. "Dark exciton brightening and its engaged valley dynamics in monolayer wse 2". In: *Phys. Rev. B* 98.19 (2018), p. 195302.

[8] Maja Feierabend et al. "Dark-exciton based strain sensing in transition metal dichalcogenides". In: *arXiv preprint arXiv:1806.07350* (2018).

[9] Maja Feierabend et al. "Proposal for dark exciton based chemical sensors". In: *Nat. Commun.* 8 (2017), p. 14776.

[10] Malte Selig et al. "Dark and bright exciton formation, thermalization, and photoluminescence in monolayer transition metal dichalcogenides". In: *2D Mater.* 5.3 (2018), p. 035017.

[11] Diana Y. Qiu, Felipe H. da Jornada, and Steven G. Louie. "Optical spectrum of MoS 2: many-body effects and diversity of exciton states". In: *Phys. Rev. Lett.* 111.21 (2013), p. 216805.

[12] J. P. Echeverry et al. "Splitting between bright and dark excitons in transition metal dichalcogenide monolayers". In: *Phys. Rev. B* 93.12 (2016), 121107(R).

[13] MR Molas et al. "Brightening of dark excitons in monolayers of semiconducting transition metal dichalcogenides". In: *2D Mater.* 4.2 (2017), p. 021003.

[14] Gang Wang et al. "Colloquium: Excitons in atomically thin transition metal dichalcogenides". In: *Rev. Mod. Phys.* 90.2 (2018), p. 021001.

[15] Ermin Malic et al. "Dark excitons in transition metal dichalcogenides". In: *Phys. Rev. Materials* 2.1 (2018), p. 014002.

[16] Gunnar Berghäuser et al. "Mapping of the dark exciton landscape in transition metal dichalcogenides". In: *Phys. Rev. B* 98.2 (2018), 020301(R).

[17] Thorsten Deilmann and Kristian Sommer Thygesen. "Finite-momentum exciton landscape in mono-and bilayer transition metal dichalcogenides". In: *2D Mater.* 6 (2019), p. 035003.

[18] Matthias Drüppel et al. "Electronic excitations in transition metal dichalcogenide monolayers from an LDA-GdW approach". In: *Physical Review B* 98.15 (2018), p. 155433.

[19] Zeyu Jiang et al. "Scaling universality between band gap and exciton binding energy of two-dimensional semiconductors". In: *Phys. Rev. Lett.* 118.26 (2017), p. 266401.

[20] W. Kohn and L. J. Sham. "Self-Consistent Equations Including Exchange and Correlation Effects". In: *Phys. Rev.* 140 (1965), A1133–A1138. DOI: 10.1103/PhysRev.140.A1133.

[21] Lars Hedin. "New method for calculating the one-particle Green's function with application to the electron-gas problem". In: *Phys. Rev.* 139.3A (1965), A796.

[22] Ig. Tamm. "Relativistic Interaction of Elementary Particles". In: *Selected Papers*. Springer Berlin Heidelberg, 1991, pp. 157–174. DOI: 10.1007/978-3-642-74626-0_12. URL: https://doi.org/10.1007/978-3-642-74626-0_12.

[23] S. M. Dancoff. "Non-Adiabatic Meson Theory of Nuclear Forces". In: *Phys. Rev.* 78.4 (May 1950), pp. 382–385. DOI: 10.1103/physrev.78.382. URL: https://doi.org/10.1103/physrev.78.382.

[24] Xia Leng et al. "GW method and Bethe–Salpeter equation for calculating electronic excitations". In: *WIREs Comput. Mol. Sci.* 6.5 (2016), pp. 532–550.

[25] Yuchen Ma, Michael Rohlfing, and Carla Molteni. "Excited states of biological chromophores studied using many-body perturbation theory: Effects of resonant-antiresonant coupling and dynamical screening". In: *Phys. Rev. B* 80.24 (2009), 241405(R).

[26] Peter Puschnig, Christian Meisenbichler, and Claudia Draxl. "Excited state properties of organic semiconductors: breakdown of the Tamm-Dancoff approximation". In: *arXiv preprint arXiv:1306.3790* (2013).

[27] Myrta Gruning, Andrea Marini, and Xavier Gonze. "Exciton-plasmon states in nanoscale materials: breakdown of the Tamm- Dancoff approximation". In: *Nano Lett.* 9.8 (2009), pp. 2820–2824.

[28] Tobias Sander, Emanuele Maggio, and Georg Kresse. "Beyond the Tamm-Dancoff approximation for extended systems using exact diagonalization". In: *Phys. Rev. B* 92.4 (2015), p. 045209.

[29] Georg Kresse and Jürgen Hafner. "Ab initio molecular dynamics for liquid metals". In: *Phys. Rev. B* 47.1 (1993), p. 558.

[30] Georg Kresse and Jürgen Furthmüller. "Efficiency of ab-initio total energy calculations for metals and semiconductors using a plane-wave basis set". In: *Comp. Mater. Sci.* 6.1 (1996), pp. 15–50.

[31] Peter E. Blöchl. "Projector augmented-wave method". In: *Phys. Rev. B* 50.24 (1994), p. 17953.

[32] Georg Kresse and D Joubert. "From ultrasoft pseudopotentials to the projector augmented-wave method". In: *Phys. Rev. B* 59.3 (1999), p. 1758.

[33] John P Perdew, Kieron Burke, and Matthias Ernzerhof. "Generalized gradient approximation made simple". In: *Phys. Rev. Lett.* 77.18 (1996), p. 3865.

[34] Pierre Hohenberg and Walter Kohn. "Inhomogeneous electron gas". In: *Phys. Rev.* 136.3B (1964), B864.

[35] Walter Kohn and Lu Jeu Sham. "Self-consistent equations including exchange and correlation effects". In: *Phys. Rev.* 140.4A (1965), A1133.

[36] Menno Bokdam et al. "Role of polar phonons in the photo excited state of metal halide perovskites". In: *Sci. Rep.* 6 (2016), p. 28618.

[37] KD Bronsema, JL De Boer, and F Jellinek. "On the structure of molybdenum diselenide and disulfide". In: *Z. Anorg. Allg. Chem.* 540.9-10 (1986), pp. 15–17.

[38] B Schönfeld, JJ Huang, and SC Moss. "Anisotropic mean-square displacements (MSD) in single-crystals of 2H-and 3R-MoS2". In: *Acta Crystallogr., Sect. B: Struct. Sci* 39.4 (1983), pp. 404–407.

[39] JC Wildervanck and F Jellinek. "Preparation and crystallinity of molybdenum and tungsten sulfides". In: *Z. Anorg. Allg. Chem.* 328.5-6 (1964), pp. 309–318.

[40] Jun Kang et al. "Band offsets and heterostructures of two-dimensional semiconductors". In: *Appl. Phys. Lett.* 102.1 (2013), p. 012111.

[41] Gui-Bin Liu et al. "Three-band tight-binding model for monolayers of group-VIB transition metal dichalcogenides". In: *Phys. Rev. B* 88.8 (2013), p. 085433.

[42] Ashwin Ramasubramaniam. "Large excitonic effects in monolayers of molybdenum and tungsten dichalcogenides". In: *Phys. Rev. B* 86.11 (2012), p. 115409.

[43] Morasae Samadi et al. "Group 6 transition metal dichalcogenide nanomaterials: synthesis, applications and future perspectives". In: *Nanoscale Horiz.* 3.2 (2018), pp. 90–204.

[44] Roscoe G Dickinson and Linus Pauling. "The crystal structure of molybdenite". In: *J. Am. Chem. Soc.* 45.6 (1923), pp. 1466–1471.

[45] Arash A Mostofi et al. "wannier90: A tool for obtaining maximally-localised Wannier functions". In: *Comput. Phys. Commun.* 178.9 (2008), pp. 685–699.

[46] Feliciano Giustino. *Materials modelling using density functional theory: properties and predictions*. Oxford University Press, 2014.

[47] Chao Zheng, Shidong Yu, and Oleg Rubel. "Structural dynamics in hybrid halide perovskites: Bulk Rashba splitting, spin texture, and carrier localization". In: *Phys. Rev. Materials* 2.11 (2018), p. 114604.

[48] Falco Hüser, Thomas Olsen, and Kristian S. Thygesen. "How dielectric screening in two-dimensional crystals affects the convergence of excited-state calculations: Monolayer MoS 2". In: *Phys. Rev. B* 88.24 (2013), p. 245309.

[49] Diana Y. Qiu, Felipe H. da Jornada, and Steven G. Louie. "Screening and many-body effects in two-dimensional crystals: Monolayer MoS 2". In: *Phys. Rev. B* 93.23 (2016), p. 235435.

[50] See Supplemental Material at [URL will be inserted by publisher] for convergence tests.

[51] See Supplemental Material at [URL will be inserted by publisher] for a comparison of TDA and full BSE results of the spectral spacing of excitons (Figure S2 b).

[52] Kin Fai Mak et al. "Atomically thin MoS 2: a new direct-gap semiconductor". In: *Phys. Rev. Lett.* 105.13 (2010), p. 136805.

[53] Krishna P Dhakal et al. "Confocal absorption spectral imaging of MoS 2: optical transitions depending on the atomic thickness of intrinsic and chemically doped MoS 2". In: *Nanoscale* 6.21 (2014), pp. 13028–13035.

[54] Maurizia Palummo, Marco Bernardi, and Jeffrey C Grossman. "Exciton radiative lifetimes in two-dimensional transition metal dichalcogenides". In: *Nano Lett.* 15.5 (2015), pp. 2794–2800.

[55] Marco Bernardi et al. "Optical and electronic properties of two-dimensional layered materials". In: *Nanophotonics* 6.2 (2017), pp. 479–493.

[56] Bablu Mukherjee et al. "Complex electrical permittivity of the monolayer molybdenum disulfide (MoS 2) in near UV and visible". In: *Opt. Mater. Express* 5.2 (2015), pp. 447–455.

[57] See Supplemental Material at [URL will be inserted by publisher] for the dependence of exciton binding energies on the k grid (Table S1).

[58] Albert F Rigosi et al. "Electronic band gaps and exciton binding energies in monolayer M o x W 1- x S 2 transition metal dichalcogenide alloys probed by scanning tunneling and optical spectroscopy". In: *Phys. Rev. B* 94.7 (2016), p. 075440.

[59] Thomas Olsen et al. "Simple screened hydrogen model of excitons in two-dimensional materials". In: *Phys. Rev. Lett.* 116.5 (2016), p. 056401.

[60] See Supplemental Material at [URL will be inserted by publisher] for the decrease of the E_b/E_g ratio with quasiparticle energy (Figure S3).

Chapter 6

Band alignment of monolayer CaP_3, $CaAs_3$, $BaAs_3$ and the role of p-d orbital interactions in the formation of conduction band minima

Author contributions:

I conceived the idea in discussions with Oleg Rubel and Himanshu Saini. I performed the calculations and data analysis. Himanshu Saini contributed to the preparation of the monolayer structure files and heterostructure calculations. The manuscript was written by me, revised by Oleg Rubel and reviewed by Himanshu Saini. The project was supervised by Oleg Rubel.

This chapter was published in Physical Chemistry Chemical Physics, 23 (2021), pp. 7418–7425, DOI: 10.1039/d1cp00099c. Reproduced with permission. Copyright by the Owner Societies 2021.

The supplementary information is available in Appendix C.

Abstract

Recently, a number of new two-dimensional (2D) materials based on puckered phosphorene and arsenene have been predicted with moderate band gaps, good absorption properties and carrier mobilities superior to transition metal dichalcogenides. For heterojunction applications, it is important to know the relative band alignment of these new 2D materials. We report the band alignment of puckered CaP_3, $CaAs_3$ and $BaAs_3$ monolayers at the quasiparticle level of theory (G_0W_0), calculating band offsets for isolated monolayers according to the electron affinity rule. Our calculations suggest that monolayer CaP_3, $CaAs_3$ and $BaAs_3$ all form type-II (staggered) heterojunctions which makes them suitable for solar-energy conversion applications. Their quasiparticle gaps are 2.1 (direct), 1.8 (direct) and 1.5 eV (indirect), respectively. We also examine trends in the electronic structure in the light of chemical bonding analysis. We show that the indirect band gap in monolayer $BaAs_3$ is caused by relatively strong As $3p$ - Ba $5d$ bonding interactions. Our results provide guidance for the design of phosphorene-like materials and their heterojunction applications.

6.1 Introduction

The optical and electronic properties of black phosphorus (bP), such as its high carrier mobility [1] and tunable band gap [2], have sparked interest in the broader family of phosphorene related 2D material structures. Recently, several new 2D materials related to phosphorene and arsenene – for which a part of the As or P atoms is replaced by group II elements [3, 4, 5] or elements of other groups (III, IV, V) [6, 7, 8, 9] – have been predicted. These layered materials show a combination of high carrier mobilities, moderate band gaps and good light absorption properties promising for next-generation electronic heterojunction devices like solar cells and transistors.

For example, monolayer (1L) CaP_3 is predicted to have a band gap of 1.15 eV [5] (using a hybrid functional, HSE06) and a high electron mobility of up to ca. 20 000 $cm^2\ V^{-1}\ s^{-1}$ (using deformation potential theory, value needs to be taken with caution as deformation potential theory usually overestimates mobility values [10, 11]).

For materials selection in heterojunction design, it is necessary to know the band alignments of the layered structures. However, band alignments for novel 2D materials of the phosphorene family have not yet been reported and the majority of the band

gaps of these 2D structures has been calculated using hybrid functionals at the density functional level of theory (DFT). Although hybrid functionals alleviate the band gap problem of DFT, it is generally accepted that GW quasiparticle calculations provide the most reliable and accurate level of theory for band structure and band alignment calculations.[12, 13, 14, 15]

Here, we calculate the band gaps of the recently predicted[5, 4, 3] CaP_3, $CaAs_3$ and $BaAs_3$ monolayers at the G_0W_0 level of theory. We estimate their band alignments according to the electron affinity rule which states that the conduction band offset of a heterojunction can be obtained from the electron affinities of the individual materials. Analyzing the electron affinity of the isolated monolayers is a valid first step in materials selection process for possible 2D heterostructures. [16, 17] Further, we explain the differences in band alignment based on structure analysis and show that the indirect nature of the band gap in 1L $BaAs_3$ is caused by increasing *p*-*d* orbital interactions. Our analysis sheds light on the influence of structure and orbital interactions on the theoretical band offsets in phosphorene-like materials. These insights may be helpful for the design of phosphorene-like materials and their heterojunctions.

6.2 Methods

6.2.1 Structural relaxation (DFT).

First, we relaxed the experimental bulk structures of $CaAs_3$, [18] CaP_3, [19] and $BaAs_3$ [18]. The structures were relaxed on the DFT level using the Vienna ab initio package (VASP) [20, 21] with projector-augmented potentials[22] as implemented by Kresse and Joubert [23]. We explicitly included eight valence and core electrons for Ca, ten electrons for Ba, 15 electrons for As and five valence electrons for P. The Perdew-Burke-Ernzerhof (PBE) [24] exchange-correlation functional with D3 van-der-Waals corrections[25] was used to obtain the electronic ground state. We used a k grid sampling of $6 \times 6 \times 6$ and a plane-wave-expansion cutoff of 550 eV. The structures were fully relaxed until the residual atomic forces were less than 0.001 eV/Å. From these, monolayer structures were obtained and subsequently relaxed with VASP. We used a $6 \times 6 \times 1$ k grid and fixed the out-of-plane lattice parameter c during the relaxation procedure. To avoid interactions between periodic images, we included a vacuum of at least 22.5 Å in the out-of-plane direction. The POSCAR structure files of the relaxed monolayers are included in the supplementary information.

The rationale for our choice of the functional and van-der-Waals correction was to get a relaxed bulk structure that is as close as possible to experiment. Relaxation with PBE-D3 resulted in a structure closest to experiment while PBE-VV10 with non-local van der Waals corrections[26] gave a structure farthest from experiment among the functionals tested. 1L $CaAs_3$ obtained from the PBE-VV10 relaxed bulk structure and relaxed with PBE-VV10 had a PBE band gap that was 25 % smaller than that of the PBE-D3 structure.

6.2.2 G_0W_0 calculations.

As input for the GW calculation, we computed DFT wavefunctions and eigenvalues with the Quantum Espresso (QE) code [27]. QE band structure calculations were performed for the relaxed monolayer structures with PBE and norm-conserving pseudopotentials [28], using a plane-wave energy cutoff of 116 Ry and k grid of $12 \times 12 \times 1$. We included ten valence and semicore states for Ca and Ba, 15 states for As and five valence states for P. The vacuum included for the QE and subsequent calculations was smaller than during the structural relaxation and was sufficient to contain at least 99% of the charge density in half the unit cell. We neglected spin orbit coupling in our calculations as it was shown by Tang et al. [3] that including relativistic effects changes the band gap by less than 0.01 eV in monolayer $BaAs_3$.

Subsequently, we performed "single-shot" G_0W_0 calculations with the BerkeleyGW software [29, 30, 31]. We employed the generalized plasmon-pole model [29], the static-remainder technique [32], and truncation of the long-range Coulomb interaction [33]. We used a k point sampling of $6 \times 6 \times 1$ and a kinetic energy cutoff of 20 Ry. About 1000 bands were included for the calculation of the dielectric function as well as for the calculation of the self-energy. To speed up the convergence of the quasiparticle band gap with respect to k grid sampling, we employed nonuniform-neck subsampling [34] with 10 radial subpoints. The convergence was tested for the $CaAs_3$ monolayer as a representative material. The quasiparticle band gap at Γ was converged within 0.05 eV with respect to calculations with a kinetic cutoff of 40 Ry and 3000 bands in the summations, and a calculation with a $12 \times 12 \times 1$ k point grid plus 10 subpoints.

To verify our approach, we also calculated the quasiparticle band gaps (not to be confused with the optical band gap where excitonic effects contribute a significant correction) of the parent structures, puckered phosphorene and arsenene, using the same

parameters. We obtained a band gap of 2.02 eV for phosphorene and 1.84 eV for arsenene. The value of phosphorene is in excellent agreement with other theoretical (Qiu, Jornada, and Louie [35]: 2.08 eV, Jornada, Qiu, and Louie [34]: 2.05 eV, Lu et al. [36]: 2.0 eV), and experimental studies (Liang et al. [37] with scanning tunneling spectroscopy: 2.05 eV). For puckered arsenene, experimental quasiparticle gaps are not available and theoretical band gaps vary between 1.54 eV [38], 1.58 eV [39] and 2.16 eV [40]. The discrepancies may, among other factors, be attributed to structural differences, as experimental structures of both 1L and bulk puckered arsenene, which would serve as starting point for DFT calculations, are still lacking.

The G_0W_0 band structure was obtained from Wannier interpolation with the wannier90 package [41]. A comparison of the directly calculated and interpolated PBE band structure is shown in the supplementary information, Figs. S1-S3, to illustrate the accuracy of the interpolation. The wannierization was performed for 100 iterations using random projections with 40 bands (20 valence and 20 conduction bands, each) as input to obtain 40 Wannier functions.

6.2.3 Data analysis.

Crystal structures were visualized with VESTA. [42] The Brillouin zone was visualized with XCrySDen. [43] The partial density of states (pDOS) and the projected charge density were obtained using VASP with the PBE exchange-correlation functional. The potential in vacuum was calculated at the DFT-PBE-D3 level using the vaspkit tool [44]. We note that the vacuum level offset varies depending on the functionals used for structural relaxation. With the PBE-VV10 functional (see above) we obtained absolute midgap levels for 1L $CaAs_3$ of about 0.6 eV lower than with the PBE-D3 functional, which is a difference of 25 %.

We estimated the G_0W_0 band alignment (electron affinity) with respect to vacuum of each monolayer using the band-gap-center approximation [45]

$$E_{\mathrm{EA}} \approx \frac{1}{2}(E_{\mathrm{c}}^{\text{DFT-PBE}} + E_{\mathrm{v}}^{\text{DFT-PBE}}) + \frac{1}{2}E_{\mathrm{g}}^{G_0W_0}, \tag{6.1}$$

which is equivalent to shifting the band edges of the PBE bands by $\pm(E_{\mathrm{g}}^{G_0W_0} - E_{\mathrm{g}}^{\text{DFT-PBE}})/2$. We note that the band-gap-center approximation works well for PBE centers and G_0W_0 gaps, however, it does not hold for results obtained with hybrid functionals [46, 47].

To estimate the heterojunction type (e.g. straddled or staggered gap) between the isolated monolayers, we applied Anderson's electron affinity rule [48]. The electron affinity rule implies that the conduction band offset of a heterojunction can be obtained by aligning the vacuum levels of the two materials forming the junction. In other words, the band alignment is in the unpinned limit; no charge transfer across the junction is considered. It has been confirmed theoretically [16] and experimentally [17] that the band alignment follows the electron affinity rule for vertically stacked heterostructures of transition metal dichalcogenides. This behaviour is attributed to the weak van der Waals bonding across the interface and the absence of dangling bonds in 2D materials [16, 17]. Now, phosphorene and arsenene related materials are expected to have stronger interlayer interactions than transition metal dichalcogenides, which is indicated by the rapid decrease of the band gap with number of layers. Therefore, the heterojunction predictions from the electron affinity rule need to be taken with caution. With interlayer interactions turned on, the band offsets can change due to charge transfer across the layer and band mixing may occur [15, 49].

To estimate the effect of charge transfer and band shifts in a heterojunction, we calculated the band alignment of a basic $CaAs_3/CaP_3$ heterostructure at the PBE level using VASP and pyprocar [50] (see supplementary information Fig. S4-S5). Our results predict that the band gaps and relative band alignments of the monolayers are only slightly affected by creating a heterostructure. Despite charge transfer and weak to moderate hybridization of the conduction bands, the electron affinity rule gives a good estimate of the band alignment of the heterostructure.

6.3 Results and discussion

6.3.1 Structure and bonding.

Figure 6.1(a-c) shows the atomic structure and Brillouin zone of 1L $CaAs_3$ as an example structure of the CaP_3 family. The Ca atom replaces one quarter of the As atoms in the puckered structure of puckered arsenene. 1L CaP_3 and 1L $BaAs_3$ are also shown in Fig 6.1d) and e). 1L CaP_3 and 1L $CaAs_3$ inherit the $\overline{P}1$ space group from the corresponding bulk structures. 1L $BaAs_3$ possesses higher symmetry and belongs to the $C2/m$ space group same as its bulk structure.

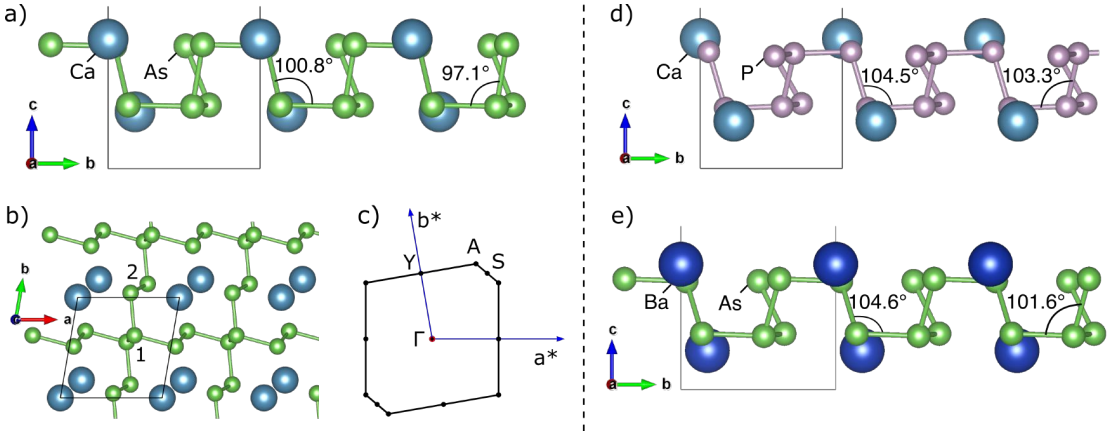

FIGURE 6.1: Structure of $CaAs_3$, CaP_3 and $BaAs_3$ monolayer. a) 1L $CaAs_3$ as a representative compound shows a puckered configuration similar to arsenene where one quarter of As atoms is replaced with Ca, the other As atoms forming a polyanionic network. b) top view of the $CaAs_3$ monolayer. The numbers 1 and 2 refer to two structural types of As atoms (see main text for details) c) Brillouin zone of the $CaAs_3$ monolayer. The structures of monolayer CaP_3 (d) and $BaAs_3$ (e) are added to show the distinct structural distortion of each material.

In pristine arsenene, the As atoms form covalent bonds. For 1L $CaAs_3$, the Ca atom is stabilized by ionic interactions between the Ca cation and the anionic As mesh. [4] We note that one can distinguish between two types of As atoms (see Fig 6.1 b)): As1 which is further away from the Ca atoms, and As2 which is closer to the Ca atoms with As2 having a more negative partial charge than As1. [4] (We note here that atoms belonging to each type are not necessarily symmetrically identical; they are only equivalent for $BaAs_3$). These considerations hold true in analogy for $BaAs_3$ and CaP_3.

6.3.2 Band alignment.

The band alignments of monolayer CaP_3, $CaAs_3$ and $BaAs_3$ obtained from G_0W_0 calculations with the band-gap center approximation are shown in Fig 6.2. The G_0W_0 gaps of 1L CaP_3, $CaAs_3$ and $BaAs_3$ are 2.11 eV, 1.79 eV and 1.50 eV, respectively. Phosphorene ("P_4") and arsenene ("As_4") have been added for comparison. Direct and indirect band gaps are signified by a dark and light blue color, respectively. The band alignment diagram shows that, according to the electron affinity rule, 1L CaP_3, $CaAs_3$ and $BaAs_3$ form type-II (staggered) heterojunctions. Between the pristine monolayers and the compound monolayers, 1L-bP/1L-CaP_3 and 1L-bP/1L-$BaAs_3$ combinations

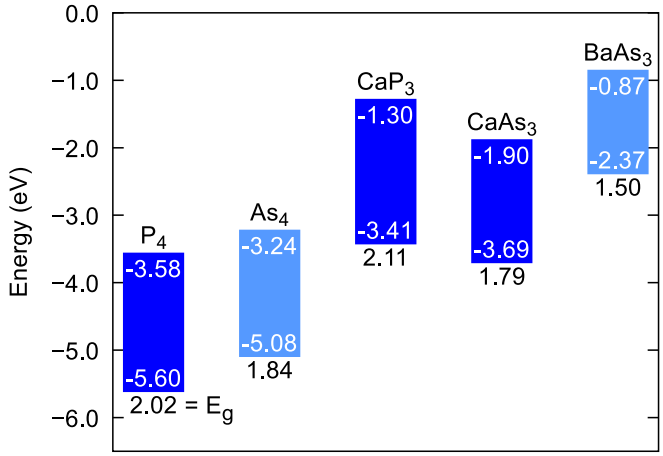

FIGURE 6.2: Band alignment of isolated monolayer CaP_3, $CaAs_3$ and $BaAs_3$ with respect to the vacuum level (0 eV). Band energies and offsets are obtained from G_0W_0 calculations with the band-gap center approximation (Eq. (6.1)). Band gaps and alignment of black phosphorene (P_4) and arsenene (As_4) have been added for reference. Indirect band gaps are indicated by light blue color, direct band gaps correspond to dark blue.

are predicted to have broken-gap band alignment (type III) whereas the other combinations show type-II alignments. Type-II heterojunctions are of interest for solar cell applications because they enable charge separation of photoinduced electrons and holes across the junction [51]. The narrow type-II and type-III alignments of the potential 1L-bP/1L-CaX_3 and 1L-arsenene/1L-CaX_3 (X = As,P) heterojunctions suggest promising material combinations for tunneling field effect transistor applications [52]. Such devices would benefit from the high carrier mobilities predicted for the monolayers of the CaP_3 family as well as from the very easily tunable band gap. We note that for real heterojunctions with enabled interlayer interactions, the band offsets may change due to the following effects: charge transfer across the interface, band mixing, and changes in the band gap [15, 49].

We will now analyze the calculated band alignments in further detail. Looking at the band alignment (Fig. 6.2), it becomes apparent that monolayer CaP_3, $CaAs_3$ and $BaAs_3$ have considerably smaller conduction band offsets with respect to the vacuum level than pure arsenene and phosphorene. Ca and Ba as group-II elements have much lower electron affinities than the group-V elements (As and P) thus leading to a higher energy of the conduction band edge in these compounds. Between monolayer $CaAs_3$ and $BaAs_3$, the midgap of $CaAs_3$ is lower in energy than for $BaAs_3$ (Fig. 6.2). The reason for this energy difference is not apparent at first sight. Therefore, we included a

hypothetical $SrAs_3$ monolayer to analyse the trend. As the alkaline metal atom becomes heavier, the conduction band minimum (CBM) shifts more toward the vacuum level.

To differentiate between effects of the chemical composition and structural effects, we swapped the Ca atoms of the 1L $CaAs_3$ structure with Ba atoms and vice versa *without* a subsequent relaxation of atomic positions or lattice parameters. We found that inserting Ca into the $BaAs_3$ structure shifted the CBM away from the vacuum level. Inserting Ba into the $CaAs_3$ structure shifted the CBM towards the vacuum level. From our data (not shown), we concluded that the band alignment offset between 1L $CaAs_3$ and 1L $BaAs_3$ is half due to structural effects and half due to effects of the chemical composition. Structural differences include a stretching of the puckered structure of 1L $BaAs_3$ within the plane in comparison to 1L $CaAs_3$ as the angles between the As atoms in the puckered mesh are greater for 1L $BaAs_3$. Also, the Ba atoms stick out of the monolayer plane more than the Ca atoms because of their larger atomic radius (compare Fig. 6.1a and Fig. 6.1e).

Interestingly, the band edges of 1L CaP_3 are higher in energy than the ones of 1L $CaAs_3$ although the midgap energy of phosphorene is lower than that of arsenene (see Fig 6.2). Swapping P for As in 1L $CaAs_3$ and As for P in 1L CaP_3 did not affect the band offset with respect to the vacuum level much. Thus we can conclude that the offset of the band edges is less influenced by the pnictogen and is likely caused by structural distortions. For example, the P-P bond length of 2.22 Å on average in 1L CaP_3 is much shorter than the As-As bond in 1L $CaAs_3$ with 2.50 Å and, as a result, the Ca atoms "stick out" of the monolayer much more than in 1L $CaAs_3$ (see Fig 6.1 d). The puckered mesh also shows larger angles than in 1L $CaAs_3$.

6.3.3 Electronic structure, the effect of p-d interactions.

We further explore and analyze the band structure and projected density of states (pDOS), pointing to trends from chemical bonding analysis. The PBE and G_0W_0 band structures of 1L CaP_3, 1L $CaAs_3$ and 1L $BaAs_3$ obtained by Wannier interpolation are shown in Fig 6.3. 1L CaP_3 and 1L $CaAs_3$ have a direct band gap at Γ while the band gap of 1L $BaAs_3$ is indirect with the conduction band minimum (CBM) between S and Γ . The valence band of the G_0W_0 band structure shows slightly less dispersion than that of the PBE band structure. The stronger dispersion of the PBE band structure is due to the underestimation of the band gap, which is consistent with the trend for other semiconductors [53] and can be rationalized in terms of a $k \cdot p$ theory that predicts $m^* \propto E_g$

scaling (see Ref. [54], p. 71). Apart from the dispersion, the band gap correction is the only noticeable difference between the band structures obtained with PBE and G_0W_0. The pDOS shows that the valence band edge is almost entirely composed of As $4p$ or P $3p$ orbitals, with the type 2 atoms (adjacent to cations) making up the major part. The conduction band edge is again primarily composed of As $4p$ (P $3p$) states, As $4s$ (P $3s$) and metal d states.

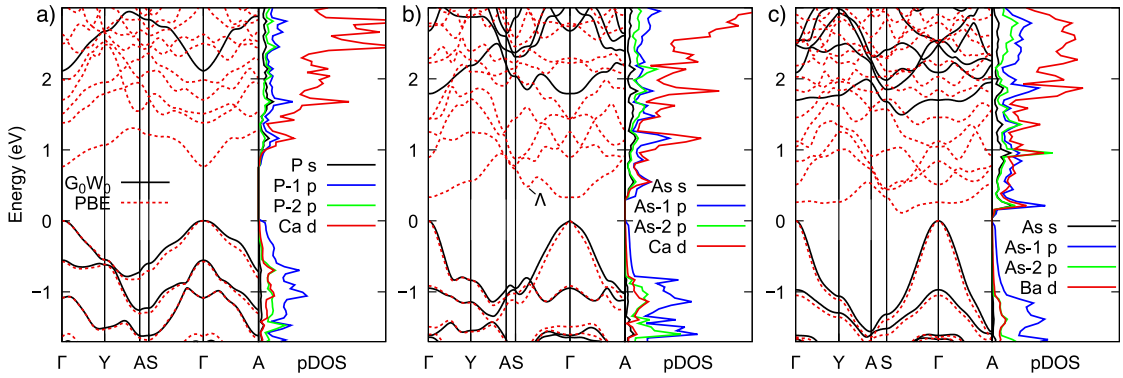

FIGURE 6.3: GW and PBE band structures from Wannier interpolation and projected density of states (pDOS) of a) monolayer CaP_3, b) monolayer $CaAs_3$ and c) monolayer $BaAs_3$. The Λ valley becomes the conduction band minimum for $BaAs_3$.

We next discuss the indirect nature of the band gap in 1L $BaAs_3$ versus the direct band gap in 1L $CaAs_3$. An interesting feature in the band structure of 1L $CaAs_3$ is the local CBM between S and Γ at $k_x = 1/3, k_y = 1/3, k_z = 0$ which we shall call Λ (see Fig 6.3b). The same valley (Λ) is the global CBM for 1L $BaAs_3$. We want to shed light on why the Λ valley is more stable with respect to the Γ valley in 1L $BaAs_3$ but not in 1L $CaAs_3$.

To that end, we analysed the orbital composition of the two valleys and then classified the interaction between the orbitals into bonding and antibonding by looking at the spatial distribution of the projected charge densities. From the pDOS we know that the valence band edge is almost entirely composed of As-2 $4p$ orbitals. Figure 6.4 a) shows the projected charge density of the topmost valence band at the Γ point for 1L $CaAs_3$. The charge density distribution shows a clear p character with lobes of adjacent atoms avoiding each other. This suggests that the p-p interaction is antibonding. The conduction band edge (CBE) is mainly composed of As $4p$, As $4s$ and metal d states. The projected charge density of the conduction band edge at Λ) for 1L $CaAs_3$ is shown in Fig 6.4 c). The As-2 $4p$ - Ca $3d$ orbital contributions are hybridized and appear as lobes of charge density in 6.4 c) (see also Fig. S6 of the supplementary information). From

the spatial distribution of the charge density we can infer that the hybridized As-2 $4p$ - Ca $3d$ states at the CBE interact in a bonding fashion, while As-1 states are not involved. The same holds true for $BaAs_3$ (see Fig. S7-S8 of the supplementary information).

In addition to analyzing the projected charge density, crystal orbital Hamilton population (COHP) bonding analysis was performed with LOBSTER[55, 56, 57, 58], which proved helpful to confirm the general picture of the antibonding nature at the valence and conduction band edges. However, the LOBSTER results are not shown because the current basis sets cannot project the empty d states of Ca and Ba. The COHP analysis of the parent structures, arsenene and phosphorene, also clearly shows the antibonding nature of the p-p interaction at the valence and conduction band edge (see supporting information, Fig. S10-S11).

With the results of the bonding analysis we can create a schematic diagram of the coupling between As orbitals and Ca and Ba d orbitals as shown in Figure 6.4 b), d). In comparison with the Γ valley, the Λ valley of the conduction band has higher contributions of As s and metal d orbitals. For example, the conduction band of 1L $BaAs_3$ (1L $CaAs_3$) at Λ is composed of 15.0% Ba $5d$ (16% Ca $3d$) orbitals while the Γ valley is composed of only 6% Ba $5d$ (7% Ca $3d$). Because the p-d interaction is of bonding nature, we can expect the state at Λ to be stabilized, i.e., lower in energy with increasing d orbital contribution. However, this alone does not provide an explanation for why the band gap is indirect for 1L $BaAs_3$ but not for 1L $CaAs_3$.

The indirect band gap of 1L $BaAs_3$ can be attributed to an *increase* in the strength of the p-d interaction from 1L $CaAs_3$ to 1L $BaAs_3$: The Ba $5d$ orbital is more delocalized than the Ca $3d$ orbital because the electrons in the $5d$ orbital experience stronger screening from the nuclear charge. Thus, the Ba $5d$ states can hybridise more strongly with As $4p$ orbitals than Ca $3d$. As a result, the stronger bonding d-p interactions in 1L $BaAs_3$ stabilize the Λ valley CB state more than the weaker interaction in 1L $CaAs_3$. This more pronounced energy shift leads to an indirect band gap in 1L $BaAs_3$. Checking the conduction band dispersion of a hypothetical 1L $SrAs_3$ (data not shown), we find a trend of the Λ valley energy decreasing with respect to Γ from the $n = 3$ to the $n = 5$ shell, i.e. from Ca $3d$ over Sr $4d$ to Ba $5d$, which strengthens the p-d interaction argument.

Next, we compare the band structures of monolayer $CaAs_3$ and CaP_3 (Fig. 6.3). The conduction band of 1L CaP_3 shows a stronger dispersion than that of 1L $CaAs_3$, which is consistent with the prediction of high electron mobilities in 1L CaP_3[5]. 1L CaP_3 has a

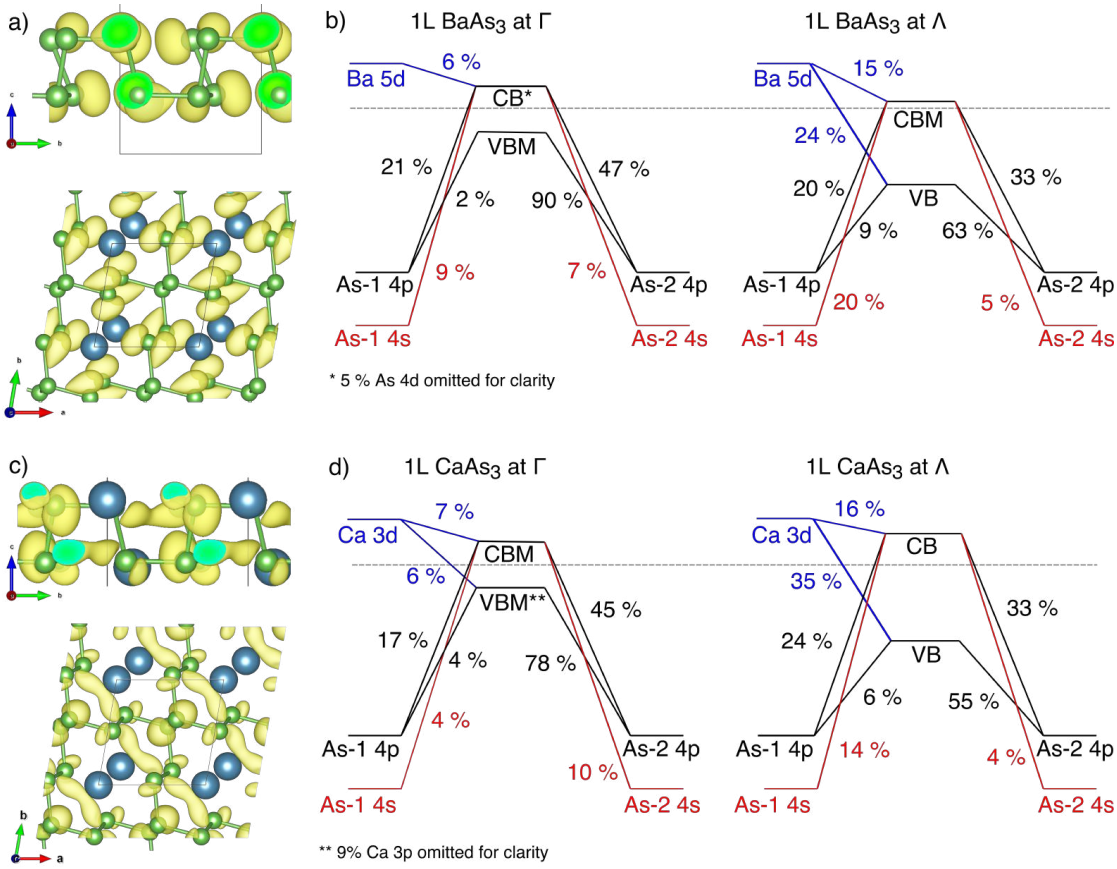

FIGURE 6.4: Orbital coupling in 1L $CaAs_3$ and 1L $BaAs_3$. a) Band and k point projected charge density of 1L $CaAs_3$ for the valence band at the Γ point. The isosurface is set at 0.004 e/Å^3. c) Band and k point projected charge density for the conduction bands at the Λ point. Isosurface: 0.004 e/Å^3. b) and d) show schematics of the orbital coupling at the Γ and Λ points for 1L $BaAs_3$ and 1L $CaAs_3$, respectively.

larger band gap than $CaAs_3$. Interestingly, 1L CaP_3 does not show any local CBM at Λ between Γ and S. And this despite the fact that the Ca 3d orbitals contribute about 53 % of the CB state at Λ, which is significantly more than for 1L $CaAs_3$. We attribute this difference in orbital composition and electronic structure to the increased asymmetry of the 1L CaP_3 structure. The lattice parameter $a = 5.71$ Å is larger than $b = 5.56$ Å, whereas for 1L $CaAs_3$ the parameters are almost identical with $a \approx b \approx 5.97$ Å. This distortion leads to considerable differences in the projected charge density at the band edges for 1L CaP_3 (see supplementary information, Fig. S9).

Finally, we would like to note a similarity between the electronic structure of 1L CaP_3, $CaAs_3$, $BaAs_3$ and that of hybrid halide perovskites. Specifically, both the top

of the valence band and bottom of the conduction band are dominated by *antibonding* orbitals [59, 60]. Defect tolerance properties inherent to hybrid halide perovskites are attributed to this feature [61, 62, 63]. Thus, we can anticipate 1L CaP_3, $CaAs_3$ and $BaAs_3$ to exhibit a similar tolerance to native defects since states associated with dangling bonds are expected to appear within the bulk of valence or conduction band states rather than in the band gap.

6.4 Conclusion

In this work, we calculated the band alignment of puckered CaP_3, $CaAs_3$ and $BaAs_3$ monolayer at the G_0W_0 level of theory for the isolated monolayers according to the electron affinity rule. Our calculations suggest that monolayer CaP_3, $CaAs_3$ and $BaAs_3$ all form type-II (staggered) heterojunctions which makes them suitable candidates for solar cell applications. Their quasiparticle gaps are 2.1 (direct), 1.8 (direct) and 1.5 eV (indirect), respectively. The differences in alignment with respect to the vacuum potential (i.e. the conduction band offsets) result from the different degree of relative stretching of the As or P anionic mesh upon insertion of the Ca or Ba ions. We also discussed trends in the electronic structure in the light of chemical bonding analysis. We found that the indirect band gap in $BaAs_3$ is caused by relatively strong As $3p$ - Ba $5d$ bonding interactions that stabilize the conduction band at Λ. Our study demonstrates the effect of structural distortion and orbital interactions on the theoretical band alignment of CaP_3, $CaAs_3$ and $BaAs_3$. These insights give guidance for future development of 2D heterojunctions based on phosphorene-like materials.

Supplementary information/Appendix

Electronic Supplementary Information (ESI) available: VASP structure files (POSCAR). Band structures plotted from Wannier functions versus band structures along a k-path from DFT (Fig. S1-S3). Band alignment of a $CaAs_3/CaP_3$ heterostructure (Fig. S4-S5). Projected charge density of monolayer $CaAs_3$, monolayer $BaAs_3$ and monolayer CaP_3 (Fig. S6-S9). COHP analysis for puckered arsenene and phosphorene (Fig. S10-S11). See Appendix C.

Acknowledgements

The authors acknowledge funding provided by the Natural Sciences and Engineering Research Council of Canada under the Discovery Grant Programs RGPIN-2020-04788. Calculations were performed using the Compute Canada infrastructure supported by the Canada Foundation for Innovation under John R. Evans Leaders Fund.

References

[1] Likai Li et al. "Black phosphorus field-effect transistors". In: *Nat. Nanotechnol.* 9.5 (May 2014), pp. 372–377. ISSN: 1748-3395. DOI: 10.1038/nnano.2014.35.

[2] Vy Tran et al. "Layer-controlled band gap and anisotropic excitons in few-layer black phosphorus". In: *Phys. Rev. B* 89.23 (June 2014), p. 235319. ISSN: 1098-0121, 1550-235X. DOI: 10.1103/PhysRevB.89.235319.

[3] Ping Tang et al. "$BaAs_3$: a narrow gap 2D semiconductor with vacancy-induced semiconductor–metal transition from first principles". In: *J. Mater. Sci.* 54.19 (Oct. 2019), pp. 12676–12687. ISSN: 1573-4803. DOI: 10.1007/s10853-019-03796-y.

[4] Feng Li et al. "Tunable topological state, high hole-carrier mobility, and prominent sunlight absorbance in monolayered calcium triarsenide". In: *J. Phys. Chem. Lett.* 10.4 (Feb. 2019), pp. 761–767. ISSN: 1948-7185. DOI: 10.1021/acs.jpclett.9b00033.

[5] Ning Lu et al. "CaP_3: A new two-dimensional functional material with desirable band gap and ultrahigh carrier mobility". In: *J. Phys. Chem. Lett.* 9.7 (Apr. 2018), pp. 1728–1733. ISSN: 1948-7185. DOI: 10.1021/acs.jpclett.8b00595.

[6] Yu Jing et al. "GeP_3: A small indirect band gap 2D crystal with high carrier mobility and strong interlayer quantum confinement". In: *Nano Lett.* 17.3 (Mar. 2017), pp. 1833–1838. ISSN: 1530-6984. DOI: 10.1021/acs.nanolett.6b05143.

[7] Abdul Jalil et al. "A phosphorene-like InP_3 monolayer: structure, stability, and catalytic properties toward the hydrogen evolution reaction". In: *J. Mater. Chem. A* 8.3 (2020), pp. 1307–1314. DOI: 10.1039/C9TA08612A.

[8] Naihua Miao et al. "Tunable magnetism and extraordinary sunlight absorbance in indium triphosphide monolayer". In: *J. Am. Chem. Soc.* 139.32 (2017), pp. 11125–11131.

[9] Hong-Yao Liu et al. "Two-dimensional BiP_3 with high carrier mobility and moderate band gap for hydrogen generation from water splitting". In: *Appl. Surf. Sci.* 501 (Jan. 2020), p. 144263. ISSN: 0169-4332. DOI: 10.1016/j.apsusc.2019.144263.

[10] Gautam Gaddemane et al. "Theoretical studies of electronic transport in monolayer and bilayer phosphorene: A critical overview". In: *Phys. Rev. B* 98.11 (Sept. 2018), p. 115416. ISSN: 2469-9950, 2469-9969. DOI: 10.1103/PhysRevB.98.115416.

[11] Long Cheng, Chenmu Zhang, and Yuanyue Liu. "Why two-dimensional semiconductors generally have low electron mobility". In: *Phys. Rev. Lett.* 125.17 (Oct. 2020), p. 177701. DOI: 10.1103/PhysRevLett.125.177701.

[12] Alejandro J. Garza and Gustavo E. Scuseria. "Predicting band gaps with hybrid density functionals". In: *J. Phys. Chem. Lett.* 7.20 (Oct. 2016), pp. 4165–4170. ISSN: 1948-7185. DOI: 10.1021/acs.jpclett.6b01807.

[13] Falco Hüser, Thomas Olsen, and Kristian S. Thygesen. "Quasiparticle GW calculations for solids, molecules, and two-dimensional materials". In: *Phys. Rev. B* 87.23 (June 2013), p. 235132. ISSN: 1098-0121, 1550-235X. DOI: 10.1103/PhysRevB.87.235132.

[14] Hong Jiang. "Electronic band structures of molybdenum and tungsten dichalcogenides by the GW approach". In: *J. Phys. Chem. C* 116.14 (Apr. 2012), pp. 7664–7671. ISSN: 1932-7447. DOI: 10.1021/jp300079d.

[15] Daniel S. Koda et al. "Trends on band alignments: Validity of Anderson's rule in SnS_2- and $SnSe_2$-based van der Waals heterostructures". In: *Phys. Rev. B* 97.16 (Apr. 2018), p. 165402. DOI: 10.1103/PhysRevB.97.165402.

[16] Yuzheng Guo and John Robertson. "Band engineering in transition metal dichalcogenides: Stacked versus lateral heterostructures". In: *Appl. Phys. Lett.* 108.23 (June 2016), p. 233104. ISSN: 0003-6951, 1077-3118. DOI: 10.1063/1.4953169.

[17] Ming-Hui Chiu et al. "Band alignment of 2D transition metal dichalcogenide heterojunctions". In: *Adv. Funct. Mater.* 27.19 (2017), p. 1603756. ISSN: 1616-3028. DOI: 10.1002/adfm.201603756.

[18] W. Bauhofer, M. Wittmann, and H. G. v. Schnering. "Structure, electrical and magnetic properties of $CaAs_3$, $SrAs_3$, $BaAs_3$ and $EuAs_3$". In: *J. Phys. Chem. Solids* 42.8 (Jan. 1981), pp. 687–695. ISSN: 0022-3697. DOI: 10.1016/0022-3697(81)90122-0.

[19] W. Dahlmann and H. G. v. Schnering. "CaP_3, ein neues Calciumphosphid". In: *Naturwissenschaften* 60.11 (Nov. 1973), pp. 518–518. ISSN: 1432-1904. DOI: 10.1007/BF00603256.

[20] G. Kresse and J. Furthmüller. "Efficient iterative schemes for ab initio total-energy calculations using a plane-wave basis set". In: *Phys. Rev. B* 54.16 (Oct. 1996), pp. 11169–11186. DOI: 10.1103/PhysRevB.54.11169.

[21] G. Kresse and J. Furthmüller. "Efficiency of ab-initio total energy calculations for metals and semiconductors using a plane-wave basis set". In: *Comput. Mater. Sci.* 6.1 (July 1996), pp. 15–50. ISSN: 0927-0256. DOI: 10.1016/0927-0256(96)00008-0.

[22] P. E. Blöchl. "Projector augmented-wave method". In: *Phys. Rev. B* 50.24 (Dec. 1994), pp. 17953–17979. DOI: 10.1103/PhysRevB.50.17953.

[23] G. Kresse and D. Joubert. "From ultrasoft pseudopotentials to the projector augmented-wave method". In: *Phys. Rev. B* 59.3 (Jan. 1999), pp. 1758–1775. DOI: 10.1103/PhysRevB.59.1758.

[24] John P. Perdew, Kieron Burke, and Matthias Ernzerhof. "Generalized gradient approximation made simple". In: *Phys. Rev. Lett.* 77.18 (Oct. 1996), pp. 3865–3868. DOI: 10.1103/PhysRevLett.77.3865.

[25] Stefan Grimme et al. "A consistent and accurate ab initio parametrization of density functional dispersion correction (DFT-D) for the 94 elements H-Pu". In: *J. Chem. Phys.* 132.15 (Apr. 2010), p. 154104. ISSN: 0021-9606. DOI: 10.1063/1.3382344.

[26] Oleg A. Vydrov and Troy Van Voorhis. "Nonlocal van der Waals density functional: The simpler the better". In: *The Journal of Chemical Physics* 133.24 (Dec. 2010), p. 244103. ISSN: 0021-9606. DOI: 10.1063/1.3521275. URL: https://aip.scitation.org/doi/abs/10.1063/1.3521275 (visited on 04/27/2018).

[27] Paolo Giannozzi et al. "QUANTUM ESPRESSO: a modular and open-source software project for quantum simulations of materials". In: *J. Phys. : Condens. Matter.* 21.39 (Sept. 2009), p. 395502. ISSN: 0953-8984. DOI: 10.1088/0953-8984/21/39/395502.

[28] M. J. van Setten et al. "The PseudoDojo: Training and grading a 85 element optimized norm-conserving pseudopotential table". In: *Comput. Phys. Commun.* 226 (May 2018), pp. 39–54. ISSN: 0010-4655. DOI: 10.1016/j.cpc.2018.01.012.

[29] Mark S. Hybertsen and Steven G. Louie. "Electron correlation in semiconductors and insulators: Band gaps and quasiparticle energies". In: *Phys. Rev. B* 34.8 (Oct. 1986), pp. 5390–5413. ISSN: 0163-1829. DOI: 10.1103/PhysRevB.34.5390.

[30] Michael Rohlfing and Steven G. Louie. "Electron-hole excitations and optical spectra from first principles". In: *Phys. Rev. B* 62.8 (Aug. 2000), pp. 4927–4944. DOI: 10.1103/PhysRevB.62.4927.

[31] Jack Deslippe et al. "BerkeleyGW: A massively parallel computer package for the calculation of the quasiparticle and optical properties of materials and nanostructures". In: *Comput. Phys. Commun.* 183.6 (June 2012), pp. 1269–1289. ISSN: 0010-4655. DOI: 10.1016/j.cpc.2011.12.006.

[32] Jack Deslippe et al. "Coulomb-hole summations and energies for GW calculations with limited number of empty orbitals: A modified static remainder approach". In: *Phys. Rev. B* 87.16 (Apr. 2013), p. 165124. DOI: 10.1103/PhysRevB.87.165124.

[33] Sohrab Ismail-Beigi. "Truncation of periodic image interactions for confined systems". In: *Phys. Rev. B* 73.23 (June 2006), p. 233103. DOI: 10.1103/PhysRevB.73.233103.

[34] Felipe H. da Jornada, Diana Y. Qiu, and Steven G. Louie. "Nonuniform sampling schemes of the Brillouin zone for many-electron perturbation-theory calculations in reduced dimensionality". In: *Phys. Rev. B* 95.3 (Jan. 2017), p. 035109. DOI: 10.1103/PhysRevB.95.035109.

[35] Diana Y. Qiu, Felipe H. da Jornada, and Steven G. Louie. "Environmental screening effects in 2D materials: Renormalization of the bandgap, electronic structure, and optical spectra of few-layer black phosphorus". In: *Nano Lett.* 17.8 (Aug. 2017), pp. 4706–4712. ISSN: 1530-6984. DOI: 10.1021/acs.nanolett.7b01365.

[36] Junpeng Lu et al. "Light–matter interactions in phosphorene". In: *Acc. Chem. Res.* 49.9 (Sept. 2016), pp. 1806–1815. ISSN: 0001-4842, 1520-4898. DOI: 10.1021/acs.accounts.6b00266.

[37] Liangbo Liang et al. "Electronic bandgap and edge reconstruction in phosphorene materials". In: *Nano Lett.* 14.11 (Nov. 2014), pp. 6400–6406. ISSN: 1530-6984. DOI: 10.1021/nl502892t.

[38] Huabing Shu and Jiyuan Guo. "Electronic and optical properties of phosphorene-like arsenic phosphorus: a many-body study". In: *Mater. Res. Express* 5.3 (Mar. 2018), p. 036302. ISSN: 2053-1591. DOI: 10.1088/2053-1591/aaace5.

[39] D. Kecik, E. Durgun, and S. Ciraci. "Stability of single-layer and multilayer arsenene and their mechanical and electronic properties". In: *Phys. Rev. B* 94.20 (Nov. 2016), p. 205409. DOI: 10.1103/PhysRevB.94.205409.

[40] Xianghong Niu et al. "Arsenene-based heterostructures: highly efficient bifunctional materials for photovoltaics and photocatalytics". In: *ACS Appl. Mater. Interfaces* 9.49 (Dec. 2017), pp. 42856–42861. ISSN: 1944-8244, 1944-8252. DOI: 10.1021/acsami.7b14842.

[41] Arash A. Mostofi et al. "An updated version of wannier90: A tool for obtaining maximally-localised Wannier functions". In: *Comput. Phys. Commun.* 185.8 (Aug. 2014), pp. 2309–2310. ISSN: 0010-4655. DOI: 10.1016/j.cpc.2014.05.003.

[42] Koichi Momma and Fujio Izumi. "VESTA 3 for three-dimensional visualization of crystal, volumetric and morphology data". In: *J. Appl. Crystallogr.* 44.6 (2011), pp. 1272–1276. DOI: 10.1107/S0021889811038970.

[43] Anton Kokalj. "XCrySDen—a new program for displaying crystalline structures and electron densities". In: *J. Mol. Graph. Model.* 17.3 (June 1999), pp. 176–179. ISSN: 1093-3263. DOI: 10.1016/S1093-3263(99)00028-5.

[44] Vei Wang et al. "VASPKIT: A User-friendly Interface Facilitating High-throughput Computing and Analysis Using VASP Code". In: (2020). arXiv: 1908.08269 [cond-mat.mtrl-sci].

[45] Yufeng Liang et al. "Quasiparticle band-edge energy and band offsets of monolayer of molybdenum and tungsten chalcogenides". In: *Appl. Phys. Lett.* 103.4 (July 2013), p. 042106. ISSN: 0003-6951, 1077-3118. DOI: 10.1063/1.4816517.

[46] Zhiming M. Wang, ed. *MoS2: Materials, Physics, and Devices*. en. Vol. 21. Lecture Notes in Nanoscale Science and Technology. Cham: Springer International Publishing, 2014. ISBN: 978-3-319-02849-1 978-3-319-02850-7. DOI: 10.1007/978-3-319-02850-7.

[47] Amine Slassi et al. "Interlayer bonding in two-dimensional materials: The special case of SnP_3 and GeP_3". In: *J. Phys. Chem. Lett.* 11.11 (June 2020), pp. 4503–4510. DOI: 10.1021/acs.jpclett.0c00780.

[48] R. L. Anderson. "Germanium-gallium arsenide heterojunctions [Letter to the Editor]". In: *IBM J. Res. Dev.* 4.3 (July 1960), pp. 283–287. ISSN: 0018-8646. DOI: 10.1147/rd.43.0283.

[49] Daniel S. Koda et al. "Tuning electronic properties and band alignments of phosphorene combined with $MoSe_2$ and WSe_2". In: *J. Phys. Chem. C* 121.7 (Feb. 2017), pp. 3862–3869. ISSN: 1932-7447. DOI: 10.1021/acs.jpcc.6b10976.

[50] Uthpala Herath et al. "PyProcar: A Python library for electronic structure pre/post-processing". In: *Computer Physics Communications* 251 (2020), p. 107080. ISSN: 0010-4655. DOI: https://doi.org/10.1016/j.cpc.2019.107080. URL: http://www.sciencedirect.com/science/article/pii/S0010465519303935.

[51] Deep Jariwala et al. "Van der Waals materials for atomically-thin photovoltaics: Promise and outlook". In: *ACS Photonics* 4.12 (Dec. 2017), pp. 2962–2970. ISSN: 2330-4022, 2330-4022. DOI: 10.1021/acsphotonics.7b01103.

[52] Yawei Lv et al. "Recent advances in low-dimensional heterojunction-based tunnel field effect transistors". In: *Adv. Electron. Mater.* 5.1 (2019), p. 1800569. ISSN: 2199-160X. DOI: 10.1002/aelm.201800569.

[53] Oleg Rubel et al. "Perturbation approach to ab initio effective mass calculations". In: *Comput. Phys. Commun.* (2020), p. 107648. DOI: 10.1016/j.cpc.2020.107648.

[54] Peter Y. Yu and Manuel Cardona. *Fundamentals of Semiconductors*. Graduate Texts in Physics. Berlin, Heidelberg: Springer Berlin Heidelberg, 2010. ISBN: 978-3-642-00709-5 978-3-642-00710-1. DOI: 10.1007/978-3-642-00710-1.

[55] Ryky Nelson et al. "LOBSTER: Local orbital projections, atomic charges, and chemical-bonding analysis from projector-augmented-wave-based density-functional theory". In: *J. Comput. Chem.* 41.21 (2020), pp. 1931–1940. ISSN: 1096-987X. DOI: 10.1002/jcc.26353.

[56] Volker L. Deringer, Andrei L. Tchougréeff, and Richard Dronskowski. "Crystal orbital Hamilton population (COHP) analysis as projected from plane-wave basis sets". In: *J. Phys. Chem. A* 115.21 (June 2011), pp. 5461–5466. ISSN: 1089-5639, 1520-5215. DOI: 10.1021/jp202489s.

[57] Stefan Maintz et al. "Analytic projection from plane-wave and PAW wavefunctions and application to chemical-bonding analysis in solids". In: *J. Comput. Chem.* 34.29 (Nov. 2013), pp. 2557–2567. ISSN: 0192-8651. DOI: 10.1002/jcc.23424.

[58] Richard Dronskowski and Peter E. Bloechl. "Crystal orbital Hamilton populations (COHP): energy-resolved visualization of chemical bonding in solids based on

density-functional calculations". In: *J. Phys. Chem.* 97.33 (Aug. 1993), pp. 8617–8624. ISSN: 0022-3654, 1541-5740. DOI: 10.1021/j100135a014.

[59] T. Umebayashi et al. "Electronic structures of lead iodide based low-dimensional crystals". In: *Phys. Rev. B* 67.15 (Apr. 2003), p. 155405. DOI: 10.1103/PhysRevB.67.155405.

[60] Shuxia Tao et al. "Absolute energy level positions in tin- and lead-based halide perovskites". In: *Nat. Commun.* 10.1 (June 2019), p. 2560. ISSN: 2041-1723. DOI: 10.1038/s41467-019-10468-7.

[61] Jongseob Kim et al. "The role of intrinsic defects in methylammonium lead iodide perovskite". In: *J. Phys. Chem. Lett.* 5.8 (Apr. 2014), pp. 1312–1317. DOI: 10.1021/jz500370k.

[62] Wan-Jian Yin, Tingting Shi, and Yanfa Yan. "Unusual defect physics in $CH_3NH_3PbI_3$ perovskite solar cell absorber". In: *Appl. Phys. Lett.* 104.6 (Feb. 2014), p. 063903. ISSN: 0003-6951. DOI: 10.1063/1.4864778.

[63] Chao Zheng et al. "Electronic properties of Pb-I deficient lead halide perovskites". In: *J. Chem. Phys.* 151.23 (Dec. 2019), p. 234704. ISSN: 0021-9606. DOI: 10.1063/1.5127513.

Chapter 7

Importance of the nonlocal exchange potential for effective mass calculations in semiconductors: Benchmarking exchange-correlation potentials with the mstar60 dataset

Author contributions:

Oleg Rubel conceived the idea and performed test system calculations. I created the dataset and conducted the main part of the calculations and data analysis. Oleg Rubel performed the Wien2k calculations and analysis. The manuscript was written by me and revised by Oleg Rubel. The project was supervised by Oleg Rubel.

This chapter is submitted to a peer-reviewed journal.

The supplementary information is available in Appendix D.

Abstract

The effective mass is an indicator of the carrier mobility, conductivity and the thermoelectric figure of merit and thus an important parameter in materials design and selection. The accuracy of effective masses predicted by density functional theory depends on the exchange-correlation functional employed, with nonlocal hybrid functionals giving more accurate results than semilocal functionals. In this article, we benchmark the performance of the Perdew–Burke–Ernzerhof, Tran-Blaha modified Becke-Johnson, and the hybrid Heyd-Scuseria-Ernzerhof (HSE) exchange-correlation functionals and potentials to calculate effective masses with perturbation theory. We introduce the `mstar60` dataset which contains 60 effective masses derived from 18 semiconductors. We reveal that the nonlocal exchange in HSE enlarges the optical transition matrix elements leading to the superior accuracy of HSE in the calculation of effective masses. The omission of nonlocal exchange in the transition operator for HSE leads to serious errors. For the semilocal PBE functional, the errors introduced by underestimation of the band gap and of the optical transition matrix elements partially cancel out for the calculation of effective masses. We then compare effective masses of transition metal dichalcogenide bulk and monolayer materials: we show that changes in the matrix elements are important in understanding the layer-dependent effective mass renormalization.

7.1 Introduction

The effective mass is an important parameter in materials design and selection. It serves as an indicator of the carrier mobility, conductivity and the thermoelectric figure of merit and is often included in high-throughput computational material studies [1, 2, 3, 4, 5]. The effective mass can be obtained from experimental measurements such as cyclotron resonance, Shubnikov-de-Haas oscillations and angle-resolved photoemission spectroscopy (ARPES).

The effective mass m^* is inversely proportional to the energy band dispersion. In the nearly-free electron model, the energy dispersion of a free electron is described by a parabola: $E = \hbar^2 k^2/(2m_0)$. In crystalline materials, the electron is no longer free as it interacts with the periodic potential of the ionic lattice. To describe the energy dispersion of the nearly free electron near a band maximum or minimum of interest in crystalline materials, particularly semiconductors, the mass of the electron m_0 in the

parabola is replaced by an effective mass m^* that acts as a scaling term to adjust the band curvature.

The standard procedure for theoretically calculating the effective mass is to fit the band of interest with a parabola or hyperbola and obtain the effective mass from the curvature. An elegant alternative is to use perturbation theory. From perturbation theory, we calculate the inverse effective mass $(m^*_{\alpha\beta,n})^{-1}$ for non-degenerate bands at a certain k-point as the following [6, Appendix E]

$$\frac{m_0}{m^*_{\alpha\beta,n}} = \delta_{\alpha\beta} + \frac{1}{m_0} \sum_{l \neq n} \frac{p^{(\alpha)}_{nl} p^{(\beta)}_{ln} + p^{(\beta)}_{nl} p^{(\alpha)}_{ln}}{E_n - E_l}, \tag{7.1}$$

where m_0 is the electron rest mass, α and β indicate directions in Cartesian coordinates (x, y, z), $\delta_{\alpha\beta}$ is the Kronecker delta, the summation is over the band index l but excludes the band of interest n. E_n and E_l denote the band energies and p_{ln} the optical transition matrix element. The k point index is omitted for simplicity.

This equation helps us to develop some intuition about the factors influencing the effective mass: The larger the interband energy difference term $E_n - E_l$, the less the interaction between the bands contributes to the band dispersion. As a result, the larger the band gap the heavier is normally the effective mass. The larger the matrix element term (the numerator of the sum), the larger the contribution to the band curvature will be. Also, the wavefunctions of two bands can only couple if symmetry selection rules are fulfilled. Otherwise, the transition is not allowed and the matrix element p_{ln} is zero [7, chap. 2.6.1]. For interatomic transitions, i.e. from cation to anion, the effect of the matrix element on the band curvature can be understood in the tight-binding framework [8, 1, 9] and [7, chap. 2.7]. The squared matrix element describes the probability of the transition and is thus related to the two-center hopping or overlap integral of tight-binding theory. Increased overlap between neighboring orbitals leads to greater band dispersion. We should also note that bands lower in energy than n make a positive contribution to the band curvature, while bands higher in energy than n make a negative contribution due to the negative energy difference [7, chap. 2.6.1].

The effective mass of charge carriers can be predicted with density functional theory (DFT) [10] which is a ground-state theory. Still, DFT is commonly used to calculate excited state properties. Density functional approximations using semilocal exchange-correlation (XC) energy functionals such as the local density or generalized gradient

approximation (LDA or GGA) are known to underestimate the band gap of semiconductors significantly [11, chaps. 6.3.1, 9.2.4]. This leads to errors in the band curvature and effective masses. Corrections from many-body theory change the band dispersion [11, chap. 16.1.3] and thus also cause an effective mass renormalization for many materials.

The most obvious renormalization after the band gap correction comes from a relative change in the interband energy difference term $E_n - E_l$ in Eq. (7.1). This has recently been illustrated for InSe with LDA and *GW* calculations, where Li and Giustino [12] showed that the out-of-plane electron effective mass was corrected three times more strongly than the in-plane mass for quasiparticles calculations. This effect was explained by symmetry selection rules that ruled out a transition matrix element p_{cv} between conduction and the valence band edge for the in-plane mass thus engaging deeper valence states ($p_{c,v-1}$) whose energy position relative to the conduction band edge is less affected by the correction of the fundamental band gap. However, what remains overlooked in Ref. [12] is that not only the band gap but also the p_{ln} matrix elements are renormalized as we transition from LDA to a higher level of theory. The latter will be a central topic of this paper.

To predict more accurate effective masses with DFT we should first find ways to inexpensively correct the band gap. This can be done using the semilocal Tran-Blaha modified Becke-Johnson exchange-correlation potential (TB-mBJ) [13, 14]. Interestingly, effective masses obtained with TB-mBJ are consistently heavier than the experimental result [8, 15, 16, 17]. The more expensive hybrid functionals used to correct the band gap, on the other hand, also result in excellent agreement of effective masses with experiment [8]. Kim et al. [8] alluded that to obtain correct effective masses, corrections beyond a semilocal potential will ultimately be required. If the band gap is almost correct in TB-mBJ, then the transition matrix element must be underestimated. The role of the matrix element p_{ln} for the renormalization of calculated effective masses has not yet been investigated in detail.

In this work, we benchmark the accuracy of effective masses calculated with several exchange-correlation potentials for a new dataset that we call `mstar60`. Our dataset comprises standard sp-semiconductors, d-semiconductors and monolayer materials. Effective masses are calculated with a perturbation theory approach. We show the extent of renormalization of effective masses caused by changes in the transition matrix elements. We explain the role of the nonlocal exchange potential V_x^{NL} concerning these renormalization effects. On average 30% heavier masses are predicted with the hybrid

functional if incorrect transition matrix elements — that do not include V_x^{NL} — are used.

7.2 Optical transition matrix elements

For the calculation of optical properties, the nonlocality of the potential becomes important when the transition matrix elements are calculated. The matrix elements can be evaluated in the velocity gauge or the length gauge [11, chap. 20.1.1]. Assuming the dipole approximation, the coupling of electrons with an external electromagnetic field is described by $\mathbf{E}\cdot\mathbf{r}$ in the length gauge and $\mathbf{A}\cdot\mathbf{p}$ in the velocity gauge [18, chap. 5-1][19, 20]. Charge conservation and gauge invariance require the equivalence of the two interaction terms [20, 21].

In the length or longitudinal gauge, the position operator $\boldsymbol{r}$ is used for the calculation of the optical transition matrix elements (in atomic units) [22]

$$p_{nl} = \lim_{q\to 0} q^{-1}(E_{l,\mathbf{k}+\mathbf{q}} - E_{n,\mathbf{k}}) \left\langle \psi_{l,\mathbf{k}+\mathbf{q}} \left| e^{i\mathbf{q}\cdot\mathbf{r}} \right| \psi_{n,\mathbf{k}} \right\rangle, \tag{7.2}$$

where $\psi_{l,\mathbf{k}}$ is the single-particle wavefunction and $\mathbf{q}$ is a small momentum vector shift.

In the velocity gauge (also called transverse or Coulomb gauge) transition matrix elements are calculated from the velocity operator (in atomic units) $\hat{v}$ [23]:

$$p_{nl} = \langle \psi_{l,\mathbf{k}} | \hat{v} | \psi_{n,\mathbf{k}} \rangle. \tag{7.3}$$

The velocity operator is expressed as the commutator of the Hamiltoninan and the position operator $\hat{v}(\boldsymbol{r}) = i[H,\boldsymbol{r}] = \hat{p} + i[V^{\mathrm{NL}}(\boldsymbol{r},\boldsymbol{r}'),\boldsymbol{r}]$. For local potentials $V(\boldsymbol{r})$, the velocity operator $\hat{v}$ is equivalent to the momentum operator $\hat{p}$ and therefore in many cases the velocity matrix element $\langle \psi_{l,\mathbf{k}} | \hat{v} | \psi_{n,\mathbf{k}} \rangle$ is substituted by the momentum matrix element $\langle \psi_{l,\mathbf{k}} | \hat{p} | \psi_{n,\mathbf{k}} \rangle$ in the velocity gauge. However, for nonlocal potentials $V^{\mathrm{NL}}(\boldsymbol{r},\boldsymbol{r}')$ the position operator no longer commutes with the nonlocal potential and the velocity operator is no longer equivalent to the momentum operator. As a result, in order to calculate transition matrix elements from nonlocal potentials in the velocity gauge, the velocity operator has to be used or else a nonlocal correction to the momentum operator needs to be applied ($\hat{p} + i[V^{\mathrm{NL}}(\boldsymbol{r},\boldsymbol{r}'),\boldsymbol{r}]$). Otherwise the gauge invariance is violated [20, 21, 23]. In other words, for accurate optical matrix elements, the nonlocal potential

must not be neglected. In the length gauge, nonlocal potentials are treated correctly automatically.

The nonlocality in the potential stems from the fact that the full-electron Hamiltonian is replaced by an approximate Hamiltonian in the independent-electron approximation with an effective potential that reintroduces electron-electron interactions in the Kohn-Sham equations [24, chap. 2]. There are several sources by which nonlocality may be introduced in the effective Hamiltonian [21, 11, 25]: an incomplete basis set, local field effects due to abrupt changes in the charge density (spatial inhomogeneity), nonlocal pseudopotentials and nonlocal exchange-correlation potentials or quasiparticle self-energies.

The importance of using the nonlocal correction in the velocity gauge has been widely discussed for nonlocal pseudopotentials [26, 25, 27]. It was shown that neglecting the nonlocal term in the velocity gauge leads to inaccurate matrix elements, especially for transitions that involve localized d-electrons [28]. Also, several works have investigated the nonlocal effects of the self-energy operator on transition matrix elements from many-body *GW* calculations [29, 21, 20]. At the DFT level, Rhim et al. [22] calculated optical matrix elements including non-local exchange with the screened-exchange LDA functional (sX-LDA). They showed that to obtain the correct band dispersion, opening the bandgap with a scissor operator is not enough and the full calculation of the matrix element effects is necessary. Further, Paier, Marsman, and Kresse [30] showed that including nonlocal exchange via hybrid functionals yields more accurate static and dynamic dielectric functions in comparison with semilocal functionals. In this work, we focus on the nonlocality introduced by a nonlocal hybrid exchange-correlation potential and its effect on the accuracy of calculated effective masses.

7.3 Methods

7.3.1 Dataset

The data set contains 14 bulk and 4 monolayer materials with a total of 60 effective masses. Materials considered include sp-semiconductors and d-element semiconductors containing one transition metal. We include both three-dimensional and two-dimensional (layered) structures. The materials considered cover a wide range of effective masses. For the creation of the effective mass data set, we collected experimental effective mass data

from the available literature. Most experimental data was taken from existing compilations in the Landolt-Börnstein database [31]. We also included several individual entries from the literature for layered and monolayer 2D materials. Wherever multiple experimental values of one effective mass were available, we took the average for comparison with our computational data. For the compilation of the database, we had to exclude materials for which the experimentally reported effective masses differed widely, as this rendered comparison with computational results unprofitable.

7.3.2 DFT functionals

We computed the effective masses using three different exchange-correlation potentials that represent different levels of theory: The first level of theory used was the Perdew–Burke–Ernzerhof (PBE) [32] GGA exchange-correlation functional, which is semilocal in its treatment of exchange and correlation.

We also computed the effective masses with the Tran-Blaha modified Becke-Johnson potential (TB-mBJ) [13, 14] potential which corresponds to the second level of theory. The TB-mBJ potential

$$V_{x,\sigma}^{\mathrm{mBJ}}(\mathbf{r}) = cV_{x,\sigma}^{\mathrm{BR}}(\mathbf{r}) + (3c-2)\frac{1}{\pi}\sqrt{\frac{5}{6}}\sqrt{\frac{t_\sigma(\mathbf{r})}{\rho_\sigma(\mathbf{r})}} \tag{7.4}$$

is also a semilocal approximation. It is based on the Becke-Roussel [33] potential $V_{x,\sigma}^{\mathrm{BR}}(\mathbf{r})$ which models the Coulomb potential of the exchange hole. σ denotes the spin. Besides $V_{x,\sigma}^{\mathrm{BR}}(\mathbf{r})$, the TB-mBJ potential includes a term proportional to $\sqrt{t_\sigma(\mathbf{r})/\rho_\sigma(\mathbf{r})}$, where t_σ is the kinetic energy density and ρ_σ is the electron density. This root term can be interpreted as a screening term [34]. While semilocal in its approach, TB-mBJ mimics nonlocal effects. The parameter c can be determined self-consistently. However, in our work we adjust the c parameter to reproduce the experimental band gap to eliminate an additional source of data scattering when comparing effective masses with experiment and hybrid functional calculations. The band gap was fitted with a maximum error of less than 2%.

On the third level of theory, we used the Heyd-Scuseria-Ernzerhof hybrid functional (HSE06) [35] to compute effective masses. In a hybrid functional, a percentage of nonlocal Hartree-Fock (HF) exchange is mixed with the local PBE exchange-correlation functional. For HSE, the exchange is divided into a short-range (SR) and a long-range (LR) contribution. Only for the short-range exchange, a part of the PBE exchange is

replaced by the exact Hartree-Fock exchange. The long-range exchange is entirely taken from the PBE functional. The HSE funtional takes the form

$$E_{\mathrm{xc}}^{\mathrm{HSE}} = aE_{\mathrm{x}}^{\mathrm{HF,SR}}(\omega) + (1-a)E_{\mathrm{x}}^{\mathrm{PBE,SR}}(\omega) + E_{\mathrm{x}}^{\mathrm{PBE,LR}}(\omega) + E_{\mathrm{c}}^{\mathrm{PBE}}, \tag{7.5}$$

where ω denotes the range separation between SR and LR. ω is set to 0.2 $\mathrm{Å}^{-1}$ for the HSE06 functional. The parameter a specifies the percentage of SR Hartree-Fock exchange included. It is typically set to 0.25. In our work, we fitted a for each material to reproduce the experimental band gap with less than 2% error. This allowed us to directly compare HSE and TB-mBJ effective masses.

Because of the inclusion of a part of the exact nonlocal exchange, nonlocal exchange effects are considered explicitly. HF exchange is unscreened. The mixing of the nonlocal Hartree-Fock exchange with the local PBE exchange-correlation amounts to an effective screening of the nonlocal exchange by the local exchange-correlation [36], leading to a very good agreement with experiment for the electronic structure of semiconductors. Due to this artificial screening, the HSE approach can be seen as an approximation to the *GW* approach [11, chap. 9.2]. *GW* includes the dynamically screened exchange W in a physically correct way.

7.3.3 Computational details

Density functional calculations were performed with the Vienna *ab initio* simulation package [37, 38] (VASP), which uses projector-augmented waves [39] as basis set, implemented by Kresse and Joubert [40]. The plane wave cutoffs were taken from the values recommended in the pseudopotentials distributed with VASP. The number of valence and semicore electrons included for each element was chosen according to the values recommended by the materials project database [41]. For molybdenum and tungsten we included additional semi-core states (14 valence and semi-core electrons in total). The Brillouin zone was sampled with k grids ranging between $6 \times 6 \times 6$ and $8 \times 8 \times 8$ for the bulk materials, depending on where the band extrema were located in the Brillouin zone. For monolayers, k grids of $6 \times 6 \times 1$ were used.

Experimental lattice parameters were used for all bulk systems, allowing only atomic positions to relax using the PBE functional with a force convergence criterium of 0.001 eV/Å. Experimental structure data were obtained from Wyckoff [42] unless otherwise specified in Table 7.1. The monolayers were obtained by theoretical exfoliation from

the corresponding bulk material. To avoid interactions between periodic images of a monolayer, more than 25 Åof vacuum were included in the out-of-plane direction. Subsequently, the monolayers were fully relaxed on the PBE level.

All systems were treated as non-magnetic. Spin-orbit coupling was included in all calculations. Additional system-dependent calculation parameters are recorded in Table S1 of the supplementary information. Table S1 lists the experimental bandgaps (Refs. [43, 44, 45, 46, 47, 48, 49]) that were used to fit the HSE and TB-mBJ band gaps, the fitting parameters and the number of bands included in the optical calculations. We performed optical calculations in VASP to compute the transition matrix elements. In VASP, the longitudinal gauge (see Eq. (7.2)) is implemented for the calculation of the transition matrix elements [27]. In this gauge, nonlocal potentials are evaluated correctly.

Effective masses were calculated with the `mstar` code [17] which uses a perturbation theory approach based on Eq. (7.1) and its extension for degenerate states. The perturbation approach includes a sum over all bands and therefore many empty bands have to be included for accurate effective mass calculations. This is especially true for heavy effective masses and band edges that interact with high-energy orbitals. For the optical calculations, we included empty bands of up to 7 Ry (96 eV) above the Fermi level to ensure an accurate calculation of the effective mass. 7 Ry suffices for most materials but not for all, as we will discuss later. In contrast to Fourier expansion methods for calculating effective masses (as implemented in the `BoltzTraP` code [50]), the perturbation approach does not require a dense k grid to accurately capture light effective masses.

7.3.4 Statistics

The computational effective masses were compared with the experimental values. For the statistical analysis, we determined the mean error (ME), mean absolute error (MAE), mean relative error (MRE) and the mean absolute relative error (MARE). The standard deviation of the error (STDE) and the relative error (STDRE) were also calculated. Only materials for which data for all functionals was collected were included in the statistical analysis. Errors with a z-score of more than 3.5 were treated as outliers.

7.4 Results and discussion

Table 7.1 shows the results for 60 effective masses of 14 bulk and 4 monolayer materials obtained with different exchange-correlation potentials. Figure 7.1 shows the data of Table 7.1 graphically. To keep with the convention, the sign of the valence band effective masses is inverted, that is, a valence band curving downwards yields a positive effective mass. Negative values denote an upwards-bent valence band or a downwards-bent conduction band.

First, we need to ensure that our method is reliable. We compare the perturbation theory results at the PBE level with band curvature fits for which the band of interest was fitted in an energy window of 25 meV (the thermal energy at room temperature) with a fourth-order polynomial and extracted the second order coefficient. For GaAs we compared m_n, $m_{p,hh}$, $m_{p,lh}$ and $m_{p,so}$ and found that perturbation theory results agreed within an error of 1% with the band curvature fit. For Si, $m_{p,hh}$, $m_{p,lh}$ and $m_{p,so}$ agreed within 2.5% error. For 1L MoS_2 at the K point the band curvature yields $m_p(K) = 0.523\ m_0$ which is 15% smaller than the perturbation theory result. The conduction band effective mass from the band curvature is $m_n(K) = 0.431\ m_0$ which is 7% larger than the perturbation theory result. This is due to challenges with representing d-states using perturbation theory as discussed further below.

Previous effective mass calculations at the PBE level agree well with our results. For example, for the conduction band effective masses of Silicon, our results agree well with the ones obtained by Zhong, Wu, and Lei [51] and Yu, Zhang, and Liu [52] (in brackets), respectively: $m_{n,\parallel} = 0.943$ (0.950; 0.95) and $m_{n,\perp} = 0.193$ (0.197; 0.19) (all effective masses in units of m_0). For GaAs, our values agree well with the results reported by Kim et al. [8] (in brackets): $m_{p,so} = 0.107$ (0.108), $m_{p,lh} = 0.034$ (0.036), $m_{p,hh} = 0.324$ (0.320) and $m_n = 0.028$ (0.030). For monolayer MoS_2 our data at the K point show satisfactory agreement with the results of Wang, Kutana, and Yakobson [53], Kormányos et al. [54] and Wang et al. [55] (in brackets), respectively: $m_p(K) = 0.603$ $(0.59; 0.56; 0.54)$, $m_n(K) = 0.402$ $(0.5; 0.47; 0.47)$. Our results for monolayer MoS_2 are discussed in more detail below. Overall, our perturbation theory results are accurate with respect to band curvature fits and agree very well with previously published data, especially for sp-semiconductors.

We begin with the discussion of the summary statistics. Table 7.2 shows the summary statistics for the `mstar60` dataset, listing the following quantities: ME, MAE, MRE, MARE, STDE, and STDRE. We included only materials for which effective masses were

obtained with all three functionals. In spite of being very effective for most solids, the TB-mBJ potential (aw well as its local version [56] designed for materials with vacuum) was unable to open the band gap beyond PBE for monolayers of MoS_2, $MoSe_2$, WS_2, and WSe_2 as also noted by Patra et al. [57] and further explained by Tran et al. [58]. As a result, we did not calculate masses in monolayers with TB-mBJ and excluded them from the statistical analysis. Black phosphorus was also excluded because representative effective masses could not be obtained at the PBE level. At the PBE level, the conduction band of black phosphorus is lower in energy than the valence band, leading to a metallic ground state with band inversion and band mixing around the band edges. This causes effective masses of inverted sign and magnitude in two directions. A proper band order is restored at a higher level of theory (HSE, TB-mBJ). Furthermore, the following effective masses were excluded from the statistical analysis as outliers with a z-score above 3.5: GaAs $m_{n,\parallel}$ (X6), CdS $m_{p,\parallel}$ (Γ, A exciton), and BN m_p ($\bar{K}$). The outliers are marked with † in Table 7.1. In total, 42 effective masses of 13 materials were included in the statistical analysis.

Effective masses calculated with the PBE functional show the largest errors, with a mean absolute relative error of 38% and a mean relative error of -27%. The negative values of mean error and mean relative error suggest that effective masses are in many cases underestimated. However, the scattering of the error is large as indicated by the standard deviation of the relative error of 40%.

Effective masses calculated with the HSE functional fitted for the band gap show the best agreement with experiment throughout with a mean absolute relative error of 10% and a mean relative error of -4.7%. The errors are much smaller than the absolute errors for HSE which shows that there is no clear trend for over- or underestimation of the effective mass using HSE.

Turning to results obtained with the TB-mBJ functional fitted for the band gap, the mean absolute relative error is 21%, which is about twice that of HSE but less than the error of PBE. The mean relative error of 16% is positive. So,in contrast to effective masses calculated with the PBE functional, effective masses obtained with TB-mBJ are very often overestimated with respect to experiment.

The main conclusion of the benchmarking of the PBE, HSE (gap fit) and TB-mBJ (gap fit) exchange-correlation potentials is that HSE gives by far the best agreement with experimental effective masses. On the other hand, PBE often yields lighter effective

masses, while TB-mBJ generally overestimates them. These trends are in agreement with the results of Kim et al. [8].

Our objective is to comprehend with greater clarity the properties of hybrid functionals that make HSE so successful in reproducing experimental effective masses. As stated earlier, the main difference of the hybrid functionals with respect to semilocal functionals is the addition of a nonlocal component via the introduction of a fraction of HF exchange. Effective masses are influenced by the nonlocal component in two ways: Firstly, by adding nonlocal exchange, the band gap opens up, which increases the effective mass. Secondly, nonlocal effects influence the optical transition matrix elements p_{ln}. The opening of the band gap can be reproduced with the TB-mBJ potential, but the errors in the effective masses are still much higher than with HSE.

We now want to probe the role of the nonlocal exchange potential V_x^{NL} for the calculation of the matrix element. To that end it is instructive to switch off the nonlocal exchange contributions in the matrix element. We achieve this by switching to the PBE potential when calculating the matrix elements while using HSE wavefunctions (see supplementary information for the detailed workflow). As a result, HSE eigenfunctions and band gaps are conserved and only the matrix element is calculated without nonlocal exchange effects. This allows us to decouple the band gap increase and the matrix element change that are both caused by the nonlocal exchange.

Switching off the nonlocal exchange contributions to the matrix elements leads to a systematic overestimation of the effective masses (see Fig. 7.1 and Table 7.1), with only a few exceptions. This is a consequence of the absolute matrix element being *smaller* when calculated without the nonlocal exchange potential.

Let us consider the example of the conduction band effective mass m_{n} of GaAs at Γ to discuss the nonlocal exchange contribution to the effective mass in more detail. Figure 7.2 shows the effective mass of the conduction band of GaAs at Γ versus the band gap for different settings of the exchange-correlation functional. For this graph, the electron effective mass was approximated as:

$$\frac{m_0}{m_{\mathrm{n}}^*} \approx 1 + \frac{2}{m_0} \sum_{\mathrm{v}} \frac{|p_{\mathrm{cv}}|^2}{E_{\mathrm{c}} - E_{\mathrm{v}}}, \tag{7.6}$$

where the 'c' and 'v' indices stand for the conduction band and valence bands, respectively. In GaAs, the effective mass of the conduction band at the Γ point is isotropic and therefore the matrix element contribution can be expressed as $2|p_{\mathrm{cv}}|^2$. In the sum, we

included the heavy-hole, light-hole and split-off bands as valence bands. As not all bands are included in the sum, this is an approximation. The matrix elements are calculated in the length gauge using VASP.

In Fig. 7.2 we observe a linear relationship between the effective mass and the band gap for all XC functionals that do not include nonlocal exchange. This is a consequence of the fact that $\sum |p_{\mathrm{cv}}|^2$ changes very little, and thus the change in effective mass depends only on the change of the band gap. Effective masses obtained from hybrid functionals considering nonlocal exchange deviate from that linear relationship. Only upon including nonlocal exchange both the experimental band gap and experimental effective mass can be reproduced correctly in the calculation. Figure 7.2 thus shows the importance of including the nonlocal exchange on the HSE level for calculating accurate matrix elements and thus accurate effective masses when employing perturbation theory. The same matrix elements are also used in the calculation of optical properties, which explains the superior accuracy of HSE for the high-frequency dielectric constant of semiconductors and small-gap insulators [30].

The deviation from the linear relationship indicates that $\sum |p_{\mathrm{cv}}|^2$ changes when the nonlocal exchange potential V_x^{NL} is included in the calculation of the matrix element. Thus, the matrix element is the key parameter we need to consider if we want to explain the superior accuracy of HSE effective masses, especially compared to TB-mBJ results.

Figure 7.3 shows the sum of the squared matrix elements $\sum |p_{\mathrm{cv}}|^2$ that enter into Eq. (7.6) versus the band gap for different settings of the exchange-correlation functional for the conduction band effective mass of GaAs at Γ. Again, the sum displayed on the vertical axis includes contributions from the transitions between the conduction band and the heavy-hole, light-hole and split-off valence bands. $\sum |p_{\mathrm{cv}}|^2$ is around 0.6 atomic units for all XC functionals that do not include nonlocal effects, irrespective of the band gap. We included data obtained with Wien2k [59, 60] at the PBE level for comparison. We also calculated the matrix elements from the semilocal SCAN [61] functional, which gives the same matrix element as TB-mBJ and PBE in spite of the band gap being intermediate between PBE and TB-mBJ. When the nonlocal exchange potential V_x^{NL} is considered in the calculation of the matrix element, $\sum |p_{\mathrm{cv}}|^2$ increases with increasing HF proportion and increasing the band gap. The change of the sum $\sum |p_{\mathrm{cv}}|^2$ is the key that leads to the deviation of full HSE results from the linear pattern of Fig. 7.2. Interestingly, the increase of $\sum |p_{\mathrm{cv}}|^2$ is strictly proportional to the increase of the HF percentage included in the functional.

Having analyzed the effect of the nonlocal exchange on the transition matrix element, we can add some comments on the general trends observed for effective masses in Fig. 7.1 and the summary statistics of Table 7.2. Starting with TB-mBJ calculated effective masses, the clear trend for overestimation comes from the too-small absolute matrix elements. This is the same for HSE effective masses for which V_x^{NL} was neglected in the calculation of the matrix element. On the other hand, for PBE calculated effective masses, no clear trend is apparent. For some PBE effective masses, e.g. Si $\mathrm{m_{n,\perp}}$ and $\mathrm{m_{n,\parallel}}$, the agreement with experiment is surprisingly good. This is because the PBE band gap is not fitted to the experimental band gap. As a result, errors in the effective mass due to an underestimated band gap and due to the underestimated matrix element partially cancel out. This error cancellation is not systematic as seen by the high standard deviation of the relative error of 41%. Therefore, no clear trend for the error of PBE effective masses can be found.

We now turn our attention to the monolayer effective mass values recorded in Table 7.1. For some effective masses at Γ, reliable PBE-derived effective masses could not be obtained with perturbation theory as the result differed by more than 30% from the band curvature fit. For effective masses at the K point, the errors with respect to the band curvature were in the range of $5-16\%$ which is significantly larger than for sp-semiconductors. The variations of the perturbation theory results with respect to the band curvature obtained with PBE can be explained with the limits of perturbation theory in connection with DFT pseudopotentials. All monolayers considered in our study are transition metal dichalcogenides for which the band edges are composed mainly of the d-orbitals of the transition metal. When it comes to the prediction of d-states, it is difficult to converge the perturbation sum. According to the optical selection rule $\Delta l = \pm 1$, l being the orbital quantum number, d-states couple with p-states and f-states. Therefore, many high-energy empty bands have to be included that describe the f-states in order to correctly converge the perturbation sum for d-states. In other words, the convergence of the sum with respect to the number of empty bands needs to be carefully tested. This is true not only for effective masses but for all electronic structure methods that are based on perturbation theory, e.g., *GW*. We included 800 bands for the calculation of the effective masses in the monolayers, which corresponds to ca. $5-6$ Ry above the Fermi level.

When we increase the number of empty bands, the predicted effective mass is slowly corrected towards the value obtained from parabolic fitting of the band edge (see Table S2 of the supplementary information). However, for the example of 1L MoS_2 even

with about 2400 bands (ca. 12 Ry above the Fermi level), the error is still high. We also notice that the effective mass predicted depends on the pseudopotential employed. For 1L MoS_2, the error is greater for the Mo_pv pseudopotential than for the Mo_sv potential and the Mo_sv_GW potential which has the lowest error. This is because in the *GW* pseudopotentials the high-energy electron scattering is more accurate, rendering the *GW* pseudopotentials better suited for calculations that include coupling to high-energy states [39, 62]. In bulk MoS_2 and WS_2, we see similar errors of PT results with respect to the band curvature, though reduced in magnitude (Table S2 of the supplementary information). We conclude that the prediction of the effective mass of d-states is challenging in two ways: Firstly, a high number of empty bands has to be included and secondly, even when they are included, the physical limits of the pseudopotentials are reached.

The sum over many empty states in the perturbative expansion can elegantly be overcomed with the Sternheimer approach [63] as shown in the context of quasiparticle *GW* calculations [64] or effective masses [65] which do not require the computation of unoccupied electronic states. Alternatively, it is possible to address this issue by including high-energy local orbitals (HELOs) to augment the basis set. This feature available in the Wien2k code was shown to improve the magnetic shielding for solid state nuclear magnetic resonance [66], effective masses derived from the perturbative expansion [17] and the *GW* band gap convergence [67]. With six high-energy local orbitals included, the effective mass of 1L MoS_2 predicted with perturbation theory is in good agreement with the band curvature fit (Table S2 of the supplementary information; see supplementary information for the detailed workflow of Wien2k calculations with HELOs).

The limits observed for d-states at the example of PBE hold also for HSE calculations. Here, a further aspect is noteworthy. To fit the transport band gap of the monolayer materials we have to include a large proportion of HF exchange in the hybrid functional (see Table S1 in the supplementary information). Relative to the HF percentage for the parent bulk structure we had to include nearly three times the HF proportion for 1L MoS_2 and about four times the HF proportion for 1L WS_2 to obtain the right band gap. Considering that the same chemical elements are used, this seems surprising. It points to the limit of the parameter fitting procedure to obtain the experimental transport band gap for monolayer 2D materials. The large percentage of HF included in the functional may lead to an unphysical increase of the matrix element, which may be the reason why many effective masses are smaller than the experimental value (see Table 7.1).

Turning away from technical aspects, we now look at the experimental effective masses for the transition metal dichalcogenide monolayers recorded in Table 7.1. We observe that the bulk MoS_2 hole effective mass at Γ is much lighter than the 1L MoS_2 effective mass. To explain this effective mass renormalization, we can consider two factors (drawing on Eq. (7.1)): the band gap change and the change of the matrix element. The band gap at Γ opens up from 2.08 eV in the bulk to 2.84 eV in the monolayer MoS_2 at the PBE level. Looking into the matrix elements, we observe that the coupling of the lower-lying conduction bands with the valence band at Γ contributes significantly to the band dispersion. Thus, an increase of the band gap affects the strength of the contribution of these interactions to the band curvature. However, the band gap renormalization accounts for only less than half of the effective mass renormalization. This means that also the matrix elements themselves change: In 1L MoS_2 the sum of these matrix elements is only about half of that in bulk MoS_2. In other words, the oscillator strength between the valence band (VB) at Γ and the lower-lying conduction bands is much weaker in the monolayer than in the bulk. As a result, the band dispersion of the VB at Γ is flatter in 1L MoS_2 and the effective mass is larger.

The layer-dependent effective mass of holes at the Γ point in MoS_2 is an example that we have to consider the change of the optical matrix element when trying to explain effective mass renormalization effects. This example shows that in order to develop a physical intuition for the renormalization of effective masses, both the band gap and the matrix element renormalization have to be considered together.

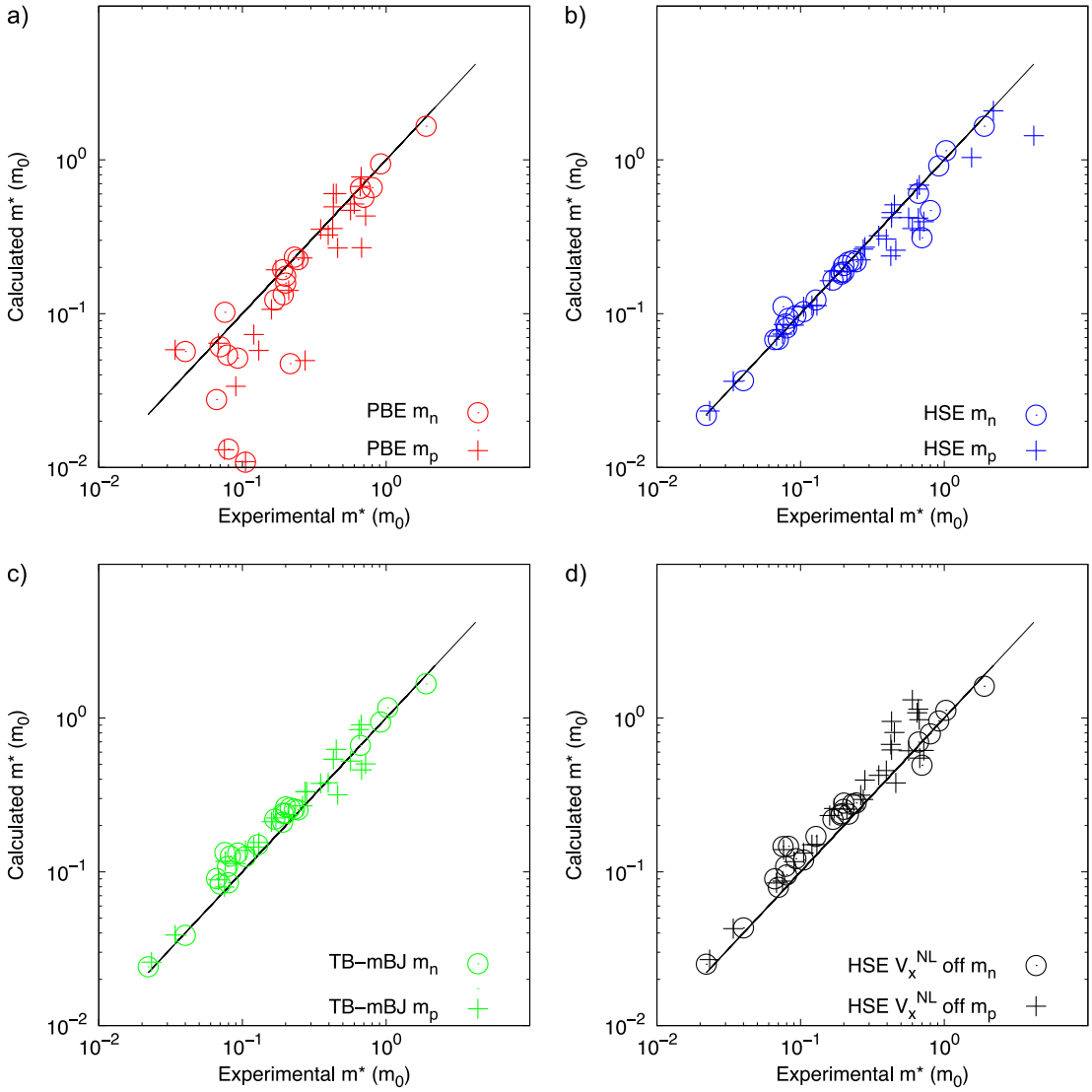

FIGURE 7.1: Calculated versus experimental effective masses for the `mstar60` dataset. This figure provides a graphical overview of Table 7.1. Circles are used for conduction band effective masses and cross symbols for valence band effective masses. Effective masses are calculated with the following exchange-correlation functionals/potentials: a) PBE, b) HSE06, c) TB-mBJ/LDA and d) HSE06 with the nonlocal exchange potential term V_x^{NL} switched off in the calculation of the matrix element. HSE-derived effective masses show the best agreement with experiment.

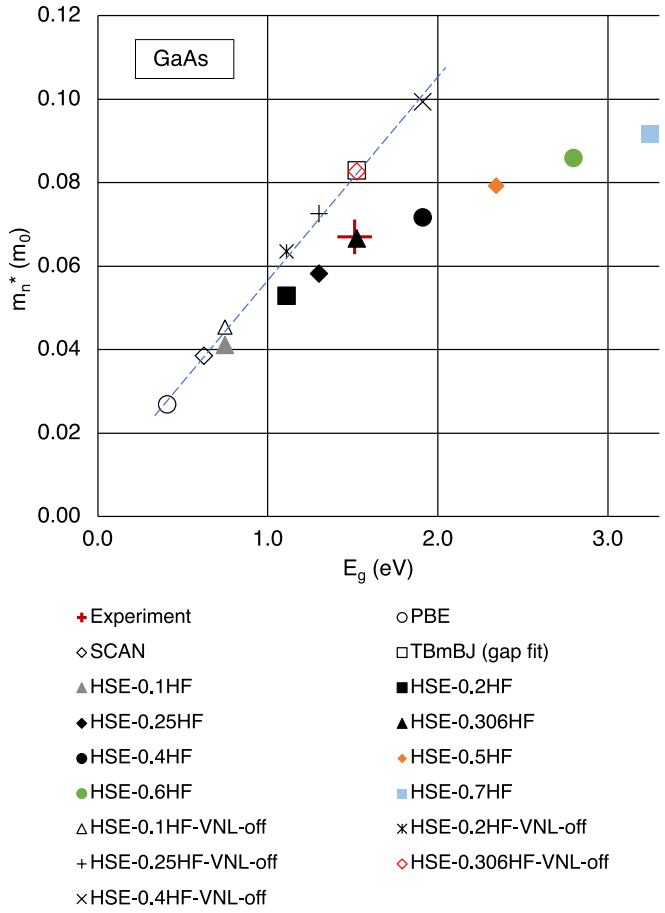

FIGURE 7.2: Effective mass of the conduction band of GaAs at Γ versus the band gap for different settings of the exchange-correlation functional. There is a linear relationship between the effective mass and the band gap for all exchange-correlation functionals that do not include nonlocal exchange. Effective masses obtained from hybrid functionals considering nonlocal exchange deviate from that linear relationship. Only upon including nonlocal exchange, both the experimental band gap and experimental effective mass can be reproduced correctly in the calculation.

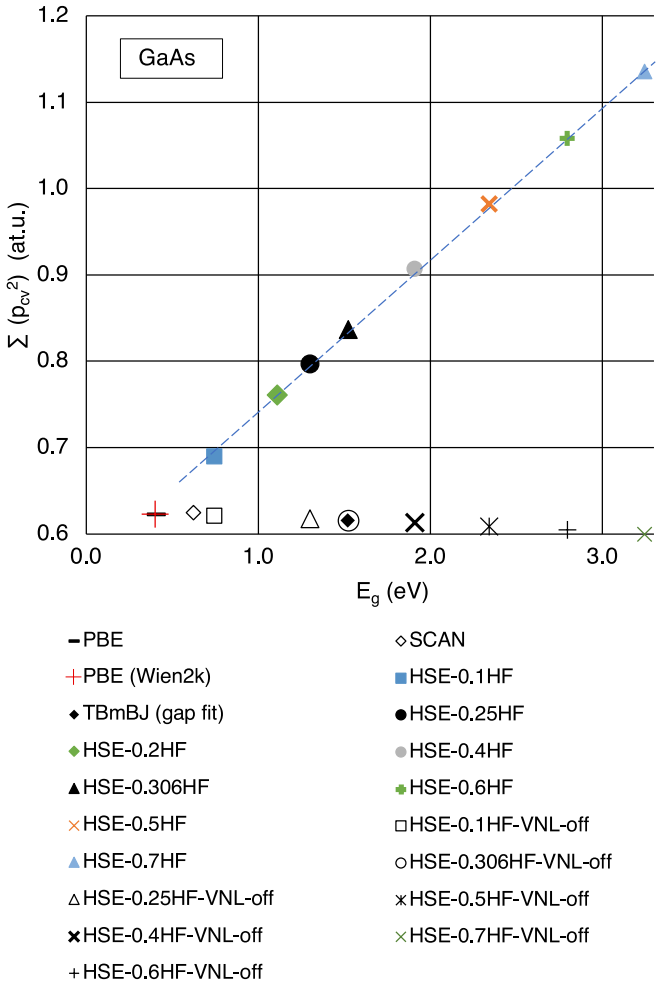

FIGURE 7.3: Sum of the squared matrix element $|p_{\mathrm{cv}}|^2$ (see Eq. (7.6)) versus the band gap for different settings of the exchange-correlation potential for the conduction band effective mass of GaAs at Γ. $\sum |p_{\mathrm{cv}}|^2$ includes contributions from the transitions between the conduction band and the heavy-hole, light-hole and split-off valence bands. $\sum |p_{\mathrm{cv}}|^2$ is roughly a constant for all exchange-correlation functionals that do not include nonlocal exchange, irrespective of the band gap. When the nonlocal exchange is considered via the V_x^{NL} term in the calculation of the matrix element, the sum increases with increasing HF proportion and increasing band gap. This graph shows the importance of including the nonlocal exchange on the HSE level for calculating accurate optical matrix elements.

7.5 Conclusion

In summary, we benchmarked the performance of three exchange-correlation potentials for the calculation of effective masses. For benchmarking we introduced the `mstar60` dataset which contains 18 semiconductors with a wide range of electronic properties and effective masses. Our calculations show that the hybrid HSE06 functional (fitted to the experimental band gap) yields by far the most accurate effective masses with respect to experiment, followed by the TB-mBJ functional (fitted to the experimental band gap). We reveal that the nonlocal exchange in HSE06 enlarges the transition matrix elements which proves to be the key to the superior accuracy in the calculation of effective masses. The omission of the commutator between the nonlocal XC potentials and position when calculating optical matrix elements in HSE leads to serious errors (about 30% underestimated p_{cv}^2 matrix elements in GaAs). For the semilocal PBE functional, the errors introduced by the band gap and the transition matrix elements partially cancel out for the calculation of effective masses. We discuss the limits of the perturbation approach to the calculation of effective masses for d-states and possible solutions. Finally, we show at the example of transition metal dichalcogenide bulk and monolayer materials that changes in the matrix elements are important in understanding the layer-dependent effective mass renormalization. In this, our analysis goes beyond the standard discussion that focusses on the interband energy difference. Our results show that changes in the matrix elements may not be ignored in the discussion of effective mass renormalization effects.

Conclusion

The authors are thankful to Peter Blaha and Fabien Tran (TU Vienna) for the insightful discussion about the performance of a (local) TB-mBJ potential for transition metal dichalcogenides. The authors acknowledge funding provided by the Natural Sciences and Engineering Research Council of Canada under the Discovery Grant Programs RGPIN-2020-04788. Calculations were performed using the Compute Canada infrastructure supported by the Canada Foundation for Innovation under John R. Evans Leaders Fund.

		experiment	PBE	HSE06	HSE06, V_x^{NL} off	TB-mBJ
Si (227)	$m_{n,\perp}$ (CBM)	0.191	0.193	0.185	0.234	0.210
	$m_{n,\parallel}$ (CBM)	0.916	0.943	0.913	0.957	0.942
	$m_{p,hh}$ (Γ) [100]	0.46 [68]	0.267	0.259	0.379	0.317
	$m_{p,lh}$ (Γ) [100]	0.171 [68]	0.193	0.189	0.258	0.224
	$m_{p,so}$ (Γ)	0.262	0.230	0.224	0.315	0.269
GaAs (216)	m_n (Γ)	0.066	0.028	0.068	0.090	0.090
	$m_{n,\perp}$ (X6)	0.23	0.233	0.220	0.276	0.255
	$m_{n,\parallel}$ (X6) † [1]	1.3	−0.534	−0.90	−1.016	−0.294
	$m_{n,\perp}$ (L6)	0.075	0.102	0.111	0.146	0.134
	$m_{n,\parallel}$ (L6)	1.9	1.656	1.654	1.609	1.671
	$m_{p,hh}$ (Γ) [100]	0.395	0.324	0.306	0.456	0.380
	$m_{p,lh}$ (Γ) [100]	0.09	0.034	0.084	0.117	0.113
	$m_{p,so}$ (Γ)	0.16	0.107	0.164	0.233	0.212
GaN (186)	$m_{n,\parallel}$ (Γ)	0.2	0.158	0.186	0.255	0.240
	$m_{n,\perp}$ (Γ)	0.2	0.175	0.206	0.280	0.264
InP (216)	m_n (Γ)	0.079	0.054	0.086	0.109	0.108
	$m_{p,hh}$ (Γ) [100]	0.565	0.469	0.422	0.612	0.525
	$m_{p,lh}$ (Γ) [100]	0.12	0.073	0.113	0.150	0.145
	$m_{p,so}$ (Γ)	0.21 [69]	0.142	0.189	0.256	0.236

Table 7.1: Calculated and experimental effective masses m^* (m_0). m_n denote effective masses of the conduction band, m_p effective masses of the valence band. 'hh', 'lh' and 'so' stand for heavy hole, light hole and split-off band, respectively. Locations and directions in the Brillouin zone are indicated. The space group number of each material is given in parenthesis.

[1] excluded from the statistical analysis
[2] excluded from the statistical analysis
[3] specifics of the valence band and direction of the experimentally obtained effective mass are unclear
[4] excluded from the statistical analysis

		experiment	PBE	HSE06	HSE06, V_x^{NL} off	TB-mBJ
CdS (186)	$m_{n,\perp}$ (Γ, A exciton)	0.192	0.133	0.181	0.239	0.242
	$m_{n,\parallel}$ (Γ, A exciton)	0.168	0.123	0.165	0.220	0.220
	$m_{p,\perp}$ (Γ, A exciton)	0.675	0.268	0.348	0.549	0.463
	$m_{p,\parallel}$ (Γ, A exciton) † [2]	5	0.993	0.827	1.57	1.57
CdTe (216)	m_n (Γ)	0.093	0.051	0.097	0.122	0.133
	$m_{p,lh}$ [100] (Γ)	0.13	0.058	0.113	0.150	0.155
	$m_{p,hh}$ [100] (Γ)	0.72	0.431	0.396	0.615	0.503
PbS (225)	$m_{n,\perp}$ (L)	0.08	0.013	0.081	0.096	0.085
	$m_{n,\parallel}$ (L)	0.105	0.011	0.103	0.119	0.126
	$m_{p,\perp}$ (L)	0.075	0.013	0.074	0.087	0.080
	$m_{p,\parallel}$ (L)	0.105	0.011	0.111	0.132	0.138
PbSe (225)	$m_{n,\perp}$ (L)	0.04	0.057	0.037	0.043	0.039
	$m_{n,\parallel}$ (L)	0.07	0.061	0.068	0.079	0.083
	$m_{p,\perp}$ (L)	0.034	0.058	0.036	0.043	0.039
	$m_{p,\parallel}$ (L)	0.068	0.064	0.071	0.085	0.089
PbTe (225)	$m_{n,\perp}$ (L)	0.022	0.003	0.022	0.025	0.024
	$m_{n,\parallel}$ (L)	0.215	0.047	0.216	0.237	0.260
	$m_{n,\perp}$ (L)	0.023	0.003	0.023	0.027	0.026
	$m_{p,\parallel}$ (L)	0.273	0.050	0.263	0.296	0.332
SiC (216)	$m_{n,\parallel}$ (X)	0.662	0.652	0.606	0.698	0.664
	$m_{n,\perp}$ (X)	0.244	0.225	0.217	0.281	0.253
	m_p (Γ) [100]	0.45 [3]	0.603	0.510	0.805	0.625
BN [70] (194)	m_p ($\bar{K}$, $\bar{\Gamma}$-$\bar{K}$) † [4]	0.49 [71]	0.971	0.775	1.515	1.185

TABLE 7.1: continued.

[5]Perturbation theory (PT) result has an error of 14% with respect to the band curvature fit
[6]PT result has an error of 5% with respect to the band curvature fit
[7]PT result has an error of 7% with respect to the band curvature fit
[8]Converged PT result could not be obtained. Band curvature fit gives an effective mass of 3.73 m_0
[9]Perturbation theory result has an error of 13% with respect to the band curvature fit
[10]Converged PT result could not be obtained
[11]PT result has an error of 15% with respect to the band curvature fit
[12]PT result has an error of 10% with respect to the band curvature fit
[13]PT result has an error of 7% with respect to the band curvature fit
[14]PT result has an error of 8% with respect to the band curvature fit
[15]PT result has an error of 16% with respect to the band curvature fit
[16]PT result has an error of 8% with respect to the band curvature fit
[17]Converged PT result could not be obtained. Band curvature fit gives an effective mass of 2.93 m_0
[18]Converged PT result could not be obtained.
[19]PT result has an error of 5% with respect to the band curvature fit
[20]PT has an error of 8% with respect to the band curvature fit
[21]Converged PT result could not be obtained. Band curvature fit gives an effective mass of 4.46 m_0
[22]Converged PT result could not be obtained.

		experiment	PBE	HSE06	HSE06, V_x^{NL} off	TB-mBJ
bP (64)	m_n (Y) [010]	1.027 [72]	—	1.15	1.12	1.17
	m_n (Y) [001]	0.128 [72]	—	0.123	0.170	0.150
	m_n (Y) [100]	0.083 [72]	—	0.093	0.146	0.126
	m_p (Y) [010]	0.648 [72]	—	0.646	1.08	0.842
	m_p (Y) [001]	0.28 [72]	—	0.270	0.395	0.332
	m_p (Y) [100]	0.076 [72]	—	0.085	0.140	0.117
MoS_2 [73] (194)	m_p ($\bar{\Gamma}$, $\bar{\Gamma}$-$\bar{K}$)	0.67 [74]	0.774[5]	0.685	0.976	0.904
WS_2(194)	m_p ($\bar{K}$, $\bar{\Gamma}$-$\bar{K}$)	0.35 [75]	0.354[6]	0.321	0.424	0.376
	$m_{p,VB-1}$ ($\bar{K}$, $\bar{\Gamma}$-$\bar{K}$)	0.43 [75]	0.495 [7]	0.454	0.620	0.539
1L MoS_2	m_p (Γ, Γ-K)	2.2 [74, 76]	— [8]	2.084 [9]	— [10]	—
	m_p (K, Γ-K)	0.52 [76, 77]	0.603 [11]	0.421 [12]	0.951	—
	m_n (K)	0.69 [78, 77]	0.402 [13]	0.312 [14]	0.494	—
1L $MoSe_2$	m_p (K, Γ-K)	0.66 [79, 80, 54]	0.672 [15]	0.418	1.141	—
	m_n (K)	0.8 [81]	0.468 [16]	0.333	0.584	—
1L WS_2	m_p ($\bar{\Gamma}$, $\bar{\Gamma}$-$\bar{K}$)	1.55 [82]	— [17]	1.04	— [18]	—
	m_p ($\bar{K}$, $\bar{\Gamma}$-$\bar{K}$)	0.425 [82, 83]	0.358 [19]	0.237	0.674	—
	$m_{p,so}$ ($\bar{K}$, $\bar{\Gamma}$-$\bar{K}$)	0.6 [82, 83]	0.517 [20]	0.358	1.31	—
1L WSe_2	m_p (Γ, Γ-K)	4.2 [80]	— [21]	1.436	— [22]	—

Table 7.1: continued.

	PBE	HSE06	HSE06, V_x^{NL} off	TB-mBJ
ME (m_0)	−0.053	−0.034	0.036	0.013
MAE (m_0)	0.075	0.043	0.065	0.054
STDE (m_0)	0.100	0.090	0.100	0.080
MRE (%)	−27	−4.7	22	16
MARE (%)	38	10	26	21
STDRE (%)	40	16	22	21

TABLE 7.2: Summary statistics for the error in the calculated effective mass for the bulk materials of the `mstar60` dataset. The statistics include 42 effective masses of 13 materials.

References

[1] Geoffroy Hautier et al. "How Does Chemistry Influence Electron Effective Mass in Oxides? A High-Throughput Computational Analysis". In: *Chem. Mater.* 26.19 (Oct. 2014), pp. 5447–5458. ISSN: 0897-4756. DOI: 10.1021/cm404079a.

[2] Stefano Curtarolo et al. "AFLOWLIB.ORG: A distributed materials properties repository from high-throughput ab initio calculations". In: *Comput. Mater. Sci.* 58 (June 2012), pp. 227–235. ISSN: 0927-0256. DOI: 10.1016/j.commatsci.2012.02.002.

[3] Geoffroy Hautier et al. "Identification and design principles of low hole effective mass p-type transparent conducting oxides". In: *Nat. Commun.* 4.1 (Aug. 2013), p. 2292. ISSN: 2041-1723. DOI: 10.1038/ncomms3292.

[4] Evgenii Tsymbalov et al. "Machine learning for deep elastic strain engineering of semiconductor electronic band structure and effective mass". In: *npj Comput. Mater.* 7.1 (May 2021), pp. 1–10. ISSN: 2057-3960. DOI: 10.1038/s41524-021-00538-0.

[5] Sten Haastrup et al. "The Computational 2D Materials Database: high-throughput modeling and discovery of atomically thin crystals". In: *2D Materials* 5.4 (2018), p. 042002.

[6] Neil W. Ashcroft et al. *Solid State Physics*. Holt, Rinehart and Winston, 1976. ISBN: 978-0-03-083993-1.

[7] Peter Y. Yu and Manuel Cardona. *Fundamentals of Semiconductors*. Graduate Texts in Physics. Berlin, Heidelberg: Springer Berlin Heidelberg, 2010. ISBN: 978-3-642-00709-5 978-3-642-00710-1. DOI: 10.1007/978-3-642-00710-1.

[8] Yoon-Suk Kim et al. "Towards efficient band structure and effective mass calculations for III-V direct band-gap semiconductors". In: *Phys. Rev. B* 82.20 (Nov. 2010), p. 205212. DOI: 10.1103/PhysRevB.82.205212.

[9] Wolfgang G. Zeier et al. "Thinking Like a Chemist: Intuition in Thermoelectric Materials". In: *Angewandte Chemie International Edition* 55.24 (June 2016), pp. 6826–6841. ISSN: 1433-7851, 1521-3773. DOI: 10.1002/anie.201508381. (Visited on 07/22/2021).

[10] W. Kohn and L. J. Sham. "Self-Consistent Equations Including Exchange and Correlation Effects". In: *Phys. Rev.* 140 (1965), A1133–A1138. DOI: 10.1103/PhysRev.140.A1133.

[11] Friedhelm Bechstedt. *Many-Body Approach to Electronic Excitations*. Vol. 181. Springer Series in Solid-State Sciences. Berlin, Heidelberg: Springer Berlin Heidelberg, 2015. ISBN: 978-3-662-44592-1 978-3-662-44593-8. DOI: 10.1007/978-3-662-44593-8.

[12] Wenbin Li and Feliciano Giustino. "Many-body renormalization of the electron effective mass of InSe". In: *Phys. Rev. B* 101.3 (Jan. 2020), p. 035201. DOI: 10.1103/PhysRevB.101.035201.

[13] Axel D. Becke and Erin R. Johnson. "A simple effective potential for exchange". In: *J. Chem. Phys.* 124.22 (June 2006), p. 221101. ISSN: 0021-9606. DOI: 10.1063/1.2213970.

[14] Fabien Tran and Peter Blaha. "Accurate Band Gaps of Semiconductors and Insulators with a Semilocal Exchange-Correlation Potential". In: *Phys. Rev. Lett.* 102.22 (June 2009), p. 226401. DOI: 10.1103/PhysRevLett.102.226401.

[15] H. Dixit et al. "Electronic structure of transparent oxides with the Tran–Blaha modified Becke–Johnson potential". In: *J. Phys.: Condens. Matter* 24.20 (Apr. 2012), p. 205503. ISSN: 0953-8984. DOI: 10.1088/0953-8984/24/20/205503.

[16] Rafael B. Araujo, J. S. de Almeida, and A. Ferreira da Silva. "Electronic properties of III-nitride semiconductors: A first-principles investigation using the Tran-Blaha modified Becke-Johnson potential". In: *J. Appl. Phys.* 114.18 (Nov. 2013), p. 183702. ISSN: 0021-8979. DOI: 10.1063/1.4829674.

[17] Oleg Rubel et al. "Perturbation approach to ab initio effective mass calculations". In: *Comput. Phys. Commun.* 261 (Apr. 2021), p. 107648. ISSN: 0010-4655. DOI: 10.1016/j.cpc.2020.107648.

[18] G. F. Bassani and Giuseppe Pastori Parravicini. *Electronic states and optical transitions in solids*. 1st ed. International series of monographs in the science of the solid state v. 8. Oxford ; New York: Pergamon Press, 1975. ISBN: 978-0-08-016846-3.

[19] D.H. Marti, M.-A. Dupertuis, and B. Deveaud. "General theory for the interference of two-photon and one-photon processes in semiconductor heterostructures". In: *Ann. Phys.* 316.1 (Mar. 2005), pp. 234–269. ISSN: 0003-4916. DOI: 10.1016/j.aop.2004.09.015.

[20] R. Del Sole and Raffaello Girlanda. "Optical properties of semiconductors within the independent-quasiparticle approximation". In: *Phys. Rev. B* 48.16 (Oct. 1993), pp. 11789–11795. DOI: 10.1103/PhysRevB.48.11789.

[21] B. Adolph et al. "Nonlocality and many-body effects in the optical properties of semiconductors". In: *Phys. Rev. B* 53.15 (Apr. 1996), pp. 9797–9808. DOI: 10.1103/PhysRevB.53.9797.

[22] S. H. Rhim et al. "Fully first-principles screened-exchange LDA calculations of excited states and optical properties of III-V semiconductors". In: *Phys. Rev. B* 71.4 (Jan. 2005), p. 045202. DOI: 10.1103/PhysRevB.71.045202.

[23] Anthony F. Starace. "Length and Velocity Formulas in Approximate Oscillator-Strength Calculations". In: *Phys. Rev. A* 3.4 (Apr. 1971), pp. 1242–1245. DOI: 10.1103/PhysRevA.3.1242.

[24] Feliciano Giustino. *Materials Modelling using Density Functional Theory Properties and Predictions*. Oxford University Press, 2014.

[25] C. J. Pickard and M. C. Payne. "Second-order $k \cdot p$ perturbation theory with Vanderbilt pseudopotentials and plane waves". In: *Phys. Rev. B* 62.7 (Aug. 2000), pp. 4383–4388. DOI: 10.1103/PhysRevB.62.4383.

[26] Sohrab Ismail-Beigi, Eric K. Chang, and Steven G. Louie. "Coupling of Nonlocal Potentials to Electromagnetic Fields". In: *Phys. Rev. Lett.* 87.8 (Aug. 2001), p. 087402. DOI: 10.1103/PhysRevLett.87.087402.

[27] M. Gajdoš et al. "Linear optical properties in the projector-augmented wave methodology". In: *Phys. Rev. B* 73.4 (Jan. 2006), p. 045112. DOI: 10.1103/PhysRevB.73.045112.

[28] A. J. Read and R. J. Needs. "Calculation of optical matrix elements with nonlocal pseudopotentials". In: *Phys. Rev. B* 44.23 (Dec. 1991), pp. 13071–13073. ISSN: 0163-1829, 1095-3795. DOI: 10.1103/PhysRevB.44.13071.

[29] Zachary H. Levine and Douglas C. Allan. "Optical second-harmonic generation in III-V semiconductors: Detailed formulation and computational results". In: *Phys. Rev. B* 44.23 (Dec. 1991), pp. 12781–12793. DOI: 10.1103/PhysRevB.44.12781.

[30] Joachim Paier, Martijn Marsman, and Georg Kresse. "Dielectric properties and excitons for extended systems from hybrid functionals". In: *Physical Review B* 78.12 (2008), p. 121201.

[31] *Landolt-Börnstein — group III condensed matter.*

[32] John P. Perdew, Kieron Burke, and Matthias Ernzerhof. "Generalized gradient approximation made simple". In: *Phys. Rev. Lett.* 77.18 (Oct. 1996), pp. 3865–3868. DOI: 10.1103/PhysRevLett.77.3865.

[33] A. D. Becke and M. R. Roussel. "Exchange holes in inhomogeneous systems: A coordinate-space model". In: *Phys. Rev. A* 39.8 (Apr. 1989), pp. 3761–3767. DOI: 10.1103/PhysRevA.39.3761.

[34] David Koller, Fabien Tran, and Peter Blaha. "Merits and limits of the modified Becke-Johnson exchange potential". In: *Phys. Rev. B* 83.19 (May 2011), p. 195134. DOI: 10.1103/PhysRevB.83.195134.

[35] Aliaksandr V. Krukau et al. "Influence of the exchange screening parameter on the performance of screened hybrid functionals". In: *J. Chem. Phys.* 125.22 (Dec. 2006), p. 224106. ISSN: 0021-9606. DOI: 10.1063/1.2404663.

[36] Axel D. Becke. "Perspective: Fifty years of density-functional theory in chemical physics". In: *J. Chem. Phys.* 140.18 (May 2014), 18A301. ISSN: 0021-9606, 1089-7690. DOI: 10.1063/1.4869598.

[37] G. Kresse and J. Furthmüller. "Efficient iterative schemes for ab initio total-energy calculations using a plane-wave basis set". In: *Phys. Rev. B* 54.16 (Oct. 1996), pp. 11169–11186. DOI: 10.1103/PhysRevB.54.11169.

[38] G. Kresse and J. Furthmüller. "Efficiency of ab-initio total energy calculations for metals and semiconductors using a plane-wave basis set". In: *Comput. Mater. Sci.* 6.1 (July 1996), pp. 15–50. ISSN: 0927-0256. DOI: 10.1016/0927-0256(96)00008-0.

[39] P. E. Blöchl. "Projector augmented-wave method". In: *Phys. Rev. B* 50.24 (Dec. 1994), pp. 17953–17979. DOI: 10.1103/PhysRevB.50.17953.

[40] G. Kresse and D. Joubert. "From ultrasoft pseudopotentials to the projector augmented-wave method". In: *Phys. Rev. B* 59.3 (Jan. 1999), pp. 1758–1775. DOI: 10.1103/PhysRevB.59.1758.

[41] Anubhav Jain et al. "Commentary: The Materials Project: A materials genome approach to accelerating materials innovation". In: *APL Mater.* 1.1 (July 2013), p. 011002. DOI: 10.1063/1.4812323.

[42] R. W. G. Wyckoff. *Crystal Structures, Vol. 1.* 2nd edition. Wiley, Jan. 1963. ISBN: 978-0-470-96860-4.

[43] Otfried Madelung. *Semiconductors: Data Handbook.* Springer Science & Business Media, 2004. ISBN: 978-3-540-40488-0.

[44] K. K. Kam and B. A. Parkinson. "Detailed photocurrent spectroscopy of the semiconducting group VIB transition metal dichalcogenides". In: *The Journal of Physical Chemistry* 86.4 (Feb. 1982), pp. 463–467. ISSN: 0022-3654, 1541-5740. DOI: 10.1021/j100393a010. URL: https://pubs.acs.org/doi/10.1021/j100393a010 (visited on 10/06/2021).

[45] D. A. Evans et al. "Determination of the optical band-gap energy of cubic and hexagonal boron nitride using luminescence excitation spectroscopy". In: *Journal of Physics: Condensed Matter* 20.7 (Jan. 2008). Publisher: IOP Publishing, p. 075233. ISSN: 0953-8984. DOI: 10.1088/0953-8984/20/7/075233.

[46] Yu Li Huang et al. "Bandgap tunability at single-layer molybdenum disulphide grain boundaries". In: *Nature Communications* 6.1 (Feb. 2015), p. 6298. ISSN: 2041-1723. DOI: 10.1038/ncomms7298. URL: http://www.nature.com/articles/ncomms7298 (visited on 10/06/2021).

[47] Miguel M. Ugeda et al. "Giant bandgap renormalization and excitonic effects in a monolayer transition metal dichalcogenide semiconductor". In: *Nature Materials* 13.12 (Dec. 2014), pp. 1091–1095. ISSN: 1476-1122, 1476-4660. DOI: 10.1038/nmat4061. URL: http://www.nature.com/articles/nmat4061 (visited on 06/11/2018).

[48] Bairen Zhu, Xi Chen, and Xiaodong Cui. "Exciton Binding Energy of Monolayer WS_2". In: *Scientific Reports* 5.1 (Aug. 2015). ISSN: 2045-2322. DOI: 10.1038/srep09218. URL: http://www.nature.com/articles/srep09218 (visited on 11/07/2018).

[49] Chendong Zhang et al. "Probing Critical Point Energies of Transition Metal Dichalcogenides: Surprising Indirect Gap of Single Layer WSe2". In: *Nano Letters* 15.10 (Oct. 2015). Publisher: American Chemical Society, pp. 6494–6500. ISSN: 1530-6984. DOI: 10.1021/acs.nanolett.5b01968. URL: https://doi.org/10.1021/acs.nanolett.5b01968 (visited on 10/06/2021).

[50] Georg K. H. Madsen and David J. Singh. "BoltzTraP. A code for calculating band-structure dependent quantities". In: *Comput. Phys. Commun.* 175.1 (July 2006), pp. 67–71. ISSN: 0010-4655. DOI: 10.1016/j.cpc.2006.03.007.

[51] Shuying Zhong, Musheng Wu, and Xueling Lei. "First-principle calculations of effective mass of silicon crystal with vacancy defects". In: *Mater. Sci.-Poland* 34.4 (2016), pp. 916–923.

[52] Decai Yu, Yu Zhang, and Feng Liu. "First-principles study of electronic properties of biaxially strained silicon: Effects on charge carrier mobility". In: *Phys. Rev. B* 78.24 (2008), p. 245204.

[53] Luqing Wang, Alex Kutana, and Boris I Yakobson. "Many-body and spin-orbit effects on direct-indirect band gap transition of strained monolayer MoS_2 and WS_2". In: *Ann. Phys.* 526.9-10 (2014), pp. L7–L12.

[54] Andor Kormányos et al. "k· p theory for two-dimensional transition metal dichalcogenide semiconductors". In: *2D Mater.* 2.2 (2015), p. 022001.

[55] Vei Wang et al. "VASPKIT: a user-friendly interface facilitating high-throughput computing and analysis using VASP code". In: *Comput. Phys. Commun.* (2021), p. 108033.

[56] Tomáš Rauch, Miguel AL Marques, and Silvana Botti. "Local modified Becke-Johnson exchange-correlation potential for interfaces, surfaces, and two-dimensional materials". In: *J. Chem. Theory Comput.* 16.4 (2020), pp. 2654–2660.

[57] Abhilash Patra et al. "Efficient Band Structure Calculation of Two-Dimensional Materials from Semilocal Density Functionals". In: *J. Phys. Chem. C* (2021).

[58] Fabien Tran et al. "Bandgap of two-dimensional materials: Thorough assessment of modern exchange–correlation functionals". In: *The Journal of Chemical Physics* 155.10 (Sept. 2021), p. 104103. ISSN: 0021-9606. DOI: 10.1063/5.0059036. URL: http://aip.scitation.org/doi/10.1063/5.0059036 (visited on 11/17/2021).

[59] Peter Blaha et al. *WIEN2k: An Augmented Plane Wave Plus Local Orbitals Program for Calculating Crystal Properties*. Techn. Universitat, 2019. ISBN: 978-3-9501031-1-3.

[60] Peter Blaha et al. "WIEN2k: An APW+ lo program for calculating the properties of solids". In: *J. Chem. Phys.* 152.7 (2020), p. 074101.

[61] Jianwei Sun, Adrienn Ruzsinszky, and John P. Perdew. "Strongly Constrained and Appropriately Normed Semilocal Density Functional". In: *Phys. Rev. Lett.* 115.3 (July 2015), p. 036402. DOI: 10.1103/PhysRevLett.115.036402.

[62] Thomas R. Mattsson et al. "Validating density-functional theory simulations at high energy-density conditions with liquid krypton shock experiments to 850 GPa on Sandia's Z machine". In: *Phys. Rev. B* 90.18 (Nov. 2014), p. 184105. ISSN: 1098-0121, 1550-235X. DOI: 10.1103/PhysRevB.90.184105.

[63] R Sternheimer. "On nuclear quadrupole moments". In: *Physical Review* 84.2 (1951), p. 244.

[64] Feliciano Giustino, Marvin L Cohen, and Steven G Louie. "GW method with the self-consistent Sternheimer equation". In: *Physical Review B* 81.11 (2010), p. 115105.

[65] J. Laflamme Janssen et al. "Precise effective masses from density functional perturbation theory". In: *Phys. Rev. B* 93.20 (May 2016), p. 205147. DOI: 10.1103/PhysRevB.93.205147.

[66] Robert Laskowski and Peter Blaha. "Calculating NMR chemical shifts using the augmented plane-wave method". In: *Physical Review B* 89.1 (2014), p. 014402.

[67] Xinguo Ren et al. "All-electron periodic G_0W_0 implementation with numerical atomic orbital basis functions: Algorithm and benchmarks". In: *Physical Review Materials* 5.1 (2021), p. 013807.

[68] RN Dexter and Benjamin Lax. "Effective masses of holes in silicon". In: *Physical Review* 96.1 (1954), p. 223.

[69] P Rochon and E Fortin. "Photovoltaic effect and interband magneto-optical transitions in InP". In: *Physical Review B* 12.12 (1975), p. 5803.

[70] Yu. G. Andreev and T. Lundström. "On the influence of nitrogen pressure on the ordering of hexagonal boron nitride". In: *J. Alloys Compd.* 216.1 (Dec. 1994), pp. L5–L7. ISSN: 0925-8388. DOI: 10.1016/0925-8388(94)91027-8.

[71] Hugo Henck et al. "Direct observation of the band structure in bulk hexagonal boron nitride". In: *Phys. Rev. B* 95.8 (Feb. 2017), p. 085410. DOI: 10.1103/PhysRevB.95.085410.

[72] Shin-ichiro Narita et al. "Far-Infrared Cyclotron Resonance Absorptions in Black Phosphorus Single Crystals". In: *J. Phys. Soc. Jpn.* 52.10 (Oct. 1983), pp. 3544–3553. ISSN: 0031-9015. DOI: 10.1143/JPSJ.52.3544.

[73] P. B. James and M. T. Lavik. "The crystal structure of $MoSe_2$". In: *Acta Crystallogr.* 16.11 (Nov. 1963), pp. 1183–1183. ISSN: 0365-110X. DOI: 10.1107/S0365110X6300311X.

[74] Wencan Jin et al. "Direct Measurement of the Thickness-Dependent Electronic Band Structure of MoS_2 Using Angle-Resolved Photoemission Spectroscopy". In: *Phys. Rev. Lett.* 111.10 (2013), p. 106801. DOI: 10.1103/PhysRevLett.111.106801.

[75] Iori Tanabe et al. "Band structure characterization of WS_2 grown by chemical vapor deposition". In: *Appl. Phys. Lett.* 108.25 (June 2016), p. 252103. ISSN: 0003-6951. DOI: 10.1063/1.4954278.

[76] Wencan Jin et al. "Substrate interactions with suspended and supported monolayer MoS_2: Angle-resolved photoemission spectroscopy". In: *Phys. Rev. B* 91.12 (Mar. 2015), p. 121409. DOI: 10.1103/PhysRevB.91.121409.

[77] T Eknapakul et al. "Electronic structure of a quasi-freestanding MoS_2 monolayer". In: *Nano letters* 14.3 (2014), pp. 1312–1316.

[78] Riccardo Pisoni et al. "Interactions and Magnetotransport through Spin-Valley Coupled Landau Levels in Monolayer MoS_2". In: *Phys. Rev. Lett.* 121.24 (Dec. 2018), p. 247701. DOI: 10.1103/PhysRevLett.121.247701.

[79] Horacio Coy Diaz et al. "Substrate dependent electronic structure variations of van der Waals heterostructures of $MoSe_2$ or $MoSe_{2(1-x)}Te_{2x}$ grown by van der Waals epitaxy". In: *2D Mater.* 4.2 (May 2017), p. 025094. ISSN: 2053-1583. DOI: 10.1088/2053-1583/aa6e6a.

[80] Neil R Wilson et al. "Determination of band offsets, hybridization, and exciton binding in 2D semiconductor heterostructures". In: *Sci. Adv.* 3.2 (2017), e1601832.

[81] Stefano Larentis et al. "Large effective mass and interaction-enhanced Zeeman splitting of K-valley electrons in $MoSe_2$". In: *Phys. Rev. B* 97.20 (May 2018), p. 201407. DOI: 10.1103/PhysRevB.97.201407.

[82] Søren Ulstrup et al. "Spatially Resolved Electronic Properties of Single-Layer WS_2 on Transition Metal Oxides". In: *ACS Nano* 10.11 (Nov. 2016), pp. 10058–10067. ISSN: 1936-0851. DOI: 10.1021/acsnano.6b04914.

[83] Maciej Dendzik et al. "Growth and electronic structure of epitaxial single-layer WS_2 on Au(111)". In: *Phys. Rev. B* 92.24 (Dec. 2015), p. 245442. DOI: 10.1103/PhysRevB.92.245442.

Appendix A

Supplementary Information: Pressure dependence of direct optical transitions in ReS_2 and $ReSe_2$

This appendix contains the supplementary information for Chapter 4.

Supplementary material for:
Pressure dependence of direct optical transitions of ReS_2 and $ReSe_2$

R. Oliva,[1†]* M. Laurien,[2†] F. Dybala,[1] J. Kopaczek ,[1] Y. Quin,[3] S. Tongay[3], O. Rubel,[2] and R. Kudrawiec[1]

[1]Department of Experimental Physics, Faculty of Fundamental Problems of Technology, Wroclaw University of Science and Technology, Wybrzeże Wyspiańskiego 27, 50-370 Wrocław, Poland
[2]Department of Materials Science and Engineering, McMaster University, JHE 359, 1280 Main Street West, Hamilton, Ontario L8S 4L8, Canada
[3]Department of Materials Science and Engineering, University of California, Berkeley, California 94720, USA
* Corresponding author: robert.oliva.vidal@pwr.edu.pl
† These authors contributed equally to this work

I. Polarization measurements

Since the broadening parameter of the excitonic transitions at ambient pressure is around ≈ 20 meV, it is difficult to spectrally resolve and fit all the transitions that coexist in a range smaller than ≈ 40 meV. In order to evaluate all the excitonic transitions and their pressure dependence, polarization-resolved measurements have been performed at selected pressures (spectra for ReS_2 are shown in Figs S1 and S2, and spectra for $ReSe_2$ in Figs. S3 and S4). From these polarization-dependent spectra the Aspnes formula was fitted assuming that the phase, energy and broadening parameters are independent of polarization angle, and taking only the amplitude as a free parameter. Within this method, we found that three transitions are enough to describe all the features present in the PR spectra at all polarization angles for ReS_2 and two for $ReSe_2$, which is in good agreement with previous polarization-resolved measurements performed at ambient pressure.[1] The energies of the three fitted transitions of ReS_2 were within a spectral range of ≈60 meV. These results are in agreement with previous polarization-resolved measurements, which also report three close excitonic transitions within a spectral range of ≈100 meV.[2–4]

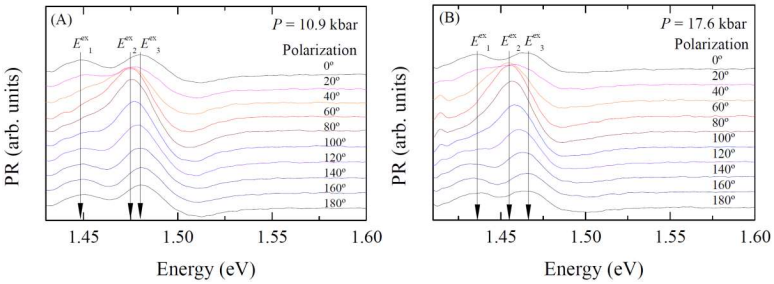

Fig. S1. Spectra of ReS_2 (Sample I) acquired at pressure 10.9 kbar (panel A) and 17.6 kbar (panel B) for different polarization angles. For visual purposes, the three excitonic energies are cualitativelly shown from the maxima of the PR signal.

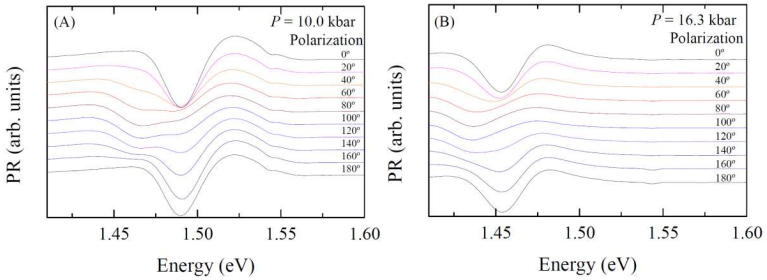

Fig. S2. Spectra of ReS_2 (sample II) acquired at pressure 10.0 kbar (panel A) and 16.3 kbar (panel B) for different polarization angles.

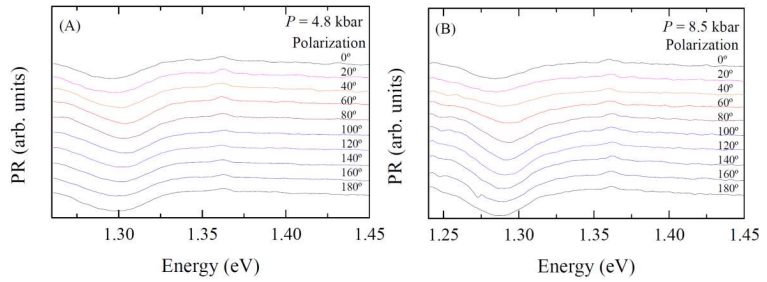

Fig. S3. Spectra of $ReSe_2$ (sample III) acquired at pressure 4.8 kbar (panel A) and 8.5 kbar (panel B) for different polarization angles.

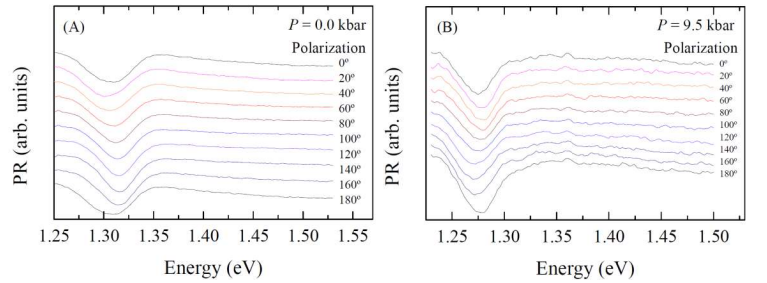

Fig. S4. Spectra of $ReSe_2$ (sample IV) acquired at pressure 0.0 kbar (panel A) and 9.5 kbar (panel B) for different polarization angles.

The polarization dependence of the amplitude of the fitted excitonic transitions of ReS_2 is shown for pressures of 10 kbar (open circles) and 16.3 kbar (full circles) in Fig. S5. and are plotted with a phase separation of 180 degrees to facilitate the comparison between pressures. By comparing the upper and lower half of the chart, it is clear that the amplitude and orientations for each transition is maintained with increasing pressure. This indicates that the sample did not suffer any structural transition, which is expected since the first phase transition takes place at higher pressures, around 113 kbar.[5] The angular dependence of the amplitudes is fitted by using a formula derived from the Malus law,

$$f(\varphi) = f_{\parallel}\cos^2(\varphi - \varphi_0) + f_{\perp}\sin^2(\varphi - \varphi_0), \qquad [S1]$$

where $f_{\parallel}$ and $f_{\perp}$ are the parallel and perpendicular components of the oscillator strength, and φ_0 the relative orientation of the excitonic transition. Following Fig. S5, the angular dependence of the amplitude of the most energetic transition (i.e. $E^{ex}{}_3$) is very weak, in agreement with previous polarization-resolved piezoreflectance measurements.[4] On the other hand, the first and second excitonic transitions (i.e. $E^{ex}{}_1$ and $E^{ex}{}_2$) are strongly polarized ($f_{\perp} \approx 0$) along the angles $\varphi_0 \approx 4°$ and 93°, respectively. These results are in relatively good agreement with previous works focused on the anisotropic properties of bulk ReS_2 by means of polarization-resolved PL performed at a temperature of 110 K.[6] This work found that the orientation of the $E^{ex}{}_1$ and $E^{ex}{}_2$ relative to the *b*-axis is $\varphi_0 \approx 17°$ and $\approx 86°$, respectively. During the loading process our samples were misoriented inside the press cell, but from the angular dependence of the excitons it was possible to determine the orientation of the *b*-axis for each sample with respect the vertical axis. These are $\varphi \approx 97°$ and $-13°$ for samples I and II, respectively.

The polarization dependence of the amplitudes for each transition in $ReSe_2$ is shown in Fig. S6 for the pressures 4.5 kbar and 8.5 kbar (upper and lower half of the chart, respectively). As it can be seen in the figure, the orientation and relative amplitude for each transition is preserved at different pressures, which is expected since $ReSe_2$ does not undergo any phase transition up to ≈100 kbar.[7] After fitting Eq. [S1] (plotted as solid curves) we found that both transitions are strongly polarized ($f_{\perp} \approx 0$) along the angles $\varphi_0 \approx 98°$ and 175°, hence with a relative angle of 77°. This result evidences that the orientation of the *b* axis for the sample III is $\varphi_0 \approx 98°$ since previous polarization-resolved measurements found that $E^{ex}{}_1$ is polarized along the *b* axis.[1,8] Using the same procedure for the sample IV we found that its orientation is $\varphi_0 \approx 157°$, which is significantly different from that of sample III.

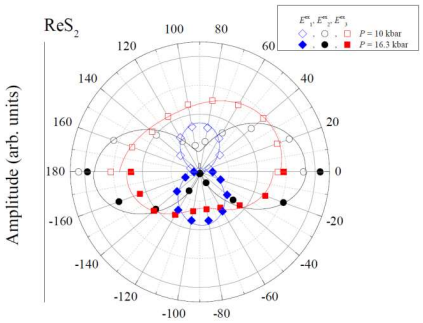

Fig. S5. Polar dependence of the amplitude for three fitted PR transitions in Sample II. The fittings have been performed at two different pressure values, 10.0 kbar (empty symbols, top) and 16.3 kbar (filled symbols, bottom). The solid curves are fits from Eq. [S1].

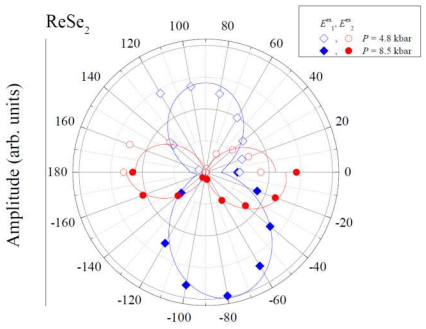

Fig. S6. Polar dependence of the amplitude for two fitted PR transitions in Sample III. The fittings have been performed at two different pressures, 4.5 kbar (empty symbols, top) and 8.5 kbar (full circles, bottom). The solid curves are fits from Eq. [S1].

II. Band structure calculations

II. A. Reciprocal coordinates

In order to intersect the space in a three-dimensional manner the k-path was prepared based on the suggestions of the seeK-path tool[79], according to which the path walks through the first Brillouin zone whilst returning frequently to the Γ (see *Figure 12 c* for illustration). Scaled reciprocal coordinates are listed for the special k-points in Table 2. The coordinates of the high-symmetry k-points can be found in Table S1.

Besides the energy eigenvalues, the optical matrix elements $M_{nm,\alpha}(k) = \langle \varphi_n(k) | d/dk_\alpha | \varphi_m(k) \rangle$ between bands n and m were calculated within a linear optical theory. The matrix element consists of three complex numbers. To estimate the scattering efficiency of the optical transition we evaluated the squared sum of the absolute values, $\sum_{\alpha=1}^{3} \left| M_{nm,\alpha} \right|^2$.

On a technical note, the number of bands was increased to 320 bands for the optical matrix element calculation, which is roughly a 2.5-fold value of the VASP default. This is necessary because the matrix calculation requires a large number of empty bands. Also, the number of frequency grid points (VASP: *NEDOS*-tag) was increased to 6000.

Table S1. Scaled reciprocal coordinates of special *k*-points of ReX_2 corresponding to the global valence band maximum (VBM) and conduction band minimum (CBM), as well as the k-points of the assigned direct transitions A and B.

Material	k-point	*a**	*b**	*c**	Function
ReS_2	Z	0.0	0.0	0.5	Transition A & CBM
	K1	0.05882	−0.05882	0.38235	Transition B
	K2	0.20588	−0.17600	0.294118	VBM
$ReSe_2$	J1	0.02941	0.14706	−0.20588	Transition A
	Z	0.0	0.0	0.5	Transition B
	J3	0.20588	0.38235	0.20588	CBM
	J2	0.08824	0.14706	−0.20588	VBM

Table S2. Scaled reciprocal coordinates of the high-symmetry k-points considered in the electronic dispersion calculations.

k-point	a*	b*	c*
Γ	0	0	0
X	0.5	0	0
Y	0	0.5	0
Z	0	0	0.5
V	0.5	0.5	0
U	0.5	0	0.5
T	0	0.5	0.5
R	0.5	0.5	0.5

The original lattices were transformed respective to their coordinate system to give credit to the convention of defining the Cartesian *z*-axis as perpendicular to the layers and lattice vector *c* as the out-of-plane vector crossing the 2D-layers (*Figure 12 b, d*). It should be noted that due to the offset in layer stacking the *c*-vector is not perpendicular to the layers. ReX_2 crystallizes in the T_d distorted octahedral configuration. In this configuration four Rhenium atoms group together to form so-called diamond-like clusters that are assembled in chains within the plane (*Figure 12 b, d*, right side, diamond chains are highlighted in red). The origin of the distortion in the crystallographic structure has been discussed in the light of the Jahn-Teller effect as well as quasi 1D-Peierls distortion.[9–11]

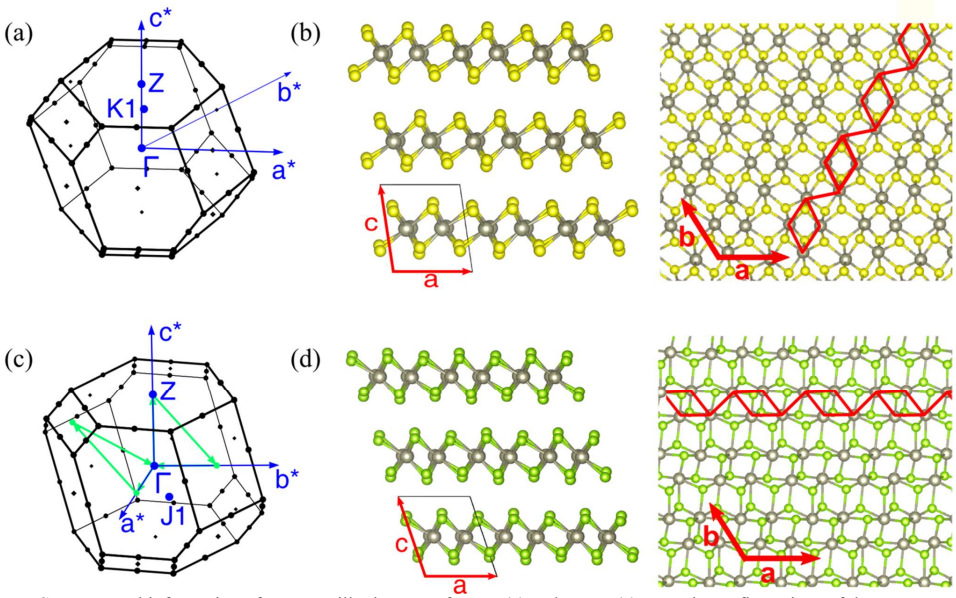

Fig. S7. Structural information of ReX_2. Brillouin zone of ReS_2, (a) and $ReSe_2$ (c). Atomic configurations of the distorted T_d structure for ReS_2 (b) and $ReSe_2$ (d).

II. B. Pressure dependence of the lattice parameters

After structure relaxation at a pressure of 0 kbar, the calculated (experimental[12,13]) lattice parameters are a = 6.438 Å (6.450 Å), b = 6.498 Å (6.390 Å), c = 6.357 Å (6.403 Å) and α = 106.556° (105.49 °), β = 88.154° (91.32 °), γ = 121.359° (119.03°) for ReS_2 and a = 6.578 Å (6.597 Å), b = 6.749 Å (6.710 Å), c = 6.784 Å (6.721 Å) and α = 95.30° (91.84°), β = 103.30° (104.9°), γ = 119.74° (118.91°) for $ReSe_2$. With increasing pressure, the c lattice parameter decreases most strongly, around 2.9-2.6 % at 20 kbar. In contrast, lattice parameters a and b are compressed by less than 0.5 % and the lattice angles vary only slightly.

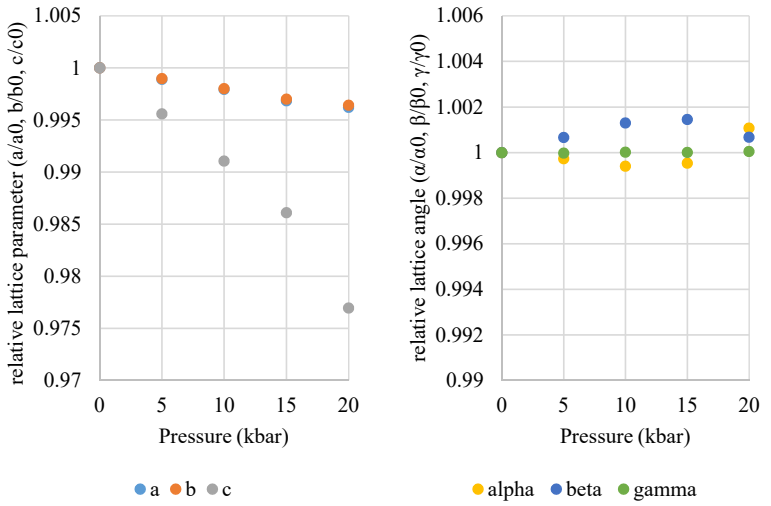

Fig. S8. Pressure dependence of the calculated lattice parameters and relative lattice angles for ReS_2

a. ReS_2

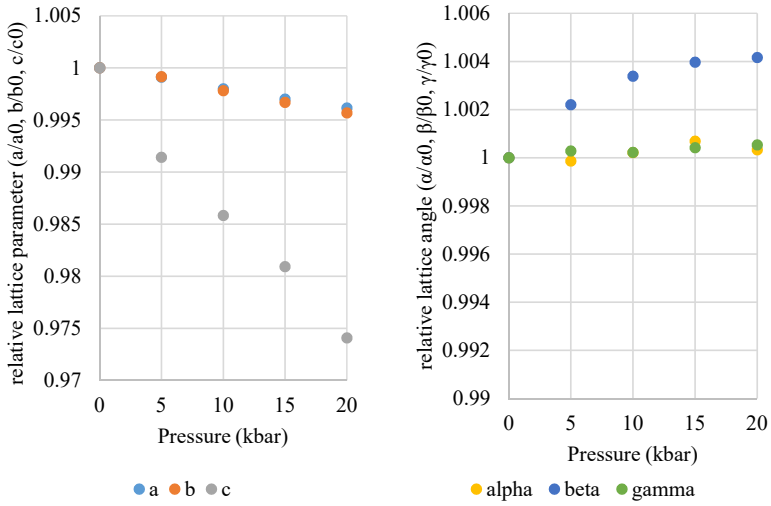

Fig. S9. Pressure dependence of the calculated lattice parameters and relative lattice angles for $ReSe_2$

4 – Theoretical pressure coefficient determination

a. ReS_2

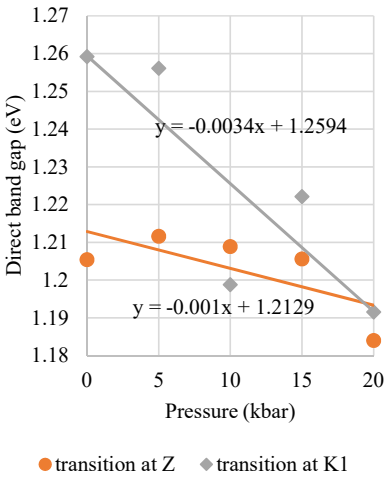

Fig. S10. Pressure dependence of the direct band gap energy for the transitions at the Z and K1 k-point of ReS2. The pressure coefficient is taken as the slope of the linear fit. Eigenvalues of the state with the highest local matrix element value are taken. The pressure coefficients are −1 meV/kbar^{-1} and −3.4 meV/kbar^{-1} for Z and K1, respectively, with respective errors of ±0.6 meV/kbar for Z and ±1.2 meV/kbar. Despite uncertainties in the calculated energies, it can be clearly seen that the transition at K1 exhibits a significantly lower pressure coefficient compared to the transition at Z.

b. $ReSe_2$

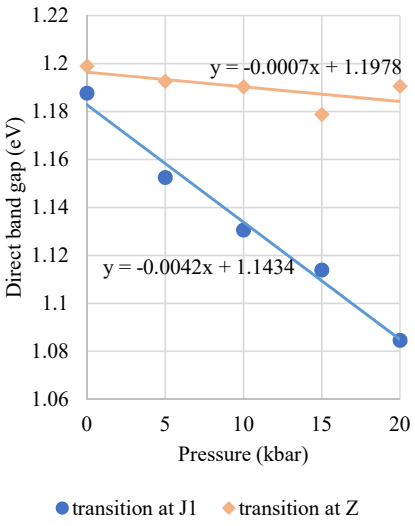

Fig. S11. Pressure dependence of the direct band gap energy for the transitions at the J1 and Z k-point of ReSe2. The pressure coefficient is taken as the slope of the linear fit. Eigenvalues of the state with the highest local matrix element value are taken. The pressure coefficients are −4.2 meV/kbar^{-1} and −0.7 meV/kbar^{-1} for J1 and Z, respectively, with errors of about ±0.3 meV/kbar for J1 and ±0.4 meV/kbar for Z.

II. C. Calculations within the HSE06 functional

Hybrid functional calculations were performed for ReX_2 following the approach of Ref. [14] to verify the relative energy levels of the valence and conduction bands at important points in momentum space. As input structure the SCAN-relaxed structures were taken. The calculations were carried out using VASP with the HSE06[15] functional. Gaussian smearing of the partial occupancies of the orbitals was set to a width of 0.05 eV to accelerate the electronic convergence.

The band gap at 0 kbar and 20 kbar was determined for the Z and K1 points for ReS_2 and the J1 and Z points for $ReSe_2$. It can be seen that the HSE direct band gaps are approximately 0.4 eV larger than the SCAN calculated band gaps, for both ReS_2 and $ReSe_2$ (see Table S2 and Table S3). Considering the exciton binding energies, the direct band gaps are close to our experimentally obtained transitions. For example, considering an exciton binding energy $E_b \approx$ 200 meV[16] for bulk ReS_2, the HSE band gap at 0 kbar is reduced to 1.42 eV which is close to the experimental value of 1.50 eV. For $ReSe_2$, with $E_b \approx$ 120 meV[17] (or $E_b \approx$ 220 meV[16]) the HSE optical band gap becomes 1.43 eV (1.31 eV for HSE-exBindEn) close to the experimental value of 1.307 eV.

A simplified pressure coefficient was calculated taking into account the change of the band gap between 0 and 20 kbar only, omitting the 5, 10, and 15 kbar steps. While the absolute values of the direct band gaps differ between HSE and SCAN calculations as expected, the trends with pressure are very similar. The pressure coefficients, though slightly higher for HSE06 calculations, allow for the same clear assignment of transitions A and B as done with the DFT results (see Table S2 and Table S3).

Table S3. Comparison of the HSE06 and DFT results for ReS_2. The HSE band gap is higher than the DFT band gap. The (simplified) pressure coefficient is very similar between both approximations: the assignment of transition A and B to the Z and K1 points in the Brilloin zone is not affected.

ReS2	Z point (Transition A)		K1 point (Transition B)	
	HSE06	DFT (SCAN)	HSE06	DFT (SCAN)
Band gap, 0 kbar (eV)	1.620	1.198	1.634	1.208
Band gap, 20 kbar(eV)	1.586	1.166	1.588	1.163
Pressure coefficient (simplified) (meV/kbar)	−1.730	−1.589	−2.313	−2.220

Table S4. Comparison of the HSE06 and DFT results for $ReSe_2$. The HSE band gap is higher than the DFT band gap. The (simplified) pressure coefficient is very similar between both approximations: the assignment of transition A and B to the J1 and Z points in the Brillouin zone is not affected.

ReSe2	J1 point (Transition A)		Z point (Transition B)	
	HSE06	DFT (SCAN)	HSE06	DFT (SCAN)
Band gap, 0 kbar (eV)	1.55	1.15	1.59	1.19
Band gap, 20 kbar (eV)	1.45	1.06	1.56	1.17
Pressure coefficient (simplified) (meV/kbar)	−4.99	−4.45	−1.15	−0.86

II. D. Convergence tests with kinetic cutoff energy

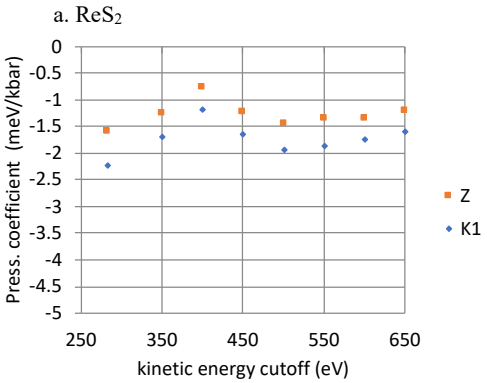

Fig. S12. Convergence of the pressure coefficient with increasing kinetic energy cutoff for ReS_2. A simplified pressure coefficient was calculated; considering only the band gap energies at 0 and 20 kbar. Structures were fully relaxed for each cutoff before calculating the band structure. The pressure coefficients of the direct band gaps at the Z and K1 point vary with the cutoff, however their relative placement does not change so that the assignment of the transitions A and B is unaffected.

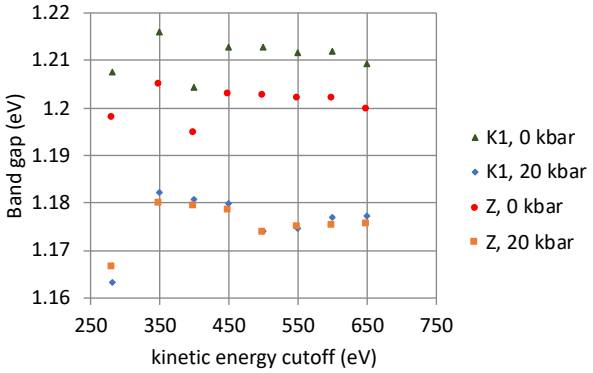

Fig. S13. Convergence of the band gap at 0 and 20 kbar with increasing kinetic energy cutoff for ReS_2. While the values vary, and a slight increase of the band gap can be noted with increasing convergence, the trends remain unchanged: At 0 kbar, the lowest energy direct band gap is located at Z, at 20 kbar the direct band gaps at the Z and K1 points are very close in energy.

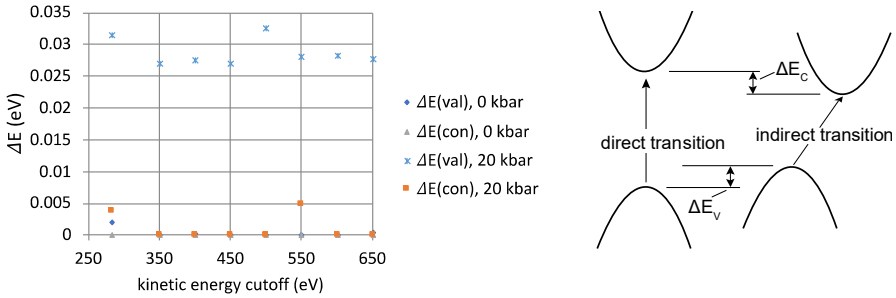

Fig. S14. Change of the band structure with increasing kinetic energy cutoff for ReS_2. Shown are the differences between the valence band energies at the direct band gap and the fundamental band gap ΔE_v and the analogous difference for the conduction band ΔE_c as visualized in the schematic picture on the right. If the direct band gap is located at the global VBM (CBM), ΔE_v (ΔE_c) has the value zero. For ReS_2 the ΔE_v and ΔE_c remain overall constant with only minor variations. This shows that the character of the band gap is conserved with increasing energy cutoff: the fundamental band gap is quasi-direct (or slightly indirect) at 0 kbar and indirect at 20 kbar. Small variations stem from the presence of many valence band maxima that are very close in energy.

b. $ReSe_2$

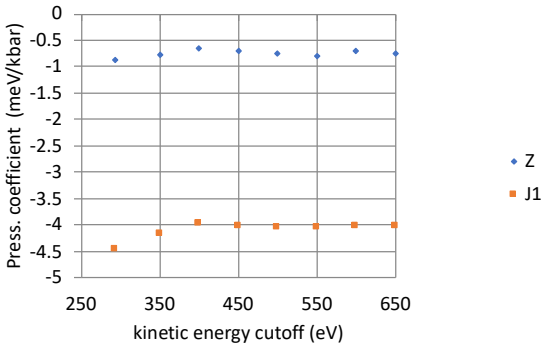

Fig. S15. Convergence of the pressure coefficient with increasing kinetic energy cutoff for $ReSe_2$. A simplified pressure coefficient was calculated; considering only the band gap energies at 0 and 20 kbar. Structures were fully relaxed for each cutoff before calculating the band structure. The pressure coefficients of the direct band gaps at the Z and J1 point vary with the cutoff, however their relative placement does not change so that the assignment of the transitions A and B is unaffected.

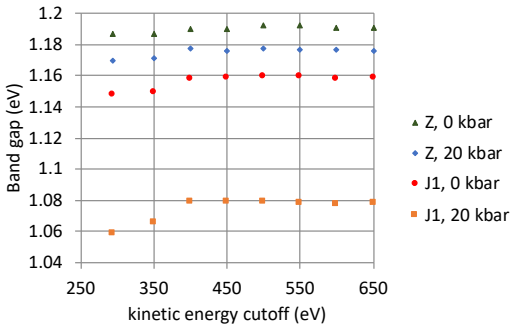

Fig. S16. Convergence of the band gap at 0 and 20 kbar with increasing kinetic energy cutoff for $ReSe_2$. While the values vary, and a slight increase of the band gap can be noted with increasing convergence, the trends remain unchanged: At 0 kbar, the lowest energy direct band gap is located off the high-symmetry points at J1 and the second-lowest at the Z point, at 20 kbar the energy difference between them is significantly greater.

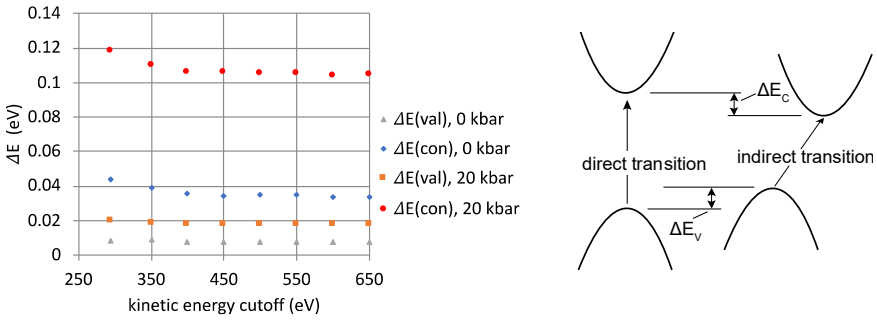

Fig. S17. Change of the band structure with increasing kinetic energy cutoff for $ReSe_2$. Shown are the differences between the valence band energies at the direct band gap and the fundamental band gap ΔE_v, and the analogous difference for the conduction band ΔE_c as visualized in the schematic picture on the right. If the direct band gap is located at the global VBM (CBM), ΔE_v (ΔE_c) has the value zero. In the graph the differences remain very similar with increasing cutoff energy. This shows that indirect character of the band gap is conserved.

References

1. Hu, S. Y. *et al.* Growth and characterization of tungsten and molybdenum-doped ReSe2 single crystals. *Journal of Alloys and Compounds* **383**, 63–68 (2004).
2. Ho, C. H., Huang, Y. S., Chen, J. L., Dann, T. E. & Tiong, K. K. Electronic structure of ReS_2 and $ReSe_2$ from first-principles calculations, photoelectron spectroscopy, and electrolyte electroreflectance. *Phys. Rev. B* **60**, 15766–15771 (1999).
3. Aslan, O. B., Chenet, D. A., van der Zande, A. M., Hone, J. C. & Heinz, T. F. Linearly Polarized Excitons in Single- and Few-Layer ReS2 Crystals. *ACS Photonics* **3**, 96–101 (2016).
4. Ho, C. H., Huang, Y. S., Tiong, K. K. & Liao, P. C. In-plane anisotropy of the optical and electrical properties of layered ReS_2 crystals. *J. Phys.: Condens. Matter* **11**, 5367 (1999).
5. Hou, D. *et al.* High pressure X-ray diffraction study of ReS2. *Journal of Physics and Chemistry of Solids* **71**, 1571–1575 (2010).
6. Lin, D. Y. *et al.* Anisotropy of Photoluminescence in Layered Semiconductors ReS_2 and ReS_2:Au. *Solid State Phenomena* **170**, 135–138 (2011).
7. Kao, Y.-C. *et al.* Anomalous structural phase transition properties in ReSe2 and Au-doped ReSe2. *J Chem Phys* **137**, 024509 (2012).
8. Jian, Y.-C., Lin, D.-Y., Wu, J.-S. & Huang, Y.-S. Optical and Electrical Properties of Au- and Ag-Doped ReSe2. *Jpn. J. Appl. Phys.* **52**, 04CH06 (2013).
9. Whangbo, M. H. & Canadell, E. Analogies between the concepts of molecular chemistry and solid-state physics concerning structural instabilities. Electronic origin of the structural modulations in layered transition metal dichalcogenides. *J. Am. Chem. Soc.* **114**, 9587–9600 (1992).

10. Kertesz, M. & Hoffmann, R. Octahedral vs. trigonal-prismatic coordination and clustering in transition-metal dichalcogenides. *J. Am. Chem. Soc.* **106**, 3453–3460 (1984).

11. Choi, J.-H. & Jhi, S.-H. Origin of distorted 1 T -phase ReS 2 : first-principles study. *J. Phys.: Condens. Matter* **30**, 105403 (2018).

12. Ho, C. H., Huang, Y. S., Liao, P. C. & Tiong, K. K. Crystal structure and band-edge transitions of $ReS_{2-x}Se_x$ layered compounds. *Journal of Physics and Chemistry of Solids* **60**, 1797–1804 (1999).

13. Lamfers, H.-J., Meetsma, A., Wiegers, G. A. & de Boer, J. L. The crystal structure of some rhenium and technetium dichalcogenides. *Journal of Alloys and Compounds* **241**, 34–39 (1996).

14. Biswas, D. *et al.* Narrow-band anisotropic electronic structure of ReS_2. *Phys. Rev. B* **96**, 085205 (2017).

15. Krukau, A. V., Vydrov, O. A., Izmaylov, A. F. & Scuseria, G. E. Influence of the exchange screening parameter on the performance of screened hybrid functionals. *J. Chem. Phys.* **125**, 224106 (2006).

16. Echeverry, J. P. & Gerber, I. C. Theoretical investigations of the anisotropic optical properties of distorted 1T ReS2 and ReSe2 monolayers, bilayers, and in the bulk limit. *Phys. Rev. B* **97**, 075123 (2018).

17. Arora, A. *et al.* Highly Anisotropic in-Plane Excitons in Atomically Thin and Bulklike 1T′-ReSe2. *Nano Lett.* **17**, 3202–3207 (2017).

Appendix B

Supplementary Information: Exploration of the bright and dark exciton landscape and fine structure of MoS_2 (using G_0W_0-BSE)

This appendix contains the supplementary information for Chapter 5.

Supplementary material for:

Exploration of the bright and dark exciton landscape and fine structure of MoS2 (using G0W0-BSE)

Hongyu Yu,[1,2] M. Laurien,[1*] Zhenpeng Hu,[2] and O. Rubel[1†]

[1]*Department of Materials Science and Engineering, McMaster University, 1280 Main Street West, Hamilton, Ontario L8S 4L7, Canada*
[2]*School of Physics, Nankai University, Tianjin 300071, China*

Convergence testing

Convergence of GW-BSE calculations is a multi-step procedure. The GW part of the calculation is the critical one, so generally convergence can focus on the GW part. For 2D-systems, though, the BSE calculation exhibits a strong dependence on the k-grid employed.

Therefore, this convergence study is laid out as follows:

1. Simplified GW calculation
    a. Screened cutoff (number of G-vectors) and the number of bands are converged together
    b. The number of frequency grid points is converged using the obtained screened cutoff and number of bands from step a)
2. Full BSE calculation
    a. Convergence with the k grid is tested

1. Simplified GW calculation

The simplifications consist of full use of symmetry, omitting spin-orbit coupling, and using a coarse k grid of 6x6x1. The convergence with respect to the k grid is independent from the other parameters, therefore we could choose an economical k grid here.

In step 1a) we first tested the dependence of the quasiparticle bandgap on the screened cutoff, keeping the number of bands and the number of frequency grid points at very high values (VASP tags: NBANDS=1000 and NOMEGA=256, respectively). In VASP, the screened cutoff is by default set to two-thirds of the plane wave cutoff (VASP tags: ENCUTGW=ENCUT*2/3).

The results are seen in Figure S1 a). At a plane wave cutoff of 550 eV (screened cutoff of 367 eV) and higher, the band gap at K varies only by less than 1 meV. At 400 eV, the value chosen for the main calculations of this paper, the band gap is converged within 3 meV.

Then, we tested the dependence of the quasiparticle bandgap on the number of bands (VASP tag: NBANDS), keeping the plane wave cutoff and the number of frequency grid points at very high values (VASP tags: ENCUT=700 and NOMEGA=256, respectively).

The results are seen in Figure S1 b). Employing 1024 bands, the band gap at K is 2.627 eV. For 640 bands, the value chosen for the main calculations of this paper, the band gap is 9 meV larger than for 1024 bands. It seems, that convergence is not yet reached at 1024 bands. From these tests we can estimate the band gap error of our main calculations to be in the range of 10s of meV.

In a subsequent step (1b), we employed a plane wave cutoff of 400 eV and set the number of bands to 640 (main calculation settings) to test the dependence of the band gap on the number of frequency grid points (VASP tag: NOMEGA).

The results are seen in Figure S2 a). For the band gap at K, we see a rapid decrease of the band gap with an increasing number of frequency grid points. Starting from 160 frequency grid points, the decrease slows down and changes happen at the meV scale, nearing convergence. Comparing the band gap at the highest number frequency grid points chosen here (256, band gap = 2.638 eV) with the value chosen for our main calculations (96, band gap = 2.70 eV), we overestimate the band gap by ca. 60 meV.

In summary, all three parameters taken together introduce an error of the band gap of less than 0.1 eV, which can be seen as the convergence goal for our purposes. Furthermore, the value of the band gap of 2.6 – 2.7 eV compares well with the benchmark of 2.67 eV established by Qiu et al.[49]. As a conclusion, our GW calculations can be regarded as a reliable basis for subsequent BSE calculations.

It should be noted that convergence tests were performed without taking the spin-orbit coupling into account. Results reported in the main text, however, included relativistic effects. We expect results of the convergence studies to be transferable.

2. Full GW-BSE calculation

In a final step, we used the full GW-BSE calculations as described in the main publication and tested the main conclusions of the spectral spacing of exciton energies at K on their k grid dependence. Here the spin-orbit coupling is included. The first main conclusion is that the spin-forbidden dark exciton at K is lower in energy than the bright exciton. This can be described by $\Delta E_{dark\text{-}bright} < 0$. The second main conclusion is that there exists an indirect exciton at K/K' that is even lower in energy than the direct dark

exciton at K. This can be described by $\Delta E_{dark\text{-}ind} > 0$. There are two different indirect excitons at K due to spin-orbit coupling: one is spin forbidden, the other spin-allowed. Therefore, we must distinguish between $\Delta E_{dark\text{-}ind\_spin\text{-}allowed}$ and $\Delta E_{dark\text{-}ind\_spin\text{-}forbidden}$.

The results are seen in Figure S2 b). It is clearly seen that after exceeding a k grid of 6 x 6 x 1, $\Delta E_{dark\text{-}bright}$ is always smaller than zero and $\Delta E_{dark\text{-}ind\_spin\text{-}allowed}$ ($\Delta E_{dark\text{-}ind\_spin\text{-}forbidden}$) is always negative (positive). Therefore, increasing the k grid does not change our main conclusions: the lowest-energy exciton is indirect at K/K' followed by the dark direct exciton at K. In fact, the differences of ΔE at different k grids are small; they are below 2 meV in all cases.

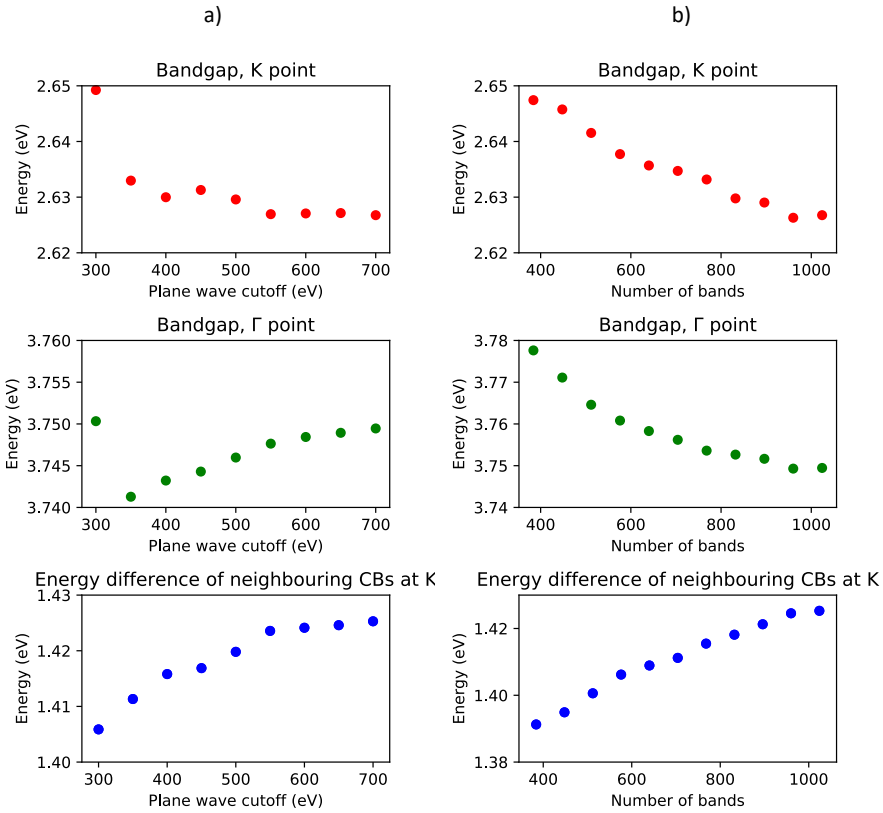

Figure S1: Convergence of the non-relativistic quasiparticle band gap with a) the screened cutoff (2/3 of the plane wave cutoff) and b) the number of bands. Shown are the bandgap at the K point, the gap at the Γ point and the differenced between the two lowest-energy conduction bands.These convergence tests were performed for a simplified GW setup.

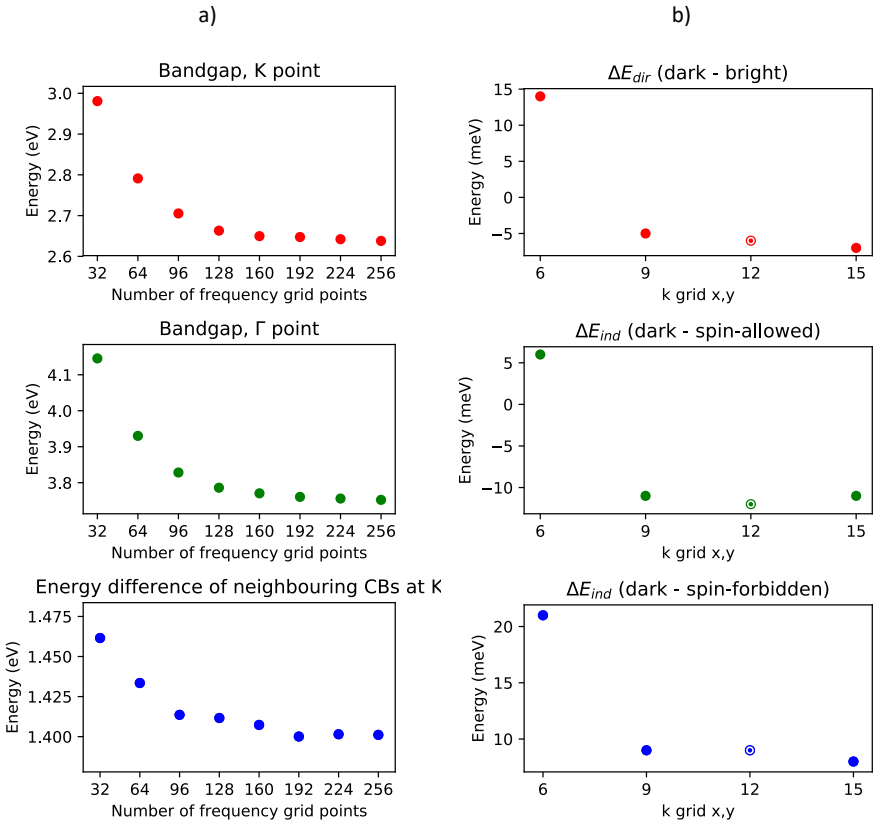

Figure S2: a) Convergence of the non-relativistic quasiparticle band gap with number of frequency grid points. Shown are the bandgap at the K point, the gap at the Γ point and the differenced between the two lowest-energy conduction bands.These convergence tests were performed for a simplified GW setup. b) Convergence of the spectral spacing of the main excitons at the K point with k grid. Shown are the energy difference between the direct bright and dark excitons at K, the energy difference between the dark direct exciton at K and the indirect spin-allowed exciton at K/K', as well as the energy difference between the dark direct exciton at K and the indirect spin-forbidden exciton at K/K'. The white circles indicate results for a calculation employing the Tamm-Dancoff approximation; the results are identical with the full BSE results.

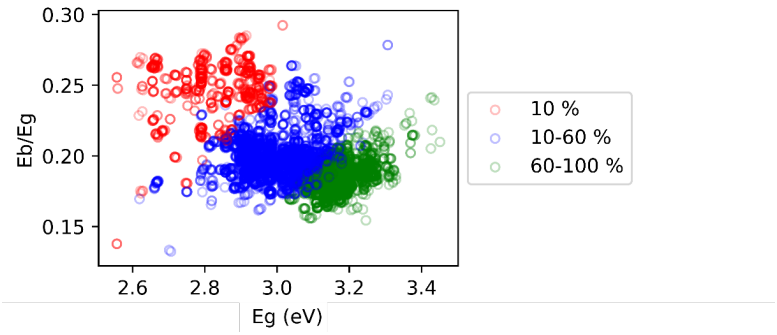

Figure S3: Change of the E_b/E_g ratio with E_g. E_b denotes the exciton binding energy and E_g the relativistic quasiparticle band gap energy. The color-coding marks reflect the percentage of lowest-energy excitons from the total of 100 excitons for each eigenstate (lowest-energy 10 % = red etc.). As a general trend, the E_b/E_g ratio decreases as the quasiparticle energy increases. This is due to screening of lower-energy excitons. This decrease explains why higher-energy excitons do not follow the E_b/E_g=0.25 rule.

Table S1: Dependence of the exciton binding energy on the *k* grid density. Here the exciton binding energy of the lowest-energy direct exciton at the K point is shown.

k grid	Exciton binding energy (eV)
15 x 15 x 1	0.551
12 x 12 x 1	0.637
9 x 9 x 1	0.790
6 x 6 x 1	1.061

Appendix C

Supplementary Information: Band alignment of monolayer CaP_3, $CaAs_3$, $BaAs_3$ and the role of p-d orbital interactions in the formation of conduction band minima

This appendix contains the supplementary information for Chapter 6.

Electronic Supplementary Material (ESI) for Physical Chemistry Chemical Physics.
This journal is © the Owner Societies 2021

Supplementary information: Band alignment of monolayer CaP_3, $CaAs_3$, $BaAs_3$ and the role of p-d orbital interactions in the formation of conduction band minima

Magdalena Laurien,[1,*] Himanshu Saini,[1] and Oleg Rubel[1,†]

[1]*Department of Materials Science and Engineering, McMaster University, 1280 Main Street West, Hamilton, Ontario L8S 4L7, Canada*

(Dated: March 4, 2021)

I. VASP STRUCTURE FILES (POSCAR)

CaAs3 monolayer

1.00000000000000

5.9673800467999998	0.0000000000000000	0.0000000000000000
1.0165732363000000	5.8803154649999998	0.0000000000000000
0.0000000000000000	0.0000000000000000	26.0000000000000000

Ca As

2 6

Direct

0.1769423339673324	0.1774698642655252	0.0843192194397560
0.0000016750081002	0.0000031145587513	0.1923299163679317
0.5550182146338116	0.5553423423773509	0.0925341103014574
0.6648516406207534	0.1335817668416936	0.0944098219129259
0.1332745527381149	0.6653217049443185	0.0944285201829231
0.0436701687153871	0.5121502125423447	0.1822206247786156
0.5120924785388894	0.0438910346111427	0.1822393138947689
0.6219257947279928	0.6221305888304300	0.1841156215831603

CaP3 monolayer

1.0

5.7089400291 0.0000000000 0.0000000000

0.9168738936 5.4873170208 0.0000000000

0.0000000000 0.0000000000 26.0000000000

Ca P

2 6

Direct

0.990673363 0.236208677 0.069827832

0.000045002 0.000023723 0.192322791

0.504078567 0.176318109 0.089228347

0.436399102 0.576579750 0.091769300

0.052144825 0.713358402 0.095917709

0.938541174 0.522884250 0.166239306

0.554308176 0.659748256 0.170394331

0.486642480 0.060008407 0.172931165

BaAs3 monolayer

1.00000000000000

6.4581198691999999 0.0000000000000000 0.0000000000000000

1.8406882982999999 6.1902486891999997 0.0000000000000000

0.0000000000000000 0.0000000000000000 26.0000000000000000

Ba As

2 6

Direct

0.1707610055466162 0.1707610052636852 0.0600013274230804

0.0000000000000000 0.0000000000000000 0.1923033457692327

0.5351630050496041 0.5351629619953329 0.0825415574615391

0.6681529921206035 0.1361709981814840 0.0858069291538470

0.1361710152654183 0.6681529718209944 0.0858069291538470

0.5026080206547903 0.0345905004387888 0.1664977440384590

0.0345905056370839 0.5026080011014997 0.1664977440384590

0.6355980209158645 0.6355979338704856 0.1697630882307664

Black phosphorene

1.00000000000000

4.5905542594727189 0.0000000000000000 0.0000000000000000

0.0000000000000000 3.2953912493002919 0.0000000000000000

0.0000000000000000 0.0000000000000000 24.6571569442999987

P

4

Direct

0.4116710144483093 0.0000000000000000 0.2588742328996148

0.5883289855290670 0.0000000000000000 0.1733393012103477

0.0883289707180026 0.5000000001209344 0.2588742328996148

0.9116710143238436 0.5000000001209344 0.1733393012103477

Puckered arsenene

1.00000000000000

4.6805338045812581 0.0000000000000000 0.0000000000000000

0.0000000000000000 3.6968139797539545 0.0000000000000000

0.0000000000000000 0.0000000000000000 24.0000000000000000

As

4

Direct

0.0687993159732372 0.0000000000000000 0.5501907684701308

0.9312007138572724 0.0000000000000000 0.4498092191132059

0.4312006842174441 0.4999999999591296 0.5501907684701308

0.5687992860791624 0.4999999999591296 0.4498092191132059

II. WANNIER INTERPOLATION OF THE BAND STRUCTURES

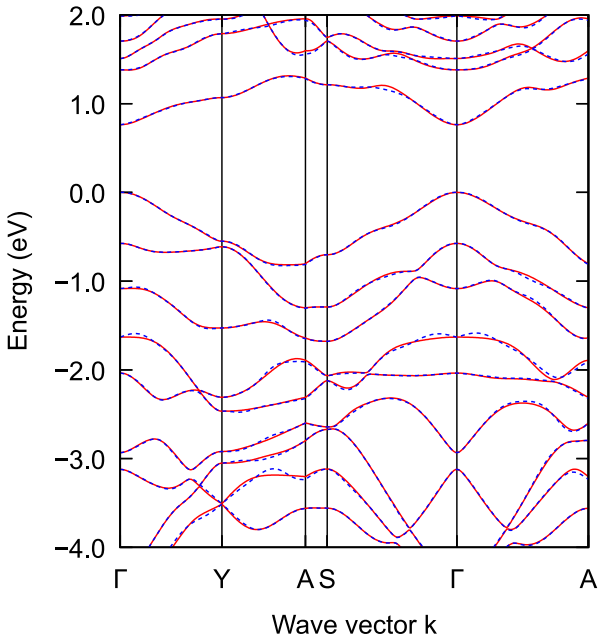

FIG. S1: PBE band structure of CaP_3. The red lines show the bandstructure obtained along a k path from Quantum Espresso[1], the blue dashed lines show the wannier interpolation along the same path from a $6 \times 6 \times 1$ k grid. The wannierization was performed with wannier90[2] for 100 iterations using random projections with 45 bands (20 valence and 25 conduction bands, each) as input to obtain 45 wannier functions.

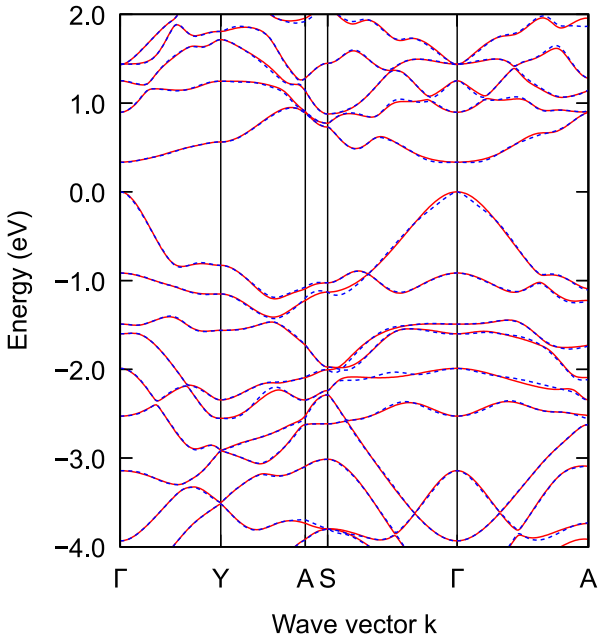

FIG. S2: PBE band structure of $CaAs_3$. The red lines show the bandstructure obtained along a k path from Quantum Espresso, the blue dashed lines show the wannier interpolation along the same path from a $6 \times 6 \times 1$ k grid. The wannierization was performed with wannier90 for 100 iterations using random projections with 40 bands (20 valence and 20 conduction bands, each) as input to obtain 40 wannier functions.

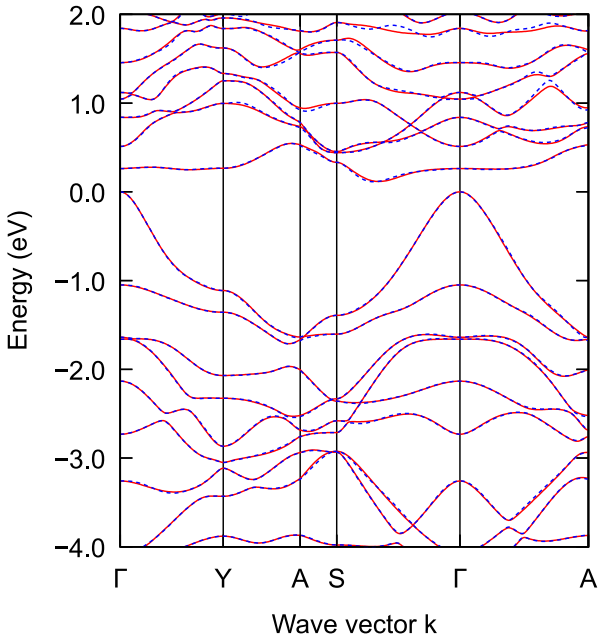

FIG. S3: PBE band structure of $BaAs_3$. The red lines show the bandstructure obtained along a k path from Quantum Espresso, the blue dashed lines show the wannier interpolation along the same path from a $6 \times 6 \times 1$ k grid. The wannierization was performed with wannier90 for 100 iterations using random projections with 40 bands (20 valence and 20 conduction bands, each) as input to obtain 40 wannier functions.

III. CALCIUM TRIARSENIDE / CALCIUM TRIPHOSPHIDE HETEROSTRUCTURE

To estimate the effect of charge transfer and band shifts in a heterojunction, we calculated the band alignment of a basic $CaAs_3$/CaP_3 heterostructure at the PBE level using VASP[11–15] (see Fig. S4). We note that for more accurate results, non-local effects should be included by using hybrid functionals.[3] The figure shows the band alignment with respect to the vacuum level (set to zero) of the unstrained monolayers, strained monolayers and the heterostructure consisting of the strained monolayers. The band alignment of the unstrained and strained monolayers reflect the alignment according to the electron affinity rule. The atom-projected band structure of the heterostructure is shown in Figure S5.

To create a heterostructure, we apply strain of less than 5 % in each direction, compressing $CaAs_3$ and straining CaP_3. As a result of the strain, the band gap of $CaAs_3$ decreases from 0.33 eV to 0.10 eV and the band gap of CaP_3 increases from 0.75 eV to 0.90 eV. The strained monolayers form a type-I heterojunction according the the electron affinity rule.

Combining the strained monolayers in a heterostructure leads to an overall downshift of the bands with respect the vacuum level. However, the relative band alignments are only slightly affected by creating a heterostructure. Also, the respective band gaps of the heterostructure do not close significantly compared to the strained monolayers. In effect, this means that there is a weaker dependence of the band gap on number of layers in the heterostructure than in a homo-bilayer.[4,5]

Further, weak to moderate hybridization of the valence and conduction band occurs which is due to overlap of the out-of-plane p_z and d_{z^2} orbital contributions. The weak nature of the hybridization allows us to still define proper band offsets. We also observe a charge transfer from CaP_3 to $CaAs_3$, which is indicated by the step in the vacuum level of -0.2 eV. Overall, the electron affinity rule predicts the band alignment of the heterostructure rather well for this $CaAs_3$/CaP_3 heterostructure.

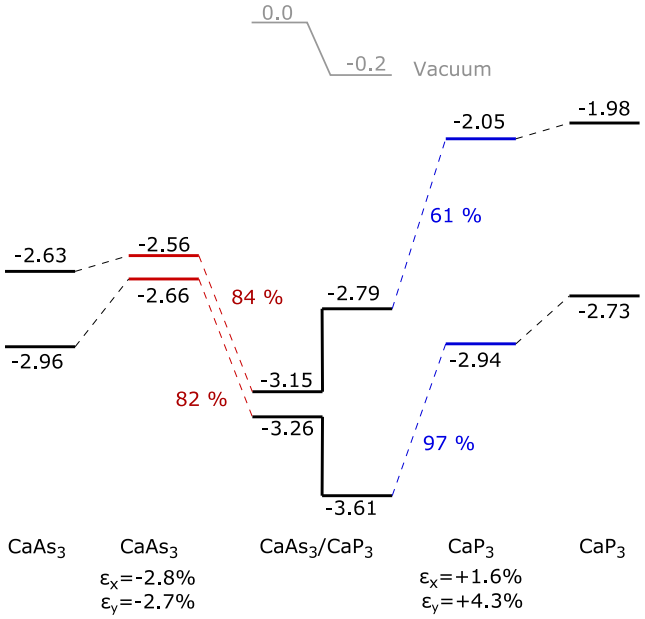

FIG. S4: Band alignment of the $CaAs_3/CaP_3$ heterostructure calculated with the PBE-D3 functional in VASP. The bands are aligned with respect to the vacuum level (set to zero) with values given in eV. Shown are the valence and conduction band at Γ of the fully relaxed monolayer, strained monolayer and for the heterostructure. Contributions to a state of the heterostructure are indicated as percentages along the dashed lines. The charge transfer from CaP_3 to $CaAs_3$ is evident from the step of the vacuum level introduced in the heterostructure.

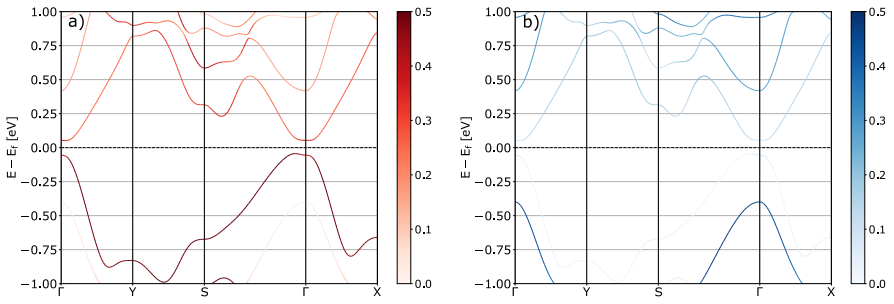

FIG. S5: PBE band structure of of the $CaAs_3/CaP_3$ heterostructure. a) Projected contribution of $CaAs_3$, b) projected contribution of CaP_3. The valence and conduction band are dominated by $CaAs_3$ while the immediate neighbouring bands are dominated by CaP_3. The band gap of the heterostructure is slightly indirect. The figures were obtained with the help the pyprocar[6] tool.

IV. PROJECTED DENSITY OF STATES

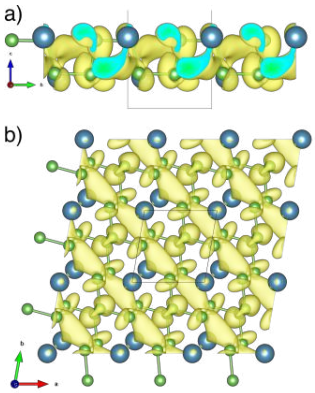

FIG. S6: a,b) Band and k point projected charge density of 1L $CaAs_3$ at for the conduction band at Λ. The isosurface is set at 0.0025 e/Å^3. At this isosurface level, the connection of the charge density lobes to the Ca atoms can be clearly seen.

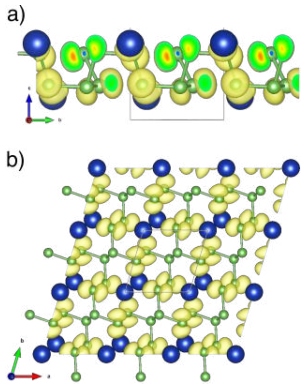

FIG. S7: a,b) Band and k point projected charge density of 1L $BaAs_3$ for the valence band at the Γ point. Isosurface: 0.004 e/Å^3.

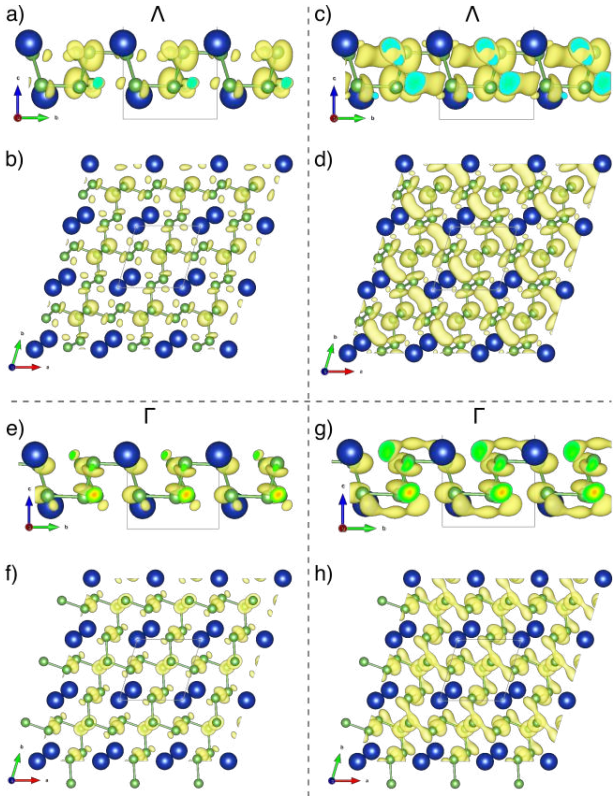

FIG. S8: a-d) Band and k point projected charge density of 1L $BaAs_3$ for the conduction band at Λ. The isosurface is set a,b) 0.004 e/Å^3 and c,d) 0.0025 e/Å^3. The 5d orbital of Ba is strongly delocalized. Because the d orbital is more spread out, the lobes become visible at an isosurface of 0.0025 e/Å^3 only. For comparison the band and k point projected charge density for the conduction band at the Γ point is shown in e-h). Isosurface: e,f) 0.004 e/Å^3, g,h) 0.0025 e/Å^3.

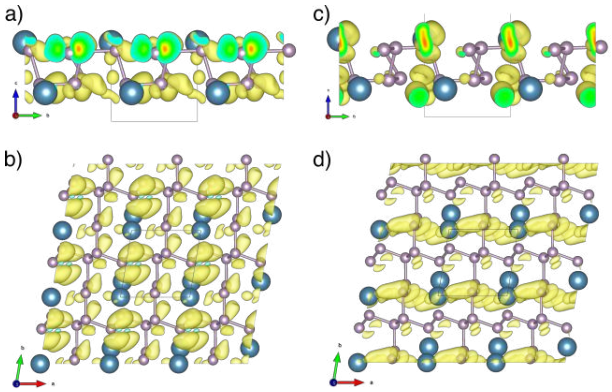

FIG. S9: a,b) Band and k point projected charge density of 1L CaP_3 for the valence band at the Γ point. The isosurface is set at 0.004 e/Å^3. c,d) Band and k point projected charge density for the conduction bands at the Λ point. Isosurface: 0.004 e/Å^3.

V. BONDING ANALYSIS OF PUCKERED PHOSPHORENE AND ARSENENE

The partial density of states (pDOS) and crystal orbital hamilton populations (COHP) were obtained using LOBSTER[7–10] with input from VASP PBE calculations[11–15]. From analysing pDOS and COHP, the orbital composition of the electronic structure and their bonding/antibonding nature can be obtained. The positive -COHP axis denotes bonding character of the covalent bonds and the negative -COHP axis antibonding character. The DOS and COHP of black phosphorene and puckered arsenene are shown in Fig. S10 and Fig. S11, respectively. We see that both the valence band edge and the conduction band edge the of phosphorene and arsenene have p character. The p-p interaction is slightly antibonding at the valence band edge and strongly antibonding for the conduction band, which is apparent from the COHP analysis.

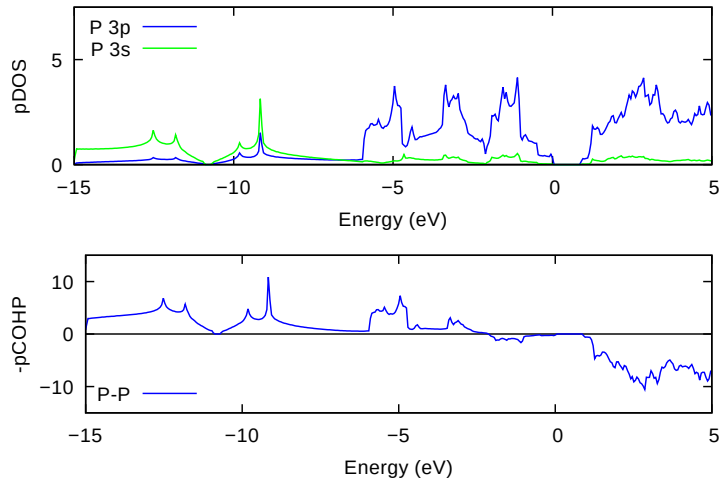

FIG. S10: Density of states (DOS) and bonding indicator (pCOHP) of black phosphorene. The energy of the valence band maximum is set to zero.

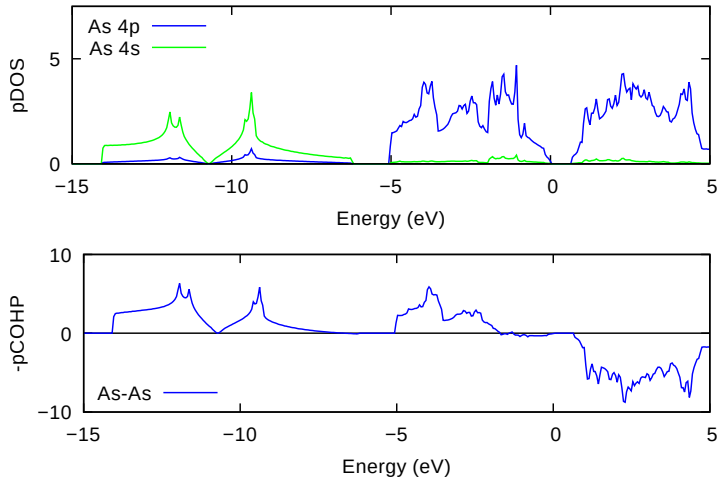

FIG. S11: Density of states (DOS) and bonding indicator (pCOHP) of puckered arsenene. The energy of the valence band maximum is set to zero.

* laurienm@mcmaster.ca

† rubelo@mcmaster.ca

[1] P. Giannozzi, S. Baroni, N. Bonini, M. Calandra, R. Car, C. Cavazzoni, D. Ceresoli, G. L. Chiarotti, M. Cococcioni, I. Dabo, A. D. Corso, S. d. Gironcoli, S. Fabris, G. Fratesi, R. Gebauer, U. Gerstmann, C. Gougoussis, A. Kokalj, M. Lazzeri, L. Martin-Samos, N. Marzari, F. Mauri, R. Mazzarello, S. Paolini, A. Pasquarello, L. Paulatto, C. Sbraccia, S. Scandolo, G. Sclauzero, A. P. Seitsonen, A. Smogunov, P. Umari and R. M. Wentzcovitch, *J. Phys. : Condens. Matter.*, 2009, **21**, 395502.

[2] A. A. Mostofi, J. R. Yates, G. Pizzi, Y.-S. Lee, I. Souza, D. Vanderbilt and N. Marzari, *Comput. Phys. Commun.*, 2014, **185**, 2309–2310.

[3] D. S. Koda, F. Bechstedt, M. Marques and L. K. Teles, *Phys. Rev. B*, 2018, **97**, 165402.

[4] N. Lu, Z. Zhuo, H. Guo, P. Wu, W. Fa, X. Wu and X. C. Zeng, *J. Phys. Chem. Lett.*, 2018, **9**, 1728–1733.

[5] F. Li, H. Wu, Z. Meng, R. Lu and Y. Pu, *J. Phys. Chem. Lett.*, 2019, **10**, 761–767.

[6] U. Herath, P. Tavadze, X. He, E. Bousquet, S. Singh, F. Muñoz and A. H. Romero, *Computer Physics Communications*, 2020, **251**, 107080.

[7] R. Nelson, C. Ertural, J. George, V. L. Deringer, G. Hautier and R. Dronskowski, *J. Comput. Chem.*, 2020, **41**, 1931–1940.

[8] V. L. Deringer, A. L. Tchougréeff and R. Dronskowski, *J. Phys. Chem. A*, 2011, **115**, 5461–5466.

[9] S. Maintz, V. L. Deringer, A. L. Tchougréeff and R. Dronskowski, *J. Comput. Chem.*, 2013, **34**, 2557–2567.

[10] R. Dronskowski and P. E. Bloechl, *J. Phys. Chem.*, 1993, **97**, 8617–8624.

[11] G. Kresse and J. Furthmüller, *Phys. Rev. B*, 1996, **54**, 11169–11186.

[12] G. Kresse and J. Furthmüller, *Comput. Mater. Sci.*, 1996, **6**, 15–50.

[13] P. E. Blöchl, *Phys. Rev. B*, 1994, **50**, 17953–17979.

[14] G. Kresse and D. Joubert, *Phys. Rev. B*, 1999, **59**, 1758–1775.

[15] J. P. Perdew, K. Burke and M. Ernzerhof, *Phys. Rev. Lett.*, 1996, **77**, 3865–3868.

Appendix D

Supplementary Information: Importance of the nonlocal exchange potential for effective mass calculations in semiconductors - Benchmarking exchange-correlation potentials with the mstar60 dataset

This appendix contains the supplementary information for Chapter 7.

Supplementary information: importance of the nonlocal potential for effective mass calculations in semiconductors: Benchmarking exchange-correlation potentials with the mstar60 dataset

Magdalena Laurien* and Oleg Rubel†
Department of Materials Science and Engineering, McMaster University, 1280 Main St W, Hamilton ON L8S 4L8, Canada
(Dated: December 13, 2021)

Input files and details of the workflow for the effective mass calculations with VASP for the example of InP are contained in the following file: VASP-mstar-InP.tar.gz.

Input files and details of the workflow for high-energy local orbital calculations with Wien2k at the PBE level for the example of monolayer MoS_2 can be found in the following file: WIEN2k-input-and-workflow.tar.gz.

The structure files of the `mstar60` data set can be found here: structures-after-atomic-relaxation.zip. The bulk structures have experimental lattice parameters, while atomic positions were relaxed with VASP at the PBE level until residual forces were less than 0.001 eV/Å. Monolayer materials were obtained by theoretical exfoliation from the corresponding bulk material. Monolayers were fully relaxed at the PBE level.

[1] O. Madelung, *Semiconductors: Data Handbook* (Springer Science & Business Media, 2004).
[2] K. K. Kam and B. A. Parkinson, The Journal of Physical Chemistry **86**, 463 (1982).
[3] D. A. Evans, A. G. McGlynn, B. M. Towlson, M. Gunn, D. Jones, T. E. Jenkins, R. Winter, and N. R. J. Poolton, Journal of Physics: Condensed Matter **20**, 075233 (2008), publisher: IOP Publishing.
[4] Y. L. Huang, Y. Chen, W. Zhang, S. Y. Quek, C.-H. Chen, L.-J. Li, W.-T. Hsu, W.-H. Chang, Y. J. Zheng, W. Chen, and A. T. S. Wee, Nature Communications **6**, 6298 (2015).
[5] M. M. Ugeda, A. J. Bradley, S.-F. Shi, F. H. da Jornada, Y. Zhang, D. Y. Qiu, W. Ruan, S.-K. Mo, Z. Hussain, Z.-X. Shen, F. Wang, S. G. Louie, and M. F. Crommie, Nature Materials **13**, 1091 (2014).
[6] B. Zhu, X. Chen, and X. Cui, Scientific Reports **5** (2015), 10.1038/srep09218.
[7] C. Zhang, Y. Chen, A. Johnson, M.-Y. Li, L.-J. Li, P. C. Mende, R. M. Feenstra, and C.-K. Shih, Nano Letters **15**, 6494 (2015), publisher: American Chemical Society.

* laurienm@mcmaster.ca
† rubelo@mcmaster.ca

TABLE S1. VASP calculation parameters. AEXX denotes the share of Hartree-Fock exchange included in the HSE06 functional in order to reproduce the experimental band gap. CBMJ denotes the fitting parameter c of the Tran-Blaha modified Becke-Johnson (TB-mBJ) exchange-correlation potential used to reproduce the experimental band gap. The experimental band gap to which TB-mBJ and HSE06 band gaps were fitted is also shown. Unless otherwise stated, all experimental band gaps are taken from Madelung [1]. For monolayers, the quasiparticle or transport band gap was used. NBANDS denotes the number of bands used for the optical calculations.

material	Exp. band gap (eV)	AEXX	CMBJ	NBANDS
Si	1.17	0.26	1.106	240
GaAs	1.52	0.305	1.231	288
GaN	3.5	0.2925	1.516	288
InP	1.42	0.2434375	1.166	288
CdS	2.48	0.32	1.24	560
CdTe	1.48	0.31375	1.217	400
PbS	0.29	0.1646875	1.04	320
PbSe	0.145	0.16257812	1.053	320
PbTe	0.187	0.1478125	1.1	400
SiC	2.4161	0.3	1.24	160
MoS_2	1.23 [2]	0.15273437	1.45	640
WS_2	1.35 [2]	0.162	1.365	640
bP	0.3125	0.308	1.25	440
BN	5.96 [3]	0.315	1.31	240
1L MoS_2	2.4 [4]	0.41044922		800
1L $MoSe_2$	2.18 [5]	0.5		800
1L WS_2	2.73 [6]	0.67517578		800
1L WSe_2	2.12 [7]	0.49007813		800

TABLE S2. Effective masses calculated with perturbation theory versus effective masses obtained from the band curvature for materials containing the transition metals Mo and W. Masses calculated from perturbation theory can be compared for different pseudopotentials and varying number of empty bands included in the optical calculations. All effective masses are given in units of m_0.

1L MoS_2, VASP	m_p (Γ)	m_p (K)	m_n (K)
PBE, band curvature	3.73	0.523	0.431
PBE, Mo_pv, 800 bands	10.6	0.613	0.445
PBE, Mo_sv, 800 bands	8.99	0.601	0.402
PBE, Mo_sv, 1600 bands	8.17	0.595	0.404
PBE, Mo_sv_GW, 800 bands	5.62	0.564	0.422
PBE, Mo_sv_GW, 1600 bands	5.11	0.559	0.425
PBE, Mo_sv_GW, 2400 bands	5.06	0.556	0.425
HSE, band curvature	2.39	0.470	0.337
HSE, Mo_pv, 800 bands	2.14	0.426	0.313
HSE, Mo_sv, 800 bands	2.08	0.421	0.312
HSE, Mo_sv_GW, 800 bands	1.75	0.396	0.320

1L MoS_2, Wien2k	m_p (Γ)	m_p (K)	m_n (K)
PBE, band curvature	3.56	0.523	0.442
PBE, Mo $4s$ as valence, $E_{max} = 19$ Ry, ca. 3500 bands	6.90	0.587	0.410
PBE, Mo $4s$ as valence, $E_{max} \approx 230$ Ry, ca. 4000 bands incl. 6 HELOs	3.60	0.527	0.439

1L $MoSe_2$, VASP		m_p (K)	m_n (K)
PBE, band curvature		0.581	0.507
PBE, Mo_pv, 800 bands		0.686	0.462
PBE, Mo_sv, 800 bands		0.672	0.468
PBE, Mo_sv_GW, 800 bands		0.637	0.488
HSE, Mo_pv, 800 bands		0.423	0.333
HSE, Mo_sv, 800 bands		0.418	0.333

1L WS_2, VASP	m_p (Γ)	m_p ($\bar{K}$)	$m_{p,so}$ ($\bar{K}$)
PBE, band curvature	2.93	0.339	0.477
PBE, W_sv, 800 bands	3.88	0.358	0.517
HSE, W_sv, 800 bands	1.04	0.237	0.358

1L WSe_2, VASP	m_p (Γ)
PBE, band curvature	4.46
PBE, W_sv, 800 bands	5.71
HSE, W_sv, 800 bands	1.44

bulk MoS_2 (2H), VASP	m_p (Γ)	m_p (K)
PBE, band curvature	0.678	0.525
PBE, Mo_pv, 640 bands	0.786	0.616
PBE, Mo_sv, 640 bands	0.774	0.603
PBE, Mo_sv, 1280 bands	0.765	0.599
PBE, Mo_sv_GW, 640 bands	0.731	0.565
PBE, Mo_sv_GW, 1280 bands	0.723	0.561
PBE, Mo_sv_GW, 1920 bands	0.721	0.560
HSE, Mo_pv, 640 bands	0.694	0.536
HSE, Mo_sv, 640 bands	0.685	0.527
HSE, Mo_sv_GW, 640 bands	0.646	0.494

bulk WS_2 (2H), VASP	m_p ($\bar{K}$)	$m_{p,VB-1}$ ($\bar{K}$)
band curvature (PBE)	0.337	0.464
PBE, W_sv, 640 bands	0.354	0.495
HSE, W_sv, 640 bands	0.321	0.454